Central Black Holes in Massive Early-Type Galaxies

Stephanie Prianto Rusli

SIGILL·UNIVERSITAT·LUDOVIC·MAXIM·

München 2012

Central Black Holes in Massive Early-Type Galaxies

Stephanie Prianto Rusli

Dissertation
an der Fakultät für Physik
der Ludwig–Maximilians–Universität
München

vorgelegt von
Stephanie Prianto Rusli
aus Jakarta, Indonesien

München, den 13 März 2012

Erstgutachter: Priv. Doz. Dr. Roberto P. Saglia
Zweitgutachter: Prof. Dr. Andreas Burkert
Tag der mündlichen Prüfung: 24 April 2012

Contents

List of Figures

List of Tables

Abstract

Supermassive black holes (SMBH) are believed to be omnipresent at the centers of galaxies. The mass of the SMBH ($M_{\rm BH}$) correlates with the stellar velocity dispersion and the luminosity of the galaxy in which it resides, creating the so-called $M_{\rm BH}$-σ and $M_{\rm BH}$-L relations. These relations suggest a strong connection between the formation and evolution of the SMBH and its host galaxy. Despite their importance, these relations are still poorly constrained in the high-$M_{\rm BH}$ regime. This is due to a small number of reliable SMBH detections in the mass range of $\sim 10^9 - 10^{10} M_\odot$. In the past decade, the shape and scatter of the $M_{\rm BH}$-σ relation have been repetitively challenged.

In this thesis, observations of the nuclei of eight massive early-type galaxies are presented and their $M_{\rm BH}$ are derived to increase the sample of SMBH in the high-$M_{\rm BH}$ regime. The eight galaxies consist of one lenticular and seven elliptical galaxies. The $M_{\rm BH}$ measurement was done by means of stellar dynamical modelling, making use of high-resolution stellar kinematic data obtained with SINFONI (Spectrograph for INtegral Field Observations in the Near Infrared) at the VLT (Very Large Telescope)*.

The SMBH masses of the seven ellipticals were derived by including a dark halo component in the modelling. To study the importance of the dark halo in $M_{\rm BH}$ determination, models without a dark halo were also evaluated. The results show that an unbiased $M_{\rm BH}$ can be derived without the need of a dark halo in the models when the spatial resolution of the kinematic data in the center is sufficiently high. For data having marginal spatial resolution, it is important that the mass-to-light ratio of the stellar component is not biased. This is because the mass-light-ratio is coupled to $M_{\rm BH}$. One way to derive an unbiased mass-to-light ratio is to take into account the dark halo in the dynamical modelling. In the case of the lenticular galaxy, $M_{\rm BH}$ was determined without a dark halo in the dynamical model. However, it is unlikely that the derived $M_{\rm BH}$ is biased because the data resolution is sufficiently good and because the mass-to-light ratios of the bulge and disc are decoupled.

The addition of the eight galaxies to the existing SMBH sample increases the slope of the $M_{\rm BH}$-σ and the $M_{\rm BH}$-L relations. The steepening of the $M_{\rm BH}$-σ relation, in particular, is mainly driven by the galaxies with $\sigma > 250$ km/s (one lenticular and six ellipticals). A SMBH of 10^{10} $M_\odot$ now corresponds to a velocity dispersion of ~ 420 km/s. This σ value is lower than previously expected for such $M_{\rm BH}$ and lower than the highest σ found in the local universe. This suggests that the most massive SMBHs that are observed in distant quasars continue to reside in the local high-σ galaxies today. The space density of SMBHs

---

*from the GTO programs 082.B-0037(A), 082.B-0037(B) and 082.B-0126(A) of Prof. Ralf Bender more massive than $3 \times 10^9\ M_\odot$ predicted by the $M_{\rm BH}$-σ relation is now closer to the one estimated from $M_{\rm BH}$-L relation, without the need to increase the intrinsic scatter of the $M_{\rm BH}$-σ relation.

In the seven elliptical galaxies, cores were identified. The core structure is thought to be the result of galaxy mergers involving SMBHs. Therefore, $M_{\rm BH}$ is expected to correlate with the core properties. By analysing the light profiles of the core galaxies with new/updated stellar dynamical $M_{\rm BH}$ measurements, it is shown that the light deficit in the core is larger for galaxies having higher velocity dispersions and higher $M_{\rm BH}$. The size of the core seems to correlate with $M_{\rm BH}$. The mass deficit varies greatly, ranging from about $0.05 M_{\rm BH}$ to $11 M_{\rm BH}$. These results are broadly consistent with the expectations from galaxy/SMBH merger simulations.

Zusammenfassung

Nach heutigem Forschungsstand vermutet man im Zentrum jeder Galaxie ein supermassereiches schwarzes Loch. Die Masse eines solchen schwarzen Lochs, $M_{\rm BH}$, korreliert sowohl mit der stellaren Geschwindigkeitsdispersion als auch mit der Leuchtkraft der Galaxie, in deren Zentrum es sich befindet. Diese Korrelationen sind als $M_{\rm BH}$-σ und $M_{\rm BH}$-L-Beziehungen bekannt. Sie legen nahe, dass zwischen der Entstehung und Entwicklung des schwarzen Lochs und seiner umgebenden Wirtsgalaxie ein enger Zusammenhang besteht. Obwohl von grundlegender Bedeutung, ist der Verlauf dieser Beziehungen für die grössten $M_{\rm BH}$ noch immer nicht genau bekannt. Der Grund ist die geringe Anzahl zuverlässiger Nachweise von schwarzen Löchern im Massenbereich zwischen $\sim 10^9$ und $\sim 10^{10} M_\odot$. In den vergangenen zehn Jahren wurden der Verlauf und die Streuung der $M_{\rm BH}$-σ-Beziehung immer wieder in Frage gestellt.

In dieser Arbeit wurden die Galaxienkerne von acht massereichen Galaxien beobachtet und die Massen ihrer zentralen schwarzen Löcher bestimmt, um die Statistik der $M_{\rm BH}$-Messungen im Bereich der grössten Massen zu verbessern. Bei den beobachteten Galaxien handelt es sich um sieben elliptische Galaxien und eine linsenförmige. Die Bestimmung der $M_{\rm BH}$ erfolgte mit Hilfe stellardynamischer Modellrechnungen, für die hochaufgelöste kinematische Daten des Feldspektrographen SINFONI am Very Large Telescope (VLT) verwendet wurden[*].

Bei der Bestimmung der Massen der schwarzen Löcher in den sieben elliptischen Galaxien wurde auch eine Halokomponente aus dunkler Materie mitberücksichtigt. Um den Einfluss der dunklen Materie auf die Bestimmung von $M_{\rm BH}$ zu untersuchen, wurden jeweils auch Vergleichsmodelle ohne dunklen Halo ausgewertet. Die Ergebnisse zeigen, dass auch ohne eine dunkle Halokomponente in den Modellen unverfälschte $M_{\rm BH}$ gewonnen werden, solange die räumliche Auflösung der kinematischen Daten im Zentrum genügend hoch ist. Haben die Daten allerdings nur eine kaum oder gerade ausreichende räumliche Auflösung, dann wird es wichtig, das Masse-Leuchtkraft-Verhältnis der stellaren Komponente korrekt zu bestimmen, da das Masse-Leuchtkraft-Verhältnis an $M_{\rm BH}$ gekoppelt ist. Eine Möglichkeit, ein unverfälschtes Masse-Leuchtkraft-Verhältnis zu erhalten, besteht darin, die dunklen Halos in die dynamische Modellierung einzubeziehen. Bei der linsenförmigen Galaxie wurde $M_{\rm BH}$ ohne einen dunklen Halo bestimmt. Es ist jedoch unwahrscheinlich, dass hierbei die $M_{\rm BH}$-Messung verfälscht wurde, da die räumliche Auflösung der Daten hinreichend gut ist und ausserdem die Masse-Leuchtkraft-Verhältnisse von Bulge (dies ist

---

[*] aus den GTO Programmen 082.B-0037(A), 082.B-0037(B) and 082.B-0126(A) von Prof. Ralf Bender

der Zentralbereich der Galaxie) und Scheibe getrennt voneinander betrachtet wurden.

Fügt man die acht Galaxien aus dieser Arbeit zu den bisher bekannten $M_{\rm BH}$ Messungen hinzu, so nimmt die Steigung der $M_{\rm BH}$-σ und $M_{\rm BH}$-L-Beziehungen zu. Speziell für die $M_{\rm BH}$-σ-Beziehung verursachen dies im wesentlichen die Galaxien mit $\sigma > 250$ km/s (die linsenförmige sowie sechs elliptische). Ein schwarzes Loch von 10^{10} $M_\odot$ entspricht nun einer Geschwindigkeitsdispersion von $\sim$ 420 km/s. Dieser Wert für ein solch massereiches schwarzes Loch ist kleiner als bisher angenommen und befindet sich damit nun in einem σ-Bereich, der im lokalen Universum durchaus vorkommt. Dies lässt darauf schliessen, dass sich die massereichsten schwarzen Löcher, die man in entfernten Quasaren beobachtet, heute in denjenigen lokalen Galaxien befinden, in denen man die höchsten Geschwindigkeitsdispersionen beobachtet. Die aus der $M_{\rm BH}$-σ-Beziehung abgeleitete Raumdichte schwarzer Löcher mit Massen größer als 3×10^9 $M_\odot$ stimmt nun – auch ohne die Notwendigkeit eine grössere intrinsische Streuung anzunehmen – besser mit derjenigen überein, die man nach der $M_{\rm BH}$-L-Beziehung erwarten würde.

Die sieben elliptischen Galaxien sind sogenannte "Core-Galaxien", d.h. ihr Leuchtkraftprofil flacht zum Zentrum hin ab. Es wird angenommen, dass diese Struktur im Leuchtkraftprofil beim Verschmelzen von Galaxien entsteht, die supermassereiche schwarze Löcher beherbergen. Daher erwartet man, dass die $M_{\rm BH}$ mit den charakteristischen Eigenschaften dieser Strukturen korrelieren. Durch die Analyse der Leuchtkraftprofile der Core-Galaxien mit den neuen bzw. aktualisierten stellardynamischen $M_{\rm BH}$-Messungen wird gezeigt, dass das Leuchtkraftdefizit im Zentrum mit der Geschwindigkeitsdispersion und mit $M_{\rm BH}$ wächst. Der Radius der zentralen Abflachung korreliert offenbar mit $M_{\rm BH}$. Das Massendefizit variiert stark zwischen etwa $0.05 M_{\rm BH}$ und $11 M_{\rm BH}$. Diese Ergebnisse liegen im Bereich dessen, was man nach Simulationen von Galaxienverschmelzungen erwarten würde.

Chapter 1

Introduction

1.1 Supermassive Black Holes

Black holes are among the most fascinating consequences of Einstein's theory of General Relativity. There is so much matter in a black hole packed into a very small volume such that gravity dominates other forces. Space and time around black holes get distorted and nothing can escape from the black hole, not even light. Theoretically, the simplest kind of black holes was discovered by K. Schwarzschild who solved Einstein's field equation for a non-rotating spherical star. The knowledge that this state could be reached by a real star was due to Chandrasekhar, who was studying the structure of white dwarfs. On theoretical grounds he proposed that there exist a maximum mass for a stable white dwarf (Chandrasekhar, 1931), now called the Chandrasekhar limit, that also applies in the case of degenerate systems like neutron stars. Many follow-up studies after this have led to the understanding that black holes are the end result of the evolution of massive stars (with masses of about $20M_\odot$ or more). When the degenerate core of a dying massive star exceeds the Chandrasekhar limit, it collapses into a black hole while ejecting the outer layers in a supernova (type II) explosion. This kind of black hole is now classified as the stellar-mass black hole, thought to be the engine of many X-ray galactic sources. The first observational detection of this class of black holes came around 1972 when the mass of the X-ray source Cygnus X-1 was found to be above the mass range of white dwarfs and neutron star, making the black hole conclusion inescapable (Mauder, 1973; Rhoades & Ruffini, 1974).

For much of the 20th century, black holes were considered more as mathematical formulations rather than real objects in nature, although observational hints (not realized) were already found in 1932 by Karl Jansky in the form of radio emission from the Galactic center and in 1943 when Seyfert galaxies were discovered (Seyfert, 1943). The existence of black holes was not generally acknowledged until the emerging period of radio astronomy brought about the discovery of quasars. One of the first quasars (quasi-stellar radio sources) that were discovered is 3C273, identified in 1963 as a radio source with a star-like optical counterpart –hence the name. The emission lines in the photographic spectrum of this object were found to be redshifted by $\sim 15\%$, corresponding to a distance of about 2 billion light years and making it the most distant object that was known at the time (Schmidt, 1963). What was astonishing is that it appeared bright. An apparent visual brightness of ∼13 mag at that distance implied a very high luminosity. In addition, quasars are shown to have flux variability on a very short time scales, down to minutes. Since the velocity of light is finite, the region from which the emission comes from must be very small.

The amount of energy released by the quasars, from a very small volume, cannot be explained by conventional processes of energy production. Nuclear reactions quickly became irrelevant due to their low efficiency. Of all the mechanisms proposed to explain this phenomena, one has become acceptable nowadays: accretion of material onto a massive compact object and the accompanying release of gravitational energy. This was first proposed by Salpeter (1964) and Zel'Dovich & Novikov (1964) and later explored by Lynden-Bell (1969) in terms of black hole formalisms. Over the years, many more galaxies showing energetic phenomena were observed, albeit with weaker activity than quasars (e.g. Seyfert galaxies, BL Lacs). It soon became clear that these are related to quasars and fall into the same category of galaxies, now called active galactic nuclei (AGN). Along with that, accretion onto massive black holes was progressively implicated as the powerhouse for the quasars and other weaker AGN. The enormous energy produced in quasars or AGN require the accreting object to be millions or billions of solar masses, giving it the name supermassive black hole to distinguish it from its stellar-mass counterpart.

Studies of the number of quasars show that the space density of bright quasars reached its peak at the redshift of $\sim 2-3$ and has been decreasing steadily since then. There are many more quasars at high redshift than at lower redshift. This implies that the local universe must be populated with quasar remnants: relic supermassive black holes that have exhausted their fuel supply that once made the quasar so bright. Soltan (1982) was the first to come up with an argument that quasar counts can be used as an indicator of the mass of dead quasars which should be accumulated in the local universe. If quasars are indeed powered by supermassive black holes through accretion, the mass density of the supermassive black holes in nearby galaxies should match that inferred from the quasars. Using the improved optical quasar survey, Soltan's argument has been revisited several times. Chokshi & Turner (1992) derived the present total mass density of quasar remnants to be $2.2 \times 10^5 (C_B/16.5)(0.1/\epsilon) M_\odot \mathrm{Mpc}^{-3}$. C_B is the bolometric correction and ϵ is the mass-to-energy conversion efficiency, generally taken to be 0.1 for optically thick but geometrically thin accretion disks. Yu & Tremaine (2002) used the quasar luminosity and redshift distribution of Boyle et al. (2000) to arrive at $2.1 \times 10^5 (C_B/11.8)[0.1(1-\epsilon)/\epsilon] M_\odot \mathrm{Mpc}^{-3}$. This generally agrees with the estimate of Chokshi & Turner (1992).

1.2 Black Hole Search

The scenario of supermassive black holes in the heart of quasars had become a popular paradigm by the early 1980, yet there was no direct evidence of supermassive black holes. The black hole search therefore became a hot topic. The past several decades have seen a rise in observational efforts to detect black holes. Black holes are not directly observable, although they can be probed through their influence on the surrounding matter, i.e the motion of stars or gas that are close enough to the hole. There is, however, one caveat. By observing these stars or gas, one detects a *massive dark object*, which is not necessarily a supermassive black hole. It could be, for example, a cluster of dark objects. This alternative can be excluded in the case of the Galactic center and NGC 4258 (see below), given the small volume within which the enclosed mass is estimated (Maoz, 1995, 1998). For other galaxies, the data are usually not sufficient to infer the exact form of the massive dark object, although a supermassive black hole is a likely candidate. In the rest of this thesis we use the term “SMBH” for supermassive black hole or simply “black hole” to refer to the massive dark object detected at the centers of galaxies.

The most compelling empirical evidence for a SMBH is provided by our own Galaxy, the Milky Way. The strong radio source Sgr A* that sits in the center of Galaxy, has long been suspected (and now proven) to be associated with SMBH. Due to its proximity, detailed orbital studies of the individual stars in the close vicinity of SMBH are possible. The orbital motion of stars in the central parsec is traced by combining the information from the proper motion (projected motion on the sky) and the radial velocity (e.g. Ghez et al. 2005; Gillessen et al. 2009). These orbits and the application of Kepler’s law provide the mass of the central compact object. The orbital data exclude possible configurations of central mass concentration, such as a dark cluster of neutron stars or fermion balls, other than a supermassive black hole. The most recent estimate of the black hole mass is 4.3×10^6 $M_\odot$.

Outside our galaxy, the black hole search becomes slightly more difficult. There are several techniques that have been employed to measure the black hole mass of nearby galaxies and AGN, as described in the following paragraphs.

Water maser

Strong stimulated emission at radio wavelengths can provide the means to detect a black hole and infer its mass. This method especially works well for Seyfert 2 galaxies (AGN with narrow optical spetral emission lines) where the dust torus around the central black hole is seen edge on, thereby allowing for optimal maser amplification. The best case for this technique is the Seyfert 2 galaxy NGC 4258. VLBA (Very Large Baseline Array) observations on this galaxy reveal that the water maser emission originates from molecular clouds that trace a thin and nearly edge-on gas disk/annulus (Miyoshi et al., 1995), making their dynamics easy to interpret. The emission regions define nearly perfect keplerian orbits with velocities that very closely scale as $v(r) \propto r^{-1/2}$. The inner edge of the annulus is ~ 0.13 pc and the velocity reaches $\sim$1000 km/s, thereby constraining the enclosed mass within 0.13 pc to 3.6×10^7 $M_\odot$.

Gas kinematics

One simple method to detect a SMBH is by exploring the ionized gas kinematics in the nucleus (e.g Harms et al. 1994; Ferrarese et al. 1996). Emission lines originating from a circumnuclear rotating gas disk are used as a tool to interpret its dynamics. The observed line velocities are compared to the prediction of a model where gas is confined in a thin disk that rotates in a Keplerian motion around the central black hole. The free parameters of the model include $M_{\rm BH}$, inclination of the disk and its projected position angle. The main assumption is that the gas motion is influenced solely by gravitational forces from the stars and the black hole. The best-fit parameters are derived through a χ^2 analysis.

Stellar dynamics

Stellar dynamical search for black holes in external galaxies is pioneered by two seminal papers by Young et al. (1978) and Sargent et al. (1978). They inferred the presence of black hole in M87 from the observations of stellar kinematics and surface brightness profile, assuming an isotropic and spherically symmetric system. However, it was soon discovered that anisotropic models can also recover the observed properties without the need of a black hole. This revealed the so-called mass-anisotropy degeneracy problem (Binney & Mamon, 1982).

Apart from theoretical uncertainties due to the unknown orbital structure, a convincing black hole detection also faces observational challenges due to the need of high spatial resolution and spectral signal-to-noise ratio. The former is usually dictated by the size of the black hole's sphere of influence, i.e. the region within which the black hole's gravitational potential dominates that of the surrounding stars. Mathematically, the radius of influence is expressed as

$$r_{\rm SoI} = GM_{\rm BH}/\sigma^2, \tag{1.1}$$

where G is the gravitational constant and σ is the characteristic stellar velocity dispersion of the host bulge. The angular size corresponding to $r_{\rm SoI}$ for a galaxy at a distance D becomes

$$\theta_{\rm SoI} \sim 1" \left(\frac{M_{\rm BH}}{10^8 M_\odot}\right) \left(\frac{\sigma}{100\,{\rm km/s}}\right)^{-2} \left(\frac{D}{10\,{\rm Mpc}}\right)^{-1}. \tag{1.2}$$

Since the work of Sargent et al., dynamical models for the stellar kinematics have improved considerably. A spherical and non-rotating isotropic model has a phase-space distribution function (positions and velocities) that can be described by only one integral of motion, i.e. the total energy of the system. Relaxing the assumption of isotropy means that the phase-space distribution function must depend on at least two integrals of motion. Axisymmetric two-integral models of many elliptical galaxies, however, still do not provide a good fit to the observed stellar kinematics (e.g. van der Marel et al. 1998, Cretton & van den Bosch 1999, Gebhardt et al. 2000b), implying the need for a third integral. Although the analytical form of this integral is unknown, the use of three-integral models allow a more general and less constrained way of modelling galaxies.

M. Schwarzschild devised a method to build models of galaxies in equilibrium without an explicit knowledge of the integrals of motion (Schwarzschild, 1979). This is done by creating an orbit library from a trial gravitational potential which may include a black hole. The weighted superposition of the orbits is then optimized to match the kinematics and to recover the light distribution of the stars. The trial potential (and so the black hole mass) which best fits the observables is selected. One apriori assumption is needed, i.e. the inclination, to be able to constrain the models given the observables. Schwarzschild method permits the construction of models in both axisymmetric and triaxial potentials. While most dynamical models assume axisymmetry, a modelling code for triaxial systems has also been developed and applied to measure a black hole mass (van den Bosch et al., 2008)

The stellar dynamical way of detecting a black hole, in particular the use of axisymmetric, three-integral models through Schwarzschild modelling is the method of choice in this thesis (see section 2.6). The gravitational potential in galaxy nuclei, close to the black hole, can be well approximated by a spherical or axisymmetric (in the case of a stellar disk around the black hole) potential. Up until 2009, the potential of the models is usually calculated from the contribution of only the black hole and stars. Gebhardt & Thomas (2009) question this for models of massive core galaxies, since the inclusion of a dark matter potential in the model increases the mass of the black hole in the case of M87 (see Chapter 4 for details).

Reverberation mapping

Dynamical methods that require good spatial resolution are generally not applicable to AGNs because they are typically farther away and the active nuclei overwhelm the stellar spectral features. So for AGNs, their variability is used as an indicator, by analysing the non-thermal continuum and broad emission lines seen in their spectra. The continuum is due to accretion onto the black hole that radiates energy and excites the surrounding gas, producing the Doppler-broadened emission lines. Variability in the continuum would reach the gas only after some time. The time delay between the change in continuum and the emission lines gives information on how far out the gas is (R) assuming light travel time. Applying a virial theorem, one can derive M_{BH} from this time delay and the width of the emission lines σ: $M_{\mathrm{BH}} = fR\sigma^2/G$. f is a fudge factor that takes into account the details of the gas (inclination, geometry) and is largely unknown. The implicit assumption in this method is that gravity is the dominant force. This technique is particularly useful to determine M_{BH} in AGN type 1 where the region that produces the broad emission lines is not hidden by the dust torus.

Fe Kα line

Iron line Fe Kα is the strongest emission line found in AGN X-ray spectra and one of the best diagnostics of the regions in the immediate vicinity of the black hole. Observational studies indicate that this line originates from the innermost part of the relativistically rotating accretion disk, close to event horizon of the black hole. The observed line appears broad and skewed showing a red wing, although intrinsically it is narrow and symmetric. It is thought that the Doppler shift changes the line shape into a double-horned shape and the Doppler boosting causes the blue part to be stronger than the red part. In addition, the line is also redshifted due to gravitational redshift (Nandra et al., 1997). The black hole spin and the disk inclination influence the exact shape of the observed line. Using the iron line reverberation mapping, $M_{\rm BH}$ can be determined, but this would have to wait until the launch of the next generation of X-ray telescopes.

X-ray emitting gas in hydrostatic equilibrium

Brighenti & Mathews (1999) suggested a method to identify SMBH in quiescent giant elliptical galaxies. They argue that the black hole should have gravitational impact on the distribution of the hot inter-stellar medium. In X-ray observations, this impact should be visible as a temperature peak in the center (radius of 50 pc or less) due to thermal heating. This temperature peak is, however, not easy to detect due to the small spatial scale and the non-thermal disturbances in the centers of many early-type galaxies. Humphrey et al. (2008) apply this method to NGC 4649, a nearby bright galaxy. NGC 4649 shows a relaxed X-ray morphology, implying that hydrostatic equilibrium is a good approximation. They report a black hole mass that is consistent with that obtained using the stellar kinematics. Galaxy candidates for which this method can be used are core galaxies with gas in hydrostatic equilibrium.

1.3 Scaling Relations

Growing evidence for the existence of supermassive black holes has led to the discovery of empirical relations between the black holes and the properties of the host galaxies/bulges. The first is the apparent correlation between the bulge luminosity $\mathrm{M_B}$ with $M_{\rm BH}$ (Kormendy & Richstone 1995; Magorrian et al. 1998). Several years after that, Ferrarese & Merritt (2000) and Gebhardt et al. (2000a) independently discovered the log-linear relationship between the stellar velocity dispersion σ of the bulge (measured outside the sphere of influence) with $M_{\rm BH}$. Over time, some other galaxy parameters, e.g. the bulge concentration and the number of globular clusters, have been shown to also correlate with $M_{\rm BH}$(Graham et al., 2001; Burkert & Tremaine, 2010). By using these correlations, in principle $M_{\rm BH}$ can be estimated indirectly from the observed properties of the bulges. The one correlation that so far has been the tool of choice in the study of SMBH demographics is the $M_{\rm BH}$-σ relation, due to its small scatter.

The $M_{\rm BH}$-σ relation allows us to compute the mass density of SMBHs and compare it to the energy density in the radiation due to quasars (Soltan, 1982). Aller & Richstone (2002) converted luminosity functions for various Hubble types to velocity dispersion functions using the Faber-Jackson relation. These were then converted to black hole mass functions using the $M_{\rm BH}$-σ relation. The total mass density of black holes at zero redshift was found to be $4.8 \times 10^5 h^2 M_\odot \mathrm{Mpc}^{-3}$. Yu & Tremaine (2002) used luminosity and velocity dispersion functions from SDSS galaxies and found $2.5 \times 10^5 M_\odot \mathrm{Mpc}^{-3}$ for $h = 0.65$. Both values are comparable. The mass density of black holes is thus approximately what is expected from the quasar statistics (section 1.1), when the energy-to-mass efficiency is around 0.1. This consistency supports the accreting-black-hole hypothesis that SMBH are the relic of quasars and have acquired most of their mass during the quasar epoch. This agreement should, however, be taken with caution. The calculation of quasar luminosity function has uncertainties in the correction for obscured quasars and the black hole mass density calculation is critically dependent on the scatter and slope of the M_{BH}-σ relation.

Netzer (2003) noted a problem posed by the detection of black holes with masses exceeding 10^{10} $M_\odot$ in luminous distant quasars. Based on the known black hole-bulge relations, these black holes should be hosted by galaxy bulges with masses and velocity dispersions higher than 10^{13} $M_\odot$ and $\sim$ 700 km/s, respectively. Such massive galaxies are not found in the nearby universe. Bechtold et al. (2003), Vestergaard (2004) and Shields et al. (2006) argued that indeed some quasars appear to have this black hole mass. Yoo et al. (2007) generated Monte Carlo merger histories of massive halos and they conclude that black holes of $\sim 10^{10} M_\odot$ should exist in galaxy clusters. If the local SMBH obtained most of their masses from the accretion during the quasar activity, they cannot be smaller than the black holes in the distant quasars. This disagreement prompted the search for local galaxies with the highest velocity dispersions (Salviander et al., 2008). They found the highest σ to be 444 km/s with no evidence for galaxies with $\sigma > 500$ km/s. Indeed, it seems that the number density of the most massive black holes in quasars far exceeds the local abundance of proportionally massive galaxies. If the black hole masses of these quasars are correct, the shape of the M_{BH}-σ relation has to be different in the high-M_{BH} end.

Further evidence that supports this indication comes from Lauer et al. (2007) who found that for luminous brightest cluster galaxies (BCGs), the prediction of the M_{BH}-σ and the M_{BH}-L (L for bulge luminosity) contradicted each other, with the latter predicting more massive M_{BH} than the former. This is due to the fact that as the galaxy luminosity increases, the velocity dispersion levels off. The local black hole mass density predicted from the M_{BH}-L relation for $M_{\mathrm{BH}} > 3 \times 10^9$ $M_\odot$ was higher than that inferred from the M_{BH}-σ relation by almost an order of magnitude. While it suggests that the M_{BH}-L might be a better standard for the masses of black holes in luminous BCGs and that it is in a better agreement with quasar's result, the problem with the M_{BH}-σ relation remains.

Presented with these contradictions, it is important to increase the number of galaxies that shape the M_{BH}-σ relation, especially galaxies that occupy the low and the high-σ end of the relation. Since its parametrization by Gebhardt et al. (2000a), the M_{BH}-σ relation has been re-evaluated multiple times as more reliable M_{BH} measurements became available. The tendency is that the slope becomes steeper. After Tremaine et al. (2002) and Gültekin et al. (2009b), the most recent evaluation was done by McConnell et al. (2011b), who took into account the discovery of 10^{10} $M_\odot$ black holes in two BCGs (Fig. 1.1) that further steepened the M_{BH}-σ slope considerably. Moreover, the finding of black holes with such masses provides an important evidence that BCGs host the remnants of luminous

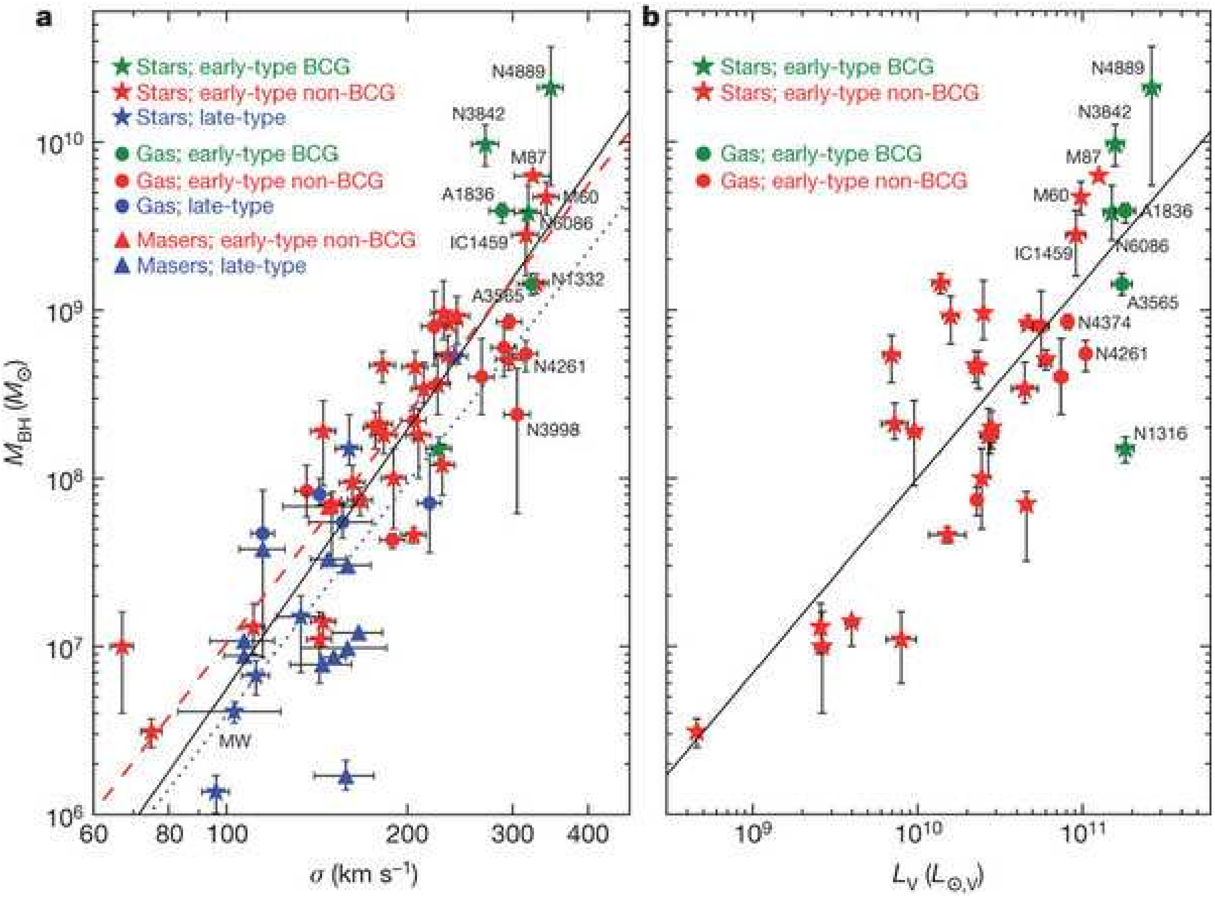

Figure 1.1: The relation between $M_{\rm BH}$ and bulge parameters in the version of McConnell et al. (2011b): the $M_{\rm BH}$-σ relation on the left and $M_{\rm BH}$-L on the right side. The solid, dash and dotted line correspond to the fit to all galaxies, early-type galaxies and spiral galaxies, respectively.

quasars and suggests that the slope, scatter or shape of the $M_{\rm BH}$-σ relation is likely still subject to change.

Apart from the unresolved issues, the scaling relations – especially the $M_{\rm BH}$-σ relation – are of significant importance in understanding how galaxies might have formed. The $M_{\rm BH}$-σ and $M_{\rm BH}$-L relations are surprisingly tight. The fact that the central black holes appear to "know" about the stars that are outside their sphere of influence implies that the black holes must somehow be involved in the formation and evolution of galaxies. In this respect, the knowledge of how the scaling relations evolve as a function of redshift (e.g. Merloni et al. 2010) becomes important. Feedback mechanisms as forms of communication between the black hole and the host galaxy to regulate the growth of both components (e.g Silk & Rees 1998) are also required . Most theoretical models use the local relations as constraints, but their redshift evolution remains as predictions. Surely, it becomes necessary to provide unbiased determinations of the behaviour of these scaling relations

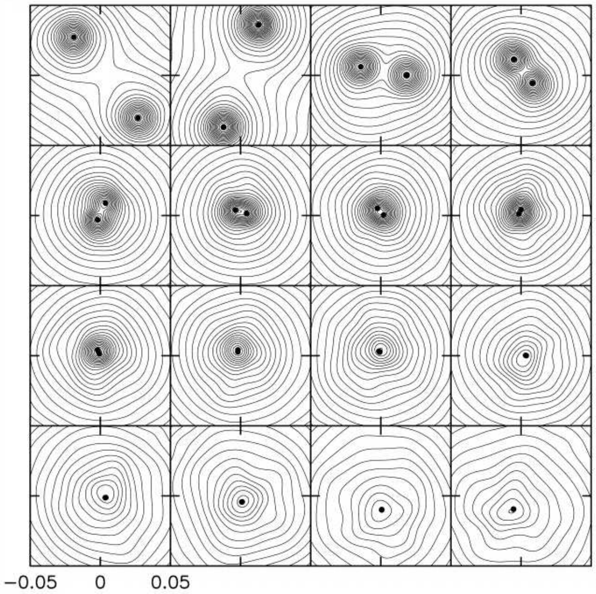

Figure 1.2: The illustration of merger of galaxies that contain central black holes, as followed by computer simulations. The curves represent the density contours of stars and the black dots represent the black holes. The binary system ejects stars from the nucleus and eventually lowers the surrounding stellar density (Milosavljević & Merritt, 2001).

now and then.

1.4 Merging Supermassive Black Holes

One exciting scenario that connects the central black hole and the galaxy was proposed by Begelman et al. (1980). They explored the possibility of a pair of black holes orbiting each other as a result of galaxy merger. In the current paradigm of galaxy formation, merger of galaxies is considered a common event during the evolution of massive galaxies. In such a merger, the supermassive black holes at the centers of the two galaxies would sink towards the center of the newly merged galaxy due to dynamical friction. At the center, the black holes would spiral further inwards that they become bound to each other and form a binary. As the orbits of the black holes decay and as the binary hardens, stars that come close enough are ejected. This would lower the density of the stars around the binary. It is therefore predicted that there should be a deficit of stars in the central region.

After the launch of the Hubble Space Telescope (HST), observations of central regions of nearby galaxies revealed two different nuclear structures (Ferrarese et al. 1994; Lauer et al. 1995). Based on the light profile, galaxies are classified into "power-law" and "core" galaxies. The former shows a surface brightness profile that can be fitted with a single power law all the way to the center, while the latter shows a break from the steep slope in the outer part to a shallower inner slope (core). Power-law galaxies generally coincide with faint galaxies and the core is mainly found in luminous massive galaxies. Nowadays, the formation paradigm is that the power-law galaxies are formed in wet mergers involving star formation. This explains the increased amount of light in the center compared to core galaxies, which are the results of dry mergers (without star formation).

Provided with observational clues, numerical studies were carried out to pursue the binary scenario further. Milosavljević & Merritt (2001) simulated galaxy mergers involving central black holes and successfully demonstrated that two galaxies with steep density cusps in the center can merge into a galaxy with shallow power-law cusp. Fig. 1.2 provides a nice illustration of this. Merritt (2006) quantified the mass deficit that was caused by the binary. He concluded that the amount of stellar mass that was lost scaled with the number of mergers experienced by the galaxy. More accurately, it can be written as $0.5 \times N \times M_{\rm BH}$ where $M_{\rm BH}$ is the final black hole mass. This was estimated by following the binary evolution up to the stalling radius/separation. At this point, the binary's hardening rate drops dramatically; the density of the surrounding stellar cluster is too low, the dynamical friction effectively shuts off and there are less stars that can be ejected to harden the binary. For luminous elliptical galaxies, stellar orbit repopulation by two-body relaxation happens on very long timescales and thus increases the likelihood of finding the stalled binary. The stalling radius is typically of order of 1 pc. Rodriguez et al. (2006) reported a projected separation of 7.3 pc between a pair of black holes with a total mass of $\sim 1.5 \times 10^8\ M_\odot$.

Binary black holes are expected to eventually merge and create a bigger hole. The circumstances under which the binary can coalesce beyond the stalling radius is, however, still poorly understood, which leads to the term "the final parsec problem". Several mechanisms that can increase the hardening rate are proposed, for example, the interaction with the accretion disk (Armitage & Natarajan, 2002), triaxial bulge (Yu, 2002) or the brownian motion of the binary (Chatterjee et al., 2003). These processes may help the binary to coalesce and when that happens, gravitational wave emission will impart a kick on the coalescing binary and eject it from the center. In dwarf galaxies or globular clusters, there is a good chance that the binary will escape but in large galaxies, this is not so likely. In what follows, the binary will decay down and fling out more stars on the way back to the center. Gualandris & Merritt (2008) simulated this and found that this process added up to the mass deficit created before the coalescense by up to $5M_{\rm BH}$. This serves as an explanation to the large cores found in giant elliptical galaxies. Given this prediction on the mass deficit due to the binary recoil, it is not easy to infer the number of mergers that a galaxy experienced just from the measured mass deficit.

Kormendy & Bender (2009) presented measurements of the light and mass deficit in elliptical galaxies with cores. They showed that the light deficit was correlated with the velocity dispersion σ and with the black hole mass. They interpreted this result as a support for the suggestion that core galaxies were made in dry mergers of galaxies with central black holes and the power-law galaxies (the ones with the extra light in the center) were formed in wet mergers. It is worth emphasizing that these correlations are based on a sample of eleven galaxies, six of which use $M_{\rm BH}$ derived from the $M_{\rm BH}$-σ relation.

1.5 The Sample and Thesis Outline

This thesis is based on a sample of high-σ galaxies, which often coincide with massive galaxies and/or galaxies with cores. The sample consists of eight early-type galaxies: one lenticular and seven ellipticals. These galaxies are part of a larger sample comprising various types of galaxies and spanning a wider σ range; all the data are collected within the framework of SINFONI black hole survey (Nowak, 2009). The primary data of all galaxies were taken using an integral-field unit (IFU) called SINFONI (Spectrograph for INtegral Field Observations in the Near Infrared), mounted on the UT4 of the Very Large Telescope. In this thesis, the black hole masses of the eight galaxies are determined, by means of stellar dynamical modelling. Table 1.1 provides a compilation of the properties of these eight galaxies and the expected black hole masses based on the M_{BH}-σ relation of Tremaine et al. (2002):

$$\log(M_{\mathrm{BH}}/M_{\odot}) = (8.13 \pm 0.06) + (4.02 \pm 0.32)\log(\sigma/200\mathrm{km/s}) \tag{1.3}$$

and Gültekin et al. (2009b):

$$\log(M_{\mathrm{BH}}/M_{\odot}) = (8.12 \pm 0.06) + (4.24 \pm 0.32)\log(\sigma/200\mathrm{km/s}). \tag{1.4}$$

The predicted angular size of the sphere of influence (equation 1.2) is also calculated based on the black hole mass inferred from the M_{BH}-σ relation of Tremaine et al.

Table 1.1: The galaxies examined in this thesis. The core classification in column 2 is based on the analysis in Chapter 5. Distance is stated in Mpc, see Chapter 3 and 4 for the references. The central velocity dispersion σ_0 is in km/s, taken from HyperLeda. The black hole mass, in the unit of $M_{\odot}$, is derived from the M_{BH}-σ relation of Tremaine et al. (2002) (T02) and Gültekin et al. (2009b) (G09). θ_{SoI} is the angular radius of the sphere of influence (arcsec) based on M_{BH} of T02.

Galaxy	Type	Distance	σ_0	M_{BH}(T02)	M_{BH}(G09)	θ_{SoI}
NGC 1332	S0	22.30	320.9 ± 13.7	9.0×10^8	1.1×10^9	0.39
NGC 1374	E/core	19.23	186.4 ± 3.9	1.0×10^8	9.7×10^7	0.15
NGC 1407	E/core	28.05	270.6 ± 6.1	4.5×10^8	5.0×10^8	0.22
NGC 1550	E/core	48.5	308.0 ± 6.2	7.7×10^8	8.9×10^8	0.17
NGC 3091	E/core	51.3	321.4 ± 9.3	9.1×10^8	1.1×10^9	0.17
NGC 4472	E/core	17.14	293.8 ± 2.9	6.3×10^8	7.2×10^8	0.43
NGC 5516	E/core	54.5	307.3 ± 11.9	7.6×10^8	8.8×10^8	0.15
NGC 7619	E/core	51.52	322.5 ± 5.5	9.2×10^8	1.1×10^9	0.17

Using this sample, we address the problems related with M_{BH} measurements in massive, luminous and core galaxies. We have mentioned these in the previous sections separately, which we summarize again here. The first is to sample better the black hole-bulge correlation at the high-M_{BH} end. This is motivated by (1) the contradiction between the quasar studies and the $M_{\rm BH}$-σ relation for black holes with $M_{\rm BH}$ of $\gtrsim 10^{10}\ M_\odot$, (2) the contradiction between $M_{\rm BH}$ predicted by the $M_{\rm BH}$-σ and $M_{\rm BH}$-L relations for luminous galaxies and (3) the relatively small number of galaxies that constrain the correlations at the high-$M_{\rm BH}$ end. Secondly, to address the notion raised by Gebhardt & Thomas (2009) that dark matter inclusion in the Schwarzschild modelling of galaxies with shallow density profiles in the central region is necessary to obtain a reliable $M_{\rm BH}$. Our sample is just the type of galaxies that they claim to be vulnerable to the bias due to the dark matter exclusion in the modelling. The third and last one, is to investigate the links between the SMBH and the existence of the core profile, thought to be the result of galaxy mergers which involves central black holes. This is possible after we succesfully identify cores in the seven sample galaxies.

The structure of the thesis is as follows. Chapter 2 is dedicated to describe the machinery and the work flow that are required for obtaining a black hole mass for each galaxy, from data acquisition up to the dynamical modelling. Chapter 3 concentrates on NGC 1332, the only lenticular galaxy in the sample, whose dynamical black hole mass provides an interesting test case for the $M_{\rm BH}$-σ and the $M_{\rm BH}$-L relations (Rusli et al., 2011). The rest of the sample (seven elliptical galaxies) are collectively presented in Chapter 4 and are used to test whether or how dark matter inclusion in the dynamical modelling influences $M_{\rm BH}$ estimates. With the seven black hole masses derived in Chapter 4, we go on to confirm the presence of cores in the elliptical galaxies and investigate whether or how the core properties are correlated with the black hole masses in Chapter 5. The thesis concludes by summarizing the results in Chapter 6.

Chapter 2

Observations and Data Analysis

This chapter gives a global overview of the whole process required to produce a black hole mass based on the stellar kinematics, starting from observations up to the dynamical modelling. There are two main aspects that are involved in the data processing prior to the modelling: stellar kinematics and image analysis, each consists of multiple stages. The scheme of these stages is presented in Fig. 2.1. A general description about the instrument with which the main data were taken and the steps of the data analysis are given below. The details of the individual cases are given in the relevant chapters (Chapter 3 for NGC 1332 and Chapter 4 for the other ellipticals).

2.1 The Instrument

SINFONI is an Adaptive-Optics-assisted integral-field spectrograph that works in the near-infrared (Bonnet et al., 2004a; Eisenhauer et al., 2003a). The main element of SINFONI is called SPIFFI (SPectrometer for Infrared Faint Field Imaging). SPIFFI is a slicer IFU (Eisenhauer et al., 2003b). The instrument is mounted at the Cassegrain focus of the Very Large Telescope (VLT). An image slicer inside SPIFFI divides the field of view (FOV) into a number of slices and rearranges them into a one-dimensional long stripe. The slicer consists of two sets of plane mirrors: the first set slices the FOV into 32 slitlets and the second set arranges them into a pseudo long slit. The long slit is then fed into a long-slit spectrograph which disperses the light of each pixel in the two-dimensional field of view simultaneously onto the Rockwell HAWAII 2048^2-pixel detector. In total, there are 32x64 (32 slitlets, each is imaged onto 64 pixels, resulting in rectangular spatial pixels) spectra. Each spectrum is 2048-pixel long. The concept of this image-slicer IFU is illustrated in Fig. 2.2.

SPIFFI operates with four gratings: J (1.1-1.4 μm), H (1.45-1.85 μm), K (1.95-2.45 μm) and H+K (1.45-2.45 μm) with spectral resolutions around 2000, 3000, 4000 and 1500, respectively. The pre-optics allow the user to select the spatial/pixel scale by changing the width of each slitlet. The options are 25 mas (milli-arcsec), 100 mas and 250 mas which correspond to FOV of 0.8×0.8 arcsec^2, 3×3 arcsec^2, or 8×8 arcsec^2.

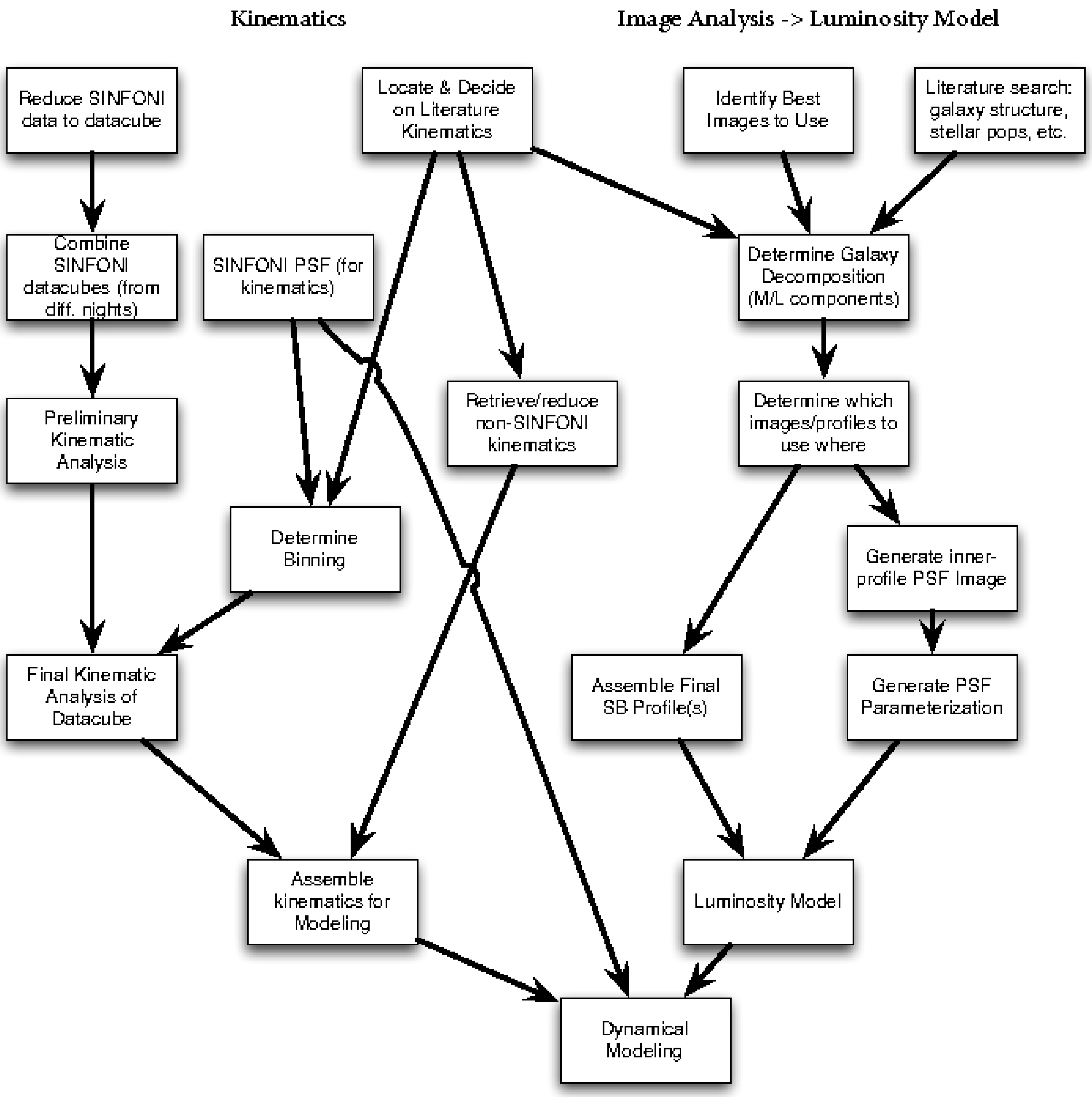

Figure 2.1: The flowchart of the stages of data analysis (courtesy of P. Erwin)

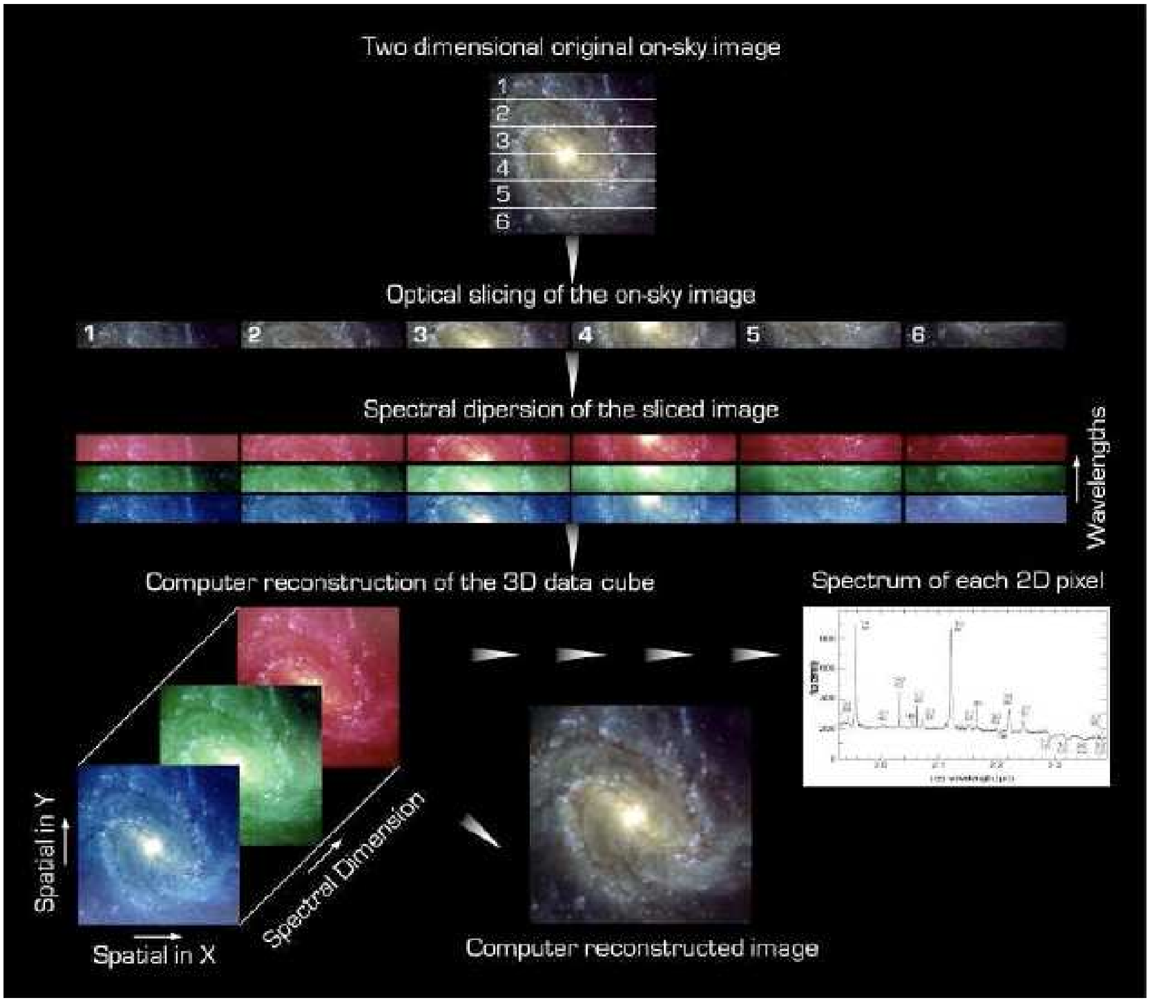

Figure 2.2: The basic concept of image-slicer IFUs (taken from Modigliani et al. 2007).

Light coming from astrophysical objects has to go through the Earth's atmosphere to reach ground-based telescopes. The atmospheric turbulence deforms the light wave and blurs the image, thereby reducing the spatial resolution. On Cerro-Paranal where the VLT is, the observed resolution from the ground due to the atmosphere can easily reach ~0.7 arcsec or more. Adaptive Optics (AO) serves as a way to correct the smearing effect of the Earth's atmosphere. The real power of SINFONI is thus exploited when AO is used. The AO module that is coupled to SPIFFI is called MACAO (Bonnet et al., 2003) which stands for Multiple Application Curvature Adaptive Optics. This module allows the observers to achieve a resolution close to the diffraction-limited resolution of the telescope (for the VLT this is 0.057 arcsec at 2.2 microns).

The AO correction requires a reference source to measure the wavefront distortion due to the atmosphere. In the so-called Natural Guide Star (NGS) mode, the reference source is a real object. Ideally, the NGS should be a bright star (R-band magnitude smaller than 14 mag) and close to the science target (less than 10-15 arcsec away). Alternatively, nuclei of galaxies that are bright ($R < 14$ mag within an aperture diameter of 3 arcsec) can also be used as the NGS. Because of these requirements, the NGS mode inevitably limits the science targets to objects with a nearby bright reference star or galaxies with bright nuclei, thereby limiting the area of sky that can be surveyed. To increase the sky coverage available to the adaptive optics, an artificial star is created in the atmosphere at an altitude of ∼90 km using a sodium laser (Laser Guide Star or LGS). This LGS system is installed at the VLT UT4 and called PARSEC (Bonaccini et al., 2002; Rabien et al., 2004). It produces an artificial reference star with a brightness of V∼11 mag. The LGS is best used in combination with the so-called tip-tilt star which is a real star that can be fainter ($R < 18$ mag) and further apart (less then 1 arcmin) from the science object than the NGS reference star. The tip-tilt star is needed to correct for the lowest-mode of the atmospheric disturbance which offsets the image position.

Compared to LGS, NGS mode still provides better AO correction. This is because in LGS mode, the light of the artificial star created at relatively low altitude has a conical shape and propagates through different turbulent atmospheric layers compared to the light coming from the science object. It is possible to use SINFONI without AO correction. In this case, the achieved resolution would be seeing limited.

2.2 Observations

The SINFONI observations of the galaxies in Table 1.1 were carried out in visitor mode in November 2008, March 2009 and April 2009. Most observations were AO-assisted. The sphere of influence of each galaxy is resolved without having to use the smallest pixel-scale option which would require a longer integration time to gain a reasonable spectral S/N. All galaxies were observed in 100-mas scale with some additional observations in 250-mas that were done without AO (NGC 1332 and NGC 3091). The 250-mas data provide useful additional kinematic constraints on the models. During all observations, the K grating was selected due to its high spectral resolution and also to minimize the effect of dust.

The integration time for each galaxy was divided into blocks of one hour, consisting of six 10-minute exposures following the object-sky-object-object-sky-object pattern. Splitting the galaxy observation into shorter exposure times and interleaving these with sky exposures were necessary. The brightness/emission of the background sky in the near-infrared fluctuates significantly on short time scales and the sky contribution has to be subtracted from the science frames. The ideal strategy would be to observe the sky simultaneously with the science object. However, this is not possible for our SINFONI observations. The science targets are the nuclei of nearby galaxies, whose angular size is much larger than the SINFONI FOV. The light from the galaxy fills the entire FOV, leaving no blank space to be used as a sky reference. Therefore, the sky exposures were taken separately but immediately before or after the science exposure. For the sky exposure, an empty region far away from the galaxy (about 1-2 arcmin away) along the minor axis was selected.

The total integration time required for each galaxy depends on the central surface brightness of the galaxy. A bright galaxy like NGC 1332 requires no more than two observation blocks using 100-mas pixelscale to reach a high S/N. The S/N is calculated based on the rms of the fit of the convolved stellar spectra to the observed spectra (CO-bandhead region, see section 2.4). During the observation, the acquired data were automatically run through a quick reduction pipeline which allows for a preliminary kinematic analysis to derive the approximate S/N. The threshold S/N value below which the kinematic fitting becomes unreliable is ∼40. The minimum integration time was therefore set by this limit.

A spatial-dithering strategy was adopted for the on-source exposures within an observation block. This was done by applying a spatial shift by a few spatial pixels (spaxels) in different spatial directions for each galaxy exposure, thus keeping the galaxy nucleus within the FOV but observed at different positions. This caused the spectrum from one spatial point of the galaxy to fall on different pixels of the detector. There are two reasons for doing this. First is to allow a full sampling of the spatial axis perpendicular to the slitlets. Without dithering, the spatial resolution of one axis would be twice smaller than the other due to the rectangular shape of SINFONI spaxels. Second is to provide a way to remove bad pixels that are missed out in the standard data reduction process or pixels that are hit by cosmic rays. By comparing different exposures/frames at the same spatial and spectral position, pixels that show deviation from their counterparts can be excluded.

The Earth's atmosphere does not only add atmospheric light (emission) to the observed spectra, which is corrected for by the above object-sky-object exposure sequence. In addition to this, as the light from the object passes through the atmosphere, it suffers from the atmospheric absorption and the residual blurring effect after the AO correction. The former results in the so-called telluric absorption lines that contaminate the galaxy spectra. The latter degrades the spatial resolution. To correct for these two effects, we need to know how much the contamination and the loss of resolution is. This is done by observing two standard stars (telluric and PSF stars) right before or after the galaxy observation block to provide the approximate atmospheric conditions during the science observation. To be able to identify and remove the atmospheric absorption lines, an object with a known (black body) spectrum was observed, i.e. the telluric star. The star is selected from the Hipparcos catalogue, i.e. a star close to the galaxy with a similar airmass and having early spectral type (B class star). The latter is chosen because of the relatively featureless spectrum without significant CO absorption lines. Since we need only the spectrum, there is only one exposure for this star with one sky exposure. To estimate the point spread function (PSF) of the observation, a point-like object (star) is observed with the same observational setup as the galaxy. This PSF star is selected to be a nearby single star that has a similar R-band magnitude and B-R colour as the central 3 arcsec of the galaxy nucleus. The PSF star exposures were divided into two with a sky observation in the middle. Spatial dithering is applied as in the galaxy observations.

2.3 Data Reduction

The aim of this pre-processing step is to transform the raw science data on two-dimensional frames into a clean datacube, which contains spectroscopic information for every spatial pixel. The data were reduced primarily using the ESO SINFONI pipeline (Modigliani et al., 2007, 2008), supplemented by recipes from the python-based SPRED (Abuter et al., 2006; Schreiber et al., 2004); the latter is the SPIFFI data reduction software developed at MPE. The ESO SINFONI pipeline is part of the common software library of ESO and written based on the SPRED package.

The galaxy observations at each observational setup (filter, pixelscale) of SINFONI include a particular set of calibration frames. These calibration frames were taken in daytime on the day after the observations and are necessary to correct for CCD-specific features (e.g. dark, flat). Only after we apply all these corrections to the observations can we construct a datacube that is ready to be used for scientific analysis. In general, the data reduction cascade includes the following steps:

1. Bad lines removal

Four pixels along the edges of the detector are not illuminated and these are used to estimate the bias level of each line of pixels. If hot pixels are present at the edges then the bias level would be overestimated and when this bias is subtracted from the frame, dark stripes would appear. This effect gets worse with longer exposure time. Since the bias subtraction is hardcoded at the detector level, all frames have to be corrected for this effect before further data reduction steps. ESO provides an IDL code to do this task.

2. Linearity

The non-linearity of the detector is estimated by using flat-field frames with increasing intensity. The non-linear pixel map is produced by running `sinfo_rec_detlin`.

3. Dark

The dark frames are taken by reading out an unilluminated detector for several exposure times ranging from 1 to 600 seconds. The master dark frame is derived and the hot pixels are flagged. The recipe for this is `sinfo_rec_mdark`.

4. Flat-field

The flat frames are obtained by taking an image of a flat featureless source, in this case: a halogen lamp. The pixel-to-pixel variations in detector sensitivity is derived from the analysis of the flat frames. Pixels whose intensity is beyond a certain threshold are marked. The master flat and the master bad pixel map are produced by running `sinfo_rec_mflat`. The final bad pixel map is the combination of the reference bad pixel map and the bad pixels identified in the linearity and flatfielding procedures.

5. Distortion correction

The detector's geometric distortion is determined by using a set of fibre flat frames, obtained by moving the calibration fibre perpendicularly to the slitlets. The distance between the slitlets is also derived. The recipe to do this is called `sinfo_rec_distortion`.

6. Wavelength calibration

The wavelength calibration makes use of the exposures of arc lamps (Neon and Argon) to determine the wavelength position for each spatial position of the spectra on the two dimensional frame. By comparing the reference line list of Ne and Ar to the corresponding peaks in the arc frames, the wavelength position can be determined. The recipe `sinfo_rec_wavecal` produces the wavelength map and the position of the slitlets.

7. Datacube construction

The `sinfo_rec_jitter` recipe reduces the science frame, the telluric and PSF standard frames using the calibration frames generated in previous steps (thus, applying all the calibrations) and constructs the datacube. The sky subtraction, using the method of Davies (2007), is included in this step. The sky frame that is observed closest in time to the science frame is used to subtract the sky contribution from the galaxy spectra. The useful output of this step is a datacube and an image for each science target. For the standard star, this recipe also produces the object spectrum (by combining the spectra within a certain aperture).

8. Telluric correction and combining datacubes

This step includes the removal of the Brγ absorption line in the telluric star spectrum. It is done by fitting a Lorentz profile to the absorption line and subtracting the fit from the star spectrum. The spectrum is then normalized by dividing it with a blackbody spectrum specified by the telluric star temperature or spectral type. The resulting spectrum is further continuum-normalized to result in atmospheric transmission as a function of wavelength. The telluric correction is performed on the corresponding science datacubes produced in the previous step, by dividing the spectra with the atmospheric transmission spectrum. Finally, the multiple datacubes of each galaxy are combined into one final datacube, taking into account the dither pattern during the observations.

2.4 Stellar Kinematics

The concept of stellar kinematic measurements is based on the line-of-sight motion of stars that is imprinted in the observed spectrum. For external galaxies, this measurement cannot be performed on a star-by-star basis due to the limited spatial resolution. It is the integrated spectrum, which contains the contribution from all the stars along the line of sight, that is recorded by spectroscopic observations.

Each star has a different line of sight velocity ($V_{\rm los}$). According to the Doppler law, this motion shifts the wavelength of the spectral features by an amount that is proportional to $V_{\rm los}$. The result is a displaced and broadened stellar spectrum. Mathematically, the galaxy spectrum is described as a convolution of a stellar spectrum with the so-called line-of-sight velocity distribution (LOSVD). If the spectral contribution from the stars is known, the LOSVD can, in principle, be recovered. In practice, the stellar spectra are obtained from the empirical spectral library of nearby stars.

Kinematic properties of galaxies, e.g. the mean streaming/rotational velocity and the velocity dispersion that describes the random motion of stars, can be derived from the LOSVD. The simplest approach is to model the LOSVD using a Gaussian profile. This is good only as a first-order aproximation because real LOSVDs exhibit deviations from a perfect Gaussian. To account for this deviation, most kinematic studies use a Gauss-

Hermite parametrization for the LOSVD, as first suggested by van der Marel & Franx (1993) and Gerhard (1993). Following the notation of van der Marel & Franx, the LOSVD is written as

$$\mathscr{L}(v) = \frac{\gamma A(w)}{\sigma}\left[1 + \sum_{i=3}^{N} h_i H_i(w)\right], \tag{2.1}$$

with $w = (v - V)/\sigma$ and $A(w) = (1/2\pi)e^{-w^2/2}$. γ is the line strength, V is the systemic velocity and $H_i(w)$ is the Hermite polynomial. For relatively small deviations, it is usually sufficient to truncate the polynomial up to order 4, resulting in four kinematic parameters, i.e. the velocity v, velocity dispersion σ, and the Hermite coefficients h_3, h_4:

$$\mathscr{L}(v) = \frac{\gamma A(w)}{\sigma}[1 + h_3 H_3(w) + h_4 H_4(w)], \tag{2.2}$$

where

$$H_3(w) = \frac{1}{\sqrt{6}}(2\sqrt{2}w^3 - 3\sqrt{2}w) \tag{2.3}$$

$$H_4(w) = \frac{1}{\sqrt{24}}(4w^4 - 12w^2 + 3). \tag{2.4}$$

The h_3 and h_4 quantify the departures of the LOSVD from a Gaussian and are similar in interpretation to the skewness and kurtosis of a distribution function, respectively. Skewness describes an asymmetric deviation which appears as a tail in either side of the distribution while kurtosis is the measure of a symmetric deviation which makes the distribution more strongly peaked or more flattened. Fig. 2.3 shows variations in the shape of LOSVDs due to different values of h_3 and h_4.

The Gauss-Hermite moments, especially h_4, are useful to infer the orbital structure of the observed galaxies. A positive h_3 corresponds to a distribution that is skewed towards lower velocities with respect to the systemic velocity. A positive h_4 means that the velocity distribution is more pointy than a Gaussian at small velocities with more extended high-velocity wings. This generally indicates a radial anisotropy in the velocity distribution. Conversely, the tangential orbits dominate when $h_4 < 0$. Thus, measuring h_3 and h_4 adds constraints to the stellar distribution function and provides the key to break the mass-anisotropy degeneracy.

To derive LOSVDs from the SINFONI spectra, we use a maximum penalized likelihood (MPL) method Gebhardt et al. (2000b), which is similar to that in Saha & Williams (1994) and Merritt (1997). Its implementation is as follows: an initial binned-LOSVD is generated and then convolved with a linear combination of the stellar template spectra. The LOSVD and the weights of the template stars are iteratively adapted until the convolved spectrum matches the galaxy spectrum. This is achieved by minimising the penalised χ^2:

$$\chi_P^2 = \chi^2 + \alpha_S P = \chi^2 + \alpha_S \int_V \left(\frac{\partial^2 \mathscr{L}(v)}{\partial v^2}\right) dv, \tag{2.5}$$

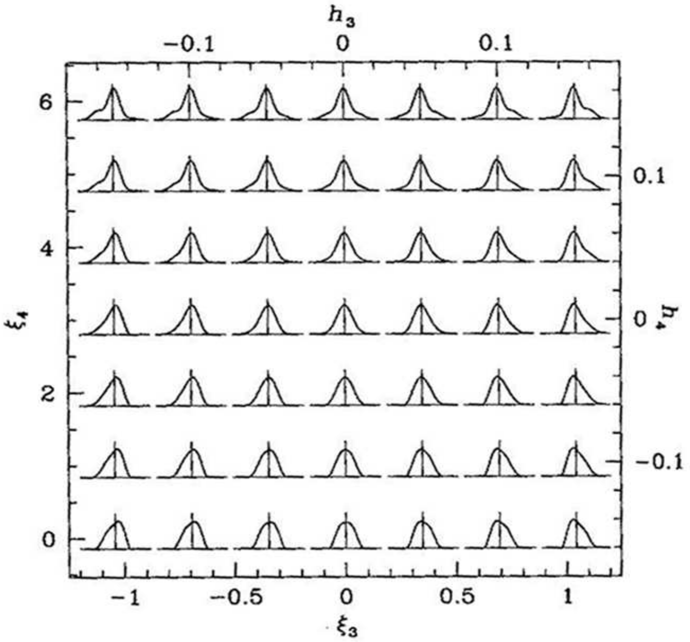

Figure 2.3: Variations of LOSVD shape due to the change of h_3 and h_4 (v and σ are fixed). The bottom and left axes are marked ξ_3 and ξ_4 which are the shape parameters for skewness and kurtosis (see text). Figure was taken from Binney & Merrifield (1998).

where α_S is the smoothing parameter and P is the penalty function that imposes smoothness. The stellar spectra that are used in the fitting are observed with SINFONI using the same setup as the galaxies.

The uncertainties of the best-fit LOSVD are calculated using Monte Carlo simulations. A model spectrum is created by convolving the derived LOSVD with the template spectrum. Gaussian noise is then added to that model spectrum to create 100 realizations. The LOSVD of each realization is determined using the method above. The 68% confidence interval is then derived from those 100 LOSVDs.

The LOSVD is derived by fitting only a specific part of the spectrum i.e. the CO bandheads. There are four bandheads in the K-band spectral range. They are the strongest stellar absorption features in the K-band spectrum and they do not suffer from blending with other stellar absorption or gas emission lines. We use only the first two bandheads in deriving the kinematics. The third and fourth ones, if these are not redshifted out of the K-band, lie in regions strongly affected by sky emissions.

Since SINFONI does not have a large enough FOV, additional large scale kinematics are usually necessary. The main source of this is the literature. When this is not available, spectroscopic observations are taken. In most cases, the additional kinematics have already been derived in terms of Gauss-Hermite moments. The LOSVD is then derived from these moments and the uncertainties are calculated from the errors of the moments, assuming Gaussian noise, using 100 Monte Carlo realisations.

Since the central kinematic information is provided by SINFONI, we make use of the SINFONI PSF of the corresponding datacube. The PSF is included in the modelling as it is: a two-dimensional image, without any parametrisation.

2.5 Stellar Light Distribution

The light distribution of the stars is obtained from images of the galaxy, usually HST or SINFONI images for the central part and other ground-based images for the outer part of the galaxy. From the isophotes, one can derive the surface brightness, ellipticity and position angle at different radial positions, as well as the higher-order moments that describe the deviation of the isophotes from perfect ellipses. For a lenticular galaxy like NGC 1332, the bulge and the disk components are likely to have different stellar populations, which would affect the mass-to-light ratio and $M_{\rm BH}$ estimate in the dynamical modelling. In this case, the image is first decomposed into a bulge and a disk before the isophotal analysis is performed separately on each component.

The three dimensional luminosity is recovered numerically by deprojecting the two dimensional isophotes, assuming a certain inclination and axisymmetry. The deprojection is done with the code of Magorrian (1999). An initial luminosity density profile ν with a radial profile

$$\nu(m) = \frac{L}{4\pi q B(3-\alpha, 3-\beta)} \frac{m_0^{\beta-3}}{m^{\alpha}(m_0+m)^{\beta-\alpha}} \tag{2.6}$$

is constructed on an elliptical polar grid (m,θ'). The function B(-,-) is the Beta function (Abramowitz & Stegun, 1972) and q is the intrinsic axis ratio. The latter is set by the average ellipticity of the isophotes under the assumption of a certain inclination. This three-dimensional density profile is projected assuming a given inclination and the model's projected surface brightness is compared with the observed one by calculating the χ^2. The free parameters L, m_0, α and β are first determined by minimizing χ^2 using the Levenberg-Marquardt algorithm. The initial density model is further improved by iteratively applying small changes to the model at random gridpoints until its projected light matches the observed light profile within the desired accuracy. The final density profile maximizes the penalized log-likelihood. The penalty function is used to impose a certain level of smoothness on the density profile.

The original version of the code does not include a seeing correction and the observed isophotes are often not seeing corrected. To measure a black hole mass, it is important to take into account the atmospheric blurring effect (or the instrumental PSF in the case of HST image) which alters the innermost isophotes. Therefore, we have incorporated a seeing correction algorithm into the code. It is accomplished by convolving the projected density model with the PSF before being compared with the observed surface brightness profile. This convolution is done numerically on the initial model and at every iteration that follows. The PSF information is given to the code through a multi-gaussian parametrisation. For NGC 1332 the parametrisation was first restricted to circular gaussians (which turns out to be sufficient to result in a reliable $M_{\rm BH}$), but then was developed into non-circular gaussians for the other seven galaxies. This seeing correction was tested on NGC 1332 (Appendix A) for which we have HST and SINFONI images to derive the central isophotes.

2.6 Dynamical Modelling

The modelling technique that is employed here was originally developed by Schwarzschild (1979). The implementation follows the algorithm described in Gebhardt et al. (2000b, 2003), Thomas et al. (2004) and Siopis et al. (2009). The models allow variations in the three integrals of motion. Symmetry about the projected minor axis is assumed.

The galaxy model is assumed to consist of a central black hole, stars and possibly a dark matter halo. The mass of each component sums up to result in a total mass density ρ as a function of radius r:

$$\rho(r) = M_{\rm BH}\delta(r) + \sum_i \Upsilon_i \nu_i(r) + \rho_{DM}. \tag{2.7}$$

For each stellar component i, ν_i is the luminosity density profile that is obtained from the deprojection and this is multiplied with the stellar mass-to-light ratio Υ_i to result in a stellar mass profile. Υ_i is restricted to a constant value, independent of radius. There are two density distributions that are commonly used for the dark matter profile, i.e. NFW (Navarro et al., 1996) profile and the LOG profile (Binney & Tremaine, 1987).

From equation 2.7, the gravitational potential is calculated for a given trial set of input parameters ($M_{\rm BH}$, ν_i and possibly dark halo parameters). In this potential, thousands of orbits are generated. The starting point of each orbit in the phase space is chosen to properly sample the three integrals of motion: energy E, angular momentum L_z and the third integral I_3. The equations of motion for each orbit are then integrated over many orbital periods. The orbits are followed on a polar grid in the meridional plane (r, θ) where r is the radius and θ is the latitude. The luminosity (and therefore the mass) contribution of each orbit to each spatial cell is computed from the fraction of time the orbit spends in the cell. A library that contains time-averaged stellar orbits is constructed by keeping track of all the orbits.

For a given trial potential, the orbit library contains two sets of orbits, one set is different from the other only in the direction of L_z. Each set consists of about 12,000 orbits. A non-negative scalar weight is assigned to each orbit. The best-fit solution for each potential is achieved by varying the orbital weights using the method of maximum entropy (Richstone et al., 1998). These weights are adjusted iteratively until the orbit superposition reproduces the stellar distribution and best fits the observed LOSVDs. The maximum entropy technique maximizes a quantity $\hat{S} = S - Q\chi^2$ where

$$S = -\sum_{i=1}^{N_{\mathrm{orb}}} w_i \ln\left(\frac{w_i}{V_i}\right) \tag{2.8}$$

$$\chi^2 = \sum_{j}^{N_c}\sum_{k} \frac{\left[\mathscr{L}_{j,\mathrm{data}}(v_k) - \mathscr{L}_{j,\mathrm{model}}(v_k)\right]^2}{\delta_j^2(v_k)}. \tag{2.9}$$

V_i and w_i are the phase-space volume and the weight of orbit i, N_c is the total number of cells, $\mathscr{L}_j$ is the LOSVD in cell j and $\delta_j^2(v_k)$ is the uncertainty in $\mathscr{L}_{j,\mathrm{data}}$ at velocity bin v_k. Q is the smoothing parameter that controls the influence of entropy S on the fit. A small Q would cause the χ^2 to be less dominant in maximizing $\hat{S}$. Consequently, the model does not fit the data well and it is therefore a poor representation of the real galaxy. In practise, Q is initially set to 0.0 and then successively increased until the χ^2 effectively does not change anymore. Thus, we let the model to fit the data as good as possible and minimize the bias introduced by the Boltzmann entropy.

The black hole mass is found through a parameter-grid search. Trial potentials that cover the input parameter space – within a reasonable range – are calculated. The potential that best matches the observed properties of the galaxies, i.e. has the smallest χ^2, gives the best-fit black hole mass and stellar mass-to-light ratio. The uncertainties of the M_{BH} are derived by first marginalizing over mass-to-light ratios and then locating M_{BH} where the χ^2 is one higher than the minimum χ^2 ($\Delta\chi^2 = 1$). The M_{BH} difference is the 1σ error.

Due to the assumptions adopted in the modelling, there are potentially some systematic errors. One is the possibility that the exclusion of a dark halo component in the modelling systematically lowers the estimated black hole mass (see Chapter 4). The other one is due to triaxiality that is quite common for massive galaxies. van den Bosch & de Zeeuw (2010) use triaxial models to derive the black hole mass in NGC 3379 and M32. They find that the black hole mass for NGC 3379 doubles, compared to the results of axisymmetric models, while the black hole mass in M32 stays the same. The investigation of the effect of triaxiality is outside the scope of this thesis.

Chapter 3

The Central Black Hole Mass of NGC 1332[†]

Based on
The Central Black Hole Mass of the High-σ But Low-Bulge-Luminosity
Lenticular Galaxy NGC 1332
S.P. Rusli, J. Thomas, P. Erwin, R.P. Saglia, N.Nowak, R. Bender
MNRAS 410 (2011), 1223-1236

Abstract

The masses of the most massive supermassive black holes (SMBHs) predicted by the $M_{\rm BH}$-σ and $M_{\rm BH}$-L relations appear to be in conflict. Which of the two relations is the more fundamental one remains an open question. NGC 1332 is an excellent example that represents the regime of conflict. It is a massive lenticular galaxy which has a bulge with a high velocity dispersion σ of $\sim$ 320 km s^{-1}; bulge–disc decomposition suggests that only 44% of the total light comes from the bulge. The $M_{\rm BH}$-σ and the $M_{\rm BH}$-L predictions for the central black hole mass of NGC 1332 differ by almost an order of magnitude. We present a stellar dynamical measurement of the SMBH mass using an axisymmetric orbit superposition method. Our SINFONI integral-field unit (IFU) observations of NGC 1332 resolve the SMBH's sphere of influence which has a diameter of $\sim$0.76 arcsec. The σ inside 0.2 arcsec reaches $\sim$ 400 km s^{-1}. The IFU data allow us to increase the statistical significance of our results by modelling each of the four quadrants separately. We measure a SMBH mass of $(1.45 \pm 0.20) \times 10^9 M_\odot$ with a bulge mass-to-light ratio of 7.08 ± 0.39 in the R-band. With this mass, the SMBH of NGC 1332 is offset from the $M_{\rm BH}$-L relation by a full order of magnitude but is consistent with the $M_{\rm BH}$-σ relation.

[†] Based on observations at the European Southern Observatory Very Large Telescope [082.B-0037(A)]

3.1 Introduction

It is now widely accepted that massive elliptical galaxies and (classical) bulges of spiral galaxies harbour supermassive black holes (SMBHs) at their centres with masses ranging between $\sim 10^6$-$10^{10} M_\odot$. An increasing number of SMBH detections have led to the discovery of empirical correlations between the SMBH mass $M_{\rm BH}$ and the velocity dispersion σ or the luminosity L of the host bulge (Kormendy & Richstone 1995; Magorrian et al. 1998; Ferrarese & Merritt 2000; Gebhardt et al. 2000a; Tremaine et al. 2002; Marconi & Hunt 2003; Häring & Rix 2004; Gültekin et al. 2009b). These correlations indicate a strong connection between the SMBH and the host galaxy. Consequently, SMBH studies are essential for a better understanding of galaxy formation processes (Silk & Rees, 1998).

Because of its crucial role, SMBH demographics has become one of the key ingredients in cosmological simulations and theoretical models in recent years (Granato et al. 2004; Somerville et al. 2008; Di Matteo et al. 2005). An inventory of the SMBH population is therefore necessary. The number of secure measurements is presently only $\sim$ 50 and quiescent or weakly active SMBH beyond the local universe can typically not be well-studied. In this situation, the $M_{\rm BH}$-σ and $M_{\rm BH}$-L relations have become valuable tools in predicting the SMBH mass and mass function. By combining the distribution of the readily observed parameter σ (or L) with the corresponding $M_{\rm BH}$-σ (or $M_{\rm BH}$-L) relation, the SMBH abundance can be indirectly estimated.

This method, however, suffers from a bias: the $M_{\rm BH}$-σ relation predicts fewer SMBHs with masses $\gtrsim 10^9 M_\odot$ than does the $M_{\rm BH}$-L relation. This happens because the luminosity and velocity dispersion functions obtained from SDSS are different from those in the SMBH sample which define the relations (Bernardi et al. 2007; Tundo et al. 2007). Bernardi et al. (2007) argue that the bias lies in the SMBH sample. Assuming that it is due to a selection effect, their models suggest that the $M_{\rm BH}$-σ relation is more fundamental. Lauer et al. (2007) who examine a sample of brightest cluster galaxies, however, find that the local SMBH mass function for $M_{\rm BH} > 3 \times 10^9 M_\odot$ inferred from the $M_{\rm BH}$-L relation is in better agreement with the volume density of the most luminous quasars. Furthermore, from the quasar luminosity function, Shields et al. (2006) estimate the density of relic SMBH with masses $> 5 \times 10^9 M_\odot$ to be $10^{2.3}$Gpc^{-3}. This should translate to the same density for galaxies with $\sigma \gtrsim 500$ km s^{-1} based on the local $M_{\rm BH}$-σ relation. No objects with such high σ have been found in the local universe. Bernardi et al. (2006) find at most two or three candidates in SDSS with $\sigma > 500$ km s^{-1} in a volume of ~ 0.5 Gpc^{-3}, but these might be a result of superposition effects.

Several other authors (Netzer 2003; Wyithe & Loeb 2003; Shields & Gebhardt 2004) have also noted that the σ implied (via the $M_{\rm BH}$-σ relation) by the largest SMBH masses inferred from quasars exceed the largest σ found in local galaxies. If we trust that those SMBH masses are correct, then the $M_{\rm BH}$-σ relation must be different at the upper end. Wyithe (2006) argues that the $M_{\rm BH}$-σ relation is curved upwards at the high-σ end rather than linear in log-log space. If this is true, then the abundance of local SMBHs would be closer to the quasar prediction.

Since the shape of the $M_{\rm BH}$-σ relation at the upper end critically determines the space density of the most massive SMBHs, it is important to characterise its slope and intrinsic scatter. Currently, this high-σ regime is scarcely sampled and there are uncertainties as to how the relation should behave. Beifiori et al. (2009) derive upper limits of 105 SMBH masses based on HST spectroscopy of ionised gas and find that the $M_{\rm BH}$-σ relation flattens at the high-σ end, opposite to what was suggested by Wyithe (2006). To resolve these uncertainties, an increased sample of direct SMBH detections in high-σ galaxies is required. If the $M_{\rm BH}$-σ relation indeed breaks down in the high-σ regime, then a sufficiently large number of SMBH mass measurements at $\sigma \sim 300-400$ km s^{-1} will likely be able to detect this. For this reason, we undertake an observational campaign to measure SMBH masses of high-σ galaxies using the near-infrared integral-field spectrograph SINFONI at the Very Large Telescope (VLT).

NGC 1332 is a nearby massive S0 galaxy which resides in the Eridanus Cloud. Its orientation is close to edge-on and the galaxy appears to be a normal lenticular. Adopting the bulge velocity dispersion from HyperLeda[1] ($\sim$ 320 km s^{-1}), we expect that the sphere of influence has a diameter of $\sim$ 0.76 arcsec, which is resolved by our observations. The K-band magnitude of NGC 1332 from the 2MASS Large Galaxy Atlas is 7.052, which gives a K-band luminosity of $1.56 \times 10^{11} L_\odot$ after a correction for Milky Way extinction of 0.012 magnitudes (from the NASA/IPAC Extragalactic Database – NED). Our photometric bulge–disc decomposition (Section 3.4.1) implies a bulge-to-total luminosity ratio of 0.44. Given this bulge luminosity, we would expect to find a $M_{\rm BH}$ of $1.37 \times 10^8 M_\odot$ from the $M_{\rm BH}$-L_K relation of Marconi & Hunt (2003). On the other hand, the $M_{\rm BH}$-σ relation of Tremaine et al. (2002) or Gültekin et al. (2009b) constrains the $M_{\rm BH}$ to $\sim 9.0 \times 10^8 M_\odot$ or $\sim 9.7 \times 10^8 M_\odot$ respectively. The SMBH masses given by these two relations clearly differ by almost an order of magnitude which makes NGC 1332 a particularly attractive case. As a side note, the software and sources that we used to derive the bulge luminosity were different from those used by Marconi & Hunt (2003), which could introduce systematic errors. It is, however, unlikely that the situation for NGC 1332 would be significantly affected.

To date, the only published $M_{\rm BH}$ measurement for NGC 1332 is provided by a recent X-ray study of Humphrey et al. (2009) – hereafter H09. They make use of the *Chandra X-ray Observatory* data and rely on the assumption of hydrostatic equilibrium in the analysis, which results in a SMBH mass of $5.2^{+4.1}_{-2.8} \times 10^8 M_\odot$(with the $M_{\rm BH}$-σ relation as a Bayesian prior). This estimate lies in between the prediction of both relations, although considering the error bars, the $M_{\rm BH}$-σ relation is slightly favoured. It is, however, not clear if their black hole mass would lean more towards the $M_{\rm BH}$-L relation if they were to use the $M_{\rm BH}$-L instead of the $M_{\rm BH}$-σ relation for their Bayesian prior.

In this chapter, we measure the SMBH mass in NGC 1332 using a stellar dynamics approach which is not biased by any of the two relations. Throughout, we adopt a distance of 22.3 Mpc from Tonry et al. (2001), corrected for the Cepheid zero point by applying a distance modulus shift of -0.06 magnitudes (Mei et al., 2005). At this distance, 1 arcsec corresponds to 0.11 kpc.

---

[1] http://leda.univ-lyon1.fr/

This chapter proceeds as follows. We describe the data and data reduction in Section 3.2. Details on the derivation of the kinematics follow in Section 3.3. The photometry, bulge–disc decomposition and deprojection to model the luminosity profile are described in Section 3.4. In Sections 3.5 and 3.6, we present the dynamical modelling and the results. Lastly, we summarise and discuss our results in Section 3.7.

3.2 Data

3.2.1 SINFONI observations and data reduction

The integral-field data presented here were obtained on November 25, 2008, as part of the guaranteed time observations with SINFONI on the UT4 of the VLT. SINFONI (Spectrograph for INtegral Field Observations in the Near Infrared) is a Spectrometer for Infrared Faint Field Imaging (SPIFFI) (Eisenhauer et al., 2003a) combined with the Multi-Application Curvature Adaptive Optics (MACAO) module (Bonnet et al., 2004a). NGC 1332 was observed in the K-band (1.95-2.45 μm) in two different spatial resolutions, i.e. 0.05×0.1 arcsec^2 spaxel^{-1} (hereafter "100mas") resulting in a 3×3 arcsec^2 field-of-view (FOV) and 0.125×0.25 arcsec^2 spaxel^{-1} with 8×8 arcsec^2 FOV (hereafter "250mas"). For the former, adaptive optics (AO) correction was applied using the nucleus of the galaxy as the natural guide star. The observations followed a sequence of 10-minute exposures of object-sky-object-object-sky-object (O-S-O-O-S-O). Each exposure was dithered by a few spaxels to allow for bad pixel correction and cosmic ray removal. A total of 40 minutes on-source exposure time was obtained for the 250mas scale and 80 minutes for the 100mas scale. To estimate the AO performance and the point spread function (PSF) due to atmospheric turbulence, we regularly observed a PSF star after the science exposure sequence.

The reduction of SINFONI data was performed using custom reduction packages for SINFONI, i.e. ESOREX (Modigliani et al., 2007) and SPRED (Schreiber et al. 2004; Abuter et al. 2006). Except for the 250mas science data, all other frames including the PSF and telluric standard stars were reduced using ESOREX which produced cleaner spectra. Both software packages included all common and necessary steps to reduce three-dimensional data and to reconstruct a datacube. The closest sky frame was first subtracted from the science frame. The resulting frame was then flat-fielded, corrected for bad pixels and detector distortion and wavelength calibrated before the datacube was reconstructed. For telluric correction, we used three early-type stars with the spectral classes B3V and B5V, i.e. Hip014898, Hip023060 and Hip018926. As the end process, the individual science datacubes were averaged into one final three-dimensional datacube per plate scale. For a more detailed description of the data reduction, we refer the reader to Nowak et al. (2008). Fig. 3.1 shows SINFONI images of the two platescales which resulted from collapsing the datacubes along the wavelength direction.

After the reduction, the individual PSF star images for the 100mas scale were averaged, normalised and then fitted with the commonly-adopted double Gaussian function. To account for the asymmetry of the PSF, both Gaussian components, i.e. a broad and a narrow one, were set to be non-circular. The fit gave the full width at half-maximum in the x and y direction ($\mathrm{FWHM_x}$, $\mathrm{FWHM_y}$) of (1.03 arcsec, 0.94 arcsec) for the former and (0.15 arcsec, 0.13 arcsec) for the latter. The narrow component contributed to 36% of the total flux and resolved the expected sphere of influence of the SMBH. We used this SINFONI PSF parameterisation for the surface brightness deprojection (see Section 3.4.3). Fig. 3.2 presents the PSF image with the fit along the two spatial axes. We note that this PSF image does not strictly represent the true PSF since the acquisition was not done simultaneously with the galaxy observation. The fit is also admittedly not perfect, but for our purpose here the deviation does not lead to a significant error. We verify this and discuss the effect of the PSF uncertainties further in Appendix A.

3.2.2 Imaging data

We made use of three types of imaging data for NGC 1332. For the large-scale analysis, we searched the major telescope archives and found several *R*-band images obtained with the red channel of ESO Multi-Mode Instrument (EMMI) on the 3.5m New Technology Telescope (NTT) at La Silla. These images were originally taken on 2005 December 3, as part of a spectroscopic program (Program ID 076.B-0182(A), PI Aragón-Salamanca). We selected the three best 10s exposures (the fourth exposure had strong background variations) and reduced them with standard IRAF tasks (first reducing the individual amplifier sections, then scaling and joining them into single-chip images). Since the imager was actually a two-CCD mosaic, the result was three pairs of single-chip images; we combined these into a single mosaic using the SWarp package (Bertin et al., 2002). The final image had a seeing of 0.80 arcsec FWHM (mean of Moffat profiles fitted to nine bright, unsaturated stars) and a plate scale of 0.332 arcsec pixel^{-1}, and is shown in Fig. 3.3.

From the HST archive we retrieved two 160s Wide-Field Planetary Camera 2 (WFPC2) images in the F814W filter (Proposal ID 5999, PI Phillips), which were also used in Kundu & Whitmore (2001). Since the images were well aligned, we combined them directly using the STSDAS crrej task in IRAF. Finally, we generated *K*-band images from our 250mas and 100mas SINFONI datacubes by collapsing (averaging) the cubes along the spectral direction.

We first calibrated the combined NTT-EMMI mosaic image, which was large enough to ensure accurate sky subtraction, using Cousins *R* photometry obtained from the literature (Prugniel & Heraudeau, 1998). The WFPC2 image was then calibrated by matching surface brightness profiles: fitting ellipses of fixed orientation (position angle and ellipticity) to both images, then simultaneously fitting for the best combination of sky background (in the WFPC2 image) and scaling so that it matched the NTT-EMMI profile outside the central 2 arcsec (where the worse seeing of the NTT-EMMI image affected the profile). Finally, we repeated the process for profiles from the two SINFONI images by matching them against the (scaled, sky-subtracted) WFPC2 profile.

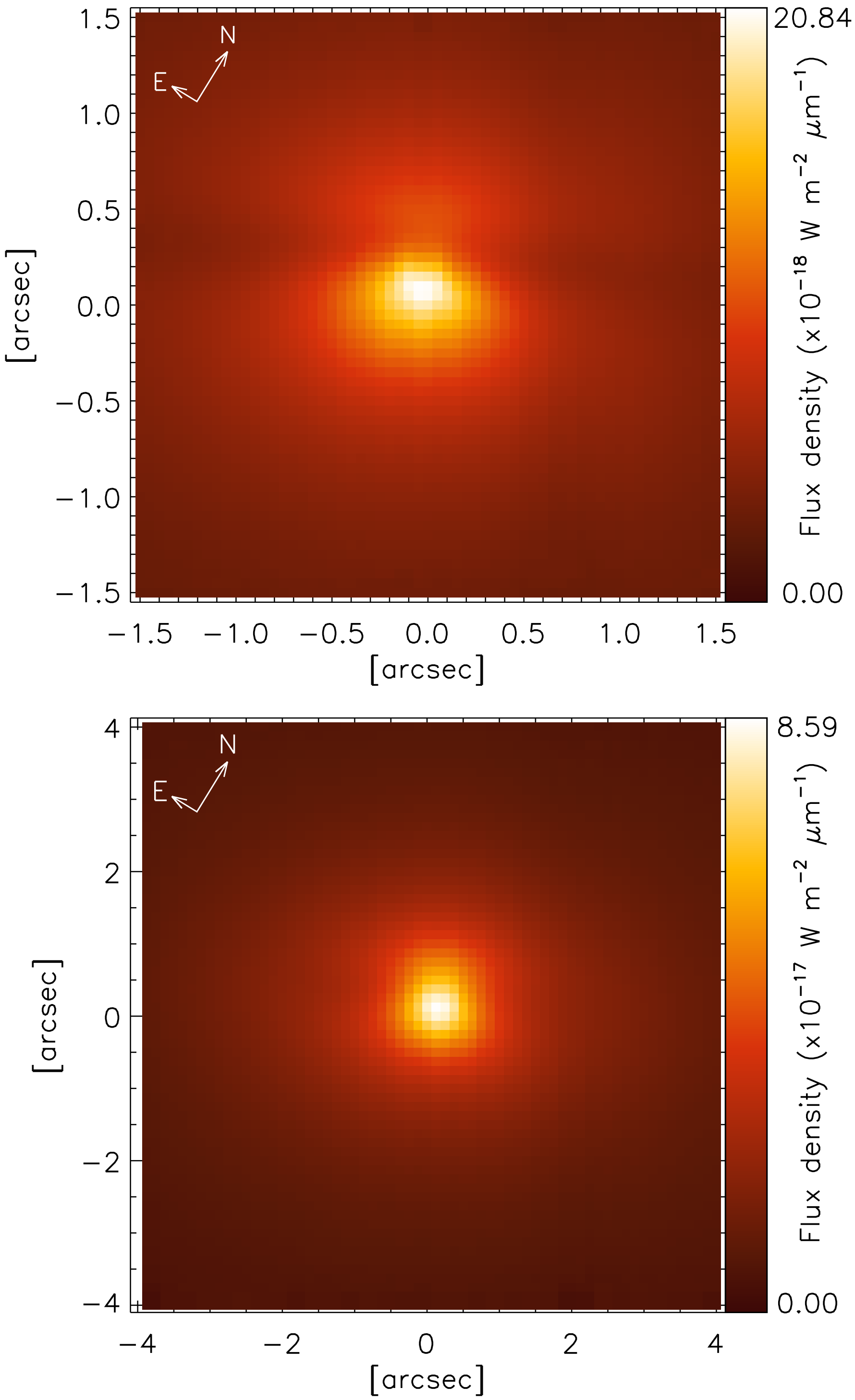

Figure 3.1: SINFONI images of NGC 1332 in two resolution scales: 100mas(upper panel) and 250mas (lower panel)

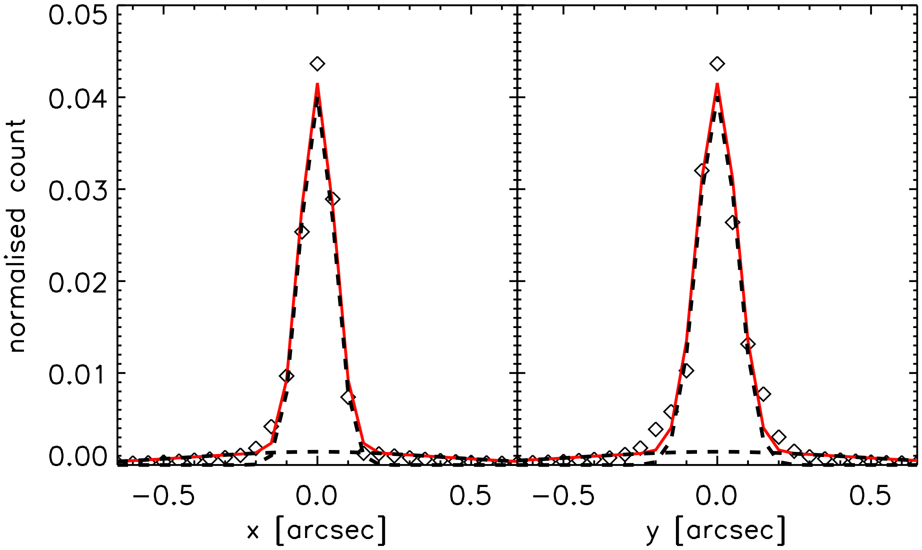

Figure 3.2: A double non-circular Gaussian fit to the SINFONI 100mas PSF. The fit along the x and the y-axis of the detector are shown in the left and the right panel respectively. The black dashed lines are the individual Gaussians and the red solid lines are the sum of the Gaussian components; diamonds are the actual PSF.

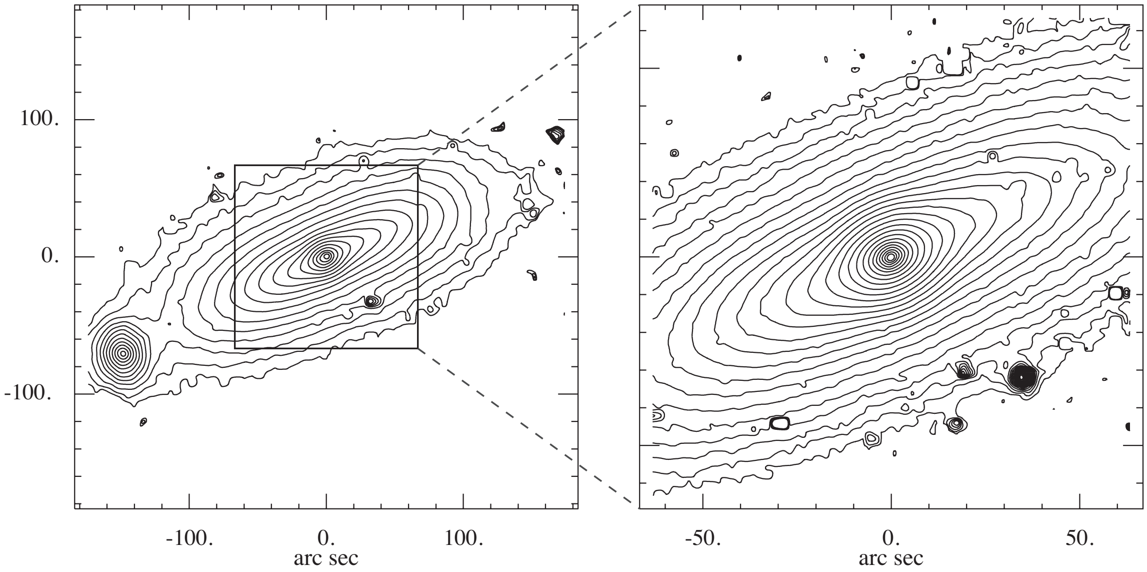

Figure 3.3: *R*-band isophotes of NGC 1332, from archival NTT-EMMI images. The left-hand panel shows the whole galaxy, plus its neighbour NGC 1331 (near the left-hand edge); the image has been smoothed with a 5-pixel-wide median filter. Contour levels run from 24.5 to 15.0, in steps of 0.5 mag/arcsec^2. The right-hand panel shows the inner regions of the galaxy, including the bulge, using an unsmoothed image; contour levels run from 23.1 to 15.0, in steps of 0.3 mag/arcsec^2. North is up and east is to the left.

3.3 Kinematics

3.3.1 SINFONI kinematics

We extracted the line-of-sight velocity distributions (LOSVDs) non-parametrically using a Maximum Penalised Likelihood (MPL) method (Gebhardt et al., 2000b). The galaxy spectra were deconvolved using the weighted linear combination of a set of stellar templates consisting of K and M stars. These stars were previously observed using SINFONI with the same instrumental setups as in the galaxy observations. We briefly describe here the kinematics analysis that we have performed. It is largely similar to that in Nowak et al. (2007) and Nowak et al. (2008), so we refer the reader to those papers for details on the kinematics derivation.

Reliable kinematics from MPL can be obtained when the S/N is sufficiently high. Therefore, to optimise and homogenise the S/N, we binned the pixels into angular and radial bins as in Gebhardt et al. (2003) by luminosity-weighted averaging of the spectra. The galaxy is divided into four quadrants bordered by the major and minor axes. Each quadrant is divided further into five angular bins. The centres of those bins are at the angles of 5.8°, 17.6°, 30.2°, 45.0°and 71.6°. For the 100mas data, there are seven or eight radial bins while for the 250mas data, 12-13 of those bins were needed to cover the FOV. We then performed the MPL method on the binned spectra as follows.

We first normalised the galaxy and stellar template spectra by dividing out the continua. The combined stellar template was convolved with a binned initial LOSVD. The LOSVD and the weights of the templates were iteratively changed until the convolved combined spectrum matched the galaxy spectrum. This fit was done by minimising the penalised χ^2: $\chi^2_p = \chi^2 + \alpha P$. A certain level of smoothing was applied to the LOSVD via the second term where P, the penalty function, is the integral of squared second derivative of the LOSVD. The smoothing parameter α determines the level of regularisation and its value depends on the velocity dispersion of the galaxy and the S/N of the data. We estimated the appropriate smoothing for our data from the kinematic analysis of a large dataset of model galaxy spectra. These models were created by broadening the template spectrum with a velocity dispersion of 400 km s^{-1}. Our data have a high S/N which reaches 70 in the central pixel. After the binning, the S/N increased to $\sim$ 90 (100mas) and $\sim$ 83 (250mas) on average. With those S/N values, the appropriate values for α found in the above simulations are on average $\sim$ 5 and $\sim$ 6, respectively.

To derive the LOSVDs, we specifically fitted the first two CO bandheads CO(2-0) and CO(3-1) in our spectra. To minimise the error due to template mismatch, we measured the equivalent width of the first CO bandhead as in Silge & Gebhardt (2003) and selected only stars with similar equivalent widths for the templates. Across the FOV of SINFONI 250mas, the measured values range from $\sim$ 11 to $\sim$ 15Å.

We calculated uncertainties for each LOSVD from 100 Monte Carlo realisations of the galaxy spectra. These spectra were obtained by convolving the measured LOSVD with the stellar templates. Each spectrum differs from the others in the amount of Gaussian noise added to the spectrum at each wavelength position. From every spectrum, an LOSVD was extracted and used to estimate the errors. For illustration purposes, we parametrised the LOSVDs in terms of Gauss-Hermite moments (van der Marel & Franx 1993; Gerhard 1993), i.e. velocity v, velocity dispersion σ and two higher order terms which measure the asymmetric and symmetric departure from a pure gaussian velocity profile h_3 and h_4. The typical errors that were derived for v and σ are 8.45 km s^{-1} and 8.87 km s^{-1} (100mas), respectively; for 250mas, the errors are 7.92 km s^{-1} and 9.21 km s^{-1}. For h_3 and h_4, the errors are typically 0.02 for both scales.

We present kinematic maps of NGC 1332 for both scales in Fig. 3.4. A significant rotation is shown by the well-ordered pattern in the velocity map and the anti-correlating h_3. The velocity dispersion is peaked at around 400 km s^{-1} and there is a rather steep decline towards the outskirts. In spite of the presence of dust in the nucleus, the kinematic centre seems to coincide with the photometric centre.

3.3.2 Long-slit kinematics

Our SINFONI data provide the required resolution to allow for an accurate measurement of the SMBH mass at the expense of the FOV size. To obtain constraints on the orbital structure at larger radii, we utilised long-slit data which were reported in Kuijken et al. (1996)– hereafter K96. They observed NGC 1332 using the Red Channel Spectrograph at the Multiple Mirror Telescope. The optical data were taken along the major axis of NGC 1332 through a 1.25 arcsec×3 arcmin slit with a spectral resolution of 2.6Å (instrumental σ=63 km s^{-1}). The major axis position angle (PA) given in K96 is 148° following RC3. This is about 30° higher than the PA we measured from the WFPC2 image, i.e. 117°. The latter PA is consistent with our SINFONI data, and also with the PA given by HyperLeda and ESO/Uppsala Survey. By simply looking at images of NGC 1332, a PA of 148° can be easily rejected. We have confirmed that the slit was indeed placed along the long axis of the galaxy and therefore the quoted PA in K96 is a typo (K. Kuijken, private communication).

The velocity profile of the slit data was derived using the Fourier Correlation Quotient (FCQ) method (Bender, 1990), parametrised into Gauss-Hermite parameters v, σ, h_3, h_4. The LOSVDs were then reconstructed from those moments as it is the full LOSVD that is fitted in the modelling. The data provide kinematics up to a radius of $\sim$ 80 arcsec on both sides of the major axis.

The SINFONI and the long-slit datasets overlap within 3.5 arcsec and they are broadly consistent with each other at radii $\gtrsim$ 2 arcsec. Inside that radius, v and σ derived from the long-slit data are systematically lower. For instance, at $\sim$ 0.2 arcsec, the slit data give a σ of $\sim$ 335 km s^{-1} while the 250mas and the 100mas SINFONI data give $\sim$ 365 km s^{-1} and $\sim$ 385 km s^{-1} respectively. Moreover, the SINFONI σ also shows a steeper gradient. We suspect that these differences are due to the seeing during the slit observation and the better resolution of the SINFONI data. Since the PSF of the slit observation is not known, it is difficult to investigate the discrepancy. However, we find that within the discrepant region SINFONI kinematics dominates and renders the slit kinematics unimportant, as briefly explained in the following. We modelled NGC 1332, as described in Section 3.5,

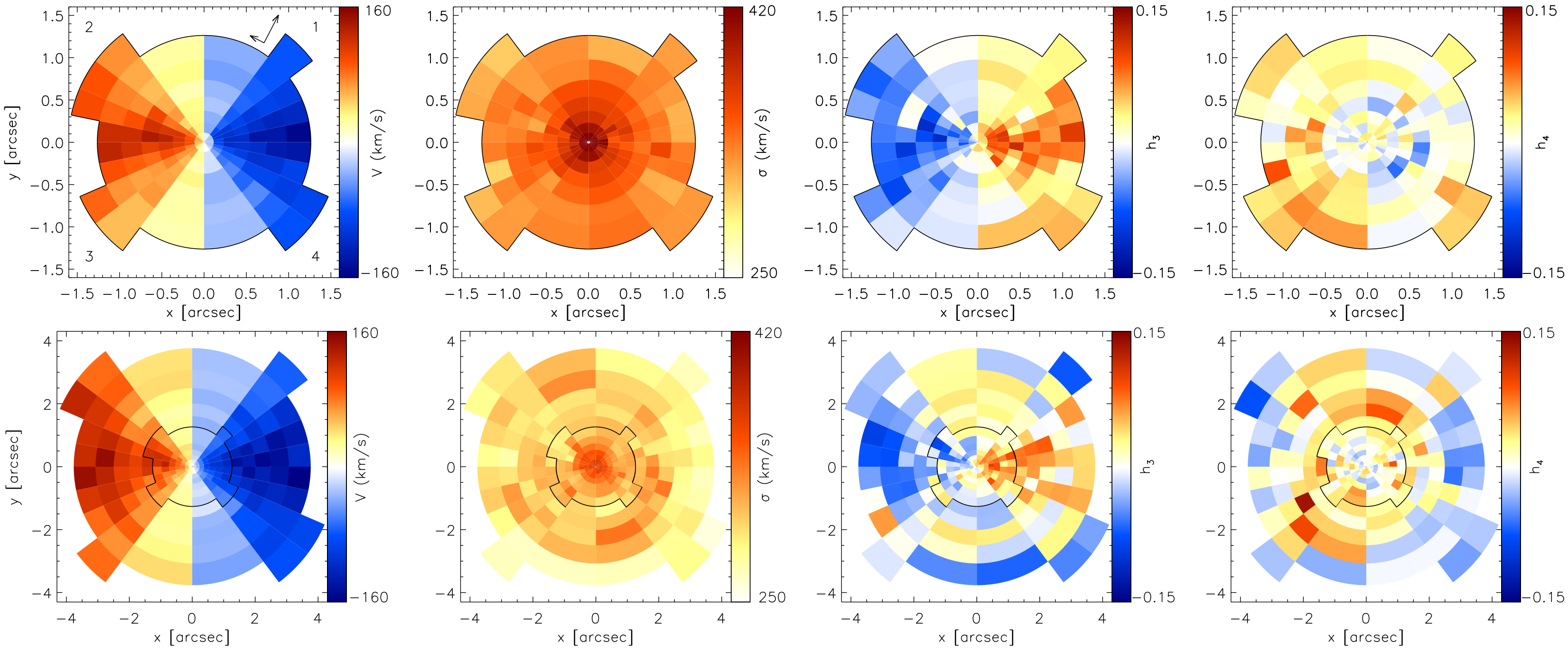

Figure 3.4: Kinematics of NGC 1332 derived from SINFONI data, illustrated in terms of Gauss-Hermite moments (v, σ, h_3 and h_4) as written on the side of each map. The first row displays 100mas data while the last row shows 250mas scale kinematics in which the spatial scope of the 100mas data is outlined. The map shows the division into radial and angular bins as described in the text. The major and minor axes of the galaxy are aligned with the abscissa and the ordinate of the coordinate system respectively. In the first map, the numbers (1-4) correspond to the quadrant numbers and the arrows indicate the orientation to the north (long) and the east (short).

using both datasets simultaneously. We ran several models using identical set-ups, varying only the slit PSF to several reasonable values (1.5 arcsec and 2 arcsec). We also ran models where we used only slit data outside the SINFONI FOV ($>$ 3.5 arcsec). We are able to show that all those variations do not alter the modelling results. With this finding, whenever we include slit kinematics in the dynamical modelling, we consider only slit datapoints outside the SINFONI FOV to ease the computational load and time.

3.4 Structural and Luminosity Modelling

3.4.1 Bulge–disc decomposition

Since NGC 1332 is an S0 galaxy with a fairly well-defined bulge and disc, we investigated bulge-disc decompositions, both for modelling purposes (i.e., in case the bulge and disc stellar populations might have different mass-to-light ratios) and so that we could estimate its bulge luminosity in order to see where NGC 1332's SMBH fell in the SMBH-bulge relations. We tried two approaches, which agreed extremely well. The first involved fitting free ellipses (i.e., with position angle and ellipticity allowed to vary) to the isophotes of the NTT-EMMI and SINFONI images (carefully masking out the dust lane in the SINFONI images) and then combining these into a single 1-D surface-brightness profile (see Section 3.4.2). The best fit to this profile was a combination of an exponential (representing the outer disc, with central surface brightness $\mu_0 = 18.78$ and scale length $h = 33.6$ arcsec), a Sérsic function (representing the bulge, with $n = 2.36$, surface brightness $\mu_e = 18.36$, and effective radius $r_e = 9.15$ arcsec), and a small, narrow Gaussian representing a possible central star cluster.

We also tried a 2D bulge–disc decomposition, using version 2.2 of the BUDDA image-fitting code (de Souza et al., 2004; Gadotti, 2008) and the NTT-EMMI image by itself; we masked the dust-affected part of the nucleus and turned on seeing correction. The best fit was with an exponential disc having an ellipticity of 0.73 ($\mu_0 = 18.66$, $h = 32.96$ arcsec), a Sérsic bulge with ellipticity = 0.27 ($n = 2.34$, $\mu_e = 18.18$, $r_e = 8.39$ arcsec), and a small point source (representing, e.g., a stellar nucleus) contributing to 1.2% of the total light. The agreement with the 1-D decomposition is excellent. We note that the 2D decomposition corresponds to a bulge-to-total light ratio of 0.43 (0.44 if we include the small point source), so NGC 1332 is, despite its high central velocity dispersion, still a (marginally) disc-dominated galaxy.

3.4.2 Photometric models

We constructed two main photometric models. The first was a single-component model, where the galaxy was represented by a single surface-brightness profile, with variable ellipticity and higher-order moments a_4, a_6, etc. (Bender & Moellenhoff, 1987). To construct this profile we fit ellipses to isophotes using three images: the NTT-EMMI R-band image and the two SINFONI images (i.e., 100mas and 250mas datacubes collapsed along the wavelength axis). For both SINFONI images, we masked out the regions affected by the nuclear dust lane before fitting ellipses. The NTT-EMMI profile was used for $r > 4.5$ arcsec; at smaller radii, where better resolution and lower dust extinction were needed, we used the SINFONI profiles (the 250mas profile was used from 4.5 arcsec in to 1.5 arcsec, with the profile at $r < 1.5$ arcsec coming from the 100mas image). We see no noticeable gradient in $V - I$ colour from HST images in the innermost 13 arcsec along the south semi-minor axis, which is less affected by dust. Since dust regions were masked out during profile extraction, $V - I$ should be flat, and so we do not expect a $R - K$ color variation, either. The combination of images from the R and K bands can therefore be justified.

The second photometric model involved separating the galaxy into a bulge and a disc, with potentially different stellar mass-to-light ratios. Since the 2D bulge-disc decomposition worked well, we decided to use the disc component from that fit as the disc component for modeling purposes. Because we wanted to match the actual surface brightness and isophote shapes in the central regions as closely as possible, using the (fixed-ellipticity) Sérsic bulge model from the 2D fit would have been too crude an approximation; even including the small Gaussian component still produces residuals and does not reproduce the actual ellipticity profile of the galaxy's inner regions. Instead, we first subtracted the disc model from our images (specifically, the NTT-EMMI image and the two SINFONI images) to create residual, "bulge-only" images and then performed variable-ellipticity fits on these images in order to generate a bulge model for modeling purposes. The result of this was that the surface brightness and ellipticity of the bulge component tracked the actual brightness and isophote shapes in the very central regions as accurately as possible; moreover, the combined light from this bulge component and the 2D disc model reproduces the original galaxy light distribution.

To construct the final bulge component, the ellipse fits to the NTT-EMMI image were used for $r > 4.5$ arcsec; the 250mas SINFONI image was used for $r = 1$–4.5 arcsec, and the 100mas image was used for $r < 1$ arcsec. As was the case for the single-component model, we carefully masked out the dust lane in both SINFONI images before running the ellipse-fitting software. At radii > 15 arcsec, the NTT-EMMI profile from the residual image became significantly affected by deviations of the disc from the 2D model which we subtracted from the image. To ensure a relatively smooth luminosity model, we replaced the data at $r > 15$ arcsec with an extrapolation of the best-fitting Sérsic component from the 2D fits (section 3.4.1), fixing its ellipticity to 0.27. At these radii, the light is dominated by the disc component, so small variations in the bulge component have minimal effect on the modelling.

Finally, we constructed an alternate single-component profile for testing purposes (see Appendix A); this was identical to the SINFONI+NTT-EMMI profile described above except that ellipse fits to the WFPC2 F814W image were used for $r < 0.5$ arcsec. Problems with strong dust extinction in the WFPC2 image ultimately led us to reject using this data for the actual modelling.

Isophotal shapes of all the models (the one-component model, bulge and disc of the two-component model and the single-component model using WFPC2/HST image) is shown in Fig. 3.5.

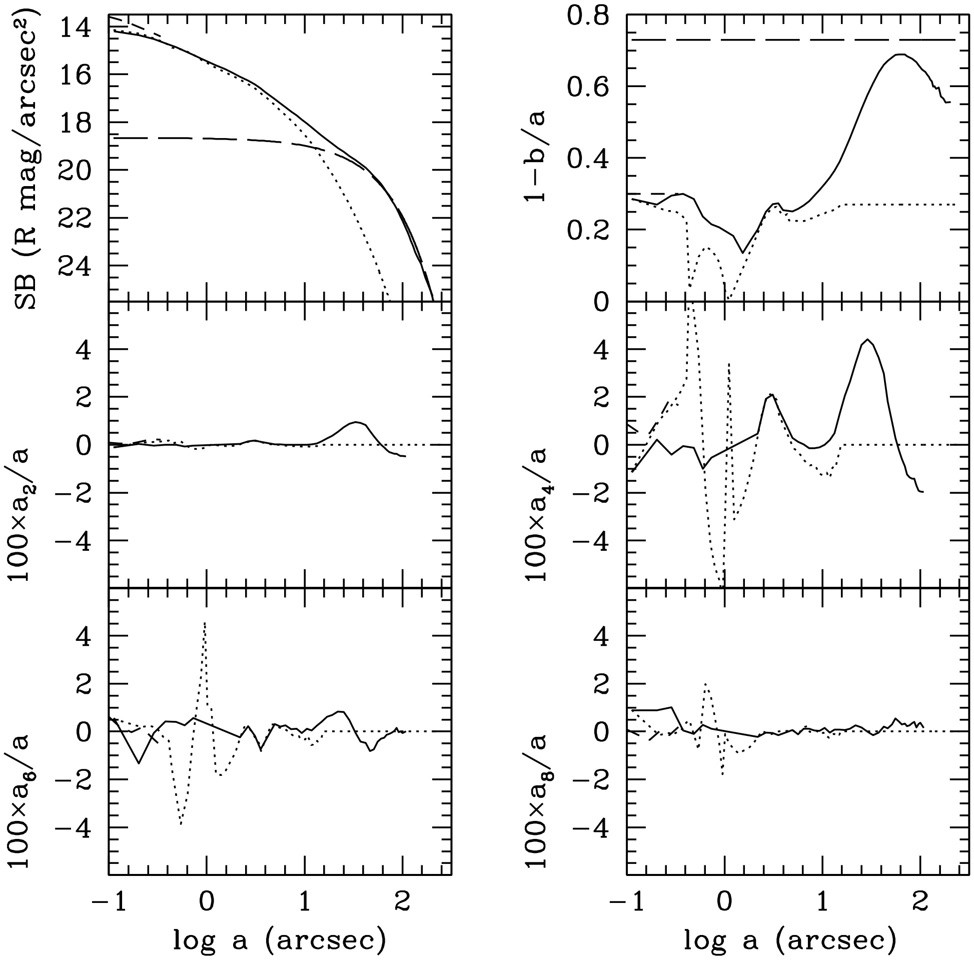

Figure 3.5: The isophotal shape analysis of NGC 1332. As a function of the logarithm of the semimajor axis distance we show the R-band surface brightness (top left), the ellipticity (top right), the a_2 (middle left), a_4 (middle right), a_6 (bottom left) and a_8 (bottom right) coefficients of the isophotal Fourier analysis. The solid lines refer to the one-component photometry. The short dashed lines show the photometric parameters as derived from the HST image in the inner 0.5 arcsec. The dotted and long dashed lines show the bulge and disc components of the two-component photometry, respectively.

3.4.3 Deprojection

The dynamical modelling requires knowledge of the three-dimensional luminosity distribution ν (cf. Section 3.5). Each photometric profile, i.e., the single-component model, the bulge and the disc model was deprojected separately, resulting in the (R-band) 3D luminosity profiles ν, ν_b and ν_d respectively. Since the disc flattening is small, the orientation of NGC 1332 must be close to edge-on. We therefore assume an inclination of 90° throughout the chapter unless otherwise stated. The edge-on deprojection gives an intrinsic flattening of 0.27 for the disc.

The deprojections of the bulge, the disc and the one-component model were done under the assumption of axisymmetry using a modified version of the code of Magorrian (1999). We briefly describe it as follows. We first constructed an initial density model, defined in equation 10 of Magorrian (1999). This was done by running through a grid of the model parameters. Each of the models was convolved and projected to be compared with the observed surface brightness. The model with the smallest χ^2 was selected as the initial model. This model was then refined by applying small changes through a simulated annealing procedure as in Magorrian (1999). The convolution, projection and comparison steps were subsequently repeated after each change. The iteration was stopped and the final density model was reached when the model matched the observations within a predetermined accuracy.

For the disc component, the PSF effect is negligible because the disc is very faint at the innermost radii where the PSF becomes important (the central luminosity density of the disc is at least three orders of magnitude lower than that of the bulge). For the bulge and the one-component model, where the innermost isophotes are based on the SINFONI 100mas image, we had to take the PSF into account during the deprojection. For this purpose, we used the double-Gaussian parameterisation of the SINFONI PSF described in Section 3.2.1 to implement the PSF convolution.

We show the PSF-deconvolved luminosity density profiles for both density models in Fig. 3.6. For the two-component models, we plot the total quantity (bulge + disc). The density of the disc exceeds that of the bulge at $r > 12$ arcsec. The difference of the density profiles at $\lesssim 1$ arcsec reflects a certain level of uncertainties in the photometry and the bulge-disc decomposition, which gets amplified in the deprojection. The luminosity densities differ mainly along the minor axis. It is apparent that the two-component density model is rounder in the centre. We investigate how these uncertainties and differences affect the SMBH mass estimate in Section 3.6.

3.5 Dynamical Modelling

We employed an orbital synthesis method based on Schwarzschild (1979) to model NGC 1332 and to measure the SMBH mass. In particular, we used the three-integral axisymmetric code described in Gebhardt et al. (2000b, 2003), Thomas et al. (2004) and Siopis et al. (2009). The modelling procedure includes the following steps. (1) Calculation

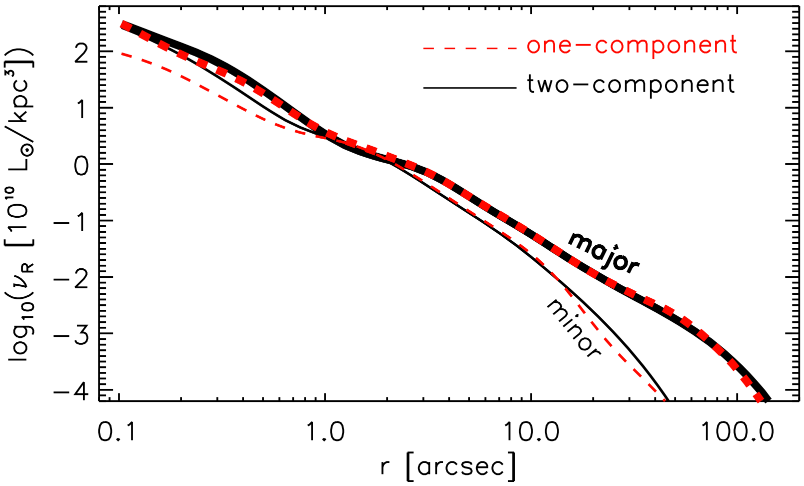

Figure 3.6: The model of PSF-deconvolved luminosity density of the one-component (red dashed line) and the two-component (black solid line) density models for an inclination of 90°. The subscript "R" refers to the *R*-band. Thick and thin lines refer to density profiles along the major and minor axes respectively.

of a trial gravitational potential consisting of the contribution from stars and the SMBH. (2) Generation of an orbit library which obeys the given potential. (3) Calculation of orbital weights such that the orbit superposition satisfies the light distribution and the kinematical constraints. (4) Repetition of steps (1)-(3) for different trial potentials obtained by varying the mass-to-light ratio(s) and the SMBH mass. The best-fitting parameters are then found through a χ^2 analysis.

We used each of the two density models described in Section 3.4.3 for the modelling. For the one-component density model, the mass distribution of NGC 1332 followed $\rho = \Upsilon\nu + M_{\mathrm{BH}}\delta(r)$, where the stellar mass-to-light ratio Υ and M_{BH} were the only free parameters. For the two-component density models, the mass distribution became $\rho = \Upsilon_b\nu_b + \Upsilon_d\nu_d + M_{\mathrm{BH}}\delta(r)$ with the bulge mass-to-light ratio Υ_b, the disc mass-to-light ratio Υ_d and M_{BH} as the free parameters.

Each of our orbit libraries consisted of about 2×15000 orbits, i.e. two identical sets of 15000 orbits, opposite in angular momentum directions. We set the maximum radius of the libraries to 100 arcsec and limit the extension of the long-slit data to 30 arcsec. For each of the modelling runs that we conducted (cf. Section 3.6), we modelled each quadrant separately, resulting in four different SMBH mass values, one for each quadrant. This highlights the benefit of having integral-field data, i.e. (1) to justify the assumption of axisymetry, (2) to have a complete spatial coverage of kinematic data and (3) to allow for four independent measurements of the SMBH mass (under the assumption of axial symmetry). In order to implement the PSF convolution in the modelling as accurately as possible, we directly used the SINFONI PSF images from both scales, instead of the double Gaussian parameterisation.

The SINFONI data were mapped into 226 spatial bins (see Fig. 3.4), 120 of which come from the 100mas data and sample the inner part. As kinematic constraints, we used the full LOSVD of each bin, sampled into 25 velocities from -1543 km s^{-1} to 1543 km s^{-1}. These provided a total of $226 \times 25 = 5650$ kinematic observables to be fitted by the dynamical models (about 1412 observables per quadrant). The LOSVDs from the long slit data (3.5 arcsec$< r <$30 arcsec) were binned in the same way, increasing the total number of observables by 650 (~ 162 for each quadrant).

3.6 Results

3.6.1 The black hole mass and stellar mass-to-light ratio

As described in the previous sections, we prepared two kinematics datasets and constructed two stellar density models. For the latter, an inclination of 90° is assumed. In this subsection we discuss the results for the edge-on models. We address the uncertainties due to inclination in another subsection (3.6.3), where we also show that the edge-on models produce better fits to the data.

We performed five different modelling runs using different combinations of the density models and kinematics to probe the possible systematic uncertainties that could arise from various constraints/datasets. For each density model, there were two runs, one with and one without slit kinematics (100mas and 250mas SINFONI kinematics were always used). We list all runs with the resulting $M_{\rm BH}$ for each quadrant in Table 3.1 and similarly for the mass-to-light ratios in Table 3.2. The naming of the five runs is described in the caption of the first table. Whenever the slit kinematics was used, only slit datapoints within 3.5 arcsec$< r <$30 arcsec were included in the modelling. For the runs with the two-component density model, we first used identical values for Υ_b and Υ_d (runs 2A and 2B) and then we let both parameters vary with respect to each other (run 2B*). For run 2A, there were 14 values of $M_{\rm BH}$ ($5 \times 10^8 M_\odot$ to $3.6 \times 10^9 M_\odot$) and 20 Υ_b (3 to 13). In run 2B, we calculated models for the same 14 values of $M_{\rm BH}$ as in run 2A and 12 Υ_b (4 to 10). A set of 14 Υ_d (2 to 11) values were then added for run 2B*. Run 1A and 1B used 20 $M_{\rm BH}$ (5×10^8 to $5 \times 10^9 M_\odot$) and 20 Υ (1 to 20).

The corresponding χ^2 curve for Table 1 is shown in Fig. 3.7. We plot the normalised χ^2 for all the models and all the quadrants. Ideally, the normalisation is done by dividing the χ^2 by the number of degrees of freedom (dof). For the SINFONI data, the smoothing parameter included in the LOSVD derivation correlates the velocity bins, such that the number of dof is smaller than the number of observables (more details can be found in Gebhardt et al. 2000b). Because the exact number of dof is unkown, we approximate it by the number of observables when normalising the chisquare for runs 1A and 2A. For runs 1B, 2B and 2B*, there are an additional dof contributed by the slit data. Each of the slit LOSVDs was generated from four Gauss-Hermite parameters (see Section 3.3.2) so there are four dof for every slit LOSVD. The normalisation factor for each run and quadrant is included in Fig. 3.7. The normalised χ^2 values are less than unity, as is commonly found in the orbit-based dynamical modelling. This is partly because the number of observables is larger than the effective number of dof due to the aforementioned smoothing parameter.

For each marginalised χ^2 curve of M_{BH} (see Fig. 3.7) or Υ we approximated the 1σ error (a $\Delta\chi^2$ of 1) by a polynomial fitting. To check whether the measurements in the four different quadrants are in agreement with each other, we compare the 1σ errors with the standard deviation/rms derived from the four measurements. We expect the rms to be comparable to the 1σ errors as the latter indicate the range of values within which the measurements (from quadrant to quadrant) would fluctuate. For most of the results in Table 1 and 2, the rms do not fall far from the 1σ errors, especially for M_{BH} measurements. It follows that (1) the four quadrants give consistent results and (2) the χ^2 analysis provides a reliable measurement of the errors in each quadrant.

All models strongly suggest the presence of a central black hole with a mass of at least $10^9 M_{\odot}$. No-SMBH models were not included in any of the runs as for these models, $\Delta\chi^2 > 20$ (compared to the best-fit model) can be readily inferred from the χ^2 curves. The signature of the SMBH is strongest in the models that include long-slit data, i.e. they give higher best-fit M_{BH} in most cases and exclude the $M_{\mathrm{BH}}=5\times10^8\ M_{\odot}$ with higher confidence (see Fig. 3.7). $M_{\mathrm{BH}}=5\times10^8 M_{\odot}$ is the lowest M_{BH} that we modelled and it coincides with the resulting M_{BH} derived from X-ray data by H09. It is, however, not favoured by any of our runs. The $\Delta\chi^2$ of the best-fitting model for $M_{\mathrm{BH}}=5\times10^8 M_{\odot}$ is larger than 10 for run 1A and larger than 20 for the other runs.

From the result of the five runs, we see that M_{BH} is rather sensitive to the change of the photometry and therefore the prescribed density profiles, as is also found by Siopis et al. (2009). As the galaxy becomes rounder in the inner part of the two-component model, M_{BH} becomes systematically higher and Υ becomes lower compared to the one-component model. The mass-to-light ratio difference between runs 1A and 2A is larger than the difference between runs 1B and 2B. The addition of slit data reduces the difference in mass-to-light ratio but the trend remains. The increase of M_{BH} in two-component models is probably related to the flatter slope of the density inside ~ 0.3 arcsec. It is, however, reassuring to see that the differences in the two mass models do not push M_{BH} beyond their 1σ errors.

The addition of the slit data seems to bring Υ_b to a lower value which ultimately increases M_{BH} to preserve the enclosed mass. Another important aspect from including the slit data is that it should reduce the statistical uncertainties in the modelling. This is indeed the case as can be seen in Table 1 and 2: 1σ errors decrease from run 1A to 1B and from run 2A to 2B. Fig. 3.7 provides a more straightforward way to assess this. The χ^2 curves of the run 1B are narrower and is enveloped by run 1A. The same is true for run 2A with respect to run 2B and also run 2B*.

In run 2B*, we repeated run 2B but allow for Υ_b and Υ_d to be different from each other. The resulting M_{BH} and Υ_b in all quadrants are unchanged with respect to run 2B. The best-fitting models of the four quadrants in run 2B* produce generally better χ^2 values since they were given extra freedom to fit the data. It appears that untying Υ_d and Υ_b does not lead to any change (or small if anything at all) in M_{BH}. Υ_d in run 2B* is not constrained well by the data since the kinematics data extend only up to 25-30 arcsec, approximately where the disc becomes important. The results suggest that the disc has a higher mass-to-light ratio than the bulge (see the caption of Table 3.2). Although we varied Υ_d quite extensively, Υ_b is stable, showing that Υ_d is not correlated with Υ_b.

In the dynamical modelling, the resulting mass-to-light ratio is closely connected to $M_{\rm BH}$. It is therefore important to constrain the orbital structure in the outer part as much as possible; this gives a stronger preference for the runs which include slit data. The resulting $M_{\rm BH}$ of the three runs with slit data (1B, 2B and 2B*) are all consistent with each other within their 1σ errors. As for the density model choice, we are more inclined towards the two-component density model. The bulge-disc decomposition was done based on the morphology of the galaxy and to allow for different components to have stellar populations with potentially different mass-to-light ratios. The results of run 2B* hint that Υ_d is higher than Υ_b, although the former is not well-constrained by the data. It turns out that even though Υ_b and Υ_d might be different, $M_{\rm BH}$ does not depend on a possible Υ gradient outside the bulge. Nevertheless, because in run 2B* we have explored the most degrees of freedom we consider its $M_{\rm BH}$ as the least biased estimate compared to the other runs. We selected the best-fitting model in run 2B* as our preferred model and quote the mean of $M_{\rm BH}$ and Υ_b estimates in four quadrants as our best estimate. To be conservative, we adopt the largest nominal of errors as the final error margin, i.e. 0.20 for the $M_{\rm BH}$ and 0.39 for the Υ_b.

The major-axis kinematics and the model fitting are presented for the four quadrants in the first and second row of Fig. 3.8. We plot v and σ to represent the kinematics. We stress that it is the LOSVD (derived from the SINFONI spectra and from the Gauss-Hermite parameters of the slit data) that is fitted by the model, not the velocity moments. Our preferred model is shown by the red line. For comparison, we overplot the best-fitting model for $M_{\rm BH}$ of $5 \times 10^8 M_\odot$ (blue line). In the centre, the blue line falls below the red line as expected from the SMBH masses of the models. It climbs over the red line at intermediate radii and lies above the red line in the outer region because Υ_b of the best-fitting model for $M_{\rm BH}$ of $5 \times 10^8 M_\odot$ is higher than that of our preferred model. This effect is shown by the dashed green line which represents the models where $M_{\rm BH}$ is 5×10^8 and Υ_b and Υ_d are the same as those of the preferred model. At a first glance, it might not be directly obvious which model fits the data best. To investigate this, we plot the χ^2 differences between the preferred model and the two models with $M_{\rm BH}$=$5 \times 10^8 M_\odot$ (averaged over the five angular bins) as a function of radius in Fig. 3.8.

The $\Delta\chi^2$ between our preferred model and the best-fitting model with $M_{\rm BH}$= $5 \times 10^8 M_\odot$ is the solid line while the $\Delta\chi^2$ between the preferred model and the other model is the dashed line. For both cases $\Delta\chi^2$=$\chi^2_{\rm preferred} - \chi^2_{\rm 5e8}$. Both lines generally lie at $\Delta\chi^2 \lesssim 0$. It is clear that models with $M_{\rm BH}$=$5 \times 10^8 M_\odot$ produce worse fits than the preferred model. There seems to be a trade-off and an inconsistency in the models with $M_{\rm BH}$=$5 \times 10^8 M_\odot$ with respect to the data, i.e., the mass-to-light ratio that better fits the slit data yields a worse fit to the SINFONI data. The importance of the slit data in constraining the mass-to-light ratio is apparent where the dashed lines lie mostly above the solid lines in the region covered by the slit data. For the solid line, $\Delta\chi^2$ is slightly lower in this region than in the SINFONI region, giving the impression that the slit data plays a more significant role in determining the black hole mass through the mass-to-light ratio. However, the dashed lines show that when the mass-to-light ratios were held fixed between models with different M_{BH}, there is still a strong preference for the preferred model from the SINFONI data. Both datasets have their own contributions in the SMBH mass determination and they complement each other.

One might argue that the presence of dust in this galaxy would bias the kinematics, mass tracers and the SMBH mass estimate. We compared the kinematics extracted from the dust-extincted and the dust-free part of the galaxy and we did not find systematic differences. There is also no asymmetric pattern in the SINFONI kinematics map that can be attributed to the dust (compare Fig. 3.1 and Fig. 3.4). The dust seems to be confined to a region inside ~ 0.5 arcsec and this was masked out in the photometric analysis for the mass models. We do not observe any large-scale dust structure in NGC 1332 that would significantly affect our results (cf. Baes et al. (2000) for a discussion of the dust effects). A minor influence would probably lower SMBH mass slightly, due to the underestimated Υ_b.

3.6.2 Comparison with stellar population models

We compared the dynamical mass-to-light ratio to that of a single stellar population (Υ_{SSP}). Estimates of stellar population properties (age and metallicity for the purpose of deriving Υ_{SSP}) of NGC 1332 can be found in Barr et al. (2007) and H09. The former measurements were based on spectra from NTT-EMMI observations while the latter made use of Lick indices provided in Trager et al. (1998). Barr et al. (2007) quote a log age of 1.103 ± 0.024 (age of 12.7 ± 0.7 Gyr) and a metallicity of 0.270 ± 0.023 while in H09, the age is $4^{+8.8}_{-1.4}$ Gyr with a metallicity of 0.32 ± 0.3. The huge difference in the ages (apart from the errors) result in very different values of Υ_{SSP}, as derived from the SSP models of Maraston (2005). Compared to Υ_{SSP}, our mass-to-light ratio is almost two times larger when using the age of H09 with a Salpeter IMF ($\Upsilon_{\mathrm{SSP}} \sim 3.6$) or about three times larger with a Kroupa IMF ($\Upsilon_{\mathrm{SSP}} \sim 2.3$).

Our dynamical mass-to-light ratio is much more consistent with Υ_{SSP} when the galaxy age is taken to be ~ 12 Gyr. This age is the one measured by Barr et al. and it is compatible with the upper limit of H09 measurement. In addition, Lick indices measured by Ogando et al. (2008) also imply an old age of at least 12 Gyr. The Barr et al. age results in Υ_{SSP} of ~ 5.0 for a Kroupa IMF or ~ 7.9 for a Salpeter IMF. Our dynamical mass-to-light ratio falls in between these two values, but is closer to the Salpeter one. The tendency that the dynamical Υ agrees better with the Salpeter-based Υ_{SSP}, rather than Kroupa, in massive early-type galaxies was previously found by Cappellari et al. (2006) and also by Thomas et al. (in preparation). Although not conclusive, this might indicate that the Salpeter IMF is a better represention of stellar populations in massive early-type galaxies (see also Grillo et al. 2009 and Treu et al. 2009).

3.6.3 Inclination effects

According to its high ellipticity (reaches ~0.7), the orientation of NGC 1332 must be close to edge-on. To check for any influence of the residual small uncertainty in the inclination, we ran models with $i < 90^\circ$. Constraining the disc to an intrinsic flattening no less than 0.2 gives 80° as the lower limit of the inclination. Using this angle, we repeated the deprojection step and the modelling for each of the four quadrants as in run 2B*. We found $M_{\rm BH}$=1.45 $\times$ $10^9 M_\odot$(rms=0.20 $\times$ $10^9 M_\odot$), Υ_b=6.95 (rms=0.30) and Υ_d=7.0 (rms=1.83). Compared to run 2B*, $M_{\rm BH}$ does not change and there is only a slight decrease in both Υ_b and Υ_d. The uncertainties that could arise from the inclination assumption appear to be negligible in the case of NGC 1332. Compared to the preferred model ($i = 90^\circ$), the best-fitting model with $i = 80^\circ$ is worse by a $\Delta\chi^2$~30-50 in every quadrant.

3.6.4 Dark matter halo

Recently, concerns have emerged that dynamical models which do not include a dark halo component underestimate the true $M_{\rm BH}$ as is the case in M87 (Gebhardt & Thomas 2009). The reason is that models without dark halo require a higher stellar mass-to-light ratio in the outer part to compensate for the missing dark mass. In a single-component (density) model this leads to an overestimation of the central stellar mass and correspondingly to an underestimation of $M_{\rm BH}$.

In this work, we do not include a dark matter halo component in any of the models. Compared to the case of M87 (Gebhardt & Thomas, 2009), the SMBH's sphere of influence in NGC 1332 is better-resolved by our SINFONI observations. The Υ_b-$M_{\rm BH}$ degeneracy then becomes less severe as there are kinematic constraints at several radii inside the sphere of influence. This kinematic data constrain the enclosed mass at each of those radii and help to disentangle the SMBH and the stellar contribution to the central potential. We decided that our measurements are sufficiently robust and it is not necessary to further investigate $M_{\rm BH}$ by including a dark halo component also for the following reasons. The kinematic data that we used in the modelling only extend out to $r \lesssim 30$ arcsec or equivalently $r \lesssim 3$ kpc. At this radius, we expect only a small fraction of the total mass to be in the dark matter halo. Empirically, the dark matter fraction found in early-type galaxies with a similar luminosity to NGC 1332 ($\rm M_B = -20.5$, as given by HyperLeda) is at most 25% at a radius of 3 kpc (Thomas et al., 2007). The mass decomposition for NGC 1332 in H09 suggests that the dark halo only takes ~10% of the total mass at 3 kpc. Furthermore, in our preferred model, the galaxy is decomposed into a bulge and a disc with each component having its own mass-to-light ratio. The bulge is well inside the region where the dark matter is expected to be unimportant. Its mass-to-light ratio Υ_b is then not affected by the assumption about the halo. Neglecting the halo could bias Υ_d to be too high. However, the central stellar mass is dominated by the bulge so it does not suffer from any bias in Υ_d and therefore the black hole mass is not affected by the exclusion of the dark halo. It is obvious from Run 2B and 2B* that Υ_b is independent of the variation in Υ_d.

3.7 Summary and Discussion

We presented SINFONI observations of the lenticular galaxy NGC 1332 in the K-band with the purpose to measure the mass of the SMBH. The sphere of influence of the SMBH ($\sim$0.76 arcsec) is resolved by the data (spatial resolution: FWHM $\approx$ 0.14 arcsec). The kinematics, derived by fitting the CO bandheads, show a moderate rotation ($v \approx 150-160$ km s^{-1} at the outermost radius of SINFONI data) and a high velocity dispersion ($\sim$ 400 km s^{-1} in the centre). To complement our SINFONI data at larger radii, we utilised major-axis long-slit data of K96. Both datasets are consistent outside $r > 2$ arcsec; inside that radius the comparison is difficult due to the PSF difference.

To determine the SMBH mass, we performed axisymmetric Schwarzschild modelling. The systematic uncertainties inherent in the dynamical models, which are due to assumptions on the inclination, the density profile and the assumption of axisymmetry, were investigated. For the modelling input, two density models were constructed: a one-component model and a two-component model; the latter consists of a bulge and a disc. For each density model, we performed runs with and without the long-slit data. Using both SINFONI ($r < 3.5$ arcsec) and long-slit data ($3.5 < r < 30$ arcsec) as the kinematic constraints, SMBH masses obtained using two different density models are consistent with each other. The inclusion of long-slit data appears to give significant constraints to the models and reduce the errors. The orientation of NGC 1332 is close to edge-on and the small uncertainties in the inclination assumption causes a negligible effect on the SMBH mass. The lack of obvious signs of triaxiality, e.g., isophotal twists or kinematics misalignments, justifies the assumption of axisymmetry. $M_{\rm BH}$ values measured in the four different quadrants are consistent with each other.

Our preferred model is based on the two-component density profile, includes both SINFONI and long-slit data and adopts an inclination angle of 90°. We find a SMBH mass of $M_{\rm BH}$=$(1.45 \pm 0.20) \times 10^9 M_\odot$ and a bulge mass-to-light ratio Υ_b=7.08 ± 0.39 in the R band. The disc mass-to-light ratio is not well-constrained by the data but falls within a range of 5.0 to 9.0 (also in R-band). The comparison of our results to previous measurements and the implication of this $M_{\rm BH}$ for the $M_{\rm BH}$-σ and the $M_{\rm BH}$-L relations are discussed in the following.

3.7.1 Comparison with results from X-ray data

Our results were preceeded by an X-ray analysis of NGC 1332 using Chandra data (H09). They derive a most probable SMBH mass of $5.2^{+4.1}_{-2.8} \times 10^8 M_\odot$ ($5.4^{+4.3}_{-2.9} \times 10^8 M_\odot$ at the distance adopted in this work), and a mass-to-light ratio in J-band of $1.16^{+0.12}_{-0.14}$ ($1.11^{+0.11}_{-0.14}$ at our distance). As shown in Section 3.6, models with $M_{\rm BH}$=$5 \times 10^8 M_\odot$ do not provide a proper fit to the kinematic data and they are separated from our preferred model by $\Delta\chi^2$ of at least 40. This is understandable since the SINFONI data give a high central velocity dispersion inside the sphere of influence and thus such a SMBH mass would be incommensurate. The $M_{\rm BH}$ value of H09 is obtained by using the $M_{\rm BH}$-σ relation as the Bayesian prior. They are unable to rule out the possibility that the SMBH mass is an underestimate. The use of X-ray data alone, without the M_{BH}-σ prior, decreases their M_{BH} estimate even further although the upper limit is similar to our M_{BH} estimate (see their Fig. 8).

Comparing our stellar mass profile with that of H09, we find that while the slope is very similar, our enclosed mass is twice as high at all radii where the stars dominate. The discrepancy is, however, not specific to H09; stellar mass profiles for NGC 1332 derived from other X-ray analyses (Fukazawa et al. 2006; Nagino & Matsushita 2009) seem to be in agreement with H09. We find that lowering the inclination to 80°only has a negligible effect to the mass profile. From the orbital structure of our preferred model we find that the rotation is only important at the outer radii. In Fig. 3.9, we plot $v_\phi/\langle\sigma\rangle$ along the major axis, where the rotation is highest. This quantity measures the importance of rotation with respect to random motion. At the inner radii, the significance of rotation is low and thus negligible for the mass estimation. The $v_\phi/\langle\sigma\rangle$ profile, however, rises with radius and peaks at a value of order unity at $r \sim 20$ arcsec. From this, we can expect that if the gas follows the stellar rotation, the X-ray-derived mass would be underestimated the most around this radius by roughly 25%. Rotation can therefore not be responsible for the systematic difference in the mass profile. The difference in mass is reflected by the difference in the resulting mass-to-light ratios in our models and the models of H09. From the stellar population point of view, the low mass-to-light ratio measured by H09 can be obtained if this galaxy is young. However, the age of 4 Gyr as derived in H09 has a large upper error which is consistent with the old age found by Barr et al. (2007) (see subsection 3.6.2).

This is not the first time that a dynamically derived mass differs from that of the X-ray (Shen & Gebhardt 2010; Johnson et al. 2009; Romanowsky et al. 2009). In those works, the invalidity of the assumption of hydrostatic equilibrium is suspected to contribute at least to some fraction of the discrepancy, as is also pointed out by Diehl & Statler (2007) and Ciotti & Pellegrini (2004). Inflowing gas and the presence of non-thermal pressure due to magnetic fields, microturbulence or cosmic rays are possible reasons as to why the X-ray derived mass can be lower than the true mass (Ciotti & Pellegrini 2004; Johnson et al. 2009; Churazov et al. 2008). In the case of NGC 1332, our dynamical modelling implies a much higher M_{BH}, which might indicate the failure of hydrostatic approximation, at least in the inner part. In the outer region, rotation can possibly account for a small part of the missing X-ray mass. All in all, the mass discrepancy probably involves a combination of systematic uncertainties in both methods, for which a detailed inspection is outside the scope of this thesis. A situation similar to that of NGC 1332 has been recently reported by Shen & Gebhardt (2010) for NGC 4649. Their orbit-based modelling results in a larger M_{BH} and a $\sim 70\%$ higher mass profile than obtained from X-rays in H09. A larger sample of galaxies would indeed be required to investigate whether this trend applies generally for these two methods.

3.7.2 SMBH-bulge relation

With our $M_{\rm BH}$ measurement, and our photometric decomposition, NGC 1332 is displaced from the standard relations in both $M_{\rm BH}$-σ and $M_{\rm BH}$-L diagrams (Fig. 3.10). The galaxy is located above the Gültekin et al. (2009b) $M_{\rm BH}$-σ relation by 0.15-0.20 dex which is still within the intrinsic scatter. The velocity dispersion of 327.7 km $\rm s^{-1}$ was calculated using the definition of σ_e in Gültekin et al. (2009b). It was measured using the slit data within the effective radius of the bulge of $8.39''$. Without the luminosity-weighting, the velocity dispersion drops to 319.2 km $\rm s^{-1}$ which is very close to the value found in HyperLeda.

In the $M_{\rm BH}$-L diagram, NGC 1332 is strikingly off of the Marconi & Hunt (2003) relation. Our $M_{\rm BH}$ is one order of magnitude higher than expected for its bulge luminosity. If the M_{BH}-L_K (L_K is the bulge luminosity in the K-band) were obeyed, it would result in a black hole mass of $1.37 \times 10^8 M_\odot$ which is highly excluded in any of our runs.

The σ-L relation in the current black hole samples is known to be different from that in the SDSS sample, on which the distributions of L and σ are based; the black hole samples have larger σ for a given L or smaller L for a given σ (Bernardi et al. 2007; Tundo et al. 2007; Lauer et al. 2007). In this case NGC 1332 is not an exception. It is in fact a rather extreme outlier in the σ-L diagram of Bernardi et al. (2007) for SMBH sample, i.e. the bias is stronger than expected from the SMBH sample. The $M_{\rm BH}$-σ and the $M_{\rm BH}$-L relations predict different SMBH masses and contradict each other by a factor of about seven.

Provided that the bias in the σ-L relation is just a selection effect, a question arises: which relation is the more fundamental one? Our result for NGC 1332 favours the $M_{\rm BH}$-σ to be the more fundamental relation since the measured $M_{\rm BH}$ for this galaxy turns out to fall much closer to the value predicted by the $M_{\rm BH}$-σ relation. This is in line with the suggestion of Bernardi et al. (2007). In addition, NGC 1332 is located slightly above the $M_{\rm BH}$-σ relation, which makes it also consistent with the suggestion that the relation curves upwards at the upper end (Wyithe 2006) or that the intrinsic scatter increases in this regime.

Acknowledgements

We thank the Paranal Observatory Team for support during the observations. We are grateful to Koenraad Kuijken for sharing the long slit spectral data which we used for the dynamical modelling and to Ortwin Gerhard for useful discussions. We would also like to acknowledge the anonymous referee, whose comments have improved this chapter. The research of P.E. is supported by the Deutsche Forschungsgemeinschaft through the Priority Programme 1177 'Galaxy Evolution'. Support for N.N. is provided by the Cluster of Excellence: 'Origin and Structure of the Universe'.

Table 3.1: The best-fitting M_{BH}, marginalised over all mass-to-light ratios, for the four quadrants and their average for all runs that we performed. All values are stated in units of $10^9 M_\odot$. The 1σ errors ($\sim 68\%$ confidence level), derived from the $\Delta\chi^2$ analysis, are given for each quadrant in square brackets. The last row gives the average of the measurements of the four quadrants with the average of their 1-σ errors. We compare these errors with the parenthesised values which are the standard deviation (rms) of the best-fitting values of the four quadrants. We expect them to be comparable (see Section 3.6). The naming of the runs is chosen as follows. The letters A and B identify the datasets used for the kinematics. Run A used SINFONI data only while run B also used slit data within $3.5'' < r < 30''$. The numbers 1 and 2 indicate the use of the one-component and two-component density models respectively. In run 2A and 2B we set Υ_b=Υ_d, whereas in run 2B* we decoupled Υ_b and Υ_d. All runs adopted an inclination angle of 90°.

	Run 1A (single-component, SINFONI)	Run 1B (single-component, SINFONI+slit)	Run 2A (two-component (Υ_b=Υ_d), SINFONI)	Run 2B (two-component (Υ_b=Υ_d), SINFONI+slit)	Run 2B* (two-component ($\Upsilon_b \neq \Upsilon_d$), SINFONI+slit)
Quadrant 1	$0.97^{+0.54}_{-0.06}$	$1.45^{+0.19}_{-0.13}$	$1.21^{+0.31}_{-0.12}$	$1.68^{+0.08}_{-0.21}$	$1.68^{+0.09}_{-0.26}$
Quadrant 2	$1.21^{+0.05}_{-0.41}$	$0.97^{+0.19}_{-0.14}$	$1.21^{+0.23}_{-0.13}$	$1.21^{+0.28}_{-0.08}$	$1.21^{+0.23}_{-0.08}$
Quadrant 3	$0.97^{+0.34}_{-0.08}$	$1.21^{+0.21}_{-0.05}$	$1.45^{+0.07}_{-0.28}$	$1.45^{+0.17}_{-0.07}$	$1.45^{+0.17}_{-0.09}$
Quadrant 4	$1.45^{+0.07}_{-0.35}$	$1.21^{+0.26}_{-0.04}$	$1.45^{+0.12}_{-0.15}$	$1.45^{+0.17}_{-0.09}$	$1.45^{+0.21}_{-0.08}$
Mean	$1.15^{+0.25}_{-0.23}(0.23)$	$1.21^{+0.21}_{-0.09}(0.20)$	$1.33^{+0.18}_{-0.17}(0.14)$	$1.45^{+0.18}_{-0.11}(0.20)$	$1.45^{+0.18}_{-0.13}(0.20)$

Table 3.2: The best-fitting Υ or Υ_b in the R-band, marginalised over all $M_{\rm BH}$, for the four quadrants and their average for all runs listed in Table 3.1. The 1σ errors ($\sim$ 68% confidence level), derived from the $\Delta\chi^2$ analysis, are given for each quadrant. The last row gives the average of the measurements of the four quadrants with the average of their 1σ errors. Descriptions of the runs are given in the caption of Table 3.1. For run 2B* where Υ_b and Υ_d were decoupled, we write down only Υ_b since Υ_d was poorly constrained. The four measurements of Υ_d in run 2B* fell within a range of 5.0 to 9.0 with an average of 8.0 and rms of 2.0

	Run 1A (Υ)	Run 1B (Υ)	Run 2A (Υ_b=Υ_d)	Run 2B (Υ_b=Υ_d)	Run 2B* (Υ_b)
Quadrant 1	$9.58^{+0.30}_{-0.99}$	$6.74^{+0.78}_{-0.12}$	$8.26^{+0.30}_{-1.20}$	$6.68^{+0.35}_{-0.18}$	$6.68^{+0.38}_{-0.38}$
Quadrant 2	$7.68^{+0.97}_{-0.31}$	$7.68^{+0.05}_{-0.44}$	$7.74^{+0.33}_{-0.77}$	$7.21^{+0.29}_{-0.58}$	$7.21^{+0.31}_{-0.37}$
Quadrant 3	$10.53^{+0.42}_{-1.48}$	$7.68^{+0.15}_{-0.25}$	$7.74^{+0.34}_{-0.66}$	$7.21^{+0.24}_{-0.30}$	$7.21^{+0.24}_{-0.33}$
Quadrant 4	$7.68^{+0.92}_{-0.26}$	$7.68^{+0.12}_{-0.77}$	$7.74^{+0.33}_{-0.77}$	$7.21^{+0.13}_{-0.26}$	$7.21^{+0.21}_{-0.46}$
Mean	$8.87^{+0.65}_{-0.76}$(1.42)	$7.45^{+0.28}_{-0.40}$(0.47)	$7.87^{+0.33}_{-0.85}$(0.26)	$7.08^{+0.25}_{-0.33}$(0.26)	$7.08^{+0.29}_{-0.39}$(0.26)

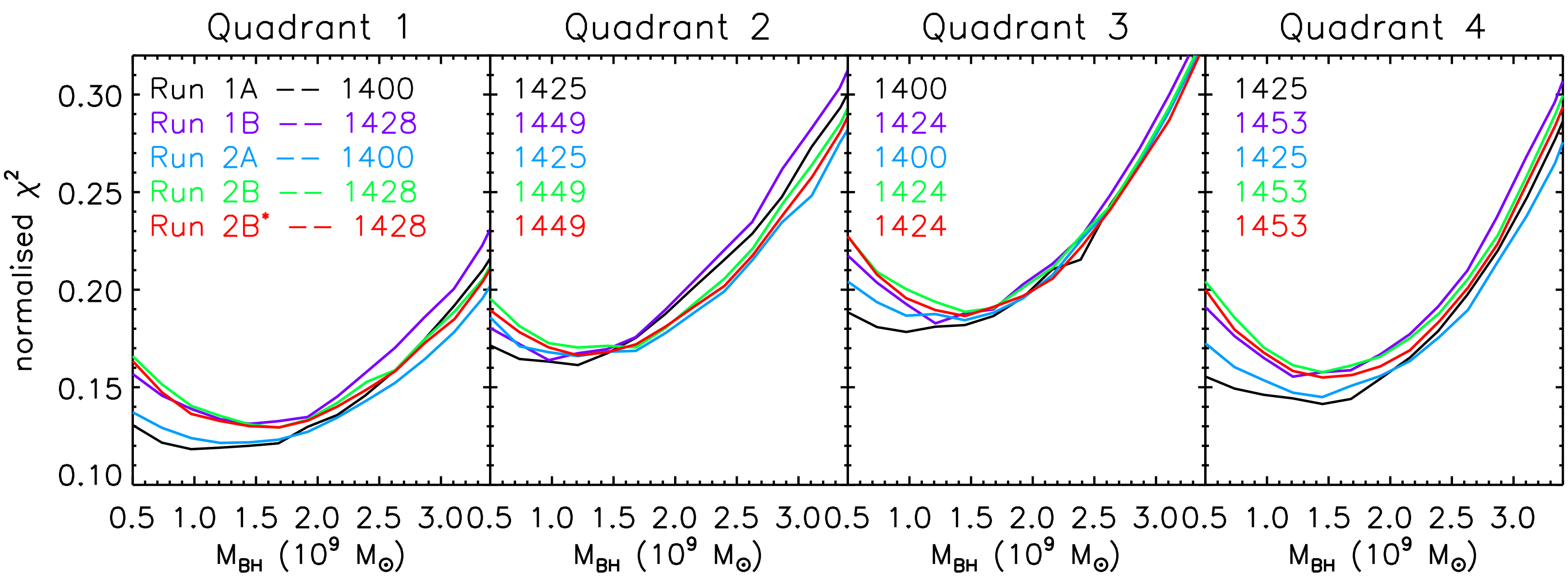

Figure 3.7: The normalised χ^2 vs $M_{\rm BH}$ marginalised over all mass-to-light ratios for the runs listed in Table 3.1 for four different quadrants. The normalisation factor, by which we divide χ^2, is written for the individual runs in each quadrant. The best-fitting $M_{\rm BH}$ is given by the model with minimum normalised χ^2 in the corresponding run and quadrant. These SMBH masses can be found in Table 3.1.

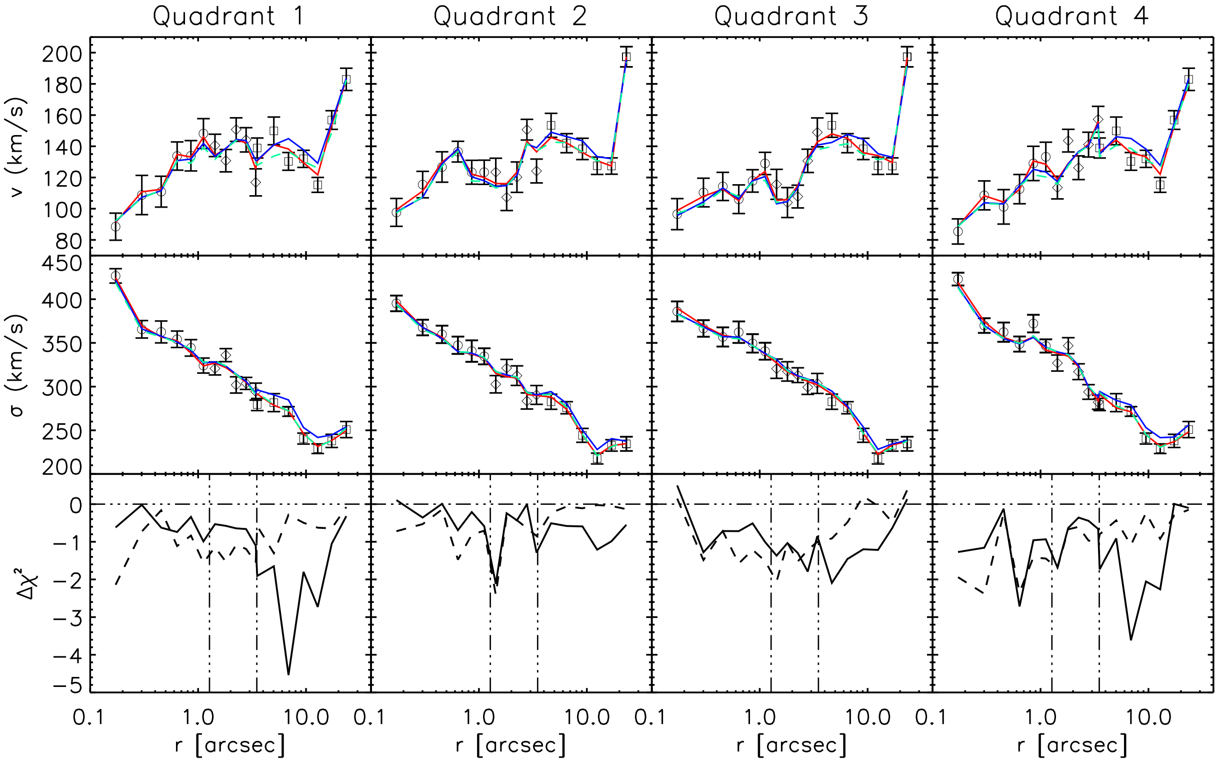

Figure 3.8: **Top and middle rows**: kinematic fit of the models to the data along the major axis, illustrated in terms of v and σ. Circles, diamonds and squares represent the SINFONI 100mas, 250mas and the long slit data, respectively, with their corresponding errors. Our preferred model from run 2B* is shown by the red line. The blue line shows the best-fitting (smallest χ^2) model for $M_{\rm BH}$=5 × $10^8 M_\odot$. The green line represents the model with $M_{\rm BH}$=5 × $10^8 M_\odot$ and the same Υ_b, Υ_d as in our preferred model. **Bottom row**: χ^2 differences between the three models shown in the top two rows, averaged over all angular bins in each quadrant. Following the colour coding above, solid and dashed lines represent $\chi^2_{\rm red} - \chi^2_{\rm blue}$ and $\chi^2_{\rm red} - \chi^2_{\rm green}$ respectively. The horizontal dash-three-dotted line is plotted along $\Delta\chi^2$=0 to guide the eye and the vertical lines separate the different datasets.

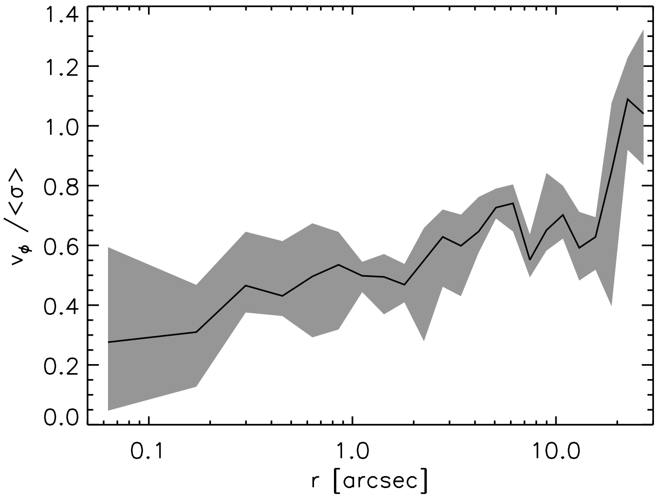

Figure 3.9: The significance of rotational velocity relative to the random motion of the stars as a function of radius along the major axis. v_ϕ is the mean rotation in the azimuthal direction where $(v_\phi^2 + \sigma_\phi^2)$ constitutes the second moment of the azimuthal velocity. $\langle\sigma\rangle$ is the local mean velocity dispersion defined as $\langle\sigma\rangle^2 = (\sigma_r^2 + \sigma_\theta^2 + \sigma_\phi^2)/3$. The shade shows the area where all models within 1σ error fall and the line represents the average.

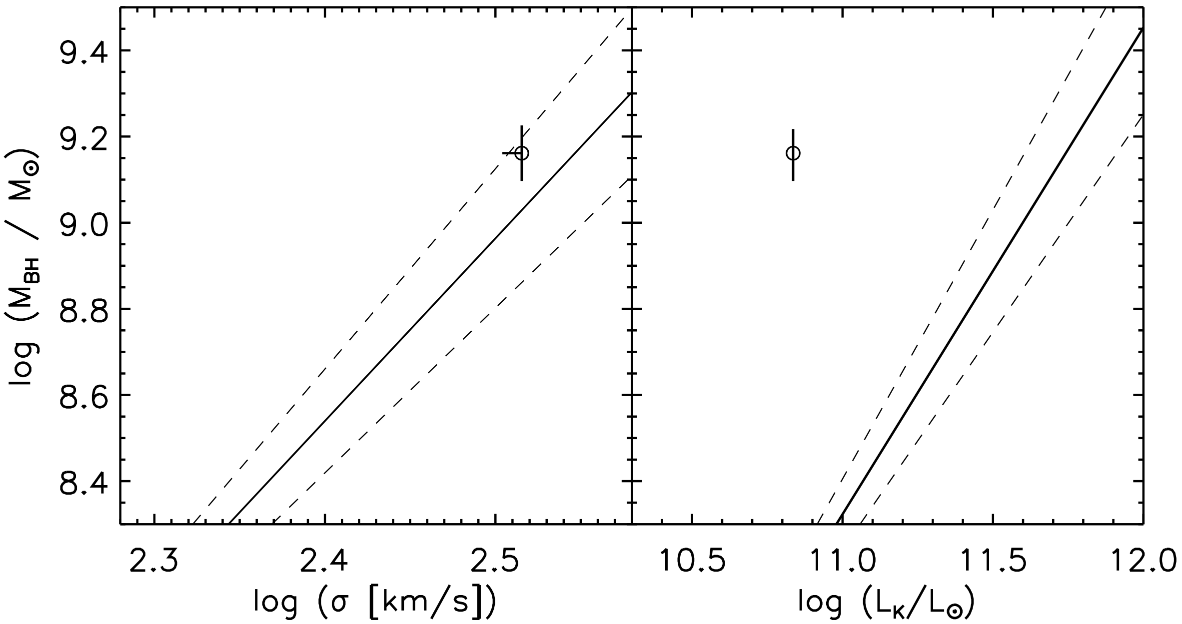

Figure 3.10: $M_{\rm BH}$-σ (left) and $M_{\rm BH}$-L (right) diagrams. NGC 1332 is plotted as a square in each panel along with the Gültekin et al. (2009b) $M_{\rm BH}$-σ relation and Marconi&Hunt (2003) $M_{\rm BH}$-L_K relation.

.

Chapter 4

The Effect of Dark Matter Halo on the Black Hole Mass

4.1 Introduction

Recent publications on dynamical masses of black holes in the center of galaxies focus on the need of including dark matter halo (DM) in the modelling (Gebhardt & Thomas 2009; Shen & Gebhardt 2010; McConnell et al. 2011a; Schulze & Gebhardt 2011; Gebhardt et al. 2011). These investigations were initialized by Gebhardt & Thomas (2009) who find that the black hole mass (M_{BH}) in M87 increases by more than a factor of two when the dark halo is taken into account. They argue that this is due to the degeneracy of the mass components, i.e. black hole, stars and DM. In dynamical modelling, only the total enclosed mass is constrained. Adding a dark halo component takes away a fraction of the stellar mass budget, i.e. the stellar mass-to-light ratio (Υ) has to decrease. Since Υ is assumed to be constant at all radii, M_{BH} has to increase to compensate for the lower stellar mass. The effect of including DM is thought to be important for massive galaxies with shallow luminosity profiles in the center: the line-of-sight kinematics close to the black hole is more affected by the contribution from the stars at large radii where DM is dominant.

The subsequent papers present several new M_{BH} measurements with and without DM present in the models and show how much M_{BH} changes by the inclusion of DM. The results vary. Shen & Gebhardt (2010) revisit NGC 4649 and see only a negligible increase in M_{BH}. McConnell et al. (2011a) report a new measurement for NGC 6086 and observe that M_{BH} becomes larger by a factor of six. Schulze & Gebhardt (2011) reanalyze M_{BH} of 12 galaxies, spanning a wide range of stellar velocity dispersions, and find an average increase of 20 percent; all the changes in M_{BH} are well within the measurement errors. M87 is remodelled by Gebhardt et al. (2011) using high-spatial-resolution data and they find similar M_{BH} with and without DM. The authors attribute the consistent M_{BH} to the data quality which resolves the sphere of influence (SoI) and thereby breaking the degeneracy between Υ and M_{BH}. The required data resolution to guarantee an unbiased M_{BH} without the need to include DM is, however, not clear.

Accurate black hole masses are important because they are the building blocks of the empirical relations between the central black hole and the properties of the host bulge, e.g. the stellar velocity dispersion σ (Ferrarese & Merritt 2000; Gebhardt et al. 2000a) and the luminosity L (Dressler 1989, Kormendy & Richstone 1995; Magorrian et al. 1998). The interpretations of the relations are crucial in understanding the black hole growth, density distribution and ultimately their roles in the formation and evolution of galaxies. It is therefore necessary to establish unbiased and well-defined correlations, if there is truly a physical connection between the black hole and the host galaxy.

The upper end of these relations is the most critical part. The galaxy sample that shape the relations in this regime is still relatively sparse. Based on the black hole sample compiled in Gültekin et al. (2009b), there are only around 10 galaxies that shape the M_{BH}-σ relation above σ of 250 km/s. The M_{BH}-σ and M_{BH}-L contradict each other in predicting the mass function of the most massive black holes (Lauer et al., 2007), with M_{BH}-L giving higher density of the black holes. In addition to that, the M_{BH}-σ implies that the largest black holes (M_{BH} of $> 10^{10} M_{\odot}$) found in distant quasars should reside in galaxies with $\sigma \gtrsim$ 500 km/s (Shields et al. 2006; Shields et al. 2006). Salviander et al. (2008) find the highest σ in SDSS galaxies to be 444 km/s and find no support of the existence of local galaxies with $\sigma = 500$ km/s or higher. These issues can be resolved if the M_{BH}-σ relation is curved upwards or has large intrinsic scatter at the high mass end. The very recent discovery of two black hole masses of 10^{10} $M_{\odot}$ in BCGs supports this view (McConnell et al., 2011b). The finding also implies that BCGs might be the host of quasar remnants.

With these new indications, enlarging the size of the black hole sample at high-σ end becomes even more important. On top of that, the accuracy of the measurements also needs to be improved. At present, the effect of DM has been examined only for half of the galaxy sample at high-mass end. To avoid systematic biases in the black hole-bulge relations, understanding the DM effect on M_{BH} measurement and providing unbiased M_{BH} measurements are essential.

We present seven new black hole measurements, primarily based on integral-field unit (IFU) data obtained using SINFONI with adaptive optics. For each galaxy, we address the question of how M_{BH} would change when DM is present in the modelling. These galaxies increase the number of M_{BH} measurements especially in the range of massive black holes. Six of the galaxies span a velocity dispersion range between 250-350 km/s and one has a lower σ ($\sim$ 180 km/s). The six galaxies are massive ellipticals, a class of galaxy whose M_{BH} is claimed to be most affected by the dark halo inclusion in the models. This work provides the first direct measurements of the black hole masses for each galaxy in the sample. The sample galaxies and their properties are listed in Table 4.1. Most distances are adopted from the SBF survey (Tonry et al., 2001), after applying the Cepheid zero-point correction of -0.06 magnitudes (Mei et al., 2005), except for NGC 3091, NGC 5516 and NGC 4472. For the first two, the distance is calculated from the redshift, corrected for the infall velocity of Local Group to the Virgo cluster (HyperLeda). For NGC 4472, we take the distance from Mei et al. (2007).

The structure of the chapter is as follows. SINFONI observations and the data reductions are described in Section 4.2. We present SINFONI kinematics and describe the additional kinematic data that we use in the modelling in Section 4.3. The surface photometry and the light distribution are discussed in Section 4.4. The details of the dynamical modelling and how we include the DM halo can be found in Section 4.5. Section 4.6 presents the resulting black hole masses, together with the corresponding mass-to-light ratios. We discuss the influence of including the DM on M_{BH} and Υ in Section 4.7. The black hole-bulge scaling relations are addressed in Section 4.8. We conclude the paper by summarizing the results in Section 4.9.

Table 4.1: The properties of the sample galaxies. Distance is stated in Mpc. $\mathrm{M_V}$ is the absolute magnitude measured in the V-band. R_e is the effective radius (in arcsec) from the RC3 and σ_0 is the central velocity dispersion (in km/s) from HyperLeda.

Galaxy	Type	Distance	$\mathrm{M_V}$	R_e	σ_0
NGC 1374	E	19.23	-20.37	24.4	186.4 ± 3.9
NGC 1407	E	28.05	-22.73	70.3	270.6 ± 6.1
NGC 1550	E	48.5	-22.16	25.5	308.0 ± 6.2
NGC 3091	E	51.3	-22.62	32.9	321.4 ± 9.3
NGC 4472	E	17.14	-22.86	225.5	293.8 ± 2.9
NGC 5516	E	54.5	-23.02	22.1	307.3 ± 11.9
NGC 7619	E	51.52	-22.86	36.9	322.4 ± 5.6

4.2 SINFONI Observations and Data Reduction

The primary data used in this work were obtained using SINFONI that is mounted at the UT4 of the VLT. SINFONI (Spectrograph for INtegral Field Observations in the Near Infrared) consists of the near IR Integral Field Spectrograph SPIFFI (Eisenhauer et al., 2003b) and the curvature-sensing adaptive optics module MACAO (Bonnet et al., 2003). The image slicer in SPIFFI divides the field-of-view into 32 slitlets. Preslit-optics enable the observer to set the width of the slitlet (pixelscale) to 0.25 arcsec, 0.1 arcsec or 0.025 arcsec, corresponding to 8×8 arcsec^2, 3×3 arcsec^2, or 0.8×0.8 arcsec^2 field-of-view, respectively. Each slitlet is imaged onto 64 detector pixels resulting in rectangular spatial pixels (spaxels). There are four gratings on the filter wheel covering J, H, K and H+K band (see Section 2.1 for a more detailed description of the instrument).

Each galaxy was observed in multiple ten-minute exposures, following the Object-Sky-Object pattern. Immediately before or after two pattern sets were completed, we observed a telluric standard star and a PSF standard star; the latter is to estimate the point spread function during the galaxy observation. The telluric stars were selected to be early-type stars (B stars) at approximately the same airmass as the galaxy. For the PSF star, a nearby (single) star with a similar brightness (R magnitude) and colour (B-R) was chosen. We use the image of the averaged and normalised PSF stars for the seeing correction in dynamical modelling and in the photometry (in the case of NGC 1550). The Object and

PSF exposures were dithered by a few spaxels to achieve a full sampling of the spatial axis perpendicular to the slitlets, that is sampling the rectangular spaxels into two square pixels.

We used only the K-band grating (1.95-2.45 microns) for all galaxies. For observations with adaptive optics, the seeing correction can be performed by using the nucleus of the galaxy as the natural guide star (NGS mode), or using the artificial/laser guide star (LGS mode) created by the laser system PARSEC (Rabien et al. 2004; Bonaccini et al. 2006). For the latter, the galaxy nucleus acts as the tip-tilt reference 'star'. When the galaxy nucleus is bright enough ($R < 14$ mag), we use the NGS mode. The PSF star corresponding to each galaxy was observed using the same mode.

The observations were carried out in three separate runs in 2008 and 2009. The majority of the observations used the 100-mas pixel scale which allowed us to resolve the expected SoI of the black hole and to achieve sufficient S/N with a reasonable exposure time. When the weather condition became less optimal, we switched to 250-mas pixel scale. These data are useful in providing kinematic constraints at a larger spatial scale for the dynamical models. The details of the observations are summarized in Table 4.2.

Most of the data reduction steps were performed using the ESO SINFONI Pipeline (Modigliani et al., 2007), which was written based on the SPIFFI Data Reduction Software SPRED (Schreiber et al. 2004; Abuter et al. 2006). The bias subtraction during the data processing left artifacts that appear as dark stripes on SINFONI raw frames, both science and calibration frames. Using an IDL code provided by ESO, we removed these dark lines prior to the data reduction. We then used the recipes in the ESO pipeline for the standard reduction cascade, involving dark subtraction, correction for optical distortion and detector non-linearity, flat-fielding, wavelength calibration, sky subtraction on the science, PSF and the telluric standard frames and construction of datacubes. For the sky subtraction, we selected a sky frame that was observed closest in time for each standard and science frame. The science datacubes were further telluric-corrected using the reduced standard telluric star spectrum. This was done by first dividing out the stellar continuum using a blackbody curve, specified by the stellar temperature. After normalization, the resulting spectrum was used to divide the galaxy spectra. Finally, the individual science datacubes were combined into a single datacube, by taking into account the dither pattern during the observations. The telluric corrections and the cube-combining step were done using SPRED.

4.3 Kinematic Data

4.3.1 SINFONI kinematics

We spatially combined the spectrum of individual pixels into radial and angular bins to improve the signal to noise ratio. Using the combined spectra, we derived the kinematics non parametrically using a Maximum Penalized Likelihood (MPL) method (Gebhardt et al., 2000b), resulting in a LOSVD for each spatial bin. We fitted the first two CO bandheads with the convolved stellar template spectrum, which was a weighted combination of several stellar spectra. These were the stars of K and M spectral type, observed with the same instrumental setup as the galaxy.

To avoid template mismatch, we chose only stars with equivalent width or line strength within the range of those derived from the galaxy spectra, i.e. we selected only stars that were representative of the stellar population of the galaxy. For this purpose, we used the line-strength index for the first CO band-head at 2.29 microns proposed by Mármol-Queraltó et al. (2008). This index definition has very little sensitivity to many aspects, most importantly S/N and velocity dispersion broadening (tested up to 400 km/s), which makes it well-suited for our work.

We derived the kinematics from the normalized spectra as follows. With the MPL method, an initial LOSVD was generated and then convolved with a linearly combined spectrum of template stars. The LOSVD and the weights of the template stars were iteratively adjusted until the convolved spectrum matched the galaxy spectrum, achieved by minimising the penalised chisquare $\chi^2_P = \chi^2 + \alpha P$, where α is the smoothing parameter and P is the penalty function. To estimate the smoothing parameter, we created a large set of model galaxy spectra with sigma of 320 km/s and added varying amount of noise to them. The smoothing required to recover the input LOSVD for each S/N was then used to infer the appropriate smoothing for the real galaxy spectra (see Appendix B of Nowak et al. (2008) for details).

The errors in the LOSVD were determined through a Monte Carlo simulation (Gebhardt et al., 2000b). The template spectrum was convolved with the measured LOSVD and gaussian noise was added to create 100 different realizations of galaxy spectra. The LOSVD of the realisations were measured and used to compute the 68 percent confidence interval. The errors of the velocity and σ measurements are about 10 km/s, the uncertainties of the h_3 and h_4 are around 0.02, on average. In Fig. 4.1-4.3, we present the two-dimensional kinematics of each galaxy, parametrised in the four Gauss-Hermite moments.

NGC 1374 and NGC 7619 are the only two galaxies that show a regular and significant rotation. NGC 1374 has the lowest velocity dispersion in the sample. The σ profile shows a strong gradient, peaking at around 260 km/s in the center. NGC 1407, NGC 1550 and NGC 5516 have complex velocity profile with no obvious rotation axis. The σ gradient in NGC 1407 is shallow with h_3 being mostly negative. NGC 3091 displays a signature of a kinematically decoupled core. The stars at $r < 1$ arcsec appear to be rotating in the opposite direction from the stars at larger radii. The h_4 within $\sim$1.5 arcsec is predominantly negative, but becomes positive outside this radius. The absolute h_3 and h_4 values in NGC 3091 are higher than in the other galaxies. NGC 4472 is lacking rotation, in agreement with van der Marel et al. (1990) who found no rotation within a radius 5 arcsec, and the dispersion shows a flat profile across the SINFONI field of view (FOV) with both h_3 and h_4 being small. NGC 7619 shows the highest rotation. The velocity dispersion profile decreases more steeply along the major axis than the minor axis. The majority of the LOSVDs are flat-topped as indicated by negative values in the h_4 map, as also the case in NGC 1374 and NGC 5516.

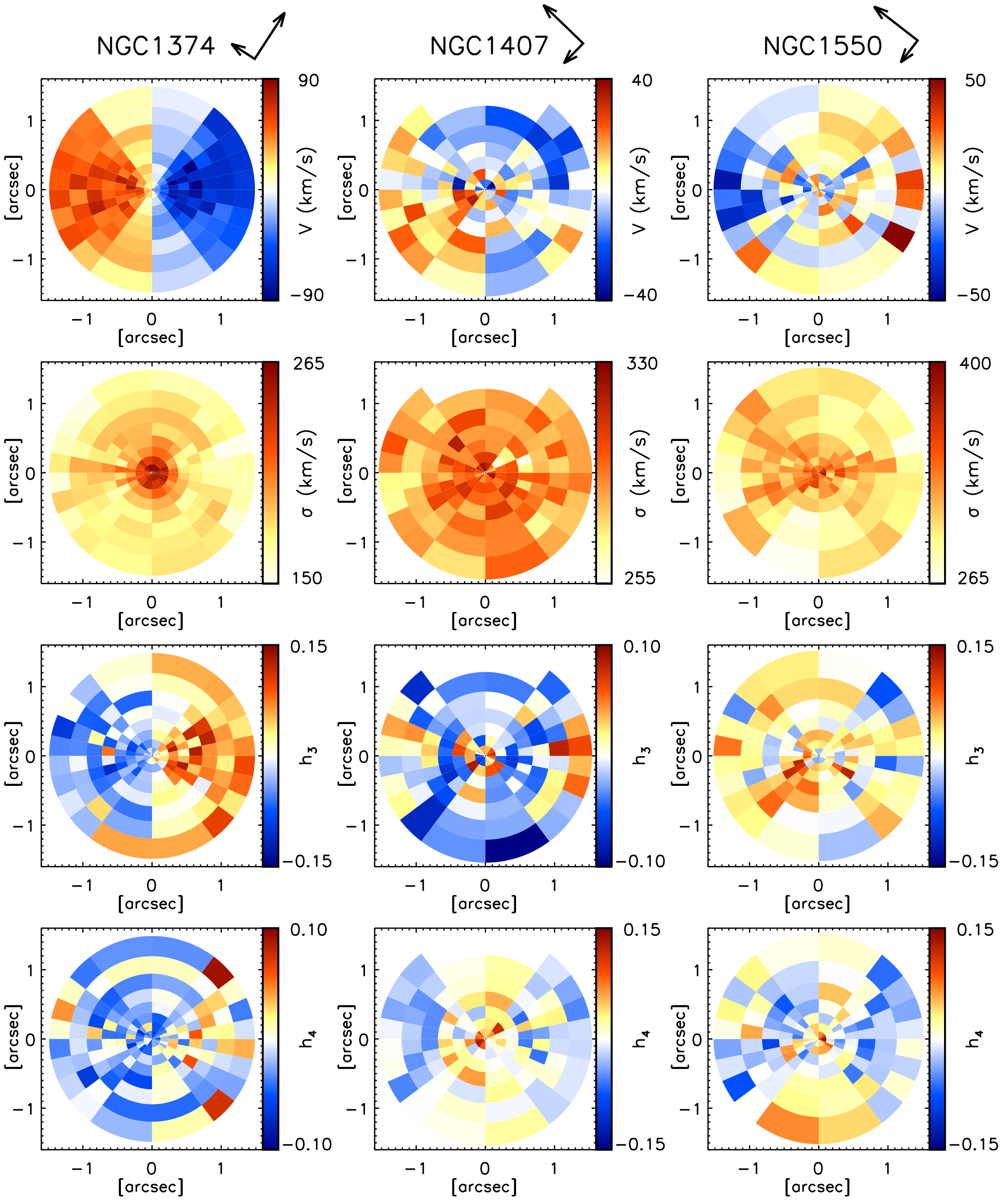

Figure 4.1: The two-dimensional kinematic maps of NGC 1374, NGC 1407 and NGC 1550, derived from SINFONI data and presented in terms of v, σ, h_3 and h_4. The major and minor axes of each galaxy are aligned with the abscissa and ordinate of the coordinate system. The arrows next to the galaxy name indicate the north (long arrow) and east (short arrow) directions.

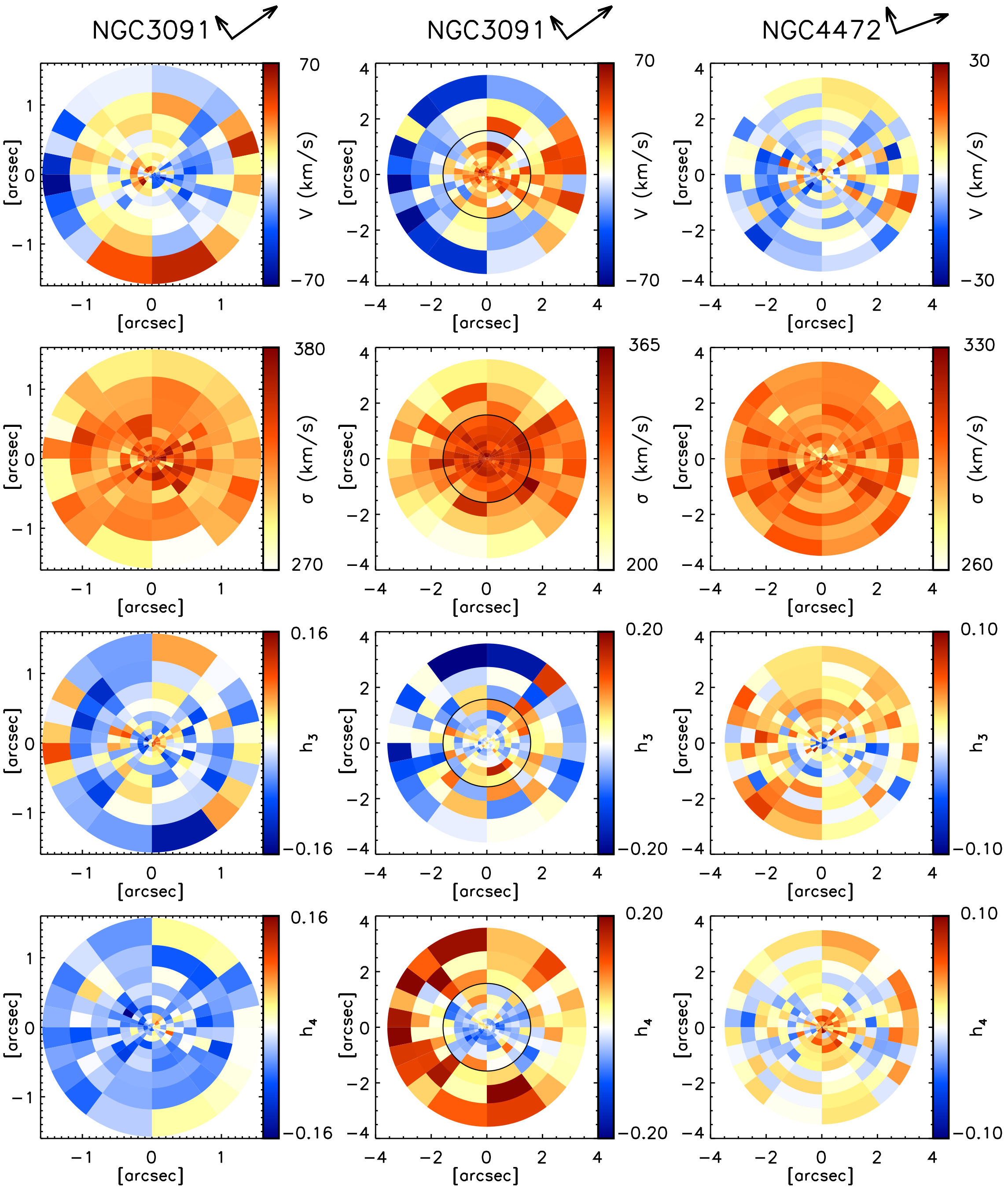

Figure 4.2: The two-dimensional kinematic maps of NGC 3091 and NGC 5516, derived from SINFONI data and presented in terms of v, σ, h_3 and h_4. The first and second columns display the 100-mas and 250-mas data for NGC 3091. The scope of the former is outlined in the latter (the black circle). The major and minor axes of each galaxy are aligned with the abscissa and ordinate of the coordinate system. The arrows next to the galaxy name indicate the north (long arrow) and east (short arrow) directions.

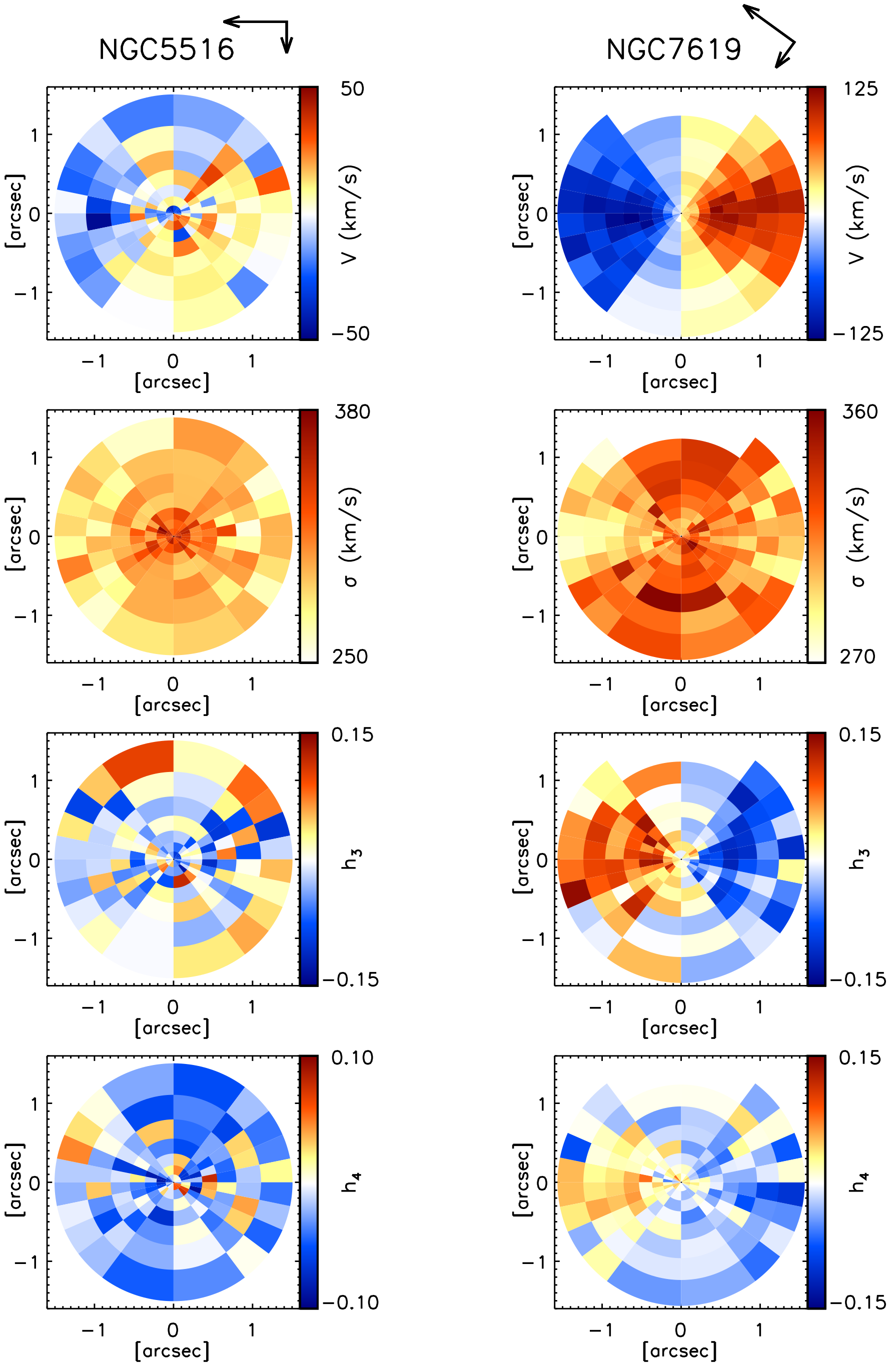

Figure 4.3: The two-dimensional kinematic maps of NGC 4472 (250mas) and NGC 7619 (100mas), derived from SINFONI data and presented in terms of v, σ, h_3 and h_4. The major and minor axes of each galaxy are aligned with the abscissa and ordinate of the coordinate system. The arrows next to the galaxy name indicate the north (long arrow) and east (short arrow) directions.

4.3.2 Additional kinematics

The modelling of each galaxy made use of a set of ground-based kinematic data at larger radii, in addition to the SINFONI data. These data were necessary to get a good handle on Υ and DM. Most of the datasets came in the form of long slit data and were taken from the literature. All these auxiliary data were presented in their kinematics moments and the respective errors. From these moments, we constructed the LOSVDs with the uncertainties (through 100 Monte-Carlo realizations). We used these LOSVDs in the modelling.

NGC 1374. The auxiliary dataset for this galaxy was long slit data along the major axis (up to ∼20 arcsec). For the details on the observation, reduction and the kinematic analysis, see Appendix B.1. There were other long slit data available in the literature, i.e. Longo et al. (1994) and D'Onofrio et al. (1995). We did not attempt to include these data because they did not provide h_3 and h_4 information and were less extended than the long-slit data that we used in this work.

NGC 1407. We used the slit data from Spolaor et al. (2008a), who provided kinematics along the major axis up to 40 arcsec, a little more than $0.5R_e$.

NGC 1550. There were long-slit kinematic data available from Simien & Prugniel (2000), who provided only V and σ measurements. We used this data to generate LOSVDs by setting h_3 and h_4 to zero with uncertainties of 0.1, to allow the models some extra freedom in fitting the LOSVD without biasing them into negative or positive h_3 and h_4 values. These data extended out to 26 arcsec along the major axis. The slit was placed at a position angle of 38°. The SINFONI data was adjusted to this PA to align the slit with the photometric major axis.

NGC 3091. For this galaxy, we obtained a set of new IFU data observed using VIRUS-W (see Appendix B.2). Each fiber had a size of 3.14 arcsec in diameter, much larger than the model bin size in the central 10 arcsec. We therefore ignored the data inside 10 arcsec. Since SINFONI data were only up to 4 arcsec, the region between 4 and 10 arcsec was not covered by any data. Between 10 and 50 arcsec, where the S/N was sufficiently good, we averaged the spectra of the fibers that fell on the same model bin and derived the kinematics from these spectra. Thus, like the SINFONI data, the VIRUS-W data was binned into radial and angular bins.

NGC 4472. We used long slit data from Bender et al. (1994), who presented kinematics of NGC 4472 out to ∼ 75 arcsec along the major and out to 60 arcsec along the minor axis.

NGC 5516. As complementary data, we used an IFU dataset obtained using the Wide-Field Spectrograph (WiFeS, see Appendix B.3). This is the galaxy with the least extensive data, reaching out only to 10 arcsec. In the modelling we used the data only up to 7 arcsec. Outside this radius the S/N was low, giving unreasonable kinematic moments or uncertainties. In the modelling, the WiFeS datapoints were treated as multiple slits across the central part of the galaxy. They were parallel to each other and did not align with the major or minor axis. Due to the axisymmetry assumption we folded the four quadrants of the galaxy; LOSVDs with identical spatial position in the folded quadrant were averaged. This resulted in two sets of slit data which were different in spatial orientations. The first set of slits was positioned at an angle of 72° and the second one at 108°, measured counter-clockwise from the major axis. Each set consisted of five parallel slits (see Fig. C.7).

NGC 7619. For this galaxy, we used the kinematic data from Pu et al. (2010) who provided v, σ, h_3 and h_4 out to 60 arcsec, almost twice the R_e, along both the major and minor axes. The spatial distribution of the datapoints was dense, slowing down the computation while not increasing the significance of the results. We spatially rebinned the data to create a dataset with less data points and we used the latter in the modelling.

4.4 Light Distribution

To put constraints on the spatial distribution of stars we performed surface photometry and deprojected this 2D information into a light density distribution. The deprojection was done axisymetrically using the code of Magorrian (1999). The seeing correction was included in the deprojection as described in Rusli et al. (2011), using a multi-gaussian profile as a representation of the actual PSF. We adopted an inclination of 90° for each galaxy, unless stated otherwise.

For two galaxies, we used the photometry that was already available in the literature. The photometry for NGC 7619 was taken from Pu et al. (2010). For NGC 4472, we used the photometry published in Kormendy et al. (2009). We describe the photometry of the other galaxies below[1].

4.4.1 The photometry of NGC 1374

We used the HST image taken with ACS-WFC and the F475W filter (Proposal ID 10911, PI Blakeslee), and also an NTT EMMI image available from the ESO archive and taken with the filter "SPEC RS", Program ID 56.A-0430, PI Macchetto/Giavalisco. We calibrated the final profile to the B band, using the aperture photometry of Caon et al. (1994). The isophotal analysis was performed using the software of Bender & Moellenhoff (1987). The matching between the HST and the ground-based profiles was performed in the region $5 < a < 20$ arcsec, where a is the semi-major distance from the center, and we used the ground-based profile for $a > 20$ arcsec. The matching procedure (used also for all the following galaxies) consists in determining the scaling and sky value that minimize the magnitude square differences between the two profiles, assuming that the ground-base profile has the correct sky subtraction performed. (Determining the sky background value for the HST image in this fashion is necessary when the galaxy fills the HST field of view.) The rms residuals in the region of the matching are small, typically 0.01-0.02 mag. The appropriate PSF to use for deprojecting the photometry is that of the ACS/WFC. We used the TinyTim program, which for the ACS/WFC generates an "observed" (i.e., optically distorted) PSF. Since the isophotal analysis was performed on the distortion-corrected

---

[1] The photometric profile for each of these galaxies will be available in electronic form which can be found at: http://www.mpe.mpg.de/opinas/newresearch/blackholes/SINFONILOSVD/

"drizzled" image, we applied the same process to the PSF image, using custom-written Python code. The PSF image output by TinyTim was copied into the flat-fielded (but still distorted) ACS/WFC image, replacing the center of the galaxy. The full image was then run through the same `multidrizzle` processing to produce a distortion-corrected WFC mosaic. The processed PSF was then cut out from the mosaic.

4.4.2 The photometry of NGC 1407

We used the HST image taken with ACS/WFC and the F435W filter and a ground-based B-band image taken at the 40-inch telescope in Siding Spring equipped with the wide field imager. On the 19.10.2001 we took 6 pointings, each with a 10-minute exposure. The images were reduced and combined using IRAF. The isophotal analysis was performed using the software of Bender & Moellenhoff (1987). The ground-based surface brightness profile was calibrated using photoelectric photometry. We matched the HST profile to the ground-based data in the region $5 < a < 20$ arcsec, where a is the semi-major axis of the galaxy, and merged the two dataset using the matched HST profile for $a < 20$ arcsec. The PSF used in the deprojection was generated using the TinyTim and passed through the *drizzle* software.

4.4.3 The photometry of NGC 1550

We used an image from the Isaac Newton Telescope's Wide Field Camera (INT-WFC), originally observed by Michael Pohlen. The observation was a 300 second exposure in the Sloan r filter, taken on 2003 December 15; the pixel scale was 0.331 arcsec/pixel and the median seeing FWHM was 1.4 arcsec. We calibrated it to the Cousins R using aperture photometry provided by Djorgovski (1985). Since there are no HST images of this galaxy, we used our K-band SINFONI image (generated by collapsing the reduced SINFONI datacube along the wavelength direction) for higher resolution in the central region of the galaxy. We perfomed the isophotal analysis on both images using the software of Bender & Moellenhoff (1987) and matched the SINFONI surface brightness profile to the ground-based profile in the region $0.8 < a < 1.6$ arcsec. The combined profile uses the SINFONI data at $a < 1$ arcsec and the ground-based profile ground-based data for $a > 1$ arcsec. The SINFONI PSF was used in the deprojection.

4.4.4 The photometry of NGC 3091

We used HST ASC/WFC images taken using tbe F814W filter (Proposal ID 10787, PI Charlton). We calibrated them to Cousins I using the approach of Sirianni et al. (2005) with the updated zero points available at http://www.stsci.edu/hst/acs/analysis/zeropoints/, along with colors from the galaxy photometry compilation of Prugniel & Heraudeau (1998). Comparison with the aperture photometry of Reid et al. (1994) shows that there is a -0.03 mag difference to the I Cousins system. The isophotal analysis was performed using the software of Bender & Moellenhoff

(1987). The PSF used in the deprojection was generated using the TinyTim software and passed through the *drizzle* software.

4.4.5 The photometry of NGC 5516

We used the HST image taken with the PC of WFPC2 and the F814W filter and a ground-based R-band image taken at the ESO-MPG 2.2m telescope in La Silla equipped with the wide field imager (WFI). The ground-based data (4 exposures of 230 seconds each) were taken on the 10.07.2010. They were reduced using the *mupipe* software [2] developed at the University Observatory in Munich (Gössl & Riffeser, 2002). After the initial bias and flat-field corrections, cosmic rays and bad pixels were masked, and the images were resampled to a common grid and stacked. A constant sky value was estimated from empty regions distant from the galaxy and subtracted from the stacked image. The calibration was performed using the photoelectic photometry in the R band of Poulain & Nieto (1994). The HST profile was matched to the ground-base one in the region 3 arcsec $< a <$ 10 arcsec, where a is the semi-major axis distance, and used for $a <$ 8.9 arcsec. The PSF was generated using TinyTim.

4.5 Dynamical Models

The dynamical modelling was performed using axisymmetric orbit superposition technique (Schwarzschild, 1979), described at length in Gebhardt et al. (2000b), Thomas et al. (2004) and Siopis et al. (2009). This technique was implemented as follows. First, the gravitational potential was calculated from the prescribed total mass distribution using Poisson equation. This total mass distribution is defined as $\rho = \Upsilon\nu + M_{\rm BH}\delta(r) + \rho_{\rm DM}$ where Υ is the mass-to-light ratio of the stars, ν is the luminosity density distribution of the stars and $\rho_{\rm DM}$ is the dark halo density. Then, thousands of time-averaged stellar orbits were generated in this potential, each of their weights was calculated such that the orbit superposition reproduced the luminosity density and fitted the kinematics as good as possible. For each potential, there were two identical sets of orbits with opposite angular momentum. Each set consisted of about 12,000 orbits. We derived the best-fitting set of parameters by setting up a parameter grid in the modelling, with each gridpoint representing a trial potential. The best-fit model was chosen based on the χ^2 analysis (see Section 2.6 for a more detailed description of the modelling).

Along with the axisymmetry assumption in the modelling, we folded the four quadrants of the galaxy into one. For the SINFONI and VIRUS-W data, this was done by averaging the LOSVD of four bins at the same angular and radial position. We used this averaged quadrant. As for the the slit data, we fitted both sides of the slit simultaneously.

---

[2] http://www.usm.lmu.de/˜ arri/mupipe/

4.5.1 The importance of DM in the modelling

The degeneracy between $M_{\rm BH}$ and Υ is often a problem in $M_{\rm BH}$ measurements. It is evident when the two-dimensional χ^2 distribution (as a function of $M_{\rm BH}$ and Υ) appears diagonal (e.g. Nowak et al. (2010), Gültekin et al. (2009a), Schulze & Gebhardt (2011). It is thought that placing more stringent constraints on the Υ will help to pin down the black hole mass more accurately and help to decrease the measurement errors at the same time. To do this, the naive tendency would be to provide as much/extended data as possible to constrain Υ. We show here that this strategy is not advisable when DM is neglected in the models.

From the slit data of NGC 1407, NGC 4472 and NGC 7619, we created multiple sets of data for each galaxy by truncating the slit data at different radii ($r_{\rm trunc}$). For each galaxy, we ran models using these kinematic datasets and also the full dataset to determine Υ without having DM present in the model (ρ_{DM} is zero). $M_{\rm BH}$ was set to zero. Fig. 4.4 plots the $\Delta\chi^2$ vs Υ obtained from these runs for each of the three galaxies, $\Delta\chi^2$ being the difference between χ^2 of each model and the minimum χ^2 of the run. As a comparison, we also show $\Delta\chi^2$ distribution when DM is included in the models for the run with the full dataset (Section 4.5.2). The Υ values along the x-axis are normalized by the best-fit Υ obtained from the run with DM (Υ with $\Delta\chi^2 = 0$ along the black line). The red line shows the run without DM, but using the full slit data, i.e. the same kinematic dataset as the run with DM. The blue and green represent the runs without DM, with decreasing $r_{\rm trunc}$.

For each galaxy, the best-fit Υ is lowest when DM is included and highest when DM is omitted, both for the models using the full slit kinematics. For the case without DM, Υ increases as $r_{\rm trunc}$ gets larger. This is expected because more extended data go farther into the region where DM halo is dominant. In the modelling, omitting the DM component would require Υ to increase in order to compensate for the missing dark mass. The larger the $r_{\rm trunc}$, the more dark mass there is to compensate, thereby increasing the Υ further. The situation is worsened by the fact that the 1σ error bars ($\Delta\chi^2 = 1$) decrease with increasing $r_{\rm trunc}$. When more extensive data are used, the χ^2 curve becomes steeper, excluding the 'true' Υ (with DM) with a higher confidence. For the three galaxies, this systematic bias appears to be as large as ~20-30 percent.

It is clear that the omitting DM in the modelling biases Υ. In principle, this bias in Υ could also affect the black hole mass due to the degeneracy. It is therefore important to consider DM in the modelling to investigate how much effect this bias has on $M_{\rm BH}$. We discuss this further in Section 4.7. In the following section, we describe how we incorporate DM in the modelling to fit $M_{\rm BH}$.

4.5.2 Inclusion of DM in the model

We used a spherical cored logarithmic (LOG) dark halo profile (Binney & Tremaine, 1987). As found in Gebhardt & Thomas (2009) and McConnell et al. (2011a), the exact shape of the dark halo is of little importance to the black hole mass and in most cases the LOG

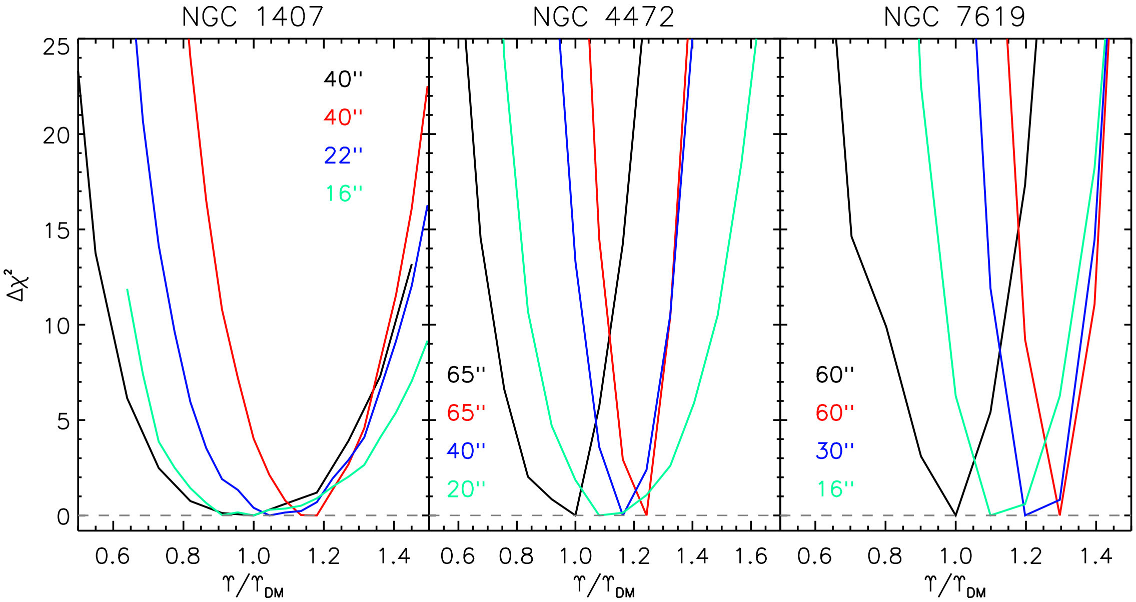

Figure 4.4: The χ^2 distribution as a function of Υ. The Υ values are all normalized by the best-fit Υ obtained from modelling with DM (black line). The red, blue and green lines are models without DM, with different $r_{\rm trunc}$. The value of $r_{\rm trunc}$ for each run is written in the plot.

halo gives a better fit compared to the other commonly used profiles. Since our aim is to constrain $M_{\rm BH}$ and not the dark halo, we avoid a detailed study of the halo parameters. The LOG halo is given by

$$\rho_{\rm LOG}(r) = \frac{V_c^2}{4\pi G}\frac{3r_c^2 + r^2}{(r_c^2 + r^2)^2} \tag{4.1}$$

where r_c is the core radius, within which the density slope of the DM is constant and v_c being the asymptotic circular velocity of the DM. When the dark halo is present in the model, there is a total of four free parameters (Υ,$M_{\rm BH}$, V_c and r_c) to be determined.

Calculating models to determine all four parameters simultaneously is computationally expensive. We circumvented this by first calculating models without a black hole to determine the best-fitting V_c and r_c for a set of Υ values, resulting in a best-fit halo parameters as a function of Υ. We then proceeded to determine the best-fit $M_{\rm BH}$ and Υ (section 6) by using the best-fit r_c and V_c for each Υ as calculated in the first step. In this way, we reduced the computational load and time quite significantly. Since the intention is not to tightly constrain the dark matter halo, but rather to synchronize the change of Υ with the change of DM, we used only a coarse grid of V_c and r_c.

Fitting the dark halo can be done only when the data are sufficiently extensive, which is not always the case. For galaxies with limited data, we skipped the first step and we directly determined $M_{\rm BH}$ and Υ by fixing r_c and V_c to values from dark matter scaling relations which was derived from a sample of Coma galaxies (Thomas et al., 2009). The relations are written as follows:

$$\log r_c = 1.54 + 0.63(\log(L_B/L_\odot) - 11.0) \tag{4.2}$$

$$\log V_c = 2.78 + 0.21(\log(L_B/L_\odot) - 11.0) \tag{4.3}$$

with r_c and V_c are stated in kpc and km/s respectively.

For four galaxies, i.e. NGC 1407, NGC 3091, NGC 4472, NGC 7619, there were extensive datasets available (section 4.3.2), allowing us to fit the dark halo. We set M_{BH} to zero and we avoid inconsistencies in these models by not using the high-resolution SINFONI data which would probe the black hole otherwise.

The additional datasets for NGC 1407, NGC 4472, NGC 7619 were long-slit data, while for NGC 3091, it was IFU data. We included all the slit datapoints to fit the dark halo. For NGC 3091 we used the IFU data and the outer part of SINFONI 250-mas data because the IFU data started only at 10 arcsec. This IFU data was advantageous because of its larger spatial coverage, but it did not deliver useful results when used by itself. Modelling Υ and DM by using only the IFU data resulted in a rather flat χ^2 distribution for Υ. We therefore included the 250mas SINFONI data as well, but only taking datapoints outside 1 arcsec.

The best-fitting r_c and V_c for the four galaxies are presented in Table 4.3. The fitted r_c and V_c are not the exact values expected from the dark matter scaling relations, but they fall within the scatter.

4.6 Black Hole Masses

In this section we present the best-fitting black hole masses along with the Υ that are derived from the dynamical modelling. In addition to the high-resolution SINFONI data, we also included the other ground based data at larger radii (section 4.3.2). For the DM, we used the best-fit LOG halo as a function of Υ for the four galaxies listed in Table 4.3. For the other galaxies we used a fixed halo according to its B absolute magnitude taken from HyperLeda (equations 4.2 and 4.3). For a comparison, we also ran models without DM, fitting only M_{BH} and Υ and using the same kinematic dataset as the runs with DM. Table 4.5 shows the results with the corresponding 1σ uncertainties. The size of the sphere of influence, calculated based on M_{BH} with DM and the central σ taken from HyperLeda, is also listed in the table. We include r_c and V_c for the three galaxies in which we use a fixed halo. The Gauss-Hermite fit of all the galaxies are shown in the Appendix C (Fig. C.1-C.8).

In Fig. 4.5 we plot the χ^2 distribution as a function of M_{BH} (marginalized over Υ and also over r_c and V_c in some cases) for each galaxy, when DM is included. In some galaxies, these profiles look noisier than the other. The ones that are relatively less noisy belong to galaxies which have more rotation over velocity dispersion, like NGC 1374 and NGC 7619. For the other galaxies, the noise does not necessarily decrease with increasing grid resolution. In spite of the noise, each profile does show a clear minimum.

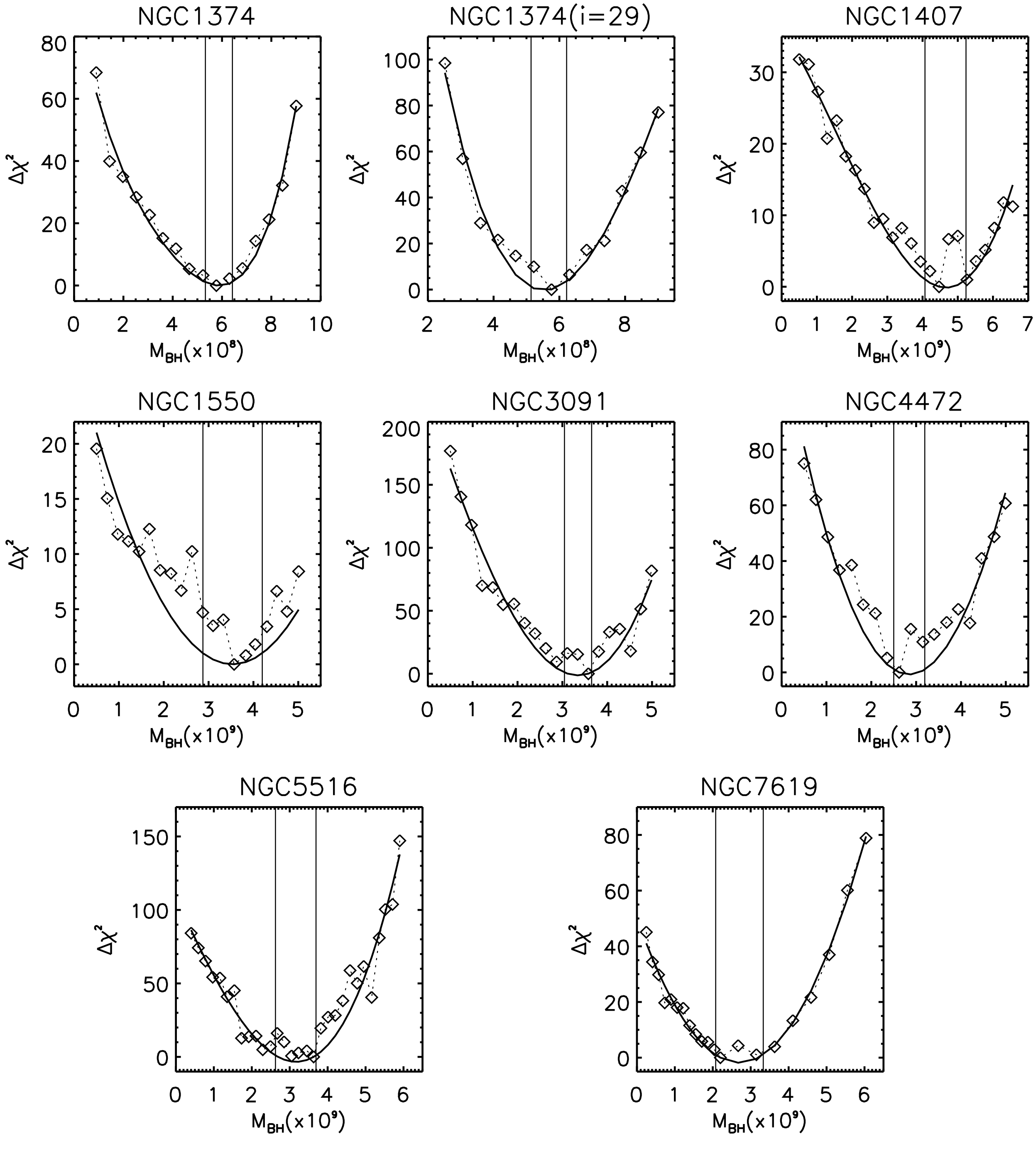

Figure 4.5: $\Delta\chi^2$ vs $M_{\rm BH}$ for models with DM. For NGC 1374, we show the plots for two inclinations. The diamonds, connected by the dotted line, show the actual $\Delta\chi^2$ values. The black curve is the polynomial fitting to the datapoints/diamonds. Two vertical lines mark the lower and upper limits of the 1σ error.

As commonly done, we measure the uncertainties of the $M_{\rm BH}$ measurements by locating $M_{\rm BH}$ where the χ^2 is one higher than the minimum χ^2 ($\Delta\chi^2 = 1$) and assign the $M_{\rm BH}$ difference as 1σ error. We do this by fitting a polynomial to these points as shown by the solid line. To guarantee that the minimum of the polynomial curve does not stray far from the best-fitting model we increase the weight of the best-fitting point. The minimum χ^2 along the polynomial curve does not always coincide with lowest-χ^2 $M_{\rm BH}$ but the lower and the upper limits always bracket the best-fitting $M_{\rm BH}$. This method is not ideal but it is good enough as a first-order approximation of the errors. Since the fitting is done on a much larger scale than $\Delta\chi^2 = 1$, it is unlikely that the uncertainties are underestimated.

Longo et al. (1994) and D'Onofrio et al. (1995) suggest that NGC 1374 might be a face-on misclassified lenticular, based on the kinematic profile derived from their long-slit data. For this reason, we additionally run models with an inclination of 29°. With this inclination, the projected flattening of 0.88 translates into an intrinsic flattening of 0.25 (disc-like). We show the results in Fig. 4.5. We see that changing the inclination to i=29 only slightly decreases the uncertainties while $M_{\rm BH}$ and Υ hardly change. The same is true when the galaxy is modelled without DM. $M_{\rm BH}$ and Υ in this galaxy seem to be robust against DM inclusion and a change of inclination.

Despite the steep change in Υ, $M_{\rm BH}$ in NGC 1407 stays almost the same. The black hole mass measured for this galaxy is more than $4{\times}10^9\ M_\odot$, comparable to $M_{\rm BH}$ in NGC 4649 which has a higher velocity dispersion of around 350 km/s (Shen & Gebhardt, 2010). NGC 1407 has the highest $M_{\rm BH}$ in the sample, although the velocity dispersion is rather low. The Υ for this galaxy is rather large for a B-band Υ, especially when it is modelled without DM. Given the central age of $12.0{\pm}1.1$ and metallicity of $0.29{\pm}0.08$ (Spolaor et al., 2008b), we derive the mass-to-light ratio using the single stellar population (SSP) model of Maraston (2005). A Kroupa IMF gives $\Upsilon_{\rm SSP}$ of 7.8 ± 1.0. This is consistent with the dynamical Υ when DM is included. A Salpeter IMF increases $\Upsilon_{\rm SSP}$ by a factor of 1.56 which would make it consistent with the dynamical Υ for the model without DM.

There are two sets of SINFONI data for NGC 3091, which overlap in the inner 1.5 arcsec radius. The 100-mas dataset excels in spatial resolution while the 250-mas data is better in S/N. To fit $M_{\rm BH}$ we use the 100-mas data up to the radius of 0.65 arcsec, which corresponds to the 6th radial bin in the kinematic maps. With $M_{\rm BH}$ of $3.6 \times 10^9 M_\odot$, the radius of the sphere of influence is 0.68 arcsec, meaning that the region within the sphere of influence is fully constrained by the high-resolution data (100-mas). Outside this radius up to ~ 4 arcsec, the kinematics is provided by the 250-mas data.

NGC 7619 shows the most significant change in $M_{\rm BH}$ (more than a factor of 5), accompanied by a large change in its Υ. SSP analysis using the same slit data in Pu et al. (2010) results in $\Upsilon_{\rm SSP}$ of about 3 in the I-band (with Kroupa IMF), in perfect agreement with the dynamical Υ when DM is included. As in the case of NGC 1407, the dynamical Υ without DM coincides with the Salpeter-based $\Upsilon_{\rm SSP}$.

4.7 The Change of $M_{\rm BH}$ Due to DM

Not in all seven galaxies do we observe a change in $M_{\rm BH}$ when we include DM. $M_{\rm BH}$ in two galaxies, NGC 1374 and NGC 1550 seems unaffected by DM inclusion while in NGC 1407 it is virtually unchanged (the nominal change is well within the 1σ errors). Out of seven, there are only two galaxies whose black hole masses change significantly outside their 1σ errors, i.e. NGC 3091 and NGC 7619. No galaxy shows a decrease in $M_{\rm BH}$ due to DM.

On average, there is an increase of $M_{\rm BH}$ by a factor of 2.1, which is similar to the increase found in $M_{\rm BH}$ in M87 (Gebhardt & Thomas, 2009). On the other hand, these results are not in agreement with the finding of Schulze & Gebhardt (2011), who perform a similar analysis on their sample galaxies. They find an average increase of only 20 percent due to DM inclusion. The effect of DM analysed from their sample is, however, effectively negligible because the change in $M_{\rm BH}$ are well within the measurement errors.

Gebhardt et al. (2011) suggest two strategies for deriving an accurate $M_{\rm BH}$. It is either by getting Υ right in the first place or by having high resolution data that covers the central region of the galaxy. Both strategies have been tested on M87 (Gebhardt & Thomas (2009) for the first one and Gebhardt et al. (2011) for the second). Below we address how these two strategies apply to our sample galaxies.

All galaxies see a nominal change in Υ, i.e. it systematically decreases from models without DM to models with DM. We show how the change in Υ is related to the change in $M_{\rm BH}$ in the left panel of Fig. 4.6. We include M87 (Gebhardt & Thomas, 2009; Gebhardt et al., 2011), NGC 6086 (McConnell et al., 2011a) and NGC 4649 (Shen & Gebhardt, 2010) in the plot to complete the sample of black holes in massive galaxies that have been studied for the DM effect. At a first glance, there is only a weak statistical correlation (if at all) between the two quantities, which could mean that the change in $M_{\rm BH}$ is not predominantly influenced by the change in Υ. This is however not the end of the story. For the two galaxies where $M_{\rm BH}$ changes outside the formal error bars, we find that we can recover the 'correct' $M_{\rm BH}$ ($M_{\rm BH,DM}$) from the models without DM when we consider only the Υ obtained from the run with DM ($\Upsilon_{\rm DM}$). In the case of NGC 3091, models without DM where Υ is 4.1 give the minimum χ^2 at $M_{\rm BH} = 3.3 \times 10^9 M_\odot$. For models of NGC 7619 with $\Upsilon = 2.9$, $M_{\rm BH,DM}$ is exactly recovered without having DM in the model.

Although the change of Υ is not directly related to the change in $M_{\rm BH}$, this finding confirms that having a correct Υ is one important aspect of measuring an accurate $M_{\rm BH}$. Based on our results in Section 4.5.1, it is clear that including the DM is necessary to derive unbiased Υ. When DM is not included, Υ obtained with less extended kinematic data is more reliable although this does not completely remove the bias. It is however not clear, in advance of the modelling, where to spatially truncate the kinematic data. R_e is not necessarily a good criterion. In the case of NGC 1407 and NGC 4472, the data go out to only a fraction of R_e (around 0.5 and 0.25 R_e respectively) but still contribute to an appreciable change of Υ, while in NGC 1550 the Υ is not biased although the data extend out to R_e (Table 4.5).

To address the second strategy, we show the plot of spatial resolution vs the change of $M_{\rm BH}$ in the right panel of Fig. 4.6. $D_{\rm res}$ is the diameter of the resolution element,

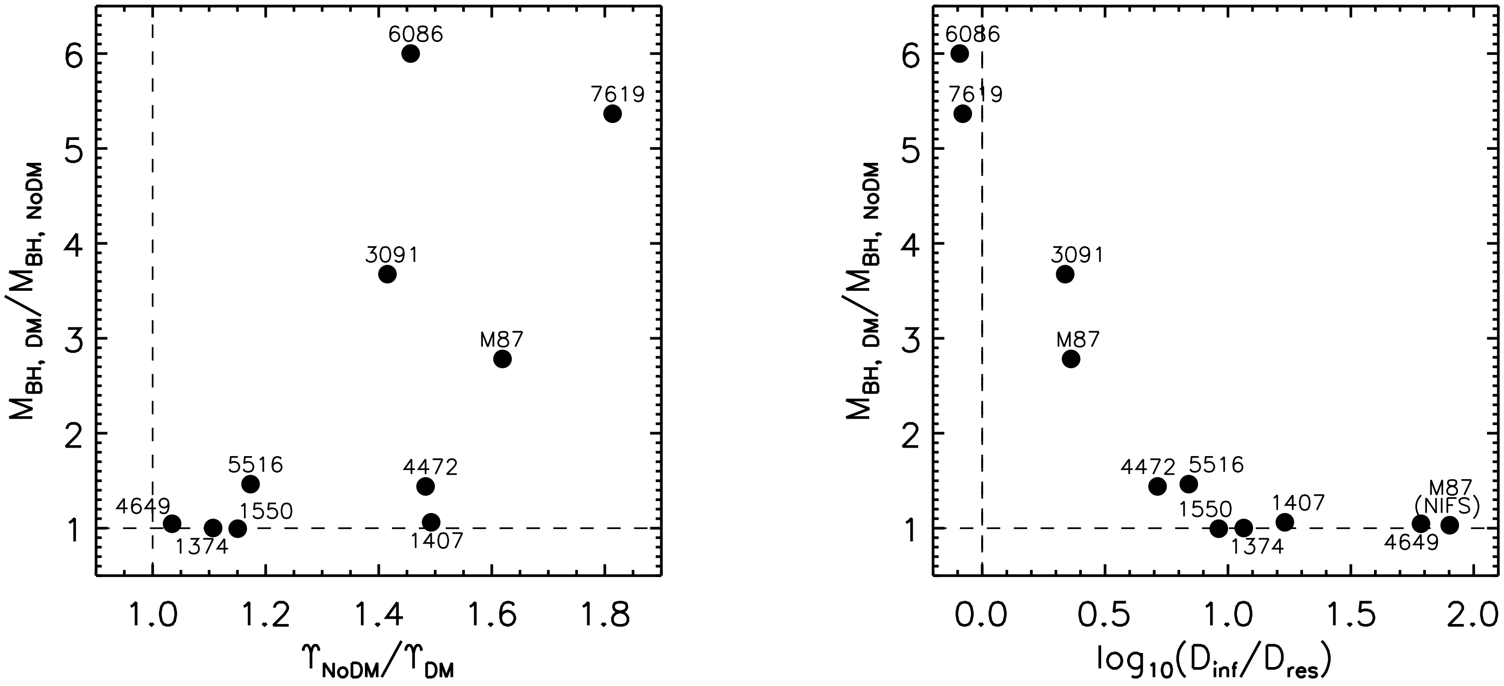

Figure 4.6: Left panel: the ratio of $M_{\rm BH}$ against the change of Υ. Note the different numerator and denominator in both ratios. Right panel: the ratio of $M_{\rm BH}$ vs the achieved spatial resolution. $D_{\rm inf}$ is the diameter of the sphere of influence of the black hole, calculated based on $M_{\rm BH}$ obtained from the modelling without DM, with central σ from HyperLeda. $D_{\rm res}$ is the diameter of the resolution element (see text). We include three galaxies outside our sample for comparison purposes (NGC 4649, NGC 6086 and M87). There are two datapoints for M87 in the right panel, corresponding to the two measurements by Gebhardt and Thomas (marked as 'M87') and Gebhardt et al. (marked as 'M87(NIFS)').

being the aperture size, seeing, the PSF FWHM or the model bin size. For our galaxies, $D_{\rm res}$ represents PSF FWHM (last column in Table 4.2), except for NGC 1407 where we use the average size of the model bins inside the SINFONI FOV, i.e. 0.24 arcsec (larger than the PSF FWHM of 0.19 arcsec). The diameter of the sphere of influence ($D_{\rm inf}$) is calculated using $M_{\rm BH}$ without dark matter. We do not use $M_{\rm BH}$ derived with the dark matter because when DM is included, Υ is constrained to the right value and in that case it is no longer clear if the spatial resolution is still the dominant factor in recovering the correct $M_{\rm BH}$, or if it plays a role at all. The velocity dispersion values from HyperLeda (σ_0 in Table 4.1) were used to derive $D_{\rm inf}$. We have checked that for the seven galaxies in our sample, the velocity dispersions from spatially-averaged SINFONI spectra are similar to these and using SINFONI σ does not change the appearance of the plot. We again include NGC 4649, NGC 6086 and M87 as in the left panel.

The plot shows a very clear trend. It confirms the importance of good data resolution for $M_{\rm BH}$ measurements, in the context of DM influence. When $D_{\rm inf}$ is not or only marginally resolved (less than a factor of 5), there is a larger risk of getting the wrong $M_{\rm BH}$. The change of $M_{\rm BH}$ becomes negligible when the resolution element is smaller than $D_{\rm inf}$ by a factor of at least $\sim$10. Between 5 and 10, $M_{\rm BH}$ is wrong by $\sim$ 30 percent, but still on the safe side given that this number is similar to a typical $M_{\rm BH}$ measurement error. Based on this plot, one can, to some degree, assess individual galaxies to see whether it is necessary to have DM present in models without first having to go through the time-consuming modelling with DM.

By comparing both plots in Fig. 4.6, it appears that the aspect of resolution gives a more straightforward implication. As long as the sphere of influence is well sampled by the data, a biased Υ is no longer a problem in recovering the correct $M_{\rm BH}$because Υ and $M_{\rm BH}$ are no longer degenerate to each other and thus, including DM is not a necessity. The example for this would be NGC 1407 and NGC 4472. When the data resolution is not sufficiently high, it is important to have an unbiased Υ to derive an accurate $M_{\rm BH}$, as in the case of NGC 3091 and NGC 7619. However, it is not easy to derive an unbiased Υ when DM is not included and it is difficult to infer a bias in $M_{\rm BH}$ from a bias in Υ. One can perhaps rely on $\Upsilon_{\rm SSP}$ as a measure of the true Υ, independent of DM. For NGC 1407 and NGC 7619, the Kroupa-based $\Upsilon_{\rm SSP}$ agrees with dynamical Υ when DM is included (Section 4.6). However, up to now the IMF in massive early-type galaxies is still a controversial issue and $\Upsilon_{\rm SSP}$ is uncertain to about a factor of two (Conroy & van Dokkum 2011; Cappellari et al. 2006; Thomas et al. 2011; Napolitano et al. 2010). Checks on a much larger sample of galaxies would be necessary to justify the use of $\Upsilon_{\rm SSP}$ as a surrogate.

4.8 Black Hole-Bulge relation

We consider the latest version of the $M_{\rm BH}$-σ and $M_{\rm BH}$-L relations derived by McConnell et al. (2011b) in the upper and lower panel of Fig. 4.7, respectively. The galaxies in the sample of McConnell et al. (2011b) are plotted in grey and their relations are shown by the black lines. In the $M_{\rm BH}$-σ diagram, the solid and dashed lines are the fit to all galaxy sample and to only early-type galaxies. We overplot our new measurements as black diamonds; the $M_{\rm BH}$ values are the ones obtained with DM. Our galaxies lie well above the relations of McConnell et al. (2011b) and therefore steepening both relations.

By including all the points (including the black diamonds), we derive new relations. The $M_{\rm BH}$-σ and $M_{\rm BH}$-L relations are defined to be $\log_{10}(M_{\rm BH}/M_\odot) = \alpha + \beta \log_{10}(\sigma/200\,{\rm km/s})$ and $\log_{10}(M_{\rm BH}/M_\odot) = \alpha + \beta \log_{10}(L_V/10^{11}L_\odot)$, respectively. This functional form is a single-index power law with α as the zero-point and β as the slope. To fit α and β, we use a Bayesian method with Gaussian errors as described in Kelly (2007). We are able to recover the $M_{\rm BH}$-σ and $M_{\rm BH}$-L relations as fitted by McConnell et al. (2011b), using just their galaxy sample. The fitting results using their sample plus the seven galaxies are given in Table 4.4 for each relation and shown in Fig. 4.7 as red lines.

The two galaxies that are farthest from the relations are NGC 1374 and NGC 1550, for which we do not see a change in $M_{\rm BH}$ due to DM. If NGC 1374 is actually close to face-on, then the actual velocity dispersion could perhaps be larger than the observed one. The average deviation of $M_{\rm BH}$ of the seven galaxies from the derived $M_{\rm BH}$-σ relation is 0.48 dex for "all1" sample and 0.43 dex for the early-type sample (see the caption of Table 4.4 for the description of the sample). These galaxies are located 0.36 dex away from the derived $M_{\rm BH}$-L relation, on average. If we use the relations of McConnell et al., then the average deviation would be higher, i.e. 0.54, 0.50 and 0.44 dex from the $M_{\rm BH}$-σ (all), $M_{\rm BH}$-σ (early-type) and the $M_{\rm BH}$-L relations, respectively. Contrary to the case of NGC 1332 in the previous chapter, the seven galaxies appear to be close to the $M_{\rm BH}$-L than to the $M_{\rm BH}$-σ relation. This could be an indication that the $M_{\rm BH}$-σ relation at the high-σ regime is different and that a single power law is perhaps not sufficient to represent its true shape. Indeed, when fitting only galaxies with $\sigma < 250$ km/s (not just early-type), the slope becomes considerably flatter, i.e. $\alpha = 8.26$ and $\beta = 4.84$.

4.9 Summary

This paper presents new AO-assisted SINFONI observations on seven nearby elliptical galaxies, five of which have velocity dispersion of > 300 km/s, the remaining two have σ between 150 and 300 km/s. The SINFONI data are complemented with other ground-based data with larger spatial scales that are found in literature or coming from new observations. We use the data to weigh $M_{\rm BH}$ in the center of these galaxies using three-integral axisymmetric orbit-superposition models. The black hole mass reported here represents the first dynamical measurement for each of the sample galaxies.

For the runs with DM, we adopt a core logarithmic profile for the DM halo in the models. For four galaxies where there are extensive data available, the DM halo is fitted. For the others, we set the halo parameters to fixed values based on the DM scaling relation (Thomas et al., 2009). The best-fitting dark halo parameters fall within the scatter of the DM scaling relation.

We first run models without black holes to show that when DM is omitted in the modelling, Υ is biased. Υ gets systematically higher than when DM is included. This bias becomes stronger when the spatial extent of the data is maximised without including DM. This suggests that it is necessary to consider DM in the dynamical modelling to derive a reliable Υ.

We then run models with and without including the DM to determine $M_{\rm BH}$ and we asses how the change in Υ or the data resolution affects the black hole mass. To complete our sample we add $M_{\rm BH}$ measurements, with and without DM, of three massive galaxies from the literature. Statistically, we find that the change in $M_{\rm BH}$ is only weakly related (if at all) to the change in Υ due to DM inclusion. This, however, does not mean that an accurate measurement of Υ is not important. We see that for two galaxies where $M_{\rm BH}$ changes significantly, the 'correct' $M_{\rm BH}$ (obtained with DM) can be recovered from the models without DM when we consider only the Υ obtained from the run with DM. In other words, when Υ is fixed to a correct value, the model returns the correct $M_{\rm BH}$.

There is a clear trend that the change in $M_{\rm BH}$ becomes larger with decreasing resolution. We define the resolution as $\rm D_{inf}/D_{res}$ where $\rm D_{inf}$ represents the size of the sphere of influence, computed using $M_{\rm BH}$ derived from models without DM and $\rm D_{res}$ is the size of the resolution element of the observations. If $\rm D_{inf}/D_{res} < 5$, $M_{\rm BH}$ is significantly underestimated when DM is not included. For $\rm D_{inf}/D_{res} > 10$, the change in $M_{\rm BH}$ is negligible, despite the large change in Υ due to DM inclusion. Between 5 and 10, $M_{\rm BH}$ is underestimated by about 30 percent, which is a typical measurement errors for $M_{\rm BH}$.

All of the measured $M_{\rm BH}$ are located above the latest $M_{\rm BH}$-σ and the $M_{\rm BH}$-L relations of McConnell et al. (2011b), thus steepening the slope of both relations.

Table 4.2: Details of the Observation Runs. PA is instrument position angle (in degrees) during the galaxy observations. T_{exp} is the combined exposure time on-source (excluding sky exposures), stated in minutes; we write the amount of the total integration time of the science frames that actually contribute to the final datacube. AO mode is the mode of the adaptive optics; No AO means that the observation is seeing-limited. PSF FWHM is the full-width at half maximum derived from the PSF star observed next in time to the galaxy. For the 100-mas data of NGC 3091, the given FWHM is based on the combined PSF from the two different runs.

Galaxy	Date	Program ID	Instrument PA	Pixelscale	T_{exp}	AO mode	PSF FWHM
NGC 1374	2008 Nov 27	082.B-0037(A)	120.0	100mas	80min	NGS	0.15 arcsec
NGC 1407	2008 Nov 23,25	082.B-0037(A)	40.0	100mas	200min	LGS	0.19 arcsec
NGC 1550	2008 Nov 26,27	082.B-0037(A)	27.8	100mas	120min	LGS	0.17 arcsec
NGC 3091	2008 Nov 24,25	082.B-0037(A)	144.3	100mas	80min	NGS	0.17 arcsec
	2009 Apr 19,20,22	083.B-0126(A)	144.3	100mas	40min	NGS	0.17 arcsec
	2008 Nov 25,26,27	082.B-0037(A)	144.3	250mas	60min	No AO	-
NGC 4472	2009 Apr 24	083.B-0126(A)	160.0	250mas	60min	NGS	0.47 arcsec
NGC 5516	2009 Mar 21,22,23	082.B-0037(B)	0.0	100mas	140min	LGS	0.14 arcsec
NGC 7619	2008 Nov 23,25,27	082.B-0037(A)	30.0	100mas	120min	LGS	0.18 arcsec

Table 4.3: The DM halo parameters. The r_c and V_c are the values with the minimum χ^2.

Galaxy	r_c(kpc)	V_c(km/s)
NGC 1407	10.9	340
NGC 3091	29.8	809
NGC 4472	13.6	780
NGC 7619	39.2	700

Table 4.4: Parametric fits for the $M_{\rm BH}$-σ and $M_{\rm BH}$-L relations. The sample "all1" refers to all galaxies in the sample of McConnell et al. (2011b) plus the seven galaxies. "early-type" sample is the early-type subset of "all1". "all2" contains the "ML" sample of McConnell et al. (2011b) plus the seven galaxies.

Diagram	Sample	α	β
$M_{\rm BH}$-σ	all1	8.34 ± 0.06	5.30 ± 0.34
$M_{\rm BH}$-σ	early-type	8.45 ± 0.06	4.70 ± 0.37
$M_{\rm BH}$-L	all2	9.26 ± 0.10	1.18 ± 0.13

Table 4.5: The best-fit M_{BH} and Υ with and without DM. The black hole mass is written in the unit of the solar mass. $\mathrm{D_{SoI}}$ is the diameter of the sphere of influence, stated in arcsec. It is calculated based on M_{BH} from models with DM ($M_{\mathrm{BH,DM}}$) and the central velocity dispersion from HyperLeda, which is listed in Table 4.1. The r_c (in kpc) and V_c (in km/s) are given for three galaxies where the DM is not fitted, but derived from equations 4.2 and 4.3.

Galaxy	$M_{\mathrm{BH,NoDM}}$	Υ_{NoDM}	$M_{\mathrm{BH,DM}}$	Υ_{DM}	r_c	V_c	$\mathrm{D_{SoI}}$	band
NGC 1374	$5.8(5.2, 6.2) \times 10^8$	$6.0(5.7, 6.6)$	$5.8(5.3, 6.4) \times 10^8$	$5.4(5.1, 6.2)$	6.0	336	1.74	B
NGC 1407	$4.2(2.6, 4.5) \times 10^9$	$12.5(11.3, 13.0)$	$4.5(4.1, 5.2) \times 10^9$	$8.4(7.2, 8.7)$	-	-	4.38	B
NGC 1550	$3.6(2.9, 4.3) \times 10^9$	$4.3(3.9, 4.5)$	$3.6(2.9, 4.2) \times 10^9$	$3.7(3.6, 4.5)$	20.7	507	1.56	R
NGC 3091	$9.7(8.8, 11.2) \times 10^8$	$5.8(5.6, 5.9)$	$3.6(3.1, 3.7) \times 10^9$	$4.1(4.0, 4.3)$	-	-	1.36	F814W
NGC 4472	$1.8(1.7, 2.7) \times 10^9$	$7.8(7.1, 7.9)$	$2.6(2.5, 3.2) \times 10^9$	$5.3(5.1, 5.7)$	-	-	3.51	V
NGC 5516	$2.5(2.3, 2.8) \times 10^9$	$2.9(2.6, 3.0)$	$3.6(2.6, 3.7) \times 10^9$	$2.5(2.2, 2.6)$	31.8	585	1.40	R
NGC 7619	$4.1(3.5, 6.6) \times 10^8$	$5.3(5.0, 5.4)$	$2.2(2.1, 3.3) \times 10^9$	$2.9(2.8, 3.8)$	-	-	0.82	I

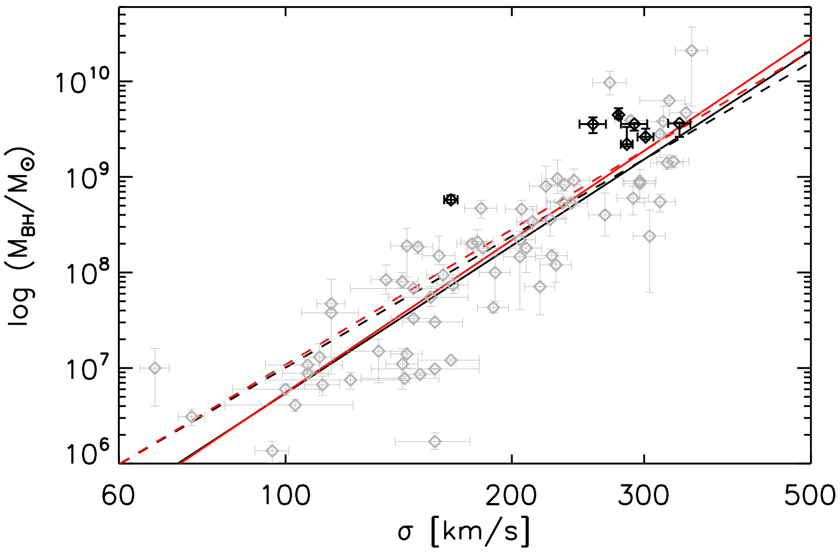

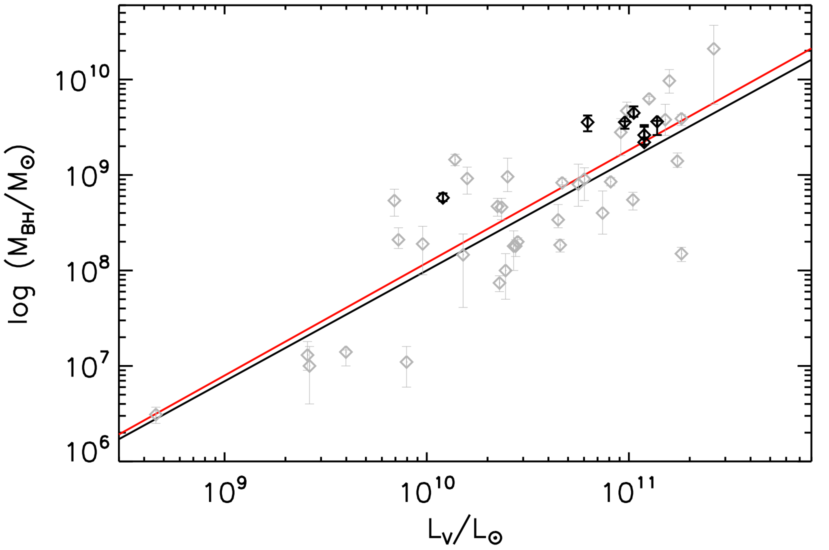

Figure 4.7: The $M_{\rm BH}$-σ (top) and $M_{\rm BH}$-L (bottom) diagrams with the updated relations. Grey diamonds are the galaxies in the sample of McConnell et al. (2011b). The relations that they derive using these galaxies are indicated by black lines. The solid and dashed black lines in the $M_{\rm BH}$-σ relation show the fit to all galaxies and to only the early-type galaxies in their sample, respectively. The black diamonds represent the seven galaxies in our sample, where we plot $M_{\rm BH}$ obtained by taking into account the DM. Using the McConnell et al sample and the seven galaxies, we updated the relations, shown by the red lines. The solid and dashed red lines in the $M_{\rm BH}$-σ relation use the 'all1' and 'early-type' sample, respectively (see Table 4.4).

Chapter 5

Supermassive Black Holes of Core Galaxies

5.1 Introduction

In the present-day view, merger is a common and important way of building up massive elliptical galaxies. With the presence of supermassive black holes in the centers of most galaxies (Kormendy & Richstone 1995; Magorrian et al. 1998; Richstone et al. 1998), merging processes are thought to have left signatures on the central structure of the remnant galaxies. Begelman et al. (1980) suggest that a binary black hole that is formed by the merger of two galaxies scours the stars from the center of the newly created system as the binary shrinks. The energy produced by the hardening of the binary evacuates the central part through the ejection of surrounding stars, causing less light in the center.

The Hubble Space Telescope (HST) observations on galaxy nuclei see two kinds of behaviour in the elliptical light profiles, leading to the terms "core" and "power-law" galaxies (Ferrarese et al., 1994, 2006; Lauer et al., 1995, 2005, 2007). The power law galaxy exhibits a light profile that can be described by a single power law all the way into the resolution limit, while the core galaxy displays a surface brightness profile that has a break from a steep outer slope to a shallower inner cusp. The core profile mainly occurs in the luminous elliptical galaxies and is considered as the result of dissipationless merger of two galaxies that have central black holes.

Much numerical work has been done to explore the binary black hole idea. The work of Ebisuzaki et al. (1991) suggest that the stellar mass ejected from the core is comparable to the mass of the central black hole $M_{\rm BH}$. Makino & Ebisuzaki (1996) find that core radius roughly doubles after each merger. Nakano & Makino (1999) suggest that the core size should scale with the final $M_{\rm BH}$. Simulations performed by Milosavljević & Merritt (2001) show for the first time that merging two galaxies with steep cusps can result in a merger remnant with a shallow power-law cusp in the inner part (core). Merritt (2006) is the first to quantify the magnitude of the mass deficit (or the mass ejected by the binary) with respect to the galaxy's merger history. By following the binary evolution up to the stalling radius, he formulates the mass deficit to be $0.5\,NM_{\mathrm{BH}}$ with N is the number of merger events. An investigation into the post-coalescense stage of the binary by Gualandris & Merritt (2008) suggests that an additional mass deficit (added to that yielded by the pre-coalesced binary) of about $5M_{\mathrm{BH}}$ for a single merger is possible.

In parallel, there have been efforts to measure the core size or the mass deficit from the observed luminosity profiles and compare it to the central black hole mass or the galaxy's global properties (e.g. Ravindranath et al. 2002; Milosavljević et al. 2002; Graham 2004; Ferrarese et al. 2006; Kormendy et al. 2009 (KFCB09); Kormendy & Bender 2009 (KB09)). Measuring the core quantities is tricky and problematic because the shape of the luminosity profile before the mass ejection by the binary is unknown (Milosavljević et al., 2002). The technical definition for a core (and thus the core size) varies. Lauer et al. (1995, 2005, 2007) define a core based on the so-called Nuker parametrization of surface brightness profiles. The Nuker model consists of two power-law profiles, separated by a break radius; it is designed to fit only the central profiles around the break radius. Trujillo et al. (2004) and Graham (2004) define a core based on a core-Sérsic model (equations 5.2 and 5.3) to fit extended radial profiles, not just the centers. To measure the mass deficit, there are basically two different approaches in the literature. Earlier works of Milosavljević & Merritt (2001), Milosavljević et al. (2002), Ravindranath et al. (2002) assume that the mass density profile, before the core is formed, has a power law slope of -2. More recent work implicitly assumes that the original light profile is an inward extrapolation of a Sérsic profile (equation 5.1) that fits the outer part of the galaxy (Graham 2004; Ferrarese et al. 2006; KFCB09; KB09). It is not clear whether there are systematic differences between the different approaches and so far there is not yet an agreement on a single method to use.

Apart from the different ways through which the core properties are determined, a major flaw in all previous analyses of how the core properties compare to M_{BH} lies in the black hole masses that are mostly derived from black hole-bulge relations, especially the M_{BH}-σ relation. The majority of core galaxies are bright massive elliptical galaxies, a class of galaxies for which the M_{BH}-σ-based M_{BH} is contradictory. Lauer et al. (2007) find that the M_{BH}-L relation predicts higher density of massive black holes ($\sim 10^{10}\ M_{\odot}$) compared to the M_{BH}-σ relation. Furthermore, the M_{BH}-σ relation also fails to predict the existence of the largest black holes ($M_{\mathrm{BH}}> 10^{10}M_{\odot}$), that are found in distant quasars (Shields et al., 2006), in the sample of local galaxies. The very recent finding of two black holes of 10 billion solar masses (McConnell et al., 2011b), which might be the missing link between the local black holes and the massive distant quasars, further supports the indications that the M_{BH}-σ for massive bright early type galaxies needs to be reevaluated. On top of these, the notion that dynamical M_{BH} could be underestimated when dark matter halo is not taken into account in the modelling (Gebhardt & Thomas, 2009) adds to the complications. In the sample of KB09, the stellar dynamical M_{BH} comes from the models without dark matter halo while most M_{BH} estimates rely on M_{BH}-σ relations of Tremaine et al. (2002).

Based on the work in the previous chapter, we are armed with seven dynamical M_{BH} measurements that have taken into account the presence of dark matter halo. In addition, the availability of extended surface brightness profiles and dynamical mass-to-light ratios allows us to extend the work to investigate the existence of cores in the galaxy sample and if or how the core properties relate to the black hole mass. To increase the statistics, we include several additional galaxies, i.e. galaxies with confirmed cores and with surface brightness profiles, black hole masses and stellar mass-to-light ratios available in the literature. As mentioned above, there are multiple approaches to quantify/define a core and so far there is no method that is strongly preferred over the other due to the lack of knowledge of the light profile before the scouring. Here, we use the core-Sérsic parametrisation. Following recent studies on the mass deficit (e.g. Graham 2004, Ferrarese et al. 2006, KB09), we assume that the original profile is the extrapolated Sérsic profile that fits the light distribution at large radii. In Section 5.2, we describe the method that we use to identify the core galaxies and to fit the observed surface brightness profiles. In Section 5.3, we present the best-fitting models for each galaxy. Section 5.4 presents the details of how the luminosity and mass deficit in the core are computed based on the best-fitting models. The core-related quantities derived in Section 5.3 and 5.4 are compared with the black hole mass in Section 5.5. The last two sections discuss and summarize the results.

5.2 The Method

5.2.1 Identifying cores

Our photometric profiles are quite extended, reaching out to at least 10 kpc. Therefore, we base our analysis on a function that is designed to fit not just the inner or the outer part of galaxies, but rather the galaxy as a whole. To identify core galaxies, we follow the criteria in Trujillo et al. (2004) who define the core as "a downward deviation from the inward extrapolation of the outer (Sérsic) profile". This involves fitting each galaxy with both the Sérsic and the core-Sérsic functions.

The Sérsic profile (Sérsic, 1963, 1968) is written as:

$$I(r) = I_e \exp\left\{-b_n\left[\left(\frac{r}{r_e}\right)^{1/n} - 1\right]\right\}. \tag{5.1}$$

I_e is the intensity at r_e, the half-light radius. n is called the Sérsic index which describes the shape or curvature of the light profile. The quantity b_n is a function of n, defined in such a way that r_e encloses half of the total luminosity. We approximate b_n by using the asymptotic expansion of Ciotti & Bertin (1999) for $n > 0.36$. Many other approximation formulas are available and are summarized in Graham & Driver (2005). For $n = 1$, the Sérsic function reduces to an exponential function and for $n = 4$, it becomes the de Vaucouleurs profile.

The core-Sérsic function introduced by Graham et al. (2003) and Trujillo et al. (2004) is expressed as:

$$I(r) = I'\left[1 + \left(\frac{r_b}{r}\right)^{\alpha}\right]^{\gamma/\alpha} \exp\left[-b_n\left(\frac{r^{\alpha} + r_b^{\alpha}}{r_e^{\alpha}}\right)^{1/n\alpha}\right] \tag{5.2}$$

with

$$I' = I_b 2^{-\gamma/\alpha} \exp\left[b_n \left(2^{1/\alpha} r_b/r_e\right)^{1/n}\right]. \tag{5.3}$$

This profile consists of a Sérsic profile in the outer part, specified by the half-light radius r_e and the Sérsic index n, and a power-law profile in the inner part with a slope of γ. The change from one to another regime occurs at the break radius r_b and the sharpness of the transition is specified by the parameter α. Higher values of α mean sharper transitions. b_n is approximated in the same way as for the Sérsic function.

We summarize four criteria in Trujillo et al. (2004) that we use to identify core galaxies below. In section 5.3 we examine each criterion on each galaxy.

1. A characteristic pattern should be visible in the residuals when fitting a Sérsic profile to an idealized core galaxy. This serves as a qualitative evidence.
2. A core-Sérsic function gives a significantly better fit than a Sérsic model. Quantitatively, it is expected that the χ^2 value for the Sérsic fit χ^2_S is larger than twice that of the core-Sérsic fit χ^2_{CS}.
3. To avoid an ambiguous core detection, the potential core must be well-resolved by the data. Quantitatively, $r_b > r_2$ where r_2 is the second innermost datapoint in the observed profile.
4. The power-law slope has to be consistently less than the slope of Sérsic fit inside r_b.

5.2.2 The fitting procedure

Using the given photometric profile, we construct a one-dimensional light profile along the circularized radius (mean profile), instead of along the semi major radius as is commonly done. The circularized radius is defined as $r = \sqrt{r_{\rm maj} r_{\rm min}}$ where $r_{\rm maj}$ and $r_{\rm min}$ are the major and minor axis radius of the isophote. This way, we take into account the variation of ellipticity with radius, giving a fair representation of the true isophotes. The use of this mean profile is consistent with the implementation of the PSF (point spread function) correction (section 5.2.3).

The fitting is done using a one-dimensional profile fitting software written by P. Erwin. An initial model is generated based on user-given starting values. It is compared to the observed profile and the χ^2 is calculated. The best-fitting solution is achieved after a certain number of iteration by minimizing the χ^2 of the fit, using the Levenberg-Marquardt algorithm (MPFIT routine). The user provides a starting value and its range (within which the solution would be located) for each free parameter of the model. There are three free parameters in the Sérsic model, i.e. n, r_e, I_e and there are six free parameters in the core-Sérsic model, i.e. n, r_b, r_e, μ_b, α, γ.

Since we are mainly interested in the inner region of the galaxy, the PSF effect that blurs the central light profile becomes important and has to be taken into account. For NGC 4472, the photometric profile is already clean from the PSF effect. It is taken from KFCB09 and they have deconvolved the image prior to extracting the light profile from the image. We fit this galaxy profile as described in the previous paragraph. For the other galaxies, we incorporate a PSF correction routine described in the next section into the fitting program such that the initial model is convolved first before being compared to the observed light profile. In this case, the minimised χ^2 represents the difference between the convolved model and the data. The PSF convolution is done at every iteration, making the fitting process more time-consuming.

5.2.3 The implementation of the PSF convolution

For galaxies whose light profiles are not yet seeing-corrected, we take the PSF into account in the fitting by means of convolution. For this, we use the same PSF image as the one used in the deprojection for the dynamical modelling, i.e. the PSF corresponding to the innermost galaxy isophotes. From these PSF images, we generate a circularized profile of the PSF by averaging its radial profile at different azimuthal angles (done using MIDAS). We further normalize the PSF such that the total light is one. The implementation of the convolution follows Saglia et al. (1993) (their Appendix A). Below we review the method.

The PSF convolution is done by multiplying the galaxy surface brightness profile and the PSF in the Fourier space. On the sky, the galaxy surface brightness is a function of a two-dimensional position **r** and so is the PSF. If I(**r**) and P(**r**) denote the surface brightness and the PSF distribution, then the convolved surface brightness profile becomes:

$$I_{\mathrm{conv}}(\mathbf{r}) = \int \exp\left(i\mathbf{k}\cdot\mathbf{r}\right)\hat{P}(\mathbf{k})\,\hat{I}(\mathbf{k})\frac{d^2k}{(2\pi)^2} \tag{5.4}$$

where $\hat{I}(\mathbf{k}) = \int \exp\left(i\mathbf{k}\cdot\mathbf{r}\right) I(\mathbf{r})\, d^2r$ and $\hat{P}(\mathbf{k}) = \int \exp\left(i\mathbf{k}\cdot\mathbf{r}\right) P(\mathbf{r})\, d^2r$.

Since we use a one-dimensional, circularized surface brightness profile, I or P is a function of only the radius r. In this case, $\int_0^{2\pi} \exp\left(ikr\,cos\,\theta\right) d\theta = 2\pi J_0(kr)$ where $J_0(kr)$ is the Bessel function of order zero. Then, equation 5.4 becomes:

$$I_{\mathrm{conv}}(r) = \int_0^{\infty} \frac{1}{2\pi} J_0(kr)\,\hat{P}(k)\,\hat{I}(k)\,k\,dk \tag{5.5}$$

with

$$\hat{P}(k) = \int_0^{\infty} 2\pi P(r) J_0(kr) r dr \tag{5.6}$$

$$\hat{I}(k) = \int_0^{\infty} 2\pi I(r) J_0(kr) r dr \tag{5.7}$$

In this way, although the light and the PSF profiles are one dimensional, the convolution is done such that the light coming from different angles is also taken into account. This is important because the light is scattered, due to the seeing, not only in the radial direction but also in the azimuthal direction. Equations 5.5-5.7 are also called the Hankel transform. We compute the convolved surface brightness profile numerically, making use of integration routines in the GNU Scientific Library.

To see if the convolution works as expected, we perform a test. We generate a galaxy image which follows a Sérsic law with $n = 2$ and zero ellipticity everywhere using the

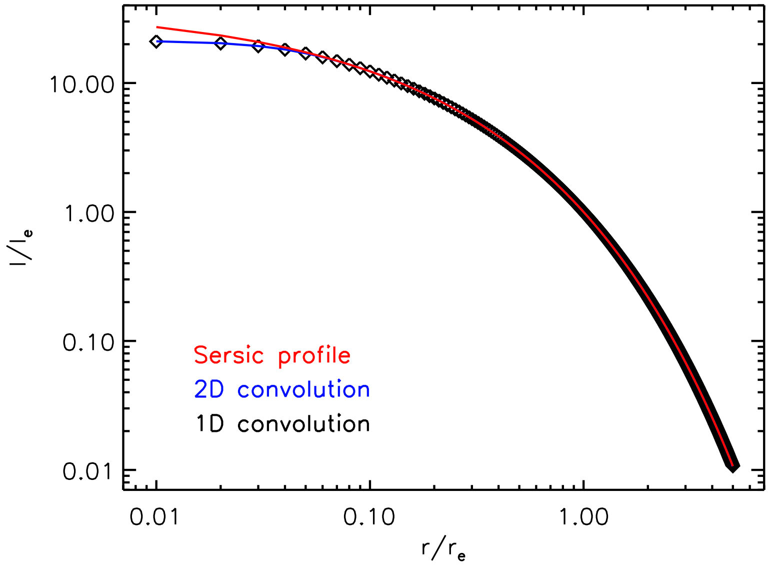

Figure 5.1: The radial profile of a Sérsic image and its convolution with a Gaussian image with σ equals to 1/40 of the half-light radius of the Sérsic model. Both the Sérsic and the Gaussian images are circular. The red line is the unconvolved Sérsic model. The black diamonds are the results of one-dimensional convolution (equation 5.5-5.7) and the blue line is the radial profile of the convolved image.

`makeimage` recipe in a two-dimensional profile fitting software `imfit` (Erwin et al. in preparation). For the PSF, we create a circular Gaussian image with $\sigma = 1/40$ of the half-light radius of the galaxy model. We extract the radial profile of both images and use these to perform the one-dimensional convolution as described above. As an independent check, we separately convolve the galaxy image with the Gaussian image in `imfit`. Fig. 5.1 shows the radial profile of this convolved image (2D-convolution), compared to the result of the convolution process above (1D-convolution). The original (unconvolved) Sérsic profile is also plotted in red. It is evident that the 1D convolution reproduces the results of 2D convolution, in the case of a circular image.

5.3 Core-Sérsic vs Sérsic fit

We fit each galaxy profile with the Sérsic and the core-Sérsic models. Using our photometric data (excluding NGC 4472 where the data comes from KFCB09), we convincingly classify five out of six galaxies as core galaxies, based on the four criteria in Section 5.2.1. The exception being NGC 1374 which is discussed separately later on in this section. Below, we first present the remaining five galaxies plus NGC 4472.

At first, we use all the available datapoints in the fitting. For all six galaxies, the core-Sérsic function gives a much better fit to the whole profile. However, there are two galaxies (NGC 3091 and NGC 5516) where we find that the fit residuals become rather large at several outermost datapoints. Since these datapoints do not seem to be well-described by a Sérsic function, they are excluded from the final fit. We keep only the datapoints where the residual is 0.1 mag or less. For the two galaxies, the fit is then repeated using only the remaining datapoints. We show the fit of both the Sérsic and the core-Sérsic functions to the data, their residuals and their χ^2 values in Fig. 5.2.

For all these galaxies we see a pattern in the residuals of the Sérsic fit that qualitatively suggests the presence of the core. This residual pattern disappears when the galaxy is fitted with the core-Sérsic profile. So the first criterion is secured. In each case, the rms of the residuals for the best Sérsic fit is much larger than that for the core-Sérsic. The χ^2 value for each galaxy is calculated by adopting the residual rms of the best core-Sérsic fit as the error on the surface brightness measurements. As discussed in KFCB09, this estimate for the real error is reasonable as long as the rms is of order of the profile measurement error, i.e. a few hundredths of a mag arcsec^{-2}, which is indeed the case for all the galaxies that we examine. Using this error approximation, the χ^2 of the core-Sérsic fit is artificially set to 1.0. We find that χ^2 value for each Sérsic fit is more than twice that of the core-Sérsic. The average ratio of χ^2_S/χ^2_{CS} is around 48 with the minimum being 7.8, easily fulfilling the second criterion. To asses the third criterion, one can compare the position of the second datapoint to the position of the dotted vertical line which marks the break radius. It is thus clear that we have cases of resolved cores. The last point is also satisfied since inside the break radius, the core-Sérsic function shows a constant deficit in light compared to the extrapolated Sérsic profile (shown by the blue line). Among all, NGC 1407 is the best case of core. For the two cases where we exclude some datapoints, the core is already well identified when fitting all the datapoints, i.e. fulfilling the four criteria simultaneously. Limiting the fitting range only improves the distinction.

Lauer et al. (2005) –hereafter L05– classify NGC 1374 as a core galaxy, based on the Nuker profile fitting to their HST imaging data. From fitting core-Sérsic models to our data, we find no solid evidence that the core exists. We have tried different fitting range by varying the maximum radii of the fitted datapoint, but there is no strong visibility of a core in all cases. In the top row of Fig. 5.3, we show the Sérsic and core-Sérsic fit to the whole profile and to a limited profile. For the latter, we limit the fitting range to $r < 7$ arcsec (for a fair comparison to the fitting using L05 data, see below). Judging by eye, there is no significant difference in fit quality between the Sérsic and the core-Sérsic profiles, although the overall residual rms and χ^2 of the core-Sérsic is smaller and $\chi^2_S > 2\chi^2_{CS}$. When fitting the whole range, the Sérsic profile actually provides a better fit in the center and instead of seeing a core, the core-Sérsic fit indicates an extra light on top of the Sérsic component. There is a slight improvement and a vague indication of a core when we fit only up to 7 arcsec. However, if we base our core classification on Trujillo et al. (2004)'s criteria, this fit fails at the second criterion.

Our next attempt is to fit the data of L05 to confirm/deny their finding. Their profile has been corrected for the PSF effect, so as in the case of NGC 4472 we directly fit it with the models without convolution. As shown in Fig. 5.3, we detect a core in this galaxy, albeit weak, by discarding the two outermost datapoints ($r > 7$ arcsec). Extending the fitting range of data does not give the same results, i.e the existence of the core becomes inconclusive and the core disappears when all the datapoints are included in the fit. L05 fit their light profile with a Nuker model and it appears that they also made the compromise of neglecting the 3-4 last datapoints in the fit, in order to detect the core.

Comparing the core-Sérsic fit to our and to L05 data for $r < 7$ arcsec, we conclude that our data lack spatial resolution. This situation is aggravated by the PSF convolution in the fitting process. It is, however, not clear whether the exclusion of the datapoints at large radii is really necessary to see the core (because the core is small and so not so well-resolved, even in L05's data) or because the galaxy does not follow a Sérsic profile at large radii. To find out, better data that go farther into the center of the galaxy will be needed.

The parameter values of the best-fit core-Sérsic model for each galaxy are provided in Table 5.1. The Sérsic index for these galaxies are all larger than 4, as also found by KFCB09 for the giant ellipticals. Although NGC 5516 can be classified as a core galaxy, the core-Sérsic fit to the light profile results in unusually large n and r_e. Fitting the whole data range reduces n and r_e to 12 and 266, driven by the last three datapoints which indicate a steeper slope at $r > 80$ arcsec. As in NGC 3091, a Sérsic profile does not seem sufficiently good to describe the light profile in the outer part of this galaxy.

5.4 The Light and Mass Deficit in the Core

We define the light deficit in the inner part of the galaxy as the difference between the luminosity of the Sérsic component of the best-fitting core-Sérsic model and the luminosity of the core-Sérsic model itself, calculated within a certain radius. Normally, this radius is set to be the break radius r_b where the transition from the outer Sérsic to the inner power-law profile occurs (as done by Graham (2004) and Ferrarese et al. (2006)). However, as can be seen in Fig. 5.2 and 5.3, this break radius (dotted lines) does not coincide with the radius where the Sérsic and core-Sérsic models start to deviate from each other by more than the rms of the fit residuals ($r_{\rm rms}$, marked by the vertical dashed lines in Fig. 5.2 and 5.3). The break radius is generally smaller and the difference is larger for galaxies with slow transitions (small α) like NGC 3091 and NGC 7619. Using the break radius as the radial limit to derive the luminosity difference would lead to an underestimate. Therefore, we used $r_{\rm rms}$ as the radial limit within which we compute the light deficit, while keeping r_b as the quantity that defines the core size.

We first calculate intensity in the physical unit of solar luminosity per pc^2 from the surface brightness μ (magnitude/arcsec^2) :

$$\begin{aligned} I(L_\odot/\mathrm{pc}^2) &= (206265)^2.10^{0.4(\mathrm{M_{sun}}-\mu-5)} && (5.8) \\ &= 4.255\times10^{8}10^{0.4(\mathrm{M_{sun}}-\mu)} && (5.9) \end{aligned}$$

where $\mathrm{M_{sun}}$ is the absolute magnitude of the sun in the same band as μ. We then obtain the luminosity L interior to $r_{\rm rms}$ by numerically integrating the intensity over a projected

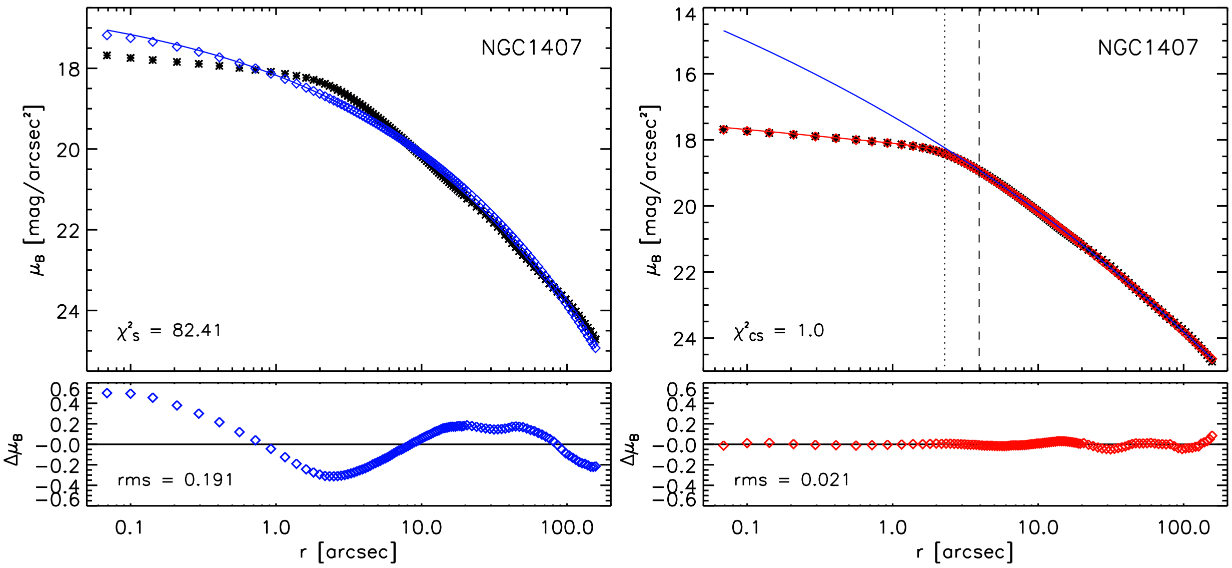

Figure 5.2: The model fits to the surface-brightness profiles of NGC 1407, NGC 1550, NGC 3091, NGC 4472, NGC 5516, NGC 7619 (top to bottom row, each row for each galaxy). The lower panel of each plot shows the residual profile, i.e. the difference between the convolved best-fit model and the observed profile. In the left column, we show the Sérsic fitting. The black asterisks show the observed profile, the blue diamonds are the convolved best-fit Sérsic function and the blue line is the intrinsic Sérsic function (before PSF convolution). In the right column, we show the core-Sérsic fitting. The red diamonds are the convolved best-fit core-Sérsic function, the red line shows the intrinsic core-sersic function (before PSF convolution) and the blue line is the Sérsic function that fits only the outer part of the galaxies. The vertical dotted and dashed lines mark the break radius (r_b) and the radius at which the core-Sérsic model deviates from the extrapolated Sérsic model by more than the rms of the residuals ($r_{\rm rms}$), respectively. The rms of the each Sérsic and core-Sérsic fitting is shown and the latter is taken as the uncertainty in the surface brightness profile, thereby setting the χ^2 value of the core-Sérsic fit to 1.0. For NGC 3091, the fitting range of both functions is limited to ~47 arcsec. For NGC 4472, the diamonds and the line with the corresponding color coincide with each other, since there is no PSF convolution; the additional dashed green line is the Sérsic function in KFCB09. For NGC 5516, the fitting range of both functions is limited to $\sim$ 80 arcsec.

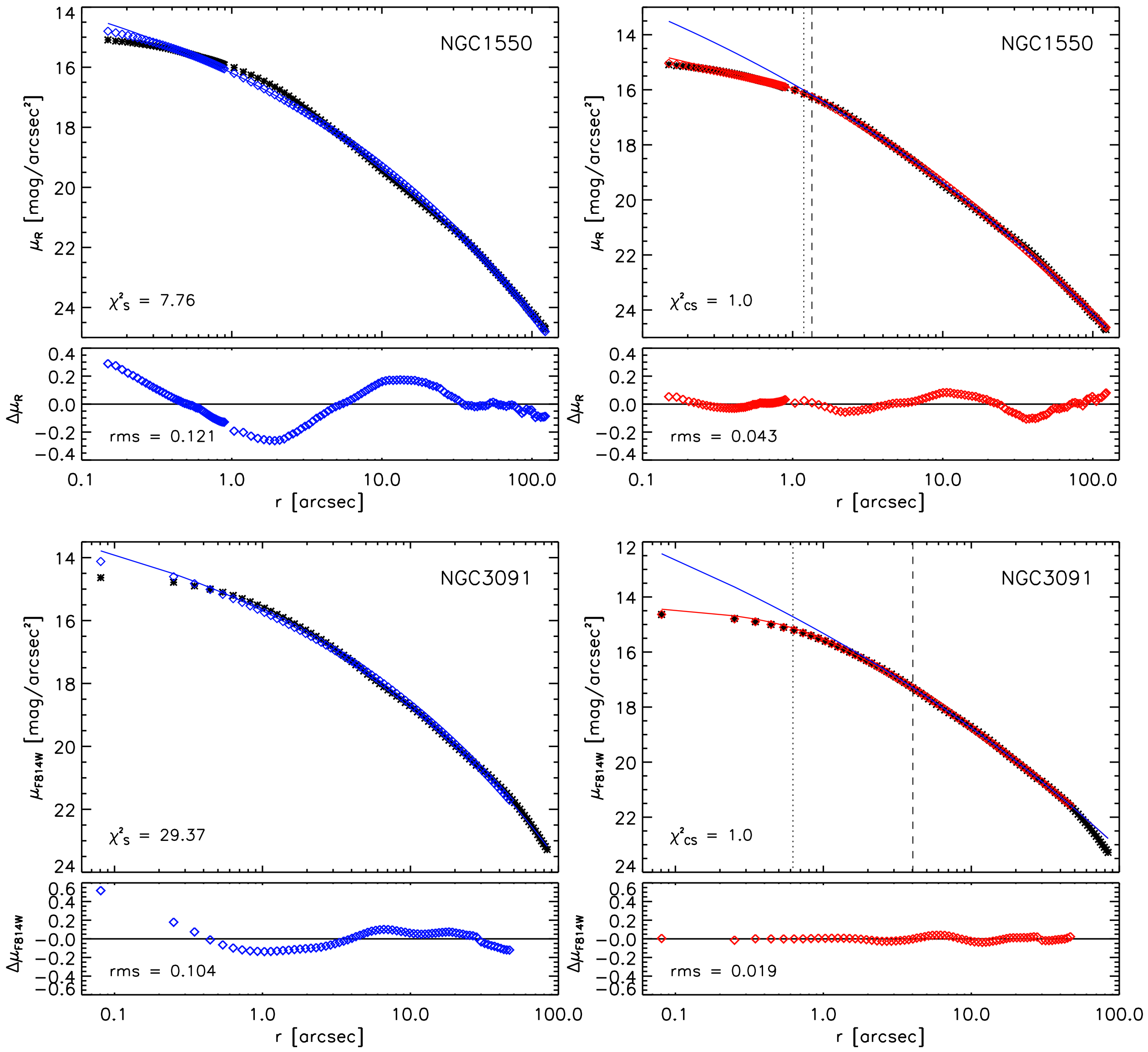

Figure 5.2: continued.

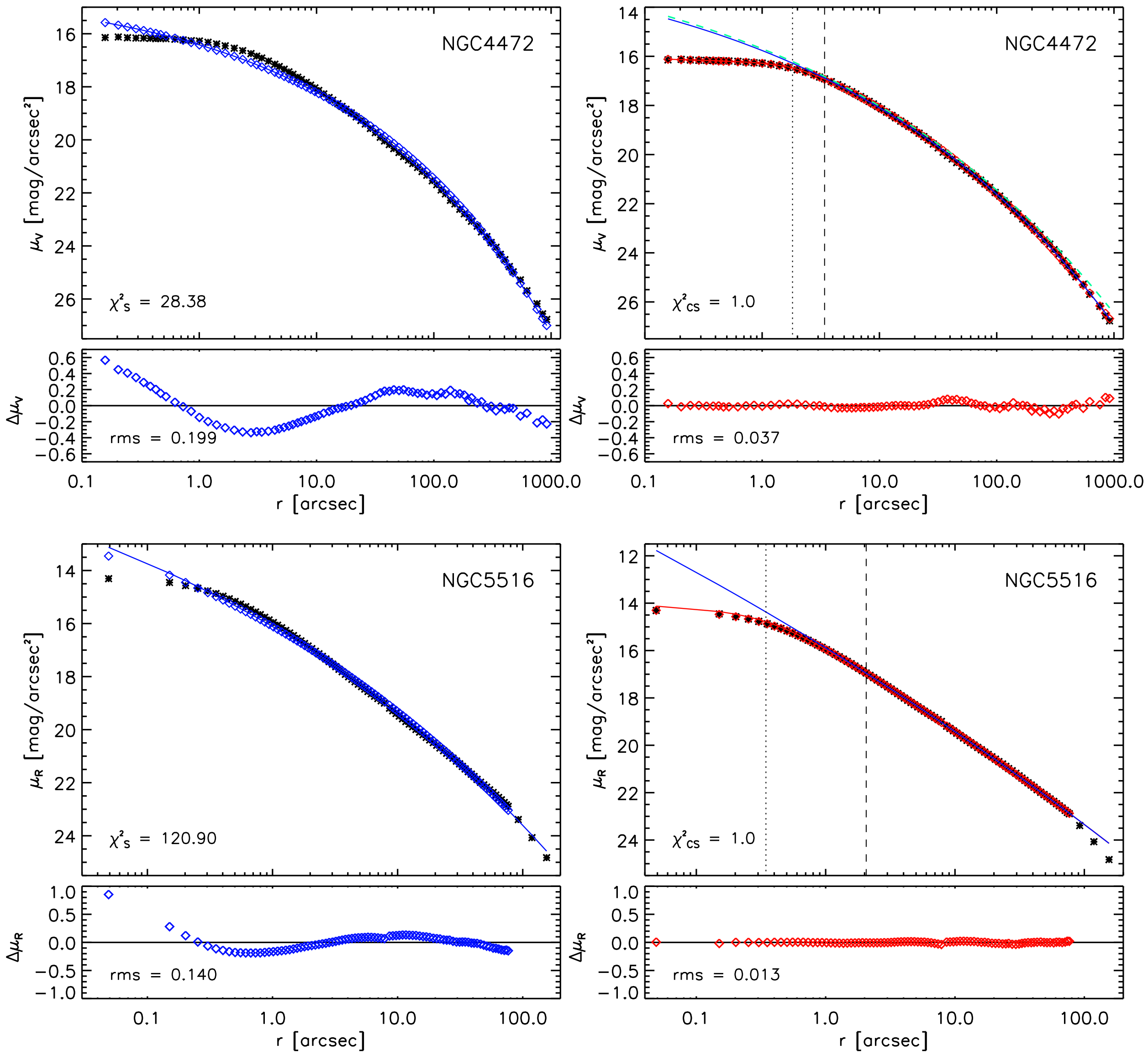

Figure 5.2: continued.

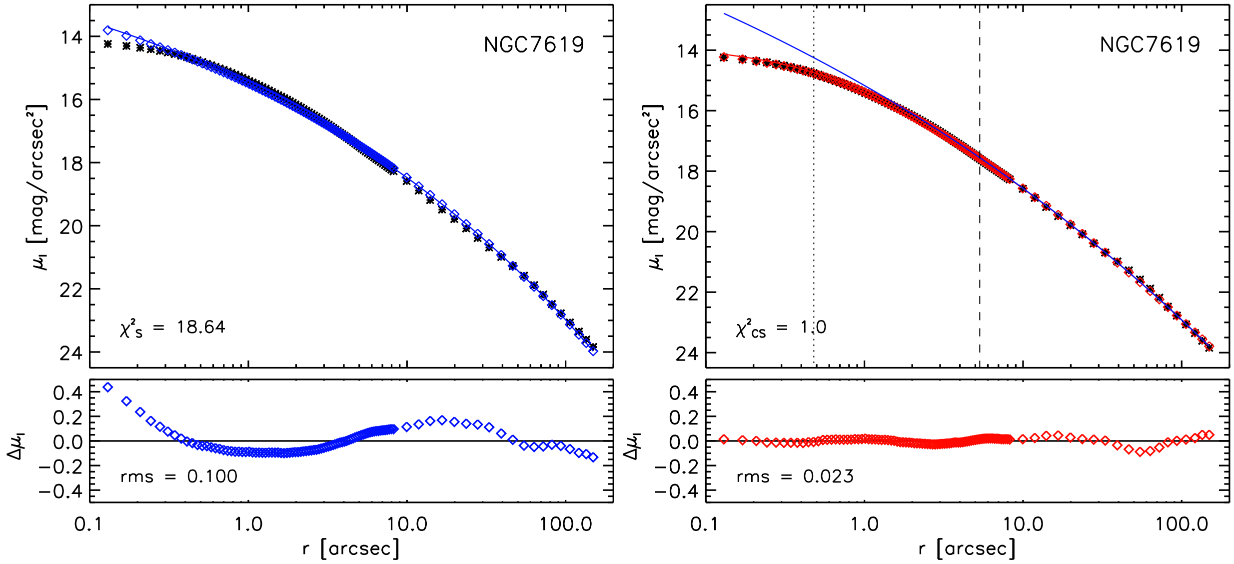

Figure 5.2: continued.

area $\pi\, r_{\rm rms}^2$:

$$L(r \leq r_{\rm rms}) = \int_0^{r_{\rm rms}} I(r) 2\pi\, r\, dr \tag{5.10}$$

This is calculated for both the core-Sérsic model and the extrapolated Sérsic component of that model. The difference between the two becomes the luminosity deficit ΔL (in $L_\odot$). This is converted back to the magnitude system to result in the absolute magnitude of the light deficit $\mathrm{M_{def}} = -2.5 \times \log_{10}(\Delta L) + \mathrm{M_{sun}}$.

In order to convert the light deficit into a mass deficit, we use the stellar mass-to-light-ratio Υ derived from the dynamical model including a dark halo component (Chapter 4). Since we use the same photometry files as in the modelling, the derived Υ and the light deficit are both in the same band so we just need to apply a simple multiplication of $(\Upsilon)\mathrm{x}\Delta L$ to obtain the mass deficit. For NGC 1374, we are able to detect the core only when using the surface brightness profile of L05 in the R-band, while the dynamical Υ is in the B-band. In this case, we calibrate the dynamical Υ from the B to the R-band by taking B-R to be 1.3, derived by matching our and L05's profiles. For this calibration, the absolute magnitude of the sun is taken to be 4.42 in the R-band and 5.48 in the B-band (Binney & Merrifield, 1998)

The uncertainties are calculated through a Monte Carlo simulation. Using the rms of the best core-Sérsic fitting as the measurement error, gaussian noise is added to create 100 realizations of the observed surface brightness profile. For each realization, a best-fit core-Sérsic is derived and the light deficit is calculated in the same way as done for the real profile. The rms of those 100 values of light deficit becomes the uncertainty. The error of the mass deficit is derived from the uncertainties of both the light deficit and Υ. From these 100 realizations, we also derive the rms of each core-Sérsic parameter and adopt this

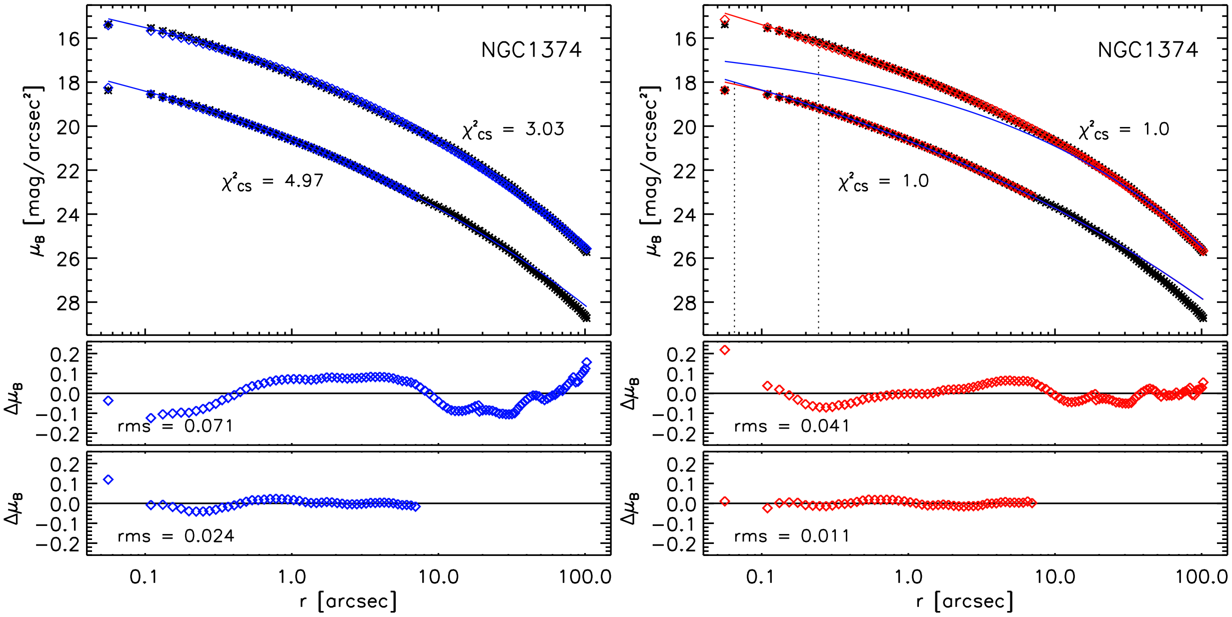

Figure 5.3: The model fits to the surface-brightness profiles of NGC 1374. **Top row:** model fits to the surface brightness profile derived in the previous chapter. On the left side, we show the Sérsic fitting to all the datapoints (upper profile) and the Sérsic fitting only to datapoints with r< 7 arcsec (lower profile). The black asterisks show the observed profile, the blue diamonds are the convolved best-fit Sérsic model and the blue line marks the intrinsic Sérsic model (before PSF convolution). The upper black asterisks show the actual values of surface brightness. The lower one is the same profile but shifted by 3 magnitude for illustration purposes. The middle and bottom panels show the residuals, i.e. the difference between the convolved best-fit model and the observed profile for the upper and lower profile respectively. Similarly on the right side, we show the core-Sérsic fitting. The red diamonds are the convolved best-fit core-Sérsic model, the red line shows the intrinsic core-Sérsic model (before PSF convolution) and the blue lines are the Sérsic model that fits only the outer part of the galaxies. **Bottom row:** model fits to the surface brightness profile reported in Lauer et al. 2005 (L05). The fitting is done for r< 7 arcsec. The vertical dotted and dashed lines mark the break radius (r_b) and the radius at which the core-Sérsic model deviates from the extrapolated Sérsic model by more than the rms of the residuals ($r_{\rm rms}$). Note that the diamonds and the line with the corresponding color coincide with each other, since there is no PSF convolution.

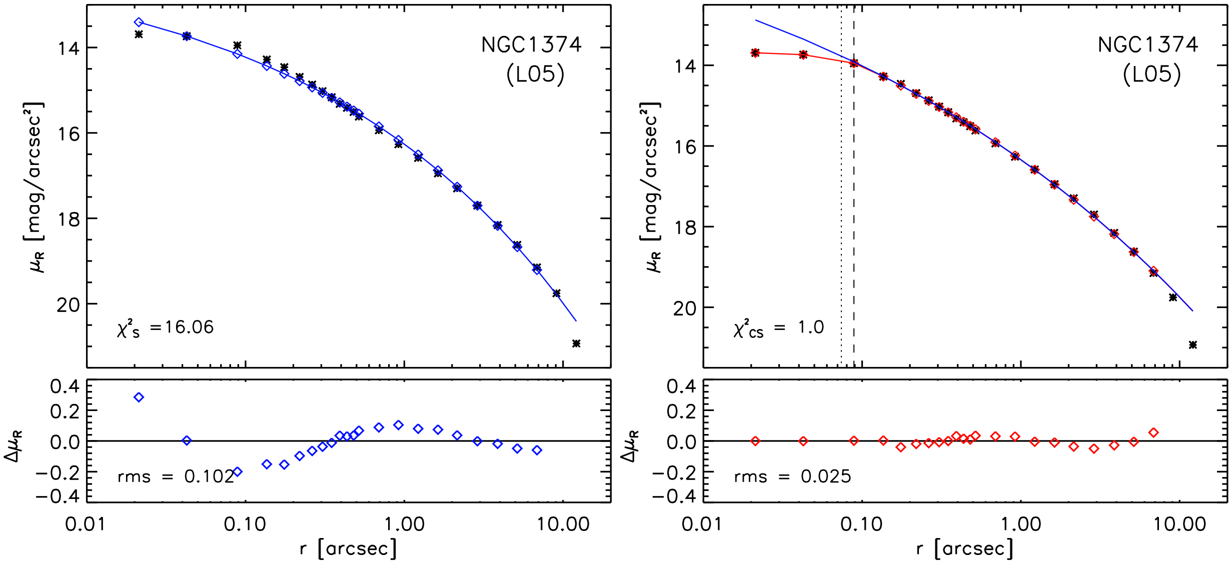

Figure 5.3: continued.

as the error of the parameter (given in Table 5.1).

To enable a statistical comparison of light deficit $M_{\rm def}$ among the galaxies, this quantity should be presented in a single photometric filter. For this purpose, we convert $M_{\rm def}$ in the given band to the V-band by applying a color correction based on a value obtained from the literature, specific for each galaxy. In the case where multiple aperture measurements are available, we take the color corresponding to the smallest aperture since we are mostly interested in the inner part of the galaxy where the core is present. Table 5.2 lists the color correction, the light and mass deficit for each galaxy. The dynamical Υ and $M_{\rm BH}$ obtained from the modelling with dark halo are also added to this table.

5.5 Black Hole-Core Correlation

Based on primarily the $M_{\rm BH}$-σ relation, previous studies find that the black hole mass correlates with the light or mass deficit in the core. It is shown in KB09 that the stellar velocity dispersion of the galaxy (σ) and the missing light correlate with $M_{\rm BH}$. In Fig. 5.4, we show such diagrams where we plot the seven sample galaxies plus two other core galaxies whose dynamical black hole masses have been revised in recent publications, i.e. NGC 4649 (Shen & Gebhardt, 2010) and NGC 4486 or M87 (Gebhardt & Thomas, 2009). The photometric profiles used in those papers come from KFCB09. We use these profiles and derive the core properties using the method described above (see Section 5.6 for details). NGC 4472, NGC 4486 and NGC 4649 are also part of KB09's sample, but there they use the old $M_{\rm BH}$ or $M_{\rm BH}$ from the $M_{\rm BH}$-σ relation. For all the nine galaxies, we quote the black hole masses derived by taking into account the presence of DM in the dynamical modelling. For completeness, we also consider NGC 4261 and NGC 4374. The two galaxies are in the sample of both KFCB09 and KB09, but the black hole masses are determined through gas dynamics (Ferrarese et al., 1996; Bower et al., 1998). Both galaxies are plotted in red in Fig. 5.4 and 5.5 and we defer the discussion on these two galaxies to the end of the section. In the following paragraphs, we concentrate on the nine galaxies with new/updated stellar dynamical $M_{\rm BH}$.

The left panel of Fig. 5.4 shows the plot of the light deficit in the V-band versus the stellar velocity dispersion calculated within the effective radius σ_e. The correlation between stellar velocity dispersion of host galaxies and $\rm M_{V,def}$ determined in KB09 is overplotted as the solid and dashed lines. Note that the velocity dispersion used to construct this correlation is defined differently: it is based on the σ averaged within a slit aperture with a length of two effective radius. Although there is probably no significant difference between the two, this means that the relation cannot be strictly compared with the individual galaxies. In the right panel, we show the plot between $\rm M_{V,def}$ and the black hole masses. We overplot again the correlation between these two quantities, as derived in KB09, using solid and dashed lines. For the galaxies that overlap with KB09's sample, the values of $\rm M_{V,def}$ derived in that paper are given in Table 5.2 (NGC 4472) and 5.3 for comparison purposes.

Overall, there is a trend for each plot that the light deficit increases for larger σ_e or $M_{\rm BH}$. However, both trends do not appear to be aligned with the correlations of KB09. In a way, this behaviour is expected as the three quantities that we examine here are derived differently from those in KB09. Especially for $M_{\rm BH}$, we use the more improved and reliable estimates. The difference between our and KB09's $\rm M_{V,def}$ is difficult to estimate (discussed in Section 5.6 where we provide the comparison for the three galaxies with the stellar dynamical $M_{\rm BH}$ measurements plus two galaxies whose $M_{\rm BH}$ estimates are based on gas dynamics). Interestingly, KB09 estimates of $\rm M_{V,def}$ put NGC 4486 and NGC 4649 farther away, while slightly moving NGC 4472 closer to their $M_{\rm V,def} - M_{\rm BH}$ correlation. Between the two diagrams in Fig. 5.4, the correlation of $\rm M_{V,def}-\sigma$ seems to be in a closer agreeement with the individual measurements, despite the different definition for σ. The galaxies in $M_{\rm V,def} - M_{\rm BH}$ diagram display a much larger offset relative to the correlation. To some degree, this reflects the deviation of the new black hole masses from the $M_{\rm BH}$-σ relation of Tremaine et al. (2002) used by KB09. If there were to be a real correlation between the two quantities, the distribution of the galaxies indicates a steeper slope (provided the light deficit NGC 1374 is robust) or a shift to a larger $M_{\rm BH}$ for a given $\rm M_{V,def}$.

N-body simulations of mergers of galaxies having central black holes predict that the size of the core is related to the final black hole mass (e.g. Makino & Ebisuzaki 1996). Taking the break radius as a measure of the core size, we plot this against $M_{\rm BH}$ in the left panel of Fig. 5.5. There seems to be a correlation whose significance is improved by the presence of NGC 1374 that is located quite far below the other galaxies. The overplotted dashed line shows the linear regression fit to all the nine galaxies. The rms scatter is 0.09 dex relative to this fit. Finally, we show the amount of mass deficit compared to the black hole mass in the right panel of the same figure. The ratio between the mass deficit and $M_{\rm BH}$ seems to vary strongly. Most galaxies have mass deficits between 1 and $5M_{\rm BH}$. NGC 1374 and NGC 4486 represent the low and high extremes with mass deficit of about

$0.05M_{\mathrm{BH}}$ and $11M_{\mathrm{BH}}$, respectively.

In principle, the broad range of mass deficit/M_{BH} that we see in Fig. 5.5 is not in contradiction with the numerical predictions or the results of previous investigations. Using the core-Sérsic function to measure the mass deficit, Graham (2004) and Ferrarese et al. (2006) converge on finding a mass deficit of around two M_{BH} for their galaxy samples. KFCB09 find that the mass deficit in their sample is at least 5 times up to just below 50 times the black hole mass. These three studies infer M_{BH} from the σ or the galaxy Sérsic index. Merritt (2006) predicts that for every merger, the mass deficit amounts to $0.5M_{\mathrm{BH}}$. However, depending on how advanced the merger state of the binary black hole is, the mass deficit can reach up to $\sim 5M_{\mathrm{BH}}$ per major merger. Merging binary black holes emits gravitational waves anisotropically, imparting some momentum and delivering a kick to the coalescing black holes. If the recoil velocity is smaller than the escape velocity, the final hole decays back to the center through dynamical friction, ejecting more stars on its way. Gualandris & Merritt (2008) find that an additional mass deficit of 4-5M_{BH} can be expected when the recoil velocity is close to the escape velocity ($\sim 0.9V_{\mathrm{esc}}$). In addition, they also find (in agreement with the previous predictions by Boylan-Kolchin et al. (2004) and Merritt et al. (2004)) that the size of the kick-induced cores can be several times the black hole radius of influence (r_{SoI}) or about five percent of the galaxy's half light radius. We indeed see that this is the case for NGC 4486 whose r_{SoI} is 3.2 arcsec. Its break radius is a factor of 2.5 larger than the radius of influence and 4.5 percent smaller than the half-light radius r_e (Table 5.3). For most of the other galaxies, r_b/r_{SoI} is generally around one and r_b/r_e is smaller than 1 per cent (Table 5.1 and 4.5).

NGC 4261 and NGC 4374 fall on the KB09's correlations of M_{BH}-$\mathrm{M}_{\mathrm{V,def}}$ and σ-$\mathrm{M}_{\mathrm{V,def}}$ and their mass deficits agree with those derived in KB09. The two galaxies follow the same trend as the other galaxies in the σ-$\mathrm{M}_{\mathrm{V,def}}$, but are outliers with respect to the nine galaxies in the three other diagrams which involve M_{BH}. That is, the black holes in NGC 4261 and NGC 4374 seem to be undermassive. This might suggests that there exists some systematics between the gas and the stellar dynamical M_{BH}. We only point this out here and do not comment further on this issue.

5.6 Discussion

Of all the galaxies presented in Fig. 5.4 and 5.5, there are five galaxies which are also part of KB09 sample, i.e. NGC 4472, NGC 4486 (M87) and NGC 4649, NGC 4261 and NGC 4374. Using the photometric data available in KFCB09, we derive the missing light using the core-Sérsic function as described in Sections 5.2 and 5.4. From these five measurements, we find that some of our $M_{\mathrm{V,def}}$ fall outside the uncertainties provided by KB09. The difference is largest for NGC 4486 and NGC 4261 (by ~0.7 magnitude or a factor of two in luminosity) and it is not systematic (see Fig. 5.4). The disagreement reflects the different details in the fitting and the derivation of the missing light:

1. We use the circularized radius, KFCB09 uses semi-major axis radius. Galaxies are not perfectly round or circular in projection. Non zero ellipticity anywhere in the galaxy,

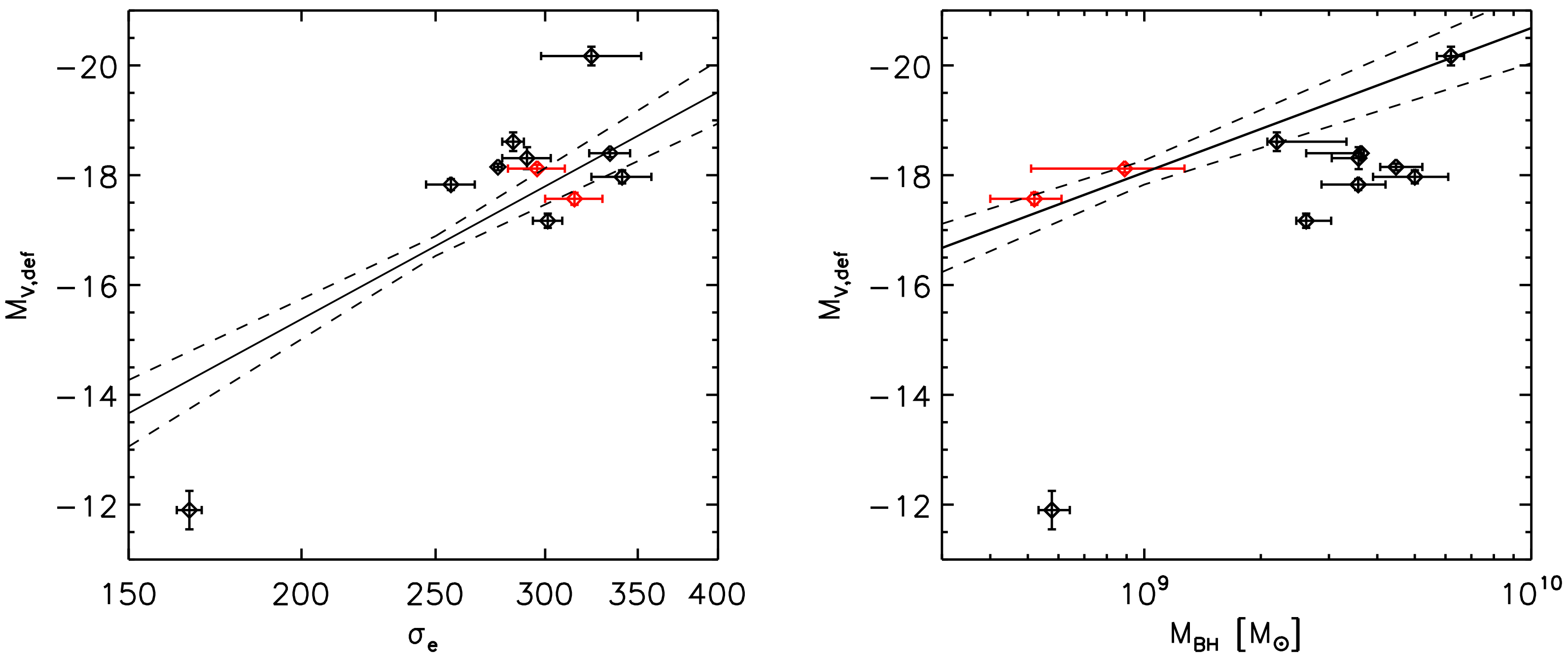

Figure 5.4: **Left panel:** the plot of σ_e vs $\mathrm{M}_{\mathrm{V,def}}$. σ_e is the velocity dispersion calculated within the effective radius. $\mathrm{M}_{\mathrm{V,def}}$ is the magnitude of the light deficit in the center, measured in the V-band. The solid and dashed lines are the relation and the corresponding uncertainties reported in KB09. **Right panel:** black hole masses plotted against the light deficits. The solid line shows the relation between the two quantities, taken from KB09 with the uncertainties shown by the dashed lines. In both plots, black diamonds represent the seven galaxies plus NGC 4486 and NGC 4649 for which the black hole masses have been revised recently. The two red diamonds correspond to NGC 4261 and NGC 4374, whose M_{BH} measurements were based on gas dynamics.

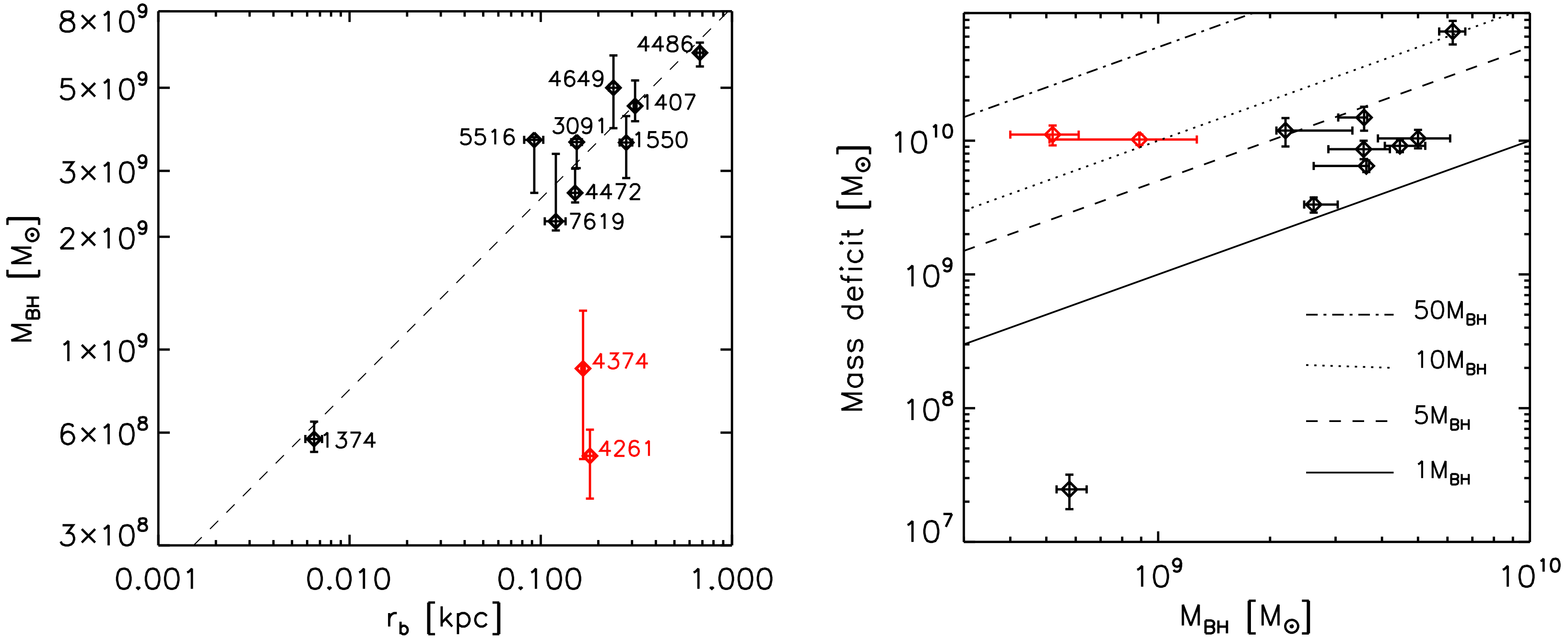

Figure 5.5: **Left panel:** break radius is plotted against the black hole mass. Black diamonds represent the seven galaxies plus NGC 4486 and NGC 4649. The dashed line is the linear regression of these nine galaxies. The red diamonds correspond to NGC 4261 and NGC 4374, whose $M_{\rm BH}$ measurements were based on gas dynamics. **Right panel:** the mass deficits of the eleven galaxies in the left panel are compared to their black hole masses.

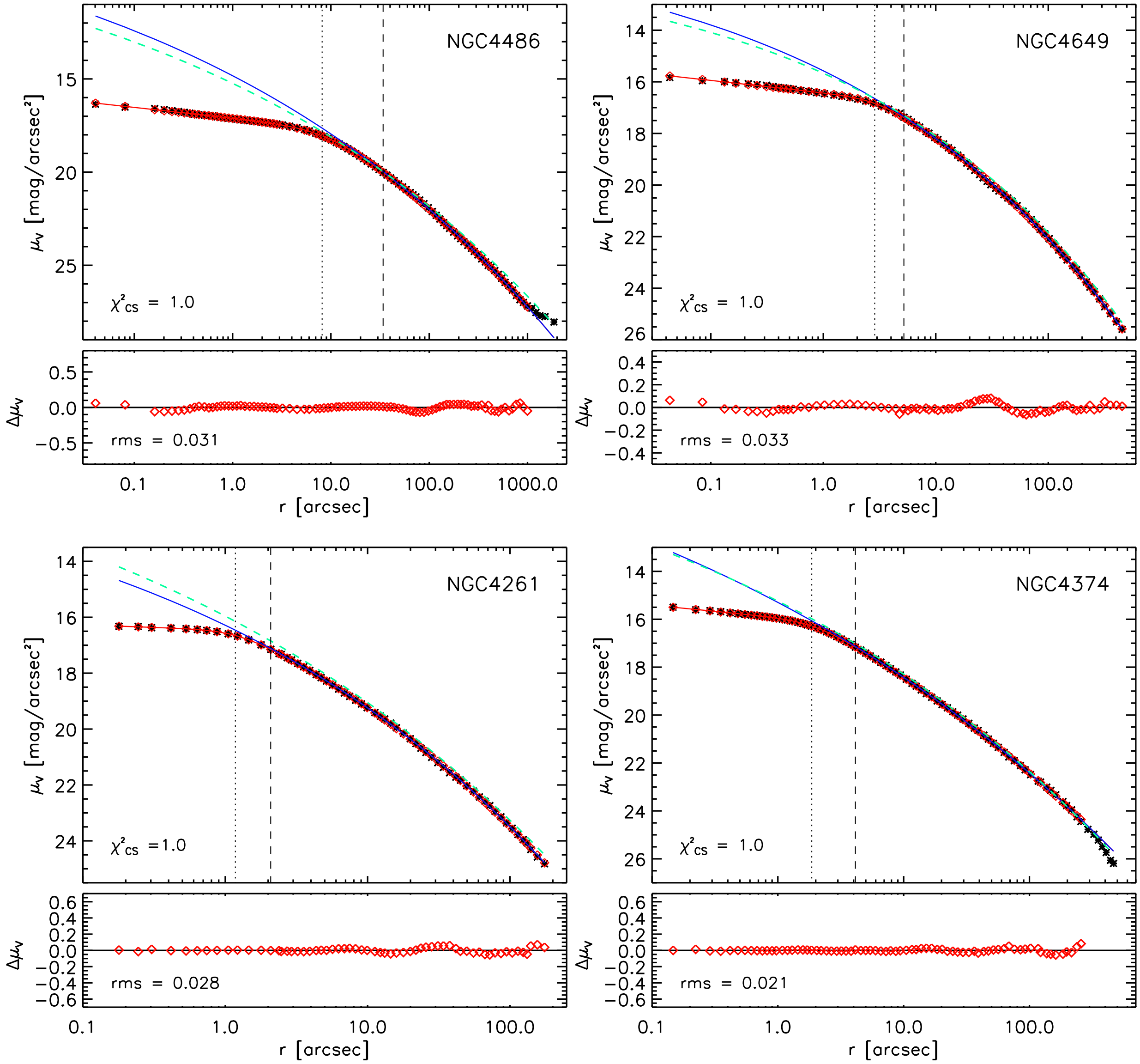

Figure 5.6: The core-Sérsic function fits to the surface-brightness profiles of NGC 4486 and NGC 4649 (top row) and also NGC 4261 and NGC 4374 (bottom row). The lower panel of each plot shows the residual profile, i.e. the difference between the convolved best-fit model and the observed profile. The red diamonds, connected by the red line, show the best-fit core-Sérsic function and the blue lines are the Sérsic function that fits only the outer part of the galaxies. The dashed green lines are the Sérsic function derived in KFCB09 based on the semi-major axis profile. The vertical dotted and dashed lines mark the break radius (r_b) and the radius at which the core-Sérsic function deviates from the extrapolated Sérsic function by more than the rms of the residuals ($r_{\rm rms}$).

not just in the center, will induce a deviation in $M_{\mathrm{V,def}}$ since the light deficit in both KFCB09 and this work depends also on the Sérsic fit to the outer part of the galaxy. The magnitude of the deviation is difficult to estimate, since this depends very much on the characteristic of each galaxy.

2. A different fitting range. Because we use the circularized radius, we take only the datapoint for which the ellipticity is given. In the photometry profiles of KFCB09, the ellipticity is often not specified for a few innermost or outermost radii. In the case of NGC 4486, KB09 calculated the light deficit based on a Sérsic fit inside $\sim$ 400 arcsec. KFCB09 argue that fitting datapoints outside that radius gives rise to a Sérsic index that is too large (almost 12) due to the cD halo. We have no problem fitting a core-Sérsic function to the (circularized) datapoints inside and outside $\sim$ 400 arcsec. We obtain a Sérsic index of $\lesssim 9$, similar to KFCB09's value when fitting only up to $\sim$ 400 arcsec, albeit different r_e and μ_e.

3. We fit the galaxy profile with a core-Sérsic profile, KFCB09 fit the outer part of the galaxy with a Sérsic profile. The critical point is the transition region between the Sérsic and the core. From the way KFCB09 defines the core, there is no transition region: the core immediately starts when the Sérsic model no longer fits the datapoints in the inner part. We use a core-Sérsic parametrization and since we fit the α parameter, instead of fixing it to infinity, we allow some part of the galaxy to be partly Sérsic partly power-law. This leads to a different inner limit of the radial range that is fitted only by the Sérsic model, which in the end results in a different best-fitting Sérsic profile.

4. The light deficit in KB09 is obtained by calculating the difference of the integrated intensity between the extrapolated Sérsic function and the actual (observed) profile after PSF deconvolution. The ellipticity of the Sérsic model is fixed to the ellipticy at the inner limit of the fitted radial range. Since our light profile is not PSF-deconvolved, we instead compute the difference between the best-fitting core-Sérsic function (the intrinsic one) and the extrapolated Sérsic component. We also implicitly assume ellipticity of zero when integrating the extrapolated Sérsic function, since we have used a circularized profile in the first place.

We show the core-Sérsic plot of NGC 4486, NGC 4649, NGC 4261 and NGC 4374 in Fig. 5.6, where the best-fitting Sérsic functions of KFCB09 is overplotted, to illustrate the points described above (see also the plot of NGC 4472 in Fig. 5.2). The best-fitting core-Sérsic parameters, the light and mass deficit that are plotted in Fig. 5.4 and 5.5 are listed in Table 5.3.

5.7 Summary

This work is based on the sample of seven galaxies presented in Chapter 4. Since most of these galaxies are massive elliptical galaxies, we investigate the occurence of cores in this sample. Based on the criteria suggested in Trujillo et al. (2004), we detect cores in all the seven galaxies. The light deficit is then computed assuming that the original profile, before the core is formed, follows a Sérsic model that fits the outer part of the galaxy. We subsequently derive the mass deficit using the dynamical mass-to-light ratios obtained in the previous chapter.

By using our galaxy sample and two other galaxies with revised stellar dynamical M_{BH} measurements, we assess if the core properties are correlated with the black hole mass. We see a trend that the amount of light deficit increases as the black hole mass or the stellar velocity dispersion of the host galaxy gets larger. It appears that most galaxies do not follow the correlation between the missing light and M_{BH} that is derived in Kormendy & Bender (2009). We suspect that part of this disagreement come from the wrong prediction of M_{BH} that is based on the M_{BH}-σ relation. As predicted in numerical work, the size of the core (the break radius) seems to correlate with the black hole mass. The mass deficit is found to be between $\sim 0.05 - 11 M_{\mathrm{BH}}$ and is not a constant multiplication of the black hole mass.

Table 5.1: The core-Sérsic function parameters. These parameter values are derived from fitting the light profiles in the previous Chapter 4, except for NGC 1374 where we used the photometric data of Lauer et al. (2005). These parameters correspond to the core-Sérsic models plotted in Fig. 5.2 and 5.3. The surface brightness profiles, calibrated to different bands, are indicated in the y-axis title of the corresponding plots. The uncertainties are calculated from 100 Monte Carlo realizations, described in Section 5.4. The distances of these galaxies are provided in Table 4.1. For NGC 4472, the n and r_e values in KFCB09 that are based on the semi-major axis profile are given in square brackets for comparison.

Galaxy	n	μ_b (mag/arcsec^2)	r_b (arcsec)	r_e (arcsec)	α	γ
NGC 1374	6.06±0.31	13.85±0.05	0.07±0.007	28.35±5.22	6.22±2.31	0.06±0.04
NGC 1407	9.77±0.29	18.41±0.01	2.29±0.04	601.84±58.20	4.35±0.31	0.16±0.008
NGC 1550	7.96±0.24	16.12±0.07	1.19±0.09	39.08±1.24	5.24±1.78	0.52±0.05
NGC 3091	9.29±0.57	15.13±0.05	0.62±0.04	91.01±11.07	1.90±0.19	0.13±0.05
NGC 4472	5.60±0.09	16.48±0.03	1.82±0.09	199.13±3.84	3.05±0.38	0.06±0.02
	[$5.992^{+0.314}_{-0.292}$]	-	-	[$269.291^{+23.634}_{-18.570}$]	-	-
NGC 5516	22.22±0.68	14.79±0.04	0.35±0.02	5959.81±946.31	2.13±0.13	0.12±0.04
NGC 7619	9.32±0.36	14.74±0.09	0.48±0.06	100.06±6.12	1.51±0.12	0.14±0.07

Table 5.2: The light and mass deficit in the core. $\mathrm{M_{def}}$ is the absolute magnitude of the light deficit in the given filter. This quantity is converted to the V-band ($\mathrm{M_{V,def}}$) using the color in col. 4. The color is specific for each galaxy, taken from the literature given in col. 5: "1" refers to Poulain & Nieto (1994), "2" refers to Prugniel & Heraudeau (1998), "3" and "4" refer to Djorgovski (1985) and Buta et al. (1995), respectively. The mass-to-light ratio Υ and the black hole mass M_{BH} are copied from Table 4.5 columns 5 and 4. For NGC 4472, the light deficit estimate from KB09 is given in square brackets for comparison purposes. For NGC 3091, the literature gives V-I; I-F814W is 0.03 as derived in Chapter 4. Υ for NGC 1374 is stated in the R-band based on a color B-R of 1.3 estimated from our and L05's surface brightness profiles. The uncertainty in the mass deficit takes into account both the uncertainties in the light deficit and Υ.

Galaxy	r_{rms} (arcsec)	$\mathrm{M_{def}}$ (mag)	Color	Source	$\mathrm{M_{V,def}}$ (mag)	Υ	Mass deficit ($M_\odot$)	$M_{\mathrm{BH}}(M_\odot)$
NGC 1374	0.09	-12.48 ± 0.35	0.58 (V-R)	1	-11.90 ± 0.35	4.3	$(2.47 \pm 0.71) \times 10^{7}$	5.8×10^{8}
NGC 1407	3.93	-17.10 ± 0.06	1.05 (B-V)	2	-18.15 ± 0.06	8.4	$(9.15 \pm 0.94) \times 10^{9}$	4.5×10^{9}
NGC 1550	1.34	-19.00 ± 0.10	1.17 (V-R)	3,4	-17.83 ± 0.10	3.7	$(8.62 \pm 1.36) \times 10^{9}$	3.6×10^{9}
NGC 3091	4.03	-19.76 ± 0.20	1.45 V-F814W	2	-18.31 ± 0.20	4.1	$(1.49 \pm 0.30) \times 10^{10}$	3.6×10^{9}
NGC 4472	3.41	-17.17 ± 0.13	0.0 (V-V)	-	-17.17 ± 0.13 $[-17.49^{+0.11}_{-0.10}]$	5.3	$(3.33 \pm 0.43) \times 10^{9}$	2.6×10^{9}
NGC 5516	2.06	-19.11 ± 0.07	0.71 (V-R)	1	-18.40 ± 0.07	2.5	$(6.47 \pm 0.64) \times 10^{9}$	3.6×10^{9}
NGC 7619	5.34	-19.95 ± 0.17	1.34 (V-I)	2	-18.61 ± 0.17	2.9	$(1.19 \pm 0.28) \times 10^{10}$	2.2×10^{9}

Table 5.3: Core parameters of NGC 4486, NGC 4649, NGC 4261 and NGC 4374. The mass-to-light ratio Υ and the black hole mass M_{BH} are taken from Gebhardt & Thomas (2009) for NGC 4486 and Shen & Gebhardt (2010) for NGC 4649. M_{BH} for NGC 4261 and NGC 4374 are the same as those quoted in KB09. Υ for NGC 4261 is taken from Häring & Rix (2004), with a color correction of 0.87 (V-R) applied. For NGC 4374, Υ is taken from Cappellari et al. (2006), with a color correction of 1.26 (V-I). All M_{BH} and Υ values are corrected for distance. For comparison purposes, the values of n, r_e and $\mathrm{M}_{\mathrm{V,def}}$ from KFCB09 or KB09 are given in square brackets.

	NGC 4486 (M87)	NGC 4649	NGC 4261	NGC 4374
n	8.91 ± 0.44	5.90 ± 0.13	6.33 ± 0.16	9.44 ± 0.24
n [KFCB09]	$[8.899^{+1.949}_{-1.299}]$	$[5.361^{+0.377}_{-0.324}]$	$[7.486^{+0.816}_{-0.599}]$	$[7.975^{+0.709}_{-0.557}]$
μ_b (mag/arcsec^2)	18.06 ± 0.04	16.84 ± 0.02	16.65 ± 0.03	16.29 ± 0.02
r_b (arcsec)	8.14 ± 0.29	2.86 ± 0.09	1.18 ± 0.05	1.86 ± 0.04
r_e (arcsec)	180.85 ± 4.13	124.54 ± 2.70	77.10 ± 2.56	229.517 ± 12.11
r_e [KFCB09]	$[376.279^{+179.988}_{-85.709}]$	$[132.047^{+11.622}_{-9.298}]$	$[99.970^{+15.778}_{-10.518}]$	$[142.079^{+19.317}_{-13.281}]$
α	2.13 ± 0.14	3.34 ± 0.43	3.78 ± 0.58	3.38 ± 0.25
γ	0.23 ± 0.006	0.19 ± 0.009	0.07 ± 0.03	0.21 ± 0.01
r_{rms} (arcsec)	33.97	5.20	2.09	4.13
$\mathrm{M}_{\mathrm{V,def}}$ (mag)	-20.17 ± 0.17	-17.97 ± 0.12	-17.57 ± 0.11	-18.12 ± 0.07
$\mathrm{M}_{\mathrm{V,def}}$ [KB09]	$[-19.51^{+0.30}_{-0.23}]$	$[-17.80^{+0.07}_{-0.07}]$	$[-18.26^{+0.03}_{-0.03}]$	$[-18.08^{+0.04}_{-0.04}]$
Υ in the V-band	6.55 ± 0.83	7.90 ± 0.91	12.22 ± 1.62	6.75 ± 0.41
Mass deficit ($M_\odot$)	$(6.54 \pm 1.31) \times 10^{10}$	$(1.04 \pm 0.16) \times 10^{10}$	$(1.11 \pm 0.19) \times 10^{8}$	$(1.02 \pm 0.09) \times 10^{10}$
$M_{\mathrm{BH}}(M_\odot)$	$(6.2 \pm 0.5) \times 10^{9}$	$(5.0 \pm 1.1) \times 10^{9}$	$5.2^{+0.9}_{-1.2} \times 10^{8}$	$(8.9 \pm 3.8) \times 10^{8}$

Chapter 6

Concluding Remarks

Empirical scaling relations between supermassive black holes and galaxies provide important constraints on our understanding of how galaxies have formed and evolved. Reliable measurements of black hole masses in the centers of (local) galaxies are necessary to ultimately recover the true shape of these scaling relations. This thesis concentrates on the high-$M_{\rm BH}$ end of the relations that are still largely uncertain and plagued by several problems. Black hole masses in eight early-type galaxies (Table 1.1) are measured based on stellar kinematics by means of axisymmetric orbit-superposition modelling. With these masses, we address the issues mentioned in Chapter 1 section 1.5:

1. We enlarge the size of black hole sample in the high-$M_{\rm BH}$ regime with these eight measurements. Despite the statistically small number of galaxies, it is a quite significant addition to the current sample of high-velocity-dispersion galaxies (σ > 250 km/s). The updated sample of Gültekin et al. (2009b) compiled by McConnell et al. (2011b) contains 66 galaxies, 14 of which have high-σ (excluding NGC 1332). Out of our eight galaxies, seven galaxies have velocity dispersions above 250 km/s. Therefore, the seven galaxies increase the number of the existing high-σ galaxies by 50%. Six out of eight galaxies are bright, having absolute B-band magnitudes of $M_{\rm B}$ < -21. The confirmation of the existence of cores in seven galaxies (Chapter 5) also means that the seven galaxies expand the sample size of core galaxies with reliable $M_{\rm BH}$ measurements (Kormendy & Bender, 2009) by more than a factor of two.

The $M_{\rm BH}$-σ relation has been dominated by the intermediate-σ galaxies and the fit was then extrapolated to the high-σ. Fig. 4.7 and Table 4.4 show the updated $M_{\rm BH}$-σ and $M_{\rm BH}$-L relations using the latest black hole sample which include the galaxies examined in this thesis. If the fitting includes only galaxies with σ < 250 km/s, the relation would be different, i.e. $\alpha = 8.26, \beta = 4.84$. While the zeropoint α is practically the same, the slope β becomes much flatter. This is an indication that the high-σ end of the relation is not a simple extrapolation of the lower-σ regime. This also emphasizes that it is important to properly sample the high-σ regime to recover the true shape of the $M_{\rm BH}$-σ relation.

Based on NGC 1332 alone (Chapter 3), the $M_{\rm BH}$-σ relation of Gültekin et al. (2009b) appears to be a much better predictor of $M_{\rm BH}$ as compared to the $M_{\rm BH}$-L relation of

Marconi & Hunt (2003) in the K-band. This is still true using the recent relations by McConnell et al. (2011b). The seven elliptical galaxies, however, lie slightly closer to the $M_{\rm BH}$-L than to the $M_{\rm BH}$-σ relation. As shown in Fig. 4.7, the ellipticals fall above the $M_{\rm BH}$-σ and $M_{\rm BH}$-L relations of McConnell et al. and therefore increasing the slope of both relations, especially the $M_{\rm BH}$-σ one. This has some implications on whether the quasar remnants could be found in local galaxies and on the space density of massive black holes, as described in the following paragraphs.

According to the $M_{\rm BH}$-σ relation of McConnell et al. (2011b) and Gültekin et al. (2009b), a black hole with a mass of $10^{10} M_\odot$ corresponds to a σ of $\sim$ 440 km/s and $\sim$ 560 km/s, respectively. With our new slope, black holes of $10^{10} M_\odot$ can now be expected to reside in galaxies with velocity dispersions of $\sim$ 420 km/s. This value is lower than the highest σ found in the local universe, i.e. 444 km/s (Salviander et al., 2008) and lower than expected for such black holes based on previous relations. This suggests that the high-σ galaxies could be the host of the quasar remnants.

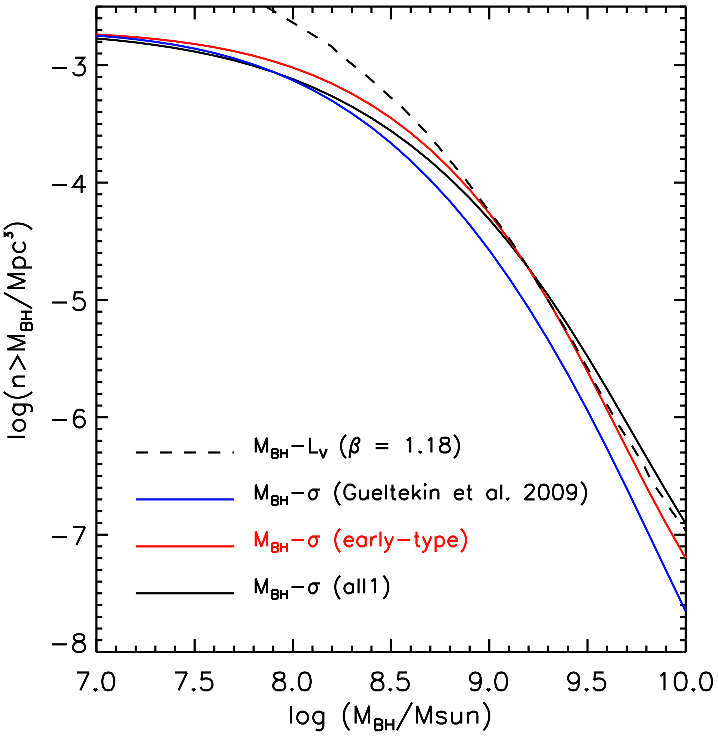

Figure 6.1: Number density of black holes as a function of $M_{\rm BH}$. The dashed line is the number density based on the $M_{\rm BH}$-L relation, taken from the best-fitting results of Gültekin et al. (2009b), adapted to $\beta = 1.18$. The solid lines are the number densities based on the $M_{\rm BH}$-σ relation. The blue line is reconstructed from the $M_{\rm BH}$-σ relation of Gültekin et al. (2009b) for early-type galaxies. The red and black lines are based on our $M_{\rm BH}$-σ relation for the early-type and all galaxies, respectively.

Lauer et al. (2007) pointed out that the number density of black holes more massive than $3 \times 10^9\ M_\odot$ as predicted by the $M_{\rm BH}$-σ relation is significantly lower than that inferred from the $M_{\rm BH}$-L relation. Gültekin et al. (2009b) confirmed this using their $M_{\rm BH}$-σ and $M_{\rm BH}$-L relations. With our updated relations, the prediction of the $M_{\rm BH}$-σ and $M_{\rm BH}$-L relations are now in a closer agreement, as shown in Fig. 6.1. The space density of massive black holes is quite sensitive to the intrinsic scatter of the relations, but we show that the broad agreement between the two relations is achieved by the increase in the slope of the $M_{\rm BH}$-σ relation and not by the increase in its intrinsic scatter.

2. The seven elliptical galaxies show that the dark matter inclusion in the modelling is not obligatory, when high spatial resolution kinematic data are used in the central region. The black hole masses derived with and without including the dark matter are consistent in this case. Chapter 4 section 4.7 describes how the resolution criterion is quantified. In addition, there is no statistical relation between the change of stellar mass-to-light ratio Υ and the change of $M_{\rm BH}$ due to the inclusion of a dark matter halo. However, the right Υ is essential to obtain a correct $M_{\rm BH}$ *when the resolution is marginal.* One way to obtain a correct Υ is to take into account the dark matter in the modelling.

In this regard, it is worth mentioning that although the dark matter was not included in the modelling of NGC 1332, it is unlikely that the black hole mass is wrong. There are several reasons for this. Two reasons are mentioned in Chapter 3 section 3.6.4: the relatively small amount of dark matter at the radius where the kinematic data is truncated and the fact that the mass-to-light ratios of the bulge and disc are decoupled. On top of these, the spatial resolution of the SINFONI data for NGC 1332 is high enough. Based on the resolution criterion in Chapter 4, we expect no significant bias in the black hole mass.

3. The cores detected in the seven elliptical galaxies in our sample, combined with a few additional galaxies with recent stellar dynamical measurements of $M_{\rm BH}$, show that the break radius appears to correlate with the measured $M_{\rm BH}$. The mass deficit in the core is found to be in the range of 0.05-11$M_{\rm BH}$ and does not scale with the black hole mass. There is a trend that the light deficit is larger for galaxies having higher velocity dispersions and more massive black holes. The trend, however, does not manifest itself in the same way as in Kormendy & Bender (2009). This might be due to the fact that half of the galaxies in their sample use the $M_{\rm BH}$-σ relation of Tremaine et al. (2002) to predict $M_{\rm BH}$.

Appendix A

Seeing correction in the deprojection

Seeing due to atmospheric turbulence flattens the slope of the light profile of extended objects obtained by ground-based observations, especially at the innermost radii. When the surface brightness profile is deprojected without PSF correction, the resulting luminosity density will also be flatter than it actually is. Since light traces stars this will then lower the stellar mass contribution. The dynamical modelling only constrains the total mass, and so $M_{\rm BH}$ will be overestimated to compensate for the decreased mass in stars. A priori, it is not known how much this effect alters the SMBH mass.

We estimated the PSF effect using two one-component models described in Section 3.4.2. The first was the one-component model used in the main analysis, where we relied on the SINFONI photometry (i.e., the collapsed datacube) for the innermost isophotes (hereafter referred to as the SINFONI dataset). The second one was the same model but we instead used the isophotes derived from the WFPC2 image to replace the SINFONI photometry at $r < 0.5$ arcsec (HST dataset). We accounted for the seeing in the deprojection step described in Section 3.4.3.

For the HST dataset, we generated a PSF for the Planetary Camera chip of WFPC2 with version 6.3 of the TinyTim software package,[1] using the location of the galaxy center and an appropriate K giant spectrum. This instrumental PSF of the WFPC2 image was then parametrised in the same way as that of the SINFONI image, i.e. as a non-circular double Gaussian function. Fig. A.1 shows the fit to the HST PSF. The resulting FWHMs are 0.067 arcsec and 0.24 arcsec for the narrow and broad components respectively ($\rm FWHM_x \approx FWHM_y$ for both components).

The top panel of Fig. A.2 shows the luminosity density profiles along the major and minor axes for both HST and SINFONI datasets. Both densities are almost identical at all radii along the major axis. There is only a small difference along the minor axis at 0.2 arcsec$\lesssim r \lesssim$0.8 arcsec, implying that the SINFONI density model is slightly more flattened at those radii. Due to the strong dust extinction in the WFPC2 image, the ellipticity in the inner part is not well constrained and is fixed to an approximate value. Together with the different shape of the HST and the SINFONI PSF, this prevents an exact

---

[1] http://www.stsci.edu/software/tinytim/tinytim.html

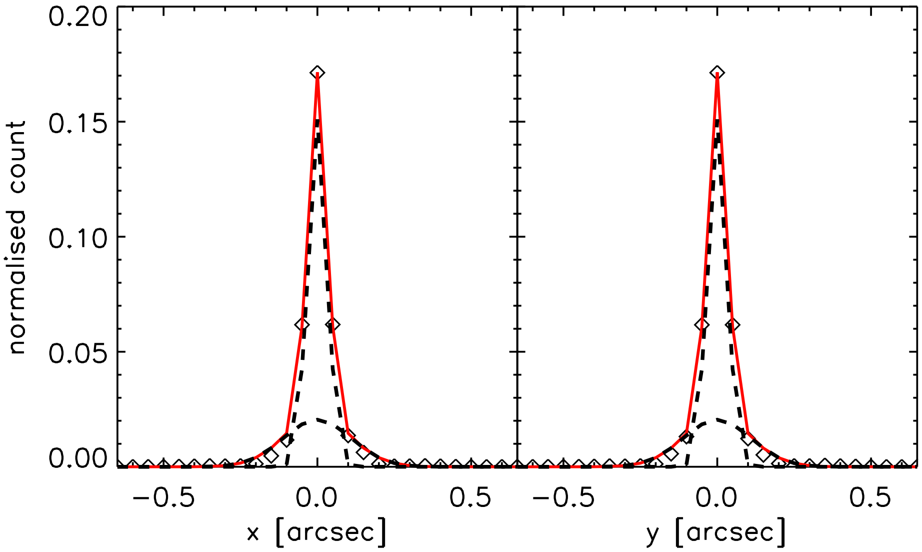

Figure A.1: A double non-circular Gaussian fit to the HST PSF. The fit along the x and the y-axis of the detector are shown in the left and right panel respectively. The black dashed lines are the individual Gaussians and the red solid lines are the sum of the Gaussian components; diamonds are the actual PSF.

match of SINFONI and HST density profiles. However, the general agreement between the two profiles is very good considering that the inner profile was constructed using different datasets, which were deconvolved using different PSF images.

The bottom panel shows the reprojection of the luminosity density models of both datasets without seeing convolution, which should reflect the intrinsic surface brightness profiles. We see that both profiles agree well with each other in the inner part where the correction is most significant ($r \lesssim 1$ arcsec). In the outer part, the profiles overlap with each other, as is also the case in the luminosity density profiles. This is expected as both profiles use the same EMMI data at $r > 4.5$ arcsec and the effect of seeing is restricted only to the innermost isophotes.

We performed the dynamical modelling using each of the luminosity density models from the two datasets, once with PSF correction and once without. The modelling setups were identical to those in Section 3.5. Our parameter grid for each of the runs consisted of 20 trial values of $M_{\rm BH}$ ranging from $5 \times 10^8 M_\odot$ to $5 \times 10^9 M_\odot$, each was paired with 20 different Υ values ranging from 1 to 10. To minimise computing time, we only used SINFONI kinematics. $M_{\rm BH}$ is sensitive to the change of the density profile and using only SINFONI data will put the least constraints to $M_{\rm BH}$. Therefore in some sense these runs should show the largest possible change in $M_{\rm BH}$ due to the PSF inclusion.

We list the best-fitting $M_{\rm BH}$ (average of four quadrants), marginalised over Υ, together with the averaged 1σ errors in Table A.1. For comparison, we rewrite the results of run 1A in Table 3.1 as the model “SINFONI with PSF correction”. When the seeing effect on the photometry is taken into account, $M_{\rm BH}$ decreases. This is expected, as the

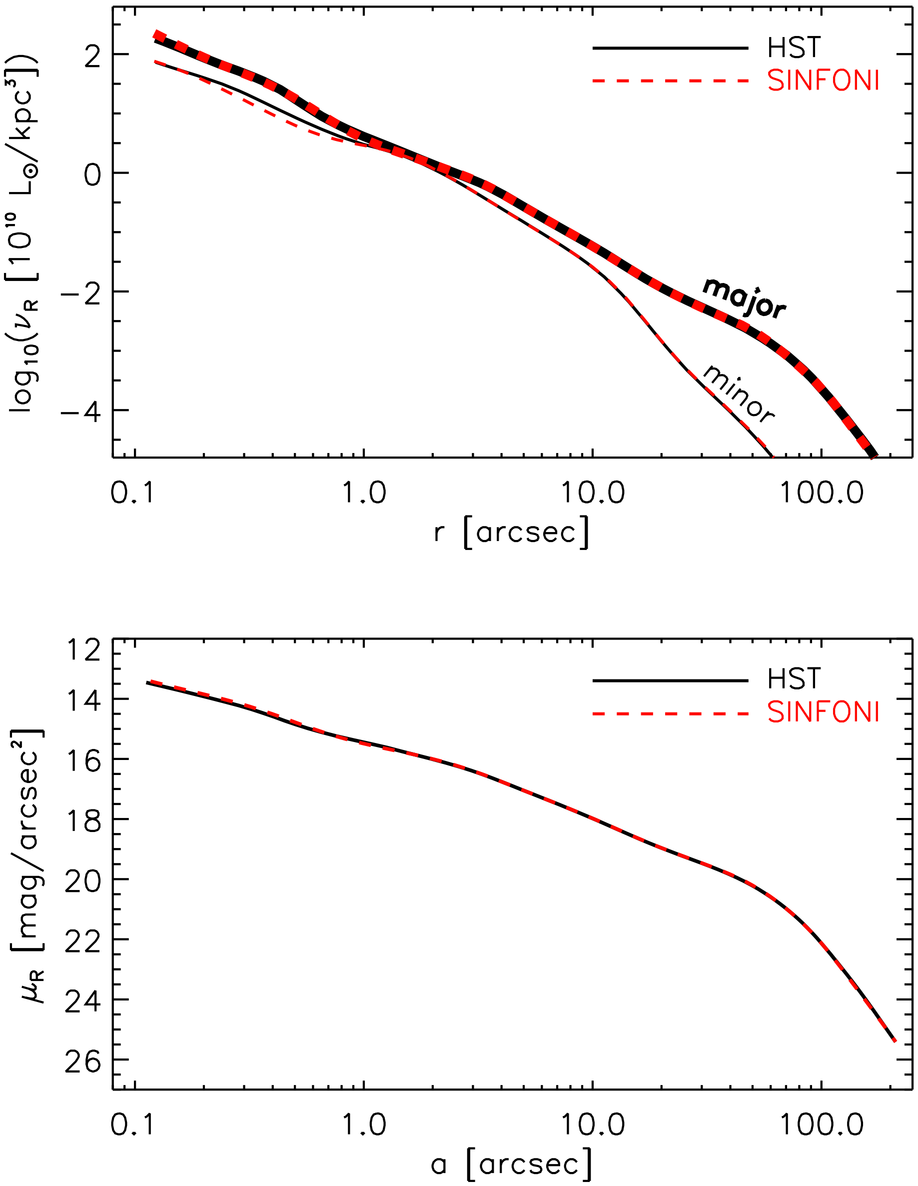

Figure A.2: The PSF-deconvolved luminosity density models (top panel). Thick and thin lines refer to density profiles along the major and minor axes respectively. The reprojection of these luminosity density models without seeing convolution resulted in the PSF-deconvolved surface brightness models (bottom panel). The SINFONI dataset (red dashed line) used SINFONI images out to 4.5 arcsec and the HST dataset (black solid line) used HST images to replace SINFONI data for the innermost isophotes ($r < 0.5$ arcsec). For $r > 4.5$ arcsec, the NTT-EMMI image was used for both profiles.

Table A.1: SMBH masses obtained for different modelling runs with different luminosity models. The given errors are the average of 1σ errors from the four quadrants. All M_{BH} are given in units of $10^9 M_\odot$.

Luminosity model	M_{BH}
HST without PSF correction	1.56 ± 0.24
SINFONI without PSF correction	1.92 ± 0.24
HST with PSF correction	1.27 ± 0.22
SINFONI with PSF correction	1.15 ± 0.24

PSF deconvolution steepens the slope of the surface brightness and the luminosity density profile, giving more mass to the stars. The mass-to-light ratio Υ increases only slightly, from ~ 8.6 for models without PSF correction to ~ 8.9 when either of the PSFs is included. The photometric difference (between the HST and the SINFONI image) in the innermost region does not seem to affect Υ.

For the runs where the PSF is not included, the SINFONI M_{BH} is higher than that of HST. When the PSF is included, the SINFONI M_{BH} decreases more dramatically (see Table A.1). These changes are expected, as the HST PSF is narrower than the SINFONI PSF. When the HST data are used, the change of M_{BH} due to the PSF is still within the 1σ error, while for SINFONI data the change is larger, but still less than a factor of two. Although this effect would not apply equally to all galaxies and observation modes, our exercise seems to suggest that the PSF can be considered a relatively minor issue for HST photometry. However, for ground-based observations which in general have broader PSFs, more care is needed.

Comparing M_{BH} obtained using the HST and the SINFONI datasets after PSF deconvolution, we see that both masses are consistent and lie well within their 1σ errors. This result is reassuring considering the uncertainties in the SINFONI PSF.

Appendix B

The large-scale kinematics of NGC 1374, NGC 3091 and NGC 5516

B.1 The Long-Slit Kinematics of NGC 1374

The long-slit observation of NGC 1374 was part of the program described by Saglia et al. (2002). NGC 1374 was observed during the period 10.11.2001-14.11.2001 at the LaSilla ESO NTT telescope, equipped with the EMMI spectrograph. We used the red arm (REMD mode with longslit, 6 arcmin long) with the 13.5 Å mm^{-1} grating (#6), the OG530 order sorting filter and the Tektronix 2048×2047 24-μm pixels CCD. The slit width was $3''$ and the scale 0.27 $''$pixel^{-1}, giving a resolution of 70 km s^{-1} and covering the wavelength range $\lambda = 8298 - 8893$Å. We observed the galaxy at PA=120 with 90 minutes integration time.

The standard CCD data reduction was carried out with the image processing package MIDAS provided by ESO. After bias subtraction and and flatfielding, the fringing disappeared, resulting in CCD spectra flat to better than 0.5% and slit illumination uniform to better than 1%. No correction for dark current was applied, since it was always negligible. Hot pixels and cosmic ray events were removed with a $\kappa - \sigma$-clipping procedure. The wavelength calibration was performed using calibration lamps (HeAr, FeNe, FeAr) for the runs 1 and 3, and sky lines for the runs 2 and 4, where the calibration lamp exposures were too weak (run 2) or not enough calibration lines were present in the wavelength range (run 4). A third order polynomial was used to perform the calibration, achieving 0.1 Å rms precision. The spectra were rebinned to a logarithmic wavelength scale and the mean sky spectrum during each exposure was derived by averaging several lines from the edges of the CCD spectra. By applying the same procedure to the blank sky observations, the systematic sky residuals were measured to be less than 1%. After subtraction of the sky spectra, spectra of the same galaxy taken at identical slit positions were centred and added; one-dimensional spectra were produced for the calibration and spectrophotometric stars. The galaxy spectra were rebinned along the slit in order to guarantee a signal-to-noise ratio that allowed the derivation of the kinematic parameters. The calibration stars were set at zero redshift measuring the positions of the CaT lines.

Table B.1: The long-slit kinematics of NGC 1374

R(arcsec)	v (km/s)	dv (km/s)	σ (km/s)	dσ (km/s)	h_3	dh_3	h_4	dh_4
-15.161	-46.18	9.42	106.82	14.21	-0.087	0.069	0.045	0.067
-4.617	-50.65	3.14	134.27	4.11	-0.090	0.024	0.042	0.028
-1.759	-51.9	2.00	144.72	2.28	-0.003	0.010	0.001	0.016
-0.630	-28.74	2.23	171.29	3.00	-0.025	0.012	0.015	0.014
0.143	10.00	2.15	180.22	2.92	0.013	0.011	-0.013	0.009
1.042	40.45	1.95	168.26	3.22	0.041	0.012	0.016	0.012
2.658	49.13	2.49	146.97	2.89	0.054	0.012	0.033	0.017
7.292	42.56	2.70	139.42	3.63	0.050	0.027	-0.012	0.023
19.826	46.67	11.75	118.26	11.72	-0.036	0.121	-0.065	0.090

The galaxy kinematics was derived using the Fourier Correlation Quotient (FCQ) method (Bender, 1990). Following Bender et al. (1994), the line-of-sight-velocity-distributions (LOSVDs) were measured and fitted to provide the stellar rotational velocities v_{rot}, the velocity dispersions σ and the first orders of asymmetric (h_3) and symmetric (h_4) deviations of the LOSVDs from real Gaussian profiles. Monte Carlo simulations were performed to establish that a fourth order polynomial in the wavelength range $\approx 8250-8950$Å provided good continuum fits, resulting in systematic residuals always smaller than the estimated statistical errors. These were calibrated using a grid of input signal-to-noise ratios, taking into account the noise contributions of the galaxy and the sky signals. The systematic errors from template mismatch were smaller than usually found around the Mg region ($\lambda \approx 5150$Å). The errors from systematics in the sky subtraction (at the 1%, see above) were less than the statistical errors. Tables B.1 gives the resulting kinematics.

B.2 The VIRUS-W Kinematics of NGC 3091

The observations of NGC 3091 were carried out using commissioning time of the new VIRUS-W spectrograph (Fabricius et al., 2008) at 2.7 m Harlan J. Smith telescope at the McDonald Observatory in Texas.

VIRUS-W offers a fiber-based Integral Field Unit (IFU) with a Field of View (FoV) of 105 arcsec×75 arcsec. The 267 individual fibers have a core diameter of 3.14 arcsec on sky. The fibers are arranged in a rectangular matrix in a densepack scheme with a fill factor of 1/3, such that three dithered observations are necessary in order to achieve 100 % coverage of the FoV. The instrument offers further two different modes of spectral resolution. We used the lower resolution mode (R = 3300) with a spectral coverage of 4320 Å to 6042 Å.

In the night of December 5th 2010, we obtained dithered observations of two off-centred and slightly overlapping regions of NGC 3091. Fig. B.1 shows an HST F814W image with two boxes outlining the field positions.

The exposure time of the individual pointings was 600 s. We repeated each pointing once for cosmic ray rejection resulting in a total on-object integration time of 2 h. All

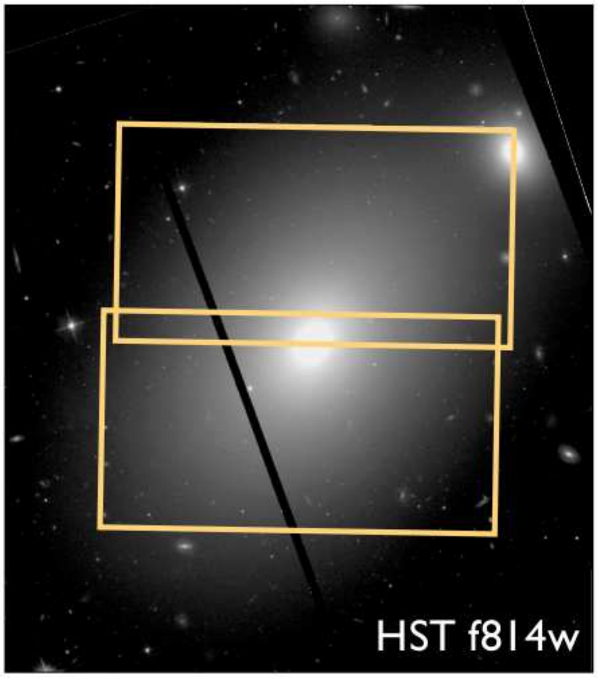

Figure B.1: HST ACS F814W image of NGC 3091. The boxes outline the FOV of our two different fields.

on-object observations were bracketed and interleaved with 300 s sky nods that were offset 9 arcmin to the north. The seeing varied from 2.0 to 2.2 arcsec which is small compared to the fiber size.

In addition to the galaxy, we also observed the two giant stars HR 7576 and HR 2600 which served as templates for the kinematic extraction.

We extracted the individual fiber spectra using the `cure` pipeline that was originally developed by Ralf Koehler, Niv Drory and Jan Snigula for the HETDEX experiment. The basic image reduction used the `fitstools` package (Gössl & Riffeser, 2002) and followed standard recipes of creation and subtraction of master bias frames and the averaging of flat fields and calibration lamp frames. `cure` traced the positions of the fiber spectra on the chip using the twilight or dome flat frames and then searched for the calibration lamp line positions along those traces. Trace and wavelength positions were modelled as a two-dimensional Chebyshev polynomial of 7-th degree across the CCD surface. The standard deviation of this wavelength/distortion solution is 0.2 pixel corresponding to 0.1 Å at the linear dispersion of 0.52 Å/pixel.

In the next step, `cure` calculated transformations between fiber number/wavelength and x/y positions and corresponding inverse and cross transformations. Given these models for fiber position and wavelength calibration, the fiber extraction walked along the trace positions across the CCD and extracts the spectra through bicubic interpolation at given wavelength steps. We used a 7 pixel wide extraction aperture around the centroid position of the individual fiber spectra. Tests showed that this resulted in less than 1 % loss of flux

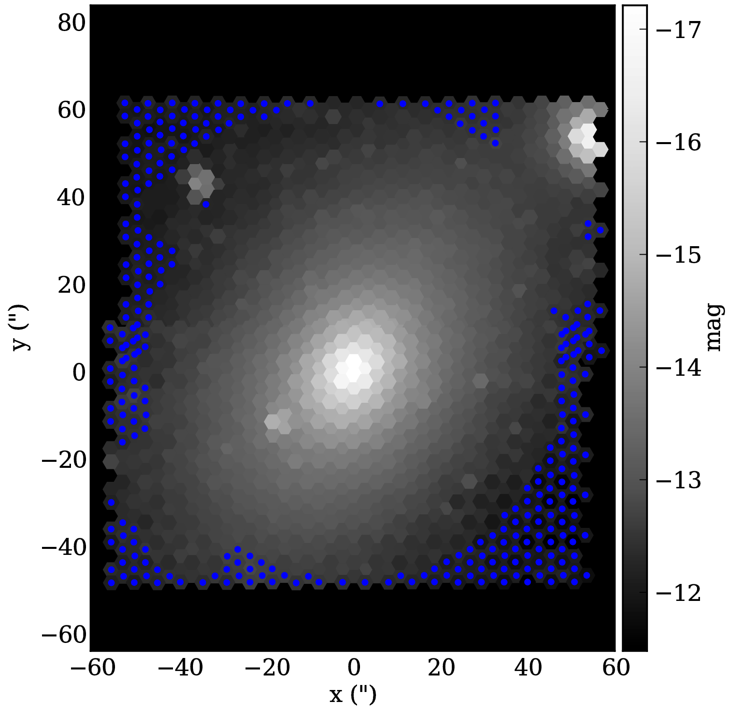

Figure B.2: Reconstructed image of NGC 3091. This image was obtained by collapsing the individual fiber spectra along the wavelength dimension. The fibers that are marked blue were used for sky subtraction.

and less than 0.1 % crosstalk between neighbouring spectra.

The extraction resulted in a total of $2 \times 3 \times 267 = 1062$ wavelength calibrated spectra, corresponding to the two fields with three dithers and 267 fiber apertures. The spectra were binned linearly in wavelength space.

We rejected the data from the sky nods. Preliminary kinematic maps showed unrealistic north-south gradients of the dispersion. We therefore identified fibers around the edges of the combined FoV. We selected them to be located further than 50 arcsec from the galaxy center and visually rejected fibers that fall on the neighbouring galaxy MCG -03-26-006. Fig. B.2 shows the positions of the sky fibres on a reconstructed image.

We averaged the skyfiber spectra for each dither position separately while rejecting spurious events using a standard, iterative $\kappa - \sigma$-clipping algorithm. The resulting average sky spectrum was subtracted from all the object spectra.

The modelling employed a radial binning scheme for the SINFONI data described in §4.3. We binned the VIRUS-W data following the same procedure. The binning step again rejected residual events. Before the $\kappa - \sigma$ clipping was applied, the spectra were first scaled according to their median flux across the covered spectral range. After identification of data that should be rejected, the scaling was then reverted before the final binning. Bins that were located inside a radius of 10 arcsec around the center were rejected because there the size of the fiber aperture was comparable or larger than the bin size of the radial binning scheme. The median signal to noise per Å in the used bins was 19.

After rebinning the spectra into log-wavelength space, we used the Fourier Correlation Quotient (FCQ) algorithm (FCQ; Bender, 1990; Bender et al., 1994) to extract the line-of-sight velocity distributions. Due to the deconvolution of the peak of the cross correlation function between galaxy spectrum and stellar template, FCQ was relatively insensitive to template mismatches. For this work, we used a single template of the K3III star HR 7576. We tested fits with the additional K2III star HR 2600 which yielded consistent results. We fitted the kinematics in the rest frame spectral range from 4537 Å to 5443 Å. The continuum was removed, using an 8th degree polynomial and the first and last three channels in the Fourier space were filtered out. We finally used Monte Carlo simulations as described in Mehlert et al. (2000) for the derivation of statistical errors.

Table B.2 provides the resulting kinematics for NGC 3091, using the SINFONI spatial binning scheme. The velocities v are given relative to the average velocity (3733 km/s).

B.3 The WiFeS Kinematics of NGC 5516

NGC 5516 was observed in May 2010 at the Australian National University 2.3m telescope at Siding Spring Observatory by Robert Sharp. The WiFeS Integral Field spectrograph was used (Dopita et al., 2007, 2010). The dual-beam system was used with the B3000 and R7000 VPH grating combination with Dichroic #3. For NGC 5516, 3x1200 sec exposures were taken on the 19 May 2010 plus a 1200 sec sky exposure. The data reduction was performed using the dedicated IRAF pipeline software of the instrument. We derived the stellar kinematics from the blue frames, focusing on the wavelength region $4900 - 5400$Å, where we achieved a spectroscopic resolution of $\sigma_{\rm inst} = 58$ km/s measured from the width of the sky lines. The stellar kinematics was measured with the software described in Saglia et al. (2010) and Fabricius et al. (2012). This used the FCQ method of Bender et al. (1994) in combination with a stellar library convolved to the instrumental resolution and can be applied iteratively to detect and subtract possible emission lines. However, no detectable emission was found. Table B.3 gives the resulting kinematics for NGC 5516. We give the kinematics along NS slits (with positive radii indicating distances in arcsec from the center of the galaxy towards the North and negative radii towards the South), shifted with respect to the center of the galaxy along the East (positive shifts in arcsec) or West (negative shifts) directions. The velocities v are given relative to the average velocity (4380 km/s).

Table B.2: The VIRUS-W kinematics of NGC 3091, binned the same way as the SINFONI data. R (in arcsec) is the radius of the midpoint of each bin: positive for positive values along the x-axis. (see the SINFONI kinematic map in Fig. 4.2). iv is the numbering for the angular bins (see Section 3.3.1). The midpoint angles for iv 1 to 5 are 5.8°, 17.6°, 30.2°, 45.0°and 71.6°. Positive and negative iv are for positive and negative y values. Velocity v and velocity dispersions σ with their uncertainties are stated in km/s.

R	iv	v	dv	σ	$d\sigma$	h_3	dh_3	h_4	dh_4
54.60	-1	137.88	25.21	229.67	32.28	-0.127	0.056	-0.003	0.039
32.75	-5	12.26	23.91	303.63	38.47	-0.012	0.041	-0.022	0.035
42.29	-5	176.27	64.11	262.68	70.99	0.223	0.091	-0.128	0.076
54.60	1	119.62	24.08	225.02	33.67	-0.154	0.056	0.013	0.047
19.61	4	60.80	9.87	293.11	11.17	0.062	0.019	-0.052	0.018
54.60	-2	158.83	41.25	259.31	64.09	-0.025	0.080	-0.024	0.062
15.16	-3	61.12	7.88	295.91	10.87	0.063	0.018	-0.002	0.018
42.29	2	-165.96	20.03	245.16	23.89	0.082	0.045	-0.048	0.033
25.35	-1	-123.40	17.88	305.57	18.58	0.016	0.029	-0.024	0.031
11.72	4	-27.94	9.89	262.14	12.67	0.070	0.020	0.033	0.023
15.16	-5	-23.37	7.91	280.58	9.72	0.033	0.017	-0.025	0.018
11.72	1	78.02	8.80	299.78	8.70	-0.010	0.017	-0.057	0.016
54.60	-3	-12.07	30.60	213.87	43.90	-0.037	0.072	-0.022	0.053
11.72	-4	-36.20	12.83	273.56	16.00	0.061	0.034	-0.021	0.026
19.61	-3	-66.47	16.40	311.73	16.56	0.087	0.031	-0.048	0.026
25.35	-4	-115.61	17.32	293.22	19.64	0.039	0.034	-0.055	0.027
32.75	-5	-8.43	30.24	323.64	35.80	0.088	0.043	0.034	0.035
42.29	3	83.20	36.10	326.33	35.84	-0.042	0.050	-0.035	0.048
32.75	-4	-73.51	24.76	296.99	32.75	0.095	0.043	-0.049	0.038
42.29	-3	40.60	31.73	301.21	40.51	0.114	0.053	-0.036	0.049
25.35	-1	148.50	13.58	293.86	22.36	0.008	0.027	0.042	0.030
19.61	-1	98.96	12.90	296.89	13.51	-0.018	0.023	-0.038	0.021
15.16	1	-95.56	9.65	308.40	12.57	0.031	0.020	0.003	0.020
25.35	-2	108.04	12.43	286.39	16.96	0.028	0.023	-0.034	0.023
42.29	-2	-151.67	42.38	364.75	94.78	0.125	0.070	0.192	0.072
42.29	3	-134.08	39.99	322.73	56.95	0.034	0.050	-0.034	0.053
32.75	2	-156.42	15.65	247.45	18.48	0.135	0.036	-0.039	0.026
11.72	1	-102.03	10.25	291.95	10.81	-0.005	0.020	-0.012	0.021
25.35	2	-119.47	12.36	287.87	14.36	0.064	0.030	-0.038	0.023
25.35	-5	-18.47	15.08	278.97	27.61	0.043	0.028	-0.004	0.038
19.61	3	-96.52	13.18	316.37	11.59	0.042	0.020	-0.112	0.015
11.72	-2	93.00	6.92	281.92	12.23	-0.001	0.016	0.037	0.018
11.72	3	-72.54	9.07	268.73	14.44	0.006	0.021	0.025	0.025

Table B.2: Continued.

R	iv	v	dv	σ	$d\sigma$	h_3	dh_3	h_4	dh_4
15.16	-2	99.25	7.52	281.85	8.19	-0.027	0.013	-0.029	0.016
19.61	5	30.49	9.17	251.34	8.83	-0.020	0.024	-0.051	0.018
32.75	5	-2.14	11.78	222.47	11.59	-0.035	0.034	-0.093	0.025
32.75	4	-71.33	17.36	263.07	22.35	0.036	0.042	-0.012	0.032
32.75	-2	-150.45	17.22	275.85	16.31	0.074	0.034	-0.125	0.022
11.72	-1	93.93	10.35	291.39	13.31	-0.012	0.023	0.008	0.022
15.16	5	5.22	6.82	259.35	9.05	-0.012	0.016	-0.002	0.017
15.16	4	56.04	7.84	254.71	9.66	-0.008	0.021	-0.035	0.017
11.72	-1	-81.37	10.21	285.14	12.63	0.048	0.019	0.024	0.020
42.29	-5	12.69	34.47	185.48	41.20	-0.110	0.093	0.014	0.064
25.35	-5	60.37	14.62	263.35	18.52	0.081	0.033	-0.032	0.030
15.16	-4	54.08	8.82	281.79	12.22	0.039	0.019	0.015	0.020
15.16	-1	107.26	7.42	262.15	8.30	0.021	0.018	-0.025	0.018
54.60	2	-166.21	35.29	227.32	45.29	-0.184	0.090	-0.035	0.069
15.16	2	-108.03	44.96	559.87	91.49	-0.089	0.046	0.220	0.060
32.75	3	-147.27	32.35	338.24	39.37	0.069	0.047	-0.044	0.038
25.35	3	92.03	9.74	252.18	13.37	-0.035	0.025	-0.019	0.023
32.75	-3	105.29	21.69	347.16	23.74	0.003	0.030	-0.029	0.026
32.75	-4	77.74	16.02	286.58	26.42	0.007	0.033	0.024	0.030
19.61	-4	-26.37	17.86	323.72	18.96	0.059	0.029	-0.055	0.022
25.35	-4	72.23	10.54	262.65	14.06	0.030	0.027	-0.008	0.024
25.35	5	-11.25	10.85	238.98	11.09	-0.032	0.025	-0.048	0.023
19.61	-4	63.98	11.33	306.12	11.97	0.009	0.022	-0.033	0.018
42.29	-4	-63.14	93.38	392.73	185.44	0.207	0.127	0.199	0.104
54.60	5	357.67	51.28	181.57	53.55	-0.157	0.125	-0.128	0.085
42.29	-3	-156.03	20.43	235.67	18.02	0.130	0.045	-0.059	0.032
19.61	2	115.01	11.30	269.66	13.62	0.013	0.026	-0.029	0.024
25.35	4	-63.43	25.66	348.72	42.20	0.058	0.039	0.018	0.040
11.72	-3	47.32	8.64	291.91	10.72	-0.009	0.016	-0.031	0.019
32.75	5	-64.11	11.56	228.80	13.75	-0.038	0.028	-0.082	0.021
19.61	1	144.14	13.66	285.30	17.18	0.006	0.024	-0.014	0.025
42.29	4	-104.06	28.36	240.05	37.39	0.143	0.063	-0.086	0.051
15.16	-4	-72.29	18.74	323.30	19.56	-0.011	0.026	-0.043	0.024
11.72	-3	-77.51	12.35	289.03	14.29	-0.028	0.022	0.002	0.024
25.35	-3	-94.16	14.87	288.03	18.81	0.035	0.029	-0.007	0.031
11.72	-4	64.76	7.68	280.07	9.71	0.056	0.018	-0.008	0.016
42.29	-4	13.30	18.37	249.39	22.34	0.028	0.043	-0.084	0.029
15.16	-3	-59.78	11.36	284.84	15.82	0.020	0.023	-0.033	0.025

Table B.2: Continued.

R	iv	v	dv	σ	$d\sigma$	h_3	dh_3	h_4	dh_4
32.75	-1	94.85	17.33	317.90	23.54	-0.026	0.030	-0.003	0.030
25.35	3	-125.76	13.03	274.49	12.27	0.061	0.028	-0.082	0.024
15.16	5	-12.29	6.29	246.61	7.33	0.040	0.016	-0.004	0.017
32.75	1	95.03	17.57	297.24	17.24	0.076	0.029	-0.059	0.023
19.61	-3	65.87	8.41	301.62	9.03	0.027	0.017	-0.042	0.015
42.29	-2	113.12	25.82	290.59	55.13	-0.041	0.053	0.012	0.056
19.61	3	82.88	7.87	249.24	8.44	-0.009	0.019	-0.064	0.017
11.72	5	32.49	5.41	287.33	6.93	0.049	0.011	0.006	0.014
42.29	5	-136.51	22.41	187.37	23.20	-0.045	0.061	-0.090	0.044
15.16	-1	-104.24	8.63	261.45	11.17	0.015	0.019	-0.024	0.018
32.75	2	137.13	18.09	281.37	18.79	0.019	0.033	-0.025	0.029
11.72	5	-8.54	6.16	264.19	10.65	0.000	0.016	0.037	0.019
15.16	-5	41.46	9.51	276.56	10.15	0.078	0.020	-0.019	0.021
19.61	5	-21.15	6.91	244.13	7.40	0.034	0.019	-0.028	0.016
42.29	4	-19.36	37.06	288.03	45.59	-0.021	0.070	-0.032	0.052
32.75	4	56.26	18.42	275.64	24.49	-0.023	0.034	-0.024	0.032
32.75	-2	97.93	19.92	344.13	24.73	0.002	0.033	-0.055	0.025
32.75	-1	-106.92	16.74	268.09	20.50	0.099	0.038	-0.037	0.031
15.16	3	56.44	13.14	272.17	16.24	-0.025	0.027	-0.019	0.024
15.16	1	91.92	8.54	301.28	11.96	-0.044	0.019	0.005	0.021
25.35	4	42.32	15.26	274.63	16.01	-0.079	0.028	-0.026	0.023
54.60	1	-208.24	24.80	235.82	37.96	-0.015	0.063	-0.023	0.060
11.72	-2	-71.26	11.31	282.50	15.10	-0.056	0.027	-0.020	0.027
15.16	3	-26.98	13.22	306.33	18.40	0.043	0.022	-0.005	0.027
19.61	-5	-3.78	8.64	242.67	9.49	0.002	0.024	-0.070	0.018
25.35	5	-24.69	8.63	271.21	11.56	-0.013	0.025	-0.042	0.018
11.72	3	97.18	12.05	305.27	13.24	0.042	0.019	-0.013	0.021
25.35	-2	-122.43	15.03	272.30	17.25	0.011	0.032	-0.008	0.030
25.35	2	100.39	10.09	245.31	13.97	-0.011	0.026	0.012	0.022
42.29	1	154.39	17.00	278.19	19.43	0.017	0.032	-0.054	0.024
11.72	-5	26.17	8.43	287.48	12.83	0.057	0.019	0.034	0.022
11.72	-5	-26.69	8.49	270.40	10.17	0.046	0.021	-0.007	0.022
19.61	-2	-118.79	13.41	286.81	21.85	0.043	0.029	0.032	0.032
32.75	1	-142.23	20.66	313.46	21.74	0.041	0.036	-0.045	0.031
11.72	2	74.02	5.95	283.19	7.00	-0.009	0.015	-0.002	0.015
19.61	-1	-96.31	18.91	320.77	21.69	0.031	0.035	-0.028	0.026
32.75	3	77.81	15.86	264.23	16.95	0.036	0.032	-0.071	0.024
42.29	-1	-150.63	18.92	272.33	25.56	0.043	0.037	-0.008	0.031

Table B.2: Continued.

R	iv	v	dv	σ	$d\sigma$	h_3	dh_3	h_4	dh_4
15.16	-2	-120.61	12.43	310.72	14.34	0.082	0.026	-0.015	0.020
19.61	-2	112.76	11.92	301.13	14.84	-0.027	0.023	-0.026	0.020
42.29	1	-207.45	15.69	221.72	21.44	0.004	0.044	-0.086	0.031
19.61	1	-124.68	12.73	282.91	15.70	0.028	0.026	-0.006	0.026
15.16	2	113.87	9.54	299.85	14.04	-0.004	0.019	0.008	0.021
11.72	2	-45.24	13.36	286.77	13.34	0.044	0.028	-0.061	0.022
25.35	1	137.85	9.80	249.81	13.49	-0.010	0.023	-0.036	0.021
19.61	-5	16.48	14.33	301.36	18.55	0.125	0.024	0.007	0.025
42.29	2	115.98	23.44	268.17	35.54	0.066	0.044	-0.005	0.046
11.72	4	40.96	6.49	287.86	7.34	0.019	0.015	-0.026	0.014
42.29	-1	128.73	20.09	284.81	26.50	-0.015	0.043	-0.023	0.037
25.35	-3	76.27	10.64	306.02	11.92	0.010	0.022	-0.059	0.018
25.35	1	-109.42	19.15	295.20	22.59	0.069	0.036	-0.030	0.025
15.16	4	-57.75	8.55	246.29	9.88	0.002	0.022	0.007	0.019
19.61	4	-77.37	14.01	319.92	15.49	0.045	0.025	-0.064	0.020
32.75	-3	-114.11	16.80	250.27	15.67	-0.066	0.038	-0.055	0.025

Table B.3: The WiFeS kinematics of NGC 5516. North is positive R and east is positive EW shift. Both R and EW shift are in arcsec. Velocity v and velocity dispersions σ with their uncertainties are stated in km/s.

R	EW shift	v	dv	σ	$d\sigma$	h_3	dh_3	h_4	dh_4
-8.0	0.0	-71.74	107.70	480.75	163.97	-0.149	0.204	0.115	0.204
-7.0	2.0	26.47	59.02	302.55	85.49	0.009	0.177	0.090	0.177
-7.0	1.0	288.60	100.49	509.38	73.97	0.187	0.179	-0.151	0.179
-7.0	0.0	0.73	51.92	264.32	39.53	-0.011	0.179	-0.142	0.179
-7.0	-1.0	30.08	64.43	325.83	70.93	0.095	0.180	-0.027	0.180
-7.0	-2.0	53.73	54.29	346.76	71.09	-0.034	0.142	0.043	0.142
-6.0	3.0	12.13	90.23	461.64	143.58	-0.065	0.178	0.139	0.178
-6.0	2.0	66.67	74.85	441.69	132.69	0.007	0.154	0.303	0.154
-6.0	1.0	53.52	41.64	290.76	41.62	-0.053	0.130	-0.062	0.130
-6.0	0.0	70.07	44.27	327.79	49.52	0.060	0.123	-0.021	0.123
-6.0	-1.0	48.19	29.68	242.08	28.43	-0.032	0.111	-0.076	0.111
-6.0	-2.0	52.23	60.78	482.13	64.78	0.045	0.115	-0.039	0.115
-6.0	-3.0	10.10	65.17	373.09	76.84	0.033	0.159	-0.001	0.159
-6.0	-4.0	44.16	57.13	331.90	57.88	0.027	0.156	-0.057	0.156
-6.0	-5.0	40.87	94.19	509.47	65.92	0.022	0.168	-0.163	0.168
-5.0	5.0	-45.05	73.78	384.48	110.29	0.078	0.174	0.106	0.174
-5.0	4.0	62.42	58.34	291.57	63.37	0.070	0.182	-0.032	0.182
-5.0	3.0	-7.38	42.33	291.92	44.65	-0.060	0.132	-0.043	0.132
-5.0	2.0	134.57	69.73	451.94	112.05	0.136	0.140	0.144	0.140
-5.0	1.0	70.82	36.98	319.39	25.42	-0.078	0.105	-0.167	0.105
-5.0	0.0	27.04	34.93	299.86	40.06	0.006	0.106	-0.012	0.106
-5.0	-1.0	63.88	29.72	308.21	35.26	-0.004	0.088	0.002	0.088
-5.0	-2.0	105.88	34.00	362.81	37.58	-0.059	0.085	-0.026	0.085
-5.0	-3.0	195.19	56.93	458.88	74.70	0.088	0.113	0.044	0.113
-5.0	-4.0	47.05	44.96	389.65	51.39	0.022	0.105	-0.013	0.105
-5.0	-5.0	80.04	44.59	271.49	51.03	0.060	0.149	-0.013	0.149
-4.0	5.0	-46.62	61.80	341.52	63.73	-0.012	0.164	-0.051	0.164
-4.0	4.0	20.32	52.27	351.23	56.61	-0.025	0.135	-0.033	0.135
-4.0	3.0	97.23	42.20	324.86	43.39	0.016	0.118	-0.052	0.118
-4.0	2.0	130.82	34.71	281.56	39.14	0.161	0.112	-0.018	0.112
-4.0	1.0	48.44	32.96	318.39	33.93	-0.016	0.094	-0.052	0.094
-4.0	0.0	63.85	26.96	299.36	30.82	-0.057	0.082	-0.013	0.082
-4.0	-1.0	17.96	26.59	369.31	24.77	-0.023	0.065	-0.085	0.065
-4.0	-2.0	42.01	30.17	354.59	42.58	-0.056	0.077	0.078	0.077
-4.0	-3.0	75.86	33.75	294.30	36.85	-0.009	0.104	-0.030	0.104

Table B.3: Continued.

R	EW shift	v	dv	σ	$d\sigma$	h_3	dh_3	h_4	dh_4
-4.0	-4.0	13.21	28.62	297.18	31.93	-0.034	0.088	-0.022	0.088
-4.0	-5.0	7.63	31.37	222.77	30.64	-0.016	0.128	-0.069	0.128
-4.0	-6.0	-13.17	52.59	317.02	67.72	0.041	0.151	0.036	0.151
-3.0	5.0	-35.61	48.04	301.53	51.17	-0.023	0.145	-0.040	0.145
-3.0	4.0	-23.17	30.43	280.74	34.63	-0.001	0.099	-0.015	0.099
-3.0	3.0	59.42	27.43	273.58	26.61	-0.020	0.091	-0.072	0.091
-3.0	2.0	44.58	26.92	291.25	23.26	0.026	0.084	-0.107	0.084
-3.0	1.0	-53.48	27.32	289.50	34.18	-0.132	0.086	0.023	0.086
-3.0	0.0	28.90	22.74	298.34	22.59	-0.047	0.069	-0.064	0.069
-3.0	-1.0	-13.31	23.76	314.40	24.55	-0.027	0.069	-0.050	0.069
-3.0	-2.0	37.47	17.14	271.72	18.73	0.051	0.057	-0.030	0.057
-3.0	-3.0	108.02	54.50	439.79	39.82	0.077	0.113	-0.153	0.113
-3.0	-4.0	32.90	24.46	296.11	27.16	0.019	0.075	-0.024	0.075
-3.0	-5.0	61.95	42.61	396.11	49.19	0.047	0.098	-0.009	0.098
-3.0	-6.0	-6.91	46.49	316.26	44.67	-0.069	0.134	-0.075	0.134
-2.0	5.0	7.74	56.34	338.38	61.13	0.084	0.151	-0.033	0.151
-2.0	4.0	64.56	27.83	270.77	36.25	0.003	0.093	0.041	0.093
-2.0	3.0	-19.96	33.83	301.73	28.44	-0.040	0.102	-0.115	0.102
-2.0	2.0	20.25	20.76	367.35	24.60	-0.021	0.051	0.001	0.051
-2.0	1.0	23.04	20.01	373.29	20.74	0.022	0.049	-0.049	0.049
-2.0	0.0	11.35	12.14	317.85	13.56	-0.031	0.035	-0.022	0.035
-2.0	-1.0	-17.38	24.01	261.82	18.05	0.078	0.083	-0.146	0.083
-2.0	-2.0	8.99	15.29	326.83	17.65	0.002	0.043	-0.009	0.043
-2.0	-3.0	64.53	36.44	374.28	32.34	0.005	0.089	-0.100	0.089
-2.0	-4.0	12.99	25.30	302.34	25.37	-0.043	0.076	-0.061	0.076
-2.0	-5.0	11.88	32.36	366.27	37.75	0.016	0.080	-0.005	0.080
-2.0	-6.0	-10.09	38.57	301.42	48.31	-0.023	0.116	0.024	0.116
-2.0	-7.0	-40.36	65.81	330.34	73.97	0.002	0.181	-0.020	0.181
-1.0	5.0	8.20	44.35	361.79	46.03	0.038	0.111	-0.049	0.111
-1.0	4.0	41.48	28.57	314.93	40.03	-0.045	0.082	0.074	0.082
-1.0	3.0	16.64	19.27	286.52	21.46	-0.049	0.061	-0.023	0.061
-1.0	2.0	15.03	15.54	307.72	16.86	-0.018	0.046	-0.033	0.046
-1.0	-2.0	-3.05	13.01	281.84	14.79	0.091	0.042	-0.015	0.042
-1.0	-3.0	21.39	19.56	326.24	22.29	0.014	0.055	-0.014	0.055
-1.0	-4.0	25.86	31.91	285.57	30.45	0.022	0.102	-0.077	0.102
-1.0	-5.0	47.87	25.53	276.47	26.19	0.010	0.084	-0.053	0.084
-1.0	-6.0	3.77	37.89	311.38	67.17	0.000	0.111	0.298	0.111
-1.0	-7.0	4.34	63.38	371.36	56.50	0.057	0.155	-0.098	0.155

Table B.3: Continued.

R	EW shift	v	dv	σ	$d\sigma$	h_3	dh_3	h_4	dh_4
0.0	7.0	-59.81	52.33	284.10	54.44	-0.044	0.167	-0.048	0.167
0.0	6.0	-65.31	44.20	336.44	43.53	0.032	0.119	-0.067	0.119
0.0	5.0	-38.97	36.20	338.07	41.29	-0.022	0.097	-0.014	0.097
0.0	4.0	31.50	24.30	323.00	29.32	0.057	0.068	0.008	0.068
0.0	3.0	-8.84	21.91	319.52	21.97	0.071	0.062	-0.061	0.062
0.0	2.0	9.96	12.23	296.84	14.87	0.065	0.037	0.012	0.037
0.0	-2.0	16.07	11.30	290.12	13.46	-0.014	0.035	0.003	0.035
0.0	-3.0	2.45	21.92	319.17	20.44	0.010	0.062	-0.084	0.062
0.0	-4.0	24.00	23.77	321.56	27.56	-0.036	0.067	-0.008	0.067
0.0	-5.0	32.86	26.82	302.21	32.64	0.023	0.081	0.012	0.081
0.0	-6.0	50.27	35.59	308.10	41.08	-0.031	0.105	-0.009	0.105
0.0	-7.0	12.13	53.40	306.30	54.50	0.006	0.158	-0.055	0.158
1.0	6.0	-47.12	34.89	265.79	32.53	0.091	0.119	-0.084	0.119
1.0	5.0	48.66	31.19	322.47	37.87	-0.100	0.088	0.011	0.088
1.0	4.0	16.21	24.29	298.29	28.12	-0.056	0.074	-0.008	0.074
1.0	3.0	-12.31	50.39	512.42	76.64	-0.020	0.089	0.115	0.089
1.0	2.0	-9.59	13.14	300.37	14.15	0.008	0.040	-0.036	0.040
1.0	-2.0	7.38	11.84	316.42	13.72	-0.011	0.034	-0.008	0.034
1.0	-3.0	-9.20	17.72	338.69	21.86	-0.024	0.048	0.018	0.048
1.0	-4.0	45.84	20.41	314.21	25.28	0.033	0.059	0.019	0.059
1.0	-5.0	-6.59	26.32	316.97	26.14	0.020	0.075	-0.064	0.075
1.0	-6.0	-19.31	37.71	308.67	45.63	-0.095	0.111	0.010	0.111
1.0	-7.0	-8.52	43.55	263.68	42.34	-0.033	0.150	-0.071	0.150
2.0	6.0	-1.95	47.80	357.23	68.27	0.033	0.122	0.083	0.122
2.0	5.0	15.74	58.54	419.77	47.02	-0.034	0.127	-0.128	0.127
2.0	4.0	18.17	26.56	327.25	23.52	-0.017	0.074	-0.100	0.074
2.0	3.0	-47.76	34.71	323.31	43.85	-0.009	0.098	0.028	0.098
2.0	2.0	-9.20	16.37	303.49	19.56	-0.019	0.049	0.004	0.049
2.0	1.0	-7.09	26.96	368.06	35.15	0.049	0.067	0.041	0.067
2.0	0.0	-7.09	17.07	300.42	16.30	0.001	0.052	-0.077	0.052
2.0	-1.0	6.99	9.52	307.81	11.49	0.009	0.028	0.009	0.028
2.0	-2.0	-14.42	11.37	294.28	13.07	-0.012	0.035	-0.011	0.035
2.0	-3.0	-21.92	17.47	299.51	18.58	-0.009	0.053	-0.040	0.053
2.0	-4.0	24.82	26.06	327.97	27.11	0.007	0.072	-0.048	0.072
2.0	-5.0	51.77	29.79	299.85	32.80	0.026	0.090	-0.027	0.090
2.0	-6.0	-26.46	29.34	208.18	31.55	-0.101	0.128	-0.036	0.128
2.0	-7.0	-9.38	55.38	331.11	55.57	-0.060	0.152	-0.060	0.152
3.0	7.0	-31.57	82.13	433.35	78.40	-0.172	0.172	-0.077	0.172

Table B.3: Continued.

R	EW shift	v	dv	σ	$d\sigma$	h_3	dh_3	h_4	dh_4
3.0	6.0	-36.43	44.09	301.01	44.95	-0.008	0.133	-0.055	0.133
3.0	5.0	70.50	38.47	342.15	34.16	0.036	0.102	-0.100	0.102
3.0	4.0	-32.93	38.14	410.57	35.69	0.012	0.084	-0.083	0.084
3.0	3.0	-19.35	27.91	319.71	32.71	-0.019	0.079	-0.003	0.079
3.0	2.0	-31.79	19.59	299.82	24.30	-0.010	0.059	0.020	0.059
3.0	1.0	-30.07	20.84	333.27	23.95	-0.043	0.057	-0.011	0.057
3.0	0.0	-11.31	14.28	284.46	17.11	0.035	0.046	0.006	0.046
3.0	-1.0	-35.65	14.08	323.63	16.05	-0.003	0.040	-0.014	0.040
3.0	-2.0	-18.39	20.44	335.40	21.85	-0.058	0.055	-0.038	0.055
3.0	-3.0	-7.23	20.16	307.50	25.72	0.044	0.060	0.032	0.060
3.0	-4.0	-3.38	29.47	314.67	36.75	-0.032	0.085	0.022	0.085
3.0	-5.0	11.17	38.45	316.47	40.75	-0.004	0.110	-0.041	0.110
3.0	-6.0	-4.88	72.18	430.07	70.52	0.023	0.153	-0.069	0.153
3.0	-7.0	-50.94	57.19	294.51	57.83	-0.065	0.177	-0.058	0.177
4.0	7.0	-34.54	97.02	451.39	80.40	-0.012	0.195	-0.120	0.195
4.0	5.0	-43.22	28.11	237.95	32.31	-0.006	0.107	-0.011	0.107
4.0	4.0	-47.58	29.84	306.33	34.87	0.060	0.089	-0.005	0.089
4.0	3.0	-40.15	26.57	283.53	30.90	0.045	0.085	-0.006	0.085
4.0	2.0	-49.33	24.73	334.38	29.56	-0.028	0.067	0.005	0.067
4.0	1.0	-35.40	24.87	311.49	24.99	0.004	0.073	-0.060	0.073
4.0	0.0	-27.14	20.85	307.58	20.71	0.002	0.062	-0.064	0.062
4.0	-1.0	-66.92	15.26	280.02	16.12	0.012	0.050	-0.043	0.050
4.0	-2.0	-65.70	25.69	325.34	26.45	-0.046	0.072	-0.052	0.072
4.0	-3.0	4.77	24.80	295.31	26.99	0.049	0.076	-0.032	0.076
4.0	-4.0	-14.06	28.33	287.44	37.10	-0.031	0.090	0.043	0.090
4.0	-5.0	16.35	46.33	332.34	47.33	0.057	0.127	-0.054	0.127
4.0	-6.0	23.96	57.32	335.25	42.39	-0.004	0.155	-0.150	0.155
5.0	5.0	-130.25	53.51	343.68	68.52	-0.032	0.142	0.033	0.142
5.0	4.0	-51.48	29.81	250.46	31.25	0.079	0.108	-0.045	0.108
5.0	3.0	-22.85	35.71	357.78	35.15	0.046	0.091	-0.067	0.091
5.0	2.0	-42.22	32.80	354.92	37.31	0.044	0.084	-0.015	0.084
5.0	1.0	-40.22	22.65	251.46	26.16	-0.034	0.082	-0.009	0.082
5.0	0.0	-54.91	31.66	358.28	41.93	-0.013	0.080	0.048	0.080
5.0	-1.0	-19.89	20.11	284.07	23.83	0.065	0.064	0.001	0.064
5.0	-2.0	-63.95	32.35	366.87	43.67	-0.027	0.080	0.057	0.080
5.0	-3.0	-13.13	34.47	311.12	39.94	0.088	0.101	-0.008	0.101
5.0	-4.0	-44.51	30.11	258.65	33.67	-0.072	0.106	-0.022	0.106
5.0	-5.0	-23.39	54.85	351.56	54.95	-0.030	0.142	-0.061	0.142

Table B.3: Continued.

R	EW shift	v	dv	σ	$d\sigma$	h_3	dh_3	h_4	dh_4
5.0	-6.0	-10.81	72.42	333.38	75.72	0.005	0.197	-0.046	0.197
6.0	6.0	-191.36	36.86	171.00	65.34	0.304	0.196	0.226	0.196
6.0	5.0	-80.25	39.85	239.32	35.62	0.073	0.151	-0.097	0.151
6.0	4.0	-83.75	55.06	364.01	64.35	-0.004	0.137	-0.004	0.137
6.0	3.0	-10.34	34.74	307.49	39.35	0.037	0.103	-0.017	0.103
6.0	2.0	10.24	36.56	395.35	58.03	0.022	0.084	0.137	0.084
6.0	-2.0	-5.31	31.64	322.09	42.64	0.012	0.089	0.056	0.089
6.0	-3.0	-1.09	53.22	401.40	91.51	0.118	0.121	0.182	0.121
6.0	-4.0	-32.29	41.97	312.09	35.96	0.106	0.122	-0.110	0.122
7.0	5.0	-54.41	61.05	300.32	73.64	0.034	0.185	0.008	0.185
7.0	4.0	-22.17	66.28	412.84	72.59	-0.055	0.146	-0.029	0.146
7.0	3.0	-20.21	37.57	284.67	37.52	-0.067	0.120	-0.062	0.120
7.0	2.0	-19.31	47.73	481.14	84.61	0.138	0.090	0.212	0.090
7.0	-2.0	13.71	17.51	146.00	17.05	-0.033	0.109	-0.070	0.109
7.0	-3.0	-6.98	56.11	342.27	67.52	0.060	0.149	0.007	0.149
7.0	-4.0	7.13	58.45	299.08	54.74	-0.030	0.178	-0.083	0.178
8.0	4.0	-47.08	54.77	273.92	57.09	0.062	0.182	-0.047	0.182
8.0	3.0	-5.06	47.20	254.79	37.68	0.200	0.168	-0.130	0.168
8.0	-2.0	-174.74	71.30	503.53	81.83	0.089	0.129	-0.012	0.129
8.0	-3.0	13.35	82.84	400.36	66.92	0.143	0.188	-0.127	0.188
9.0	2.0	-115.20	31.96	179.86	35.35	0.058	0.162	-0.026	0.162
9.0	-1.0	-50.87	23.86	187.07	32.93	0.024	0.116	0.067	0.116
9.0	-2.0	95.08	75.66	341.39	62.12	0.025	0.201	-0.122	0.201

Appendix C

Kinematic fits of the best-fit models

We show the kinematic fit of the best-fit model with DM to the data. The kinematic data are represented by the Gauss-Hermite moments up to h_4. For each galaxy, the SINFONI averaged kinematics is plotted in five columns, corresponding to the five angular bins. The leftmost column is for the major axis and the rightmost column for the minor axis. The complementary kinematic data that are used in the modelling are also shown with the model fit. The details of these data can be found in Section 4.3.2. The diamonds are the datapoints and the lines represent the model (not always plotted in the same color as the diamonds).

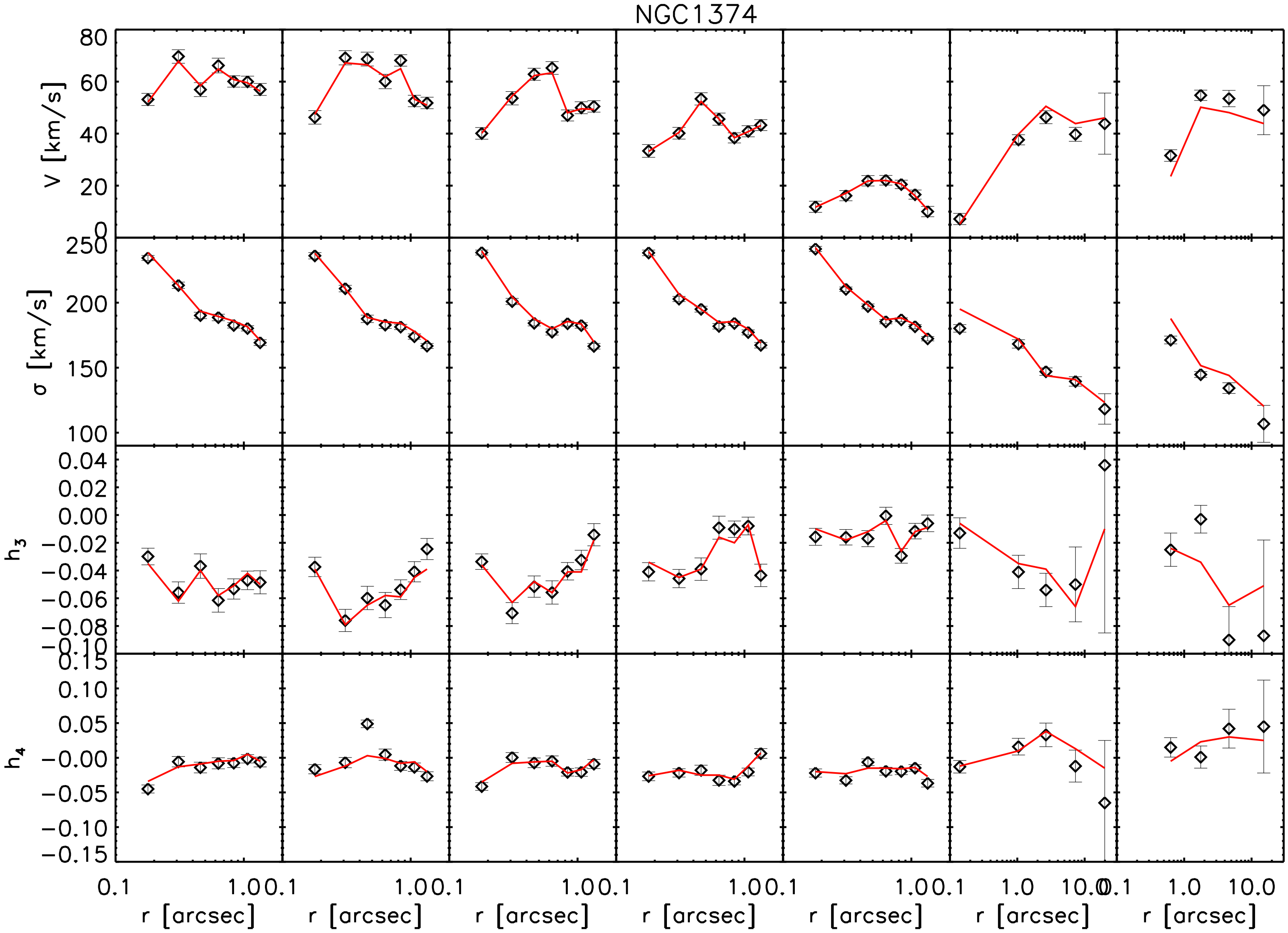

Figure C.1: Kinematic data (black diamonds) and the best-fit model (red lines) of NGC 1374. The first to fifth columns are for SINFONI data with increasing angle from major towards minor axis. The 6th and the 7th columns show both sides of the slit data along the major axis.

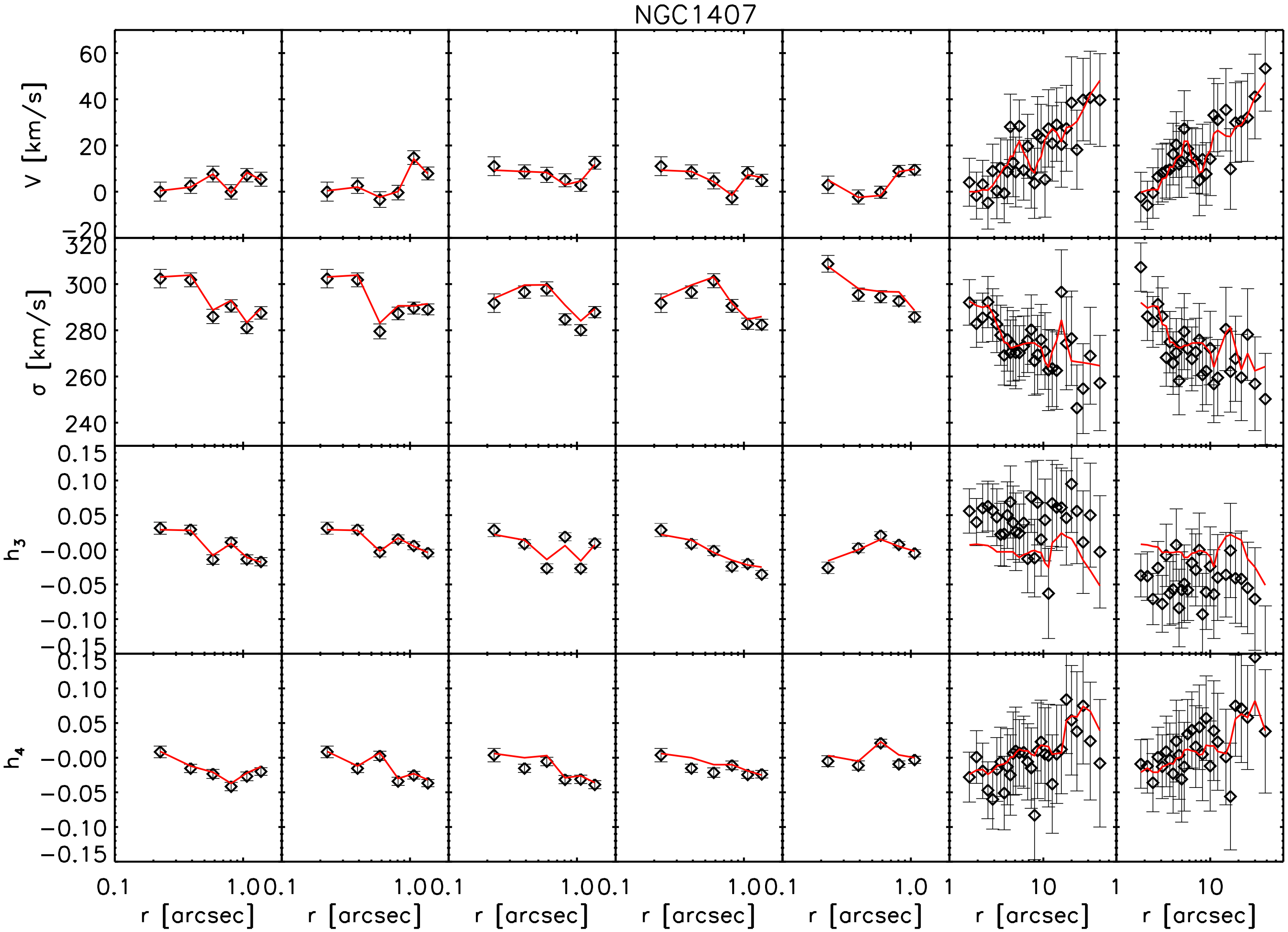

Figure C.2: Kinematic data (black diamonds) and the best-fit model (red lines) of NGC 1407. The first to fifth columns are for SINFONI data with increasing angle from major towards minor axis. The 6th and the 7th columns display both sides of the slit data shown in Spolaor et al. (2008a) along the major axis.

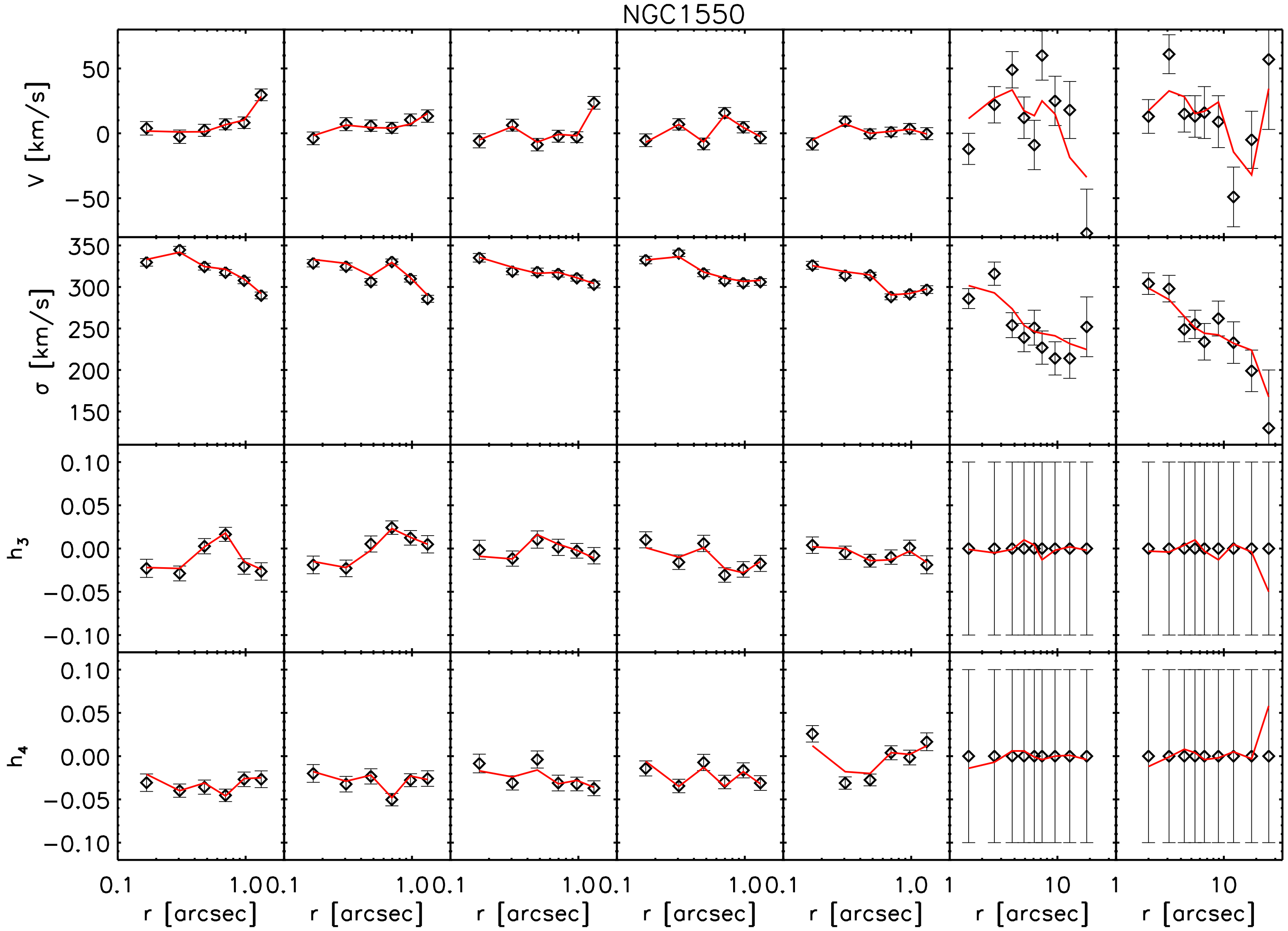

Figure C.3: Kinematic data (black diamonds) and the best-fit model (red lines) of NGC 1550. The first to fifth columns are for SINFONI data with increasing angle from major towards minor axis. The 6th and the 7th columns display both sides of the slit data from Simien & Prugniel (2000) along the major axis.

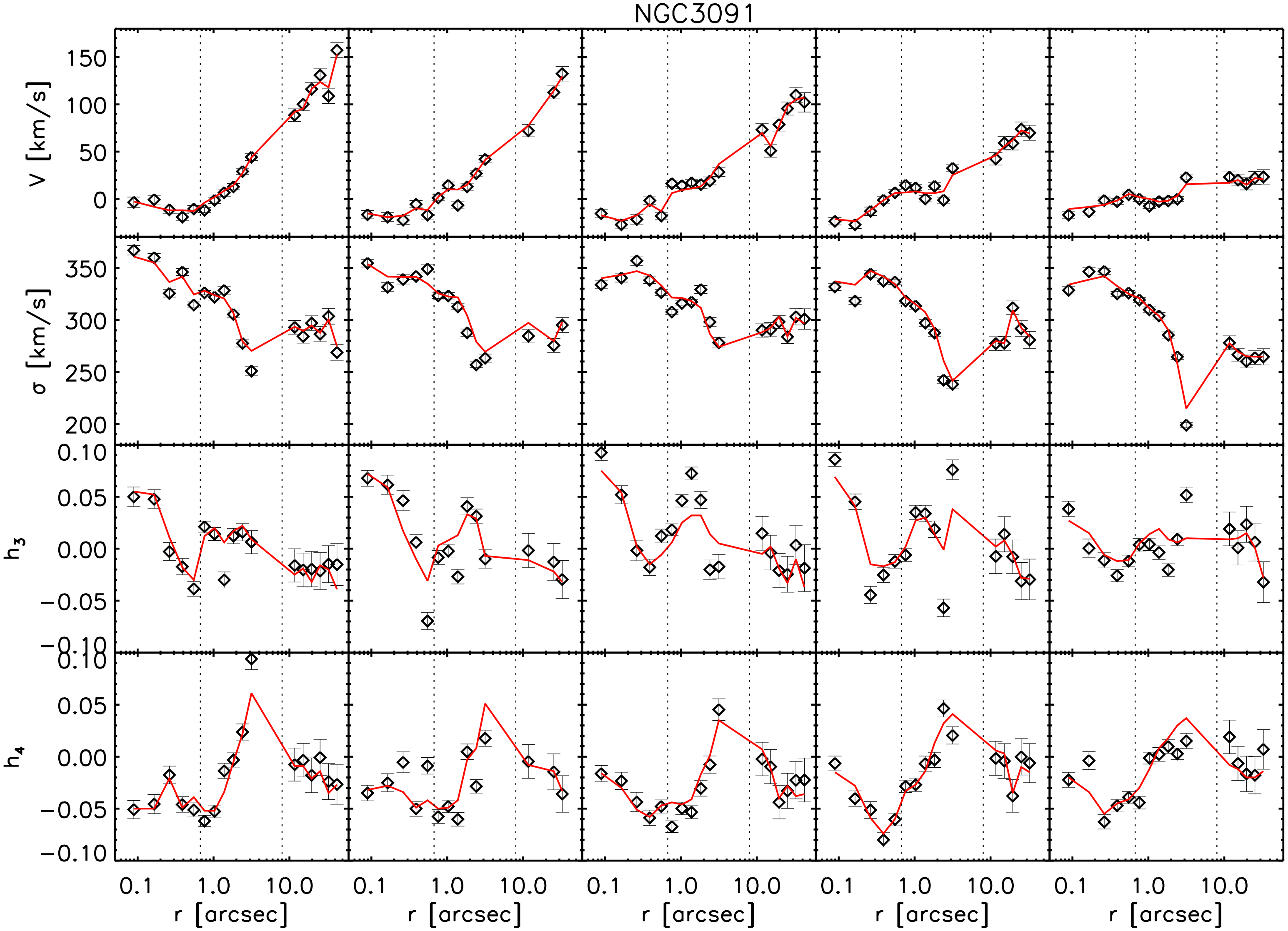

Figure C.4: Kinematic data (black diamonds) and the best-fit model (red lines) of NGC 3091. The first to fifth columns display data with increasing angle from major towards minor axis. The dotted vertical lines mark the region covered by SINFONI 100 mas data (leftmost), SINFONI 250mas data (middle) and VIRUS-W data (rightmost).

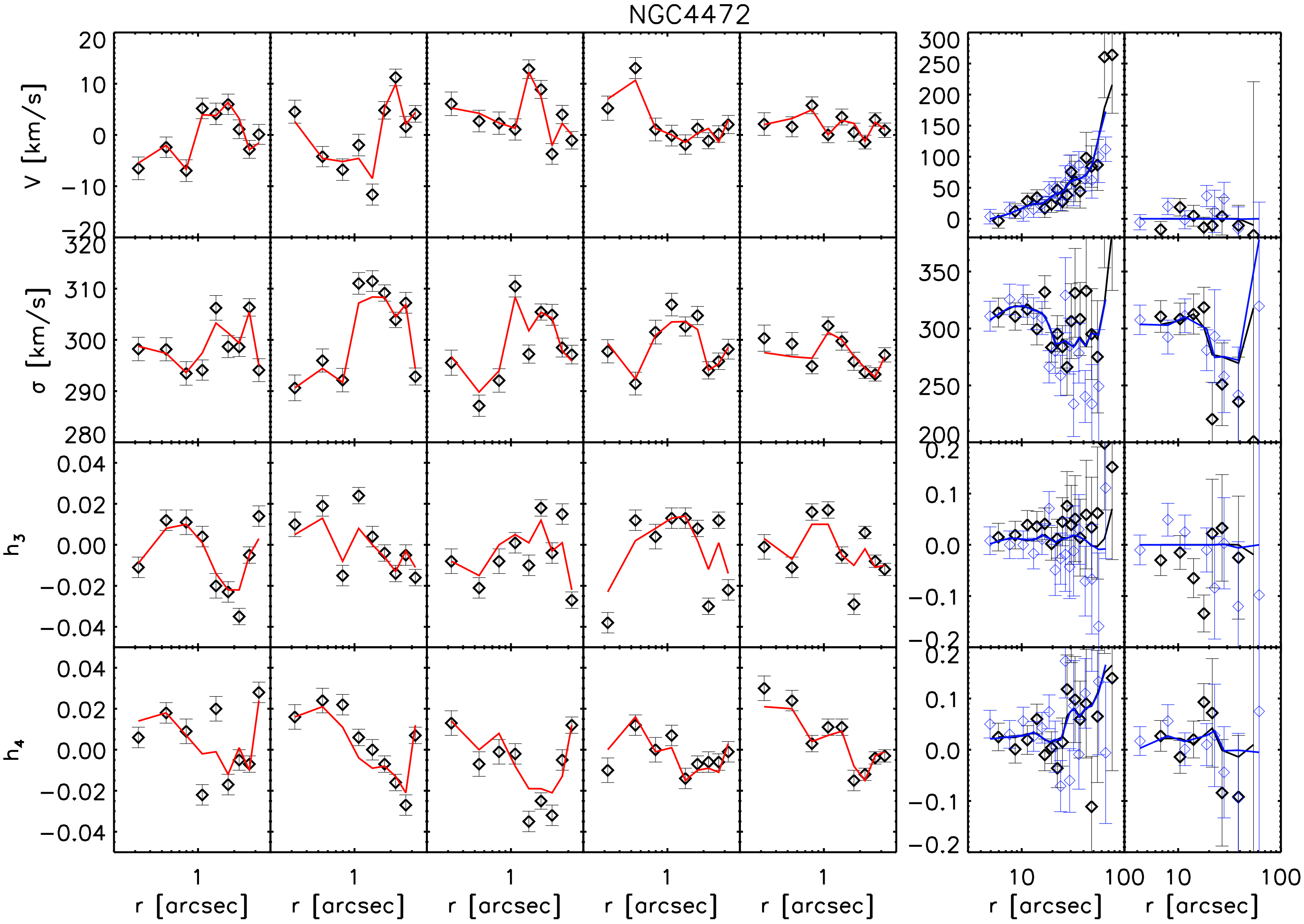

Figure C.5: Kinematic data (diamonds) and the best-fit model (lines) of NGC 4472. The first to fifth columns display SINFONI data with increasing angle from major towards minor axis. The 6th column shows both sides of the major axis data from Bender et al. (1994). The 7th column show both sides of minor axis data from the same paper. The different colors represent data from different sides.

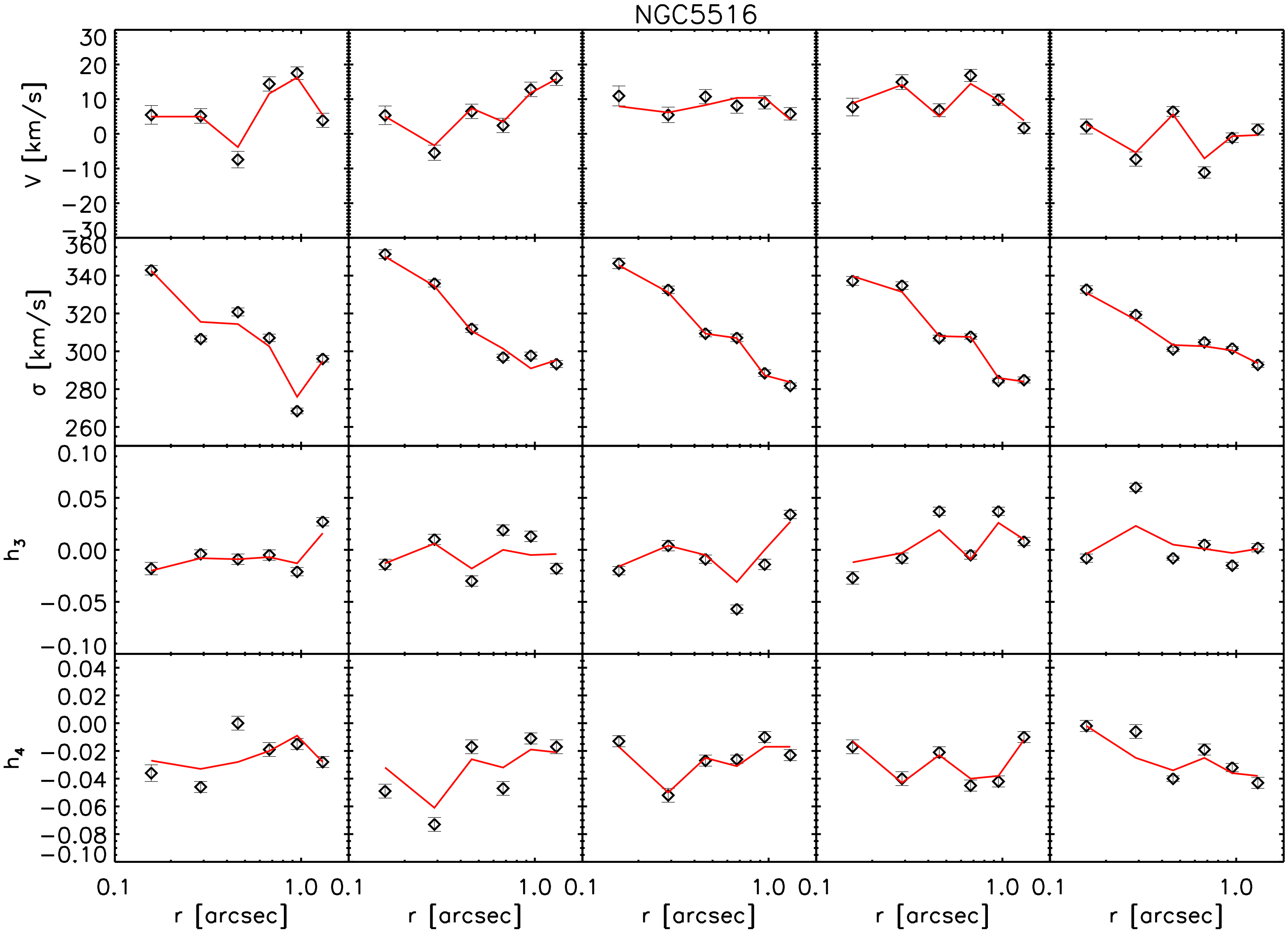

Figure C.6: SINFONI kinematic data (black diamonds) and the best-fit model (red lines) of NGC 5516. The first to fifth columns display data with increasing angle from major towards minor axis.

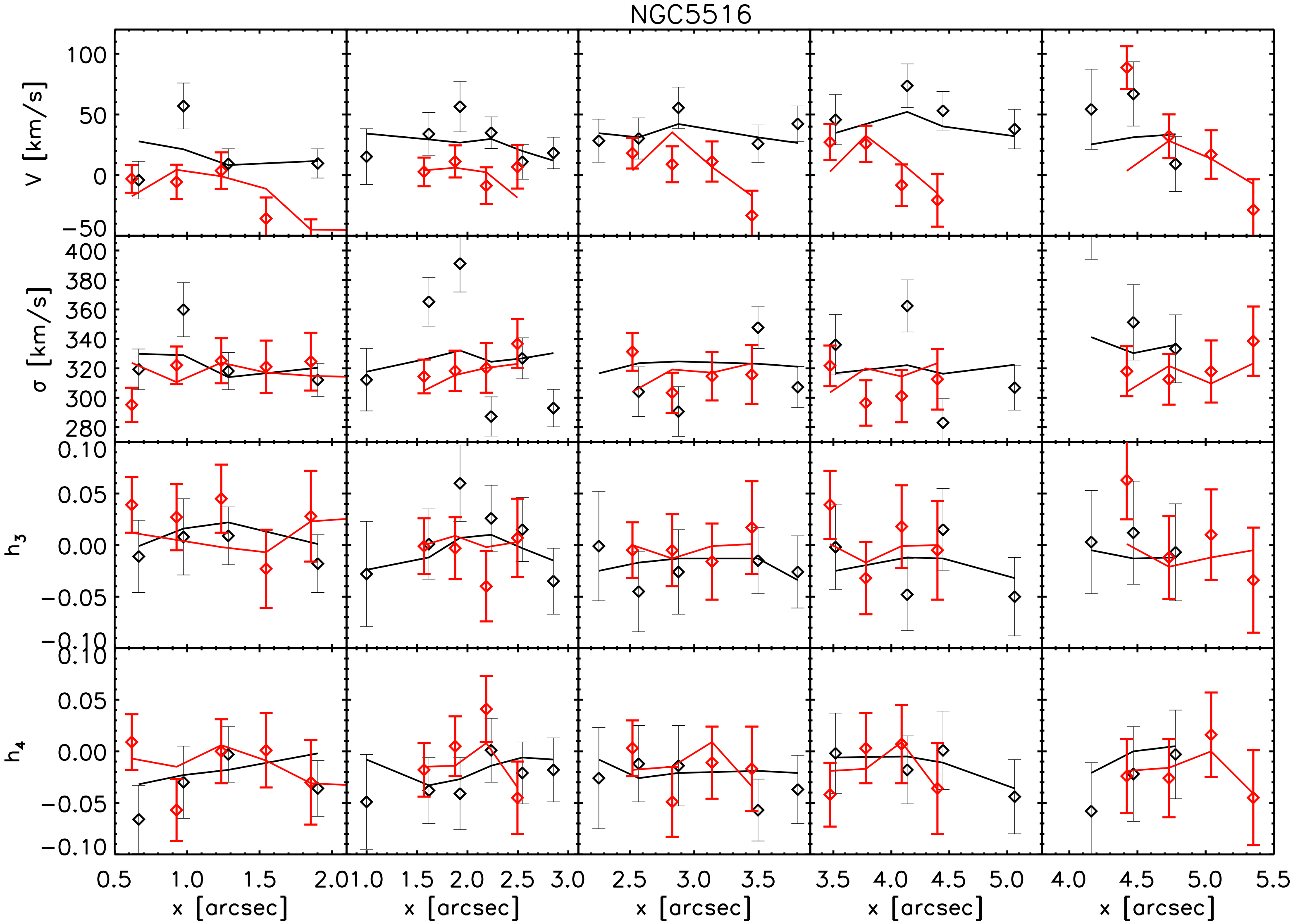

Figure C.7: WiFeS kinematic data (diamonds) and the best-fit model (lines) of NGC 5516. Note that the Gauss-Hermite moments are not plotted as a function of radius but as a function of x-values (or projected radius onto x-axis) of the datapoints. The black diamonds and lines correspond to the set of “slit” data having an angle of 108° and the red color corresponds to the one with an angle of 72° (see Section 4.3.2).

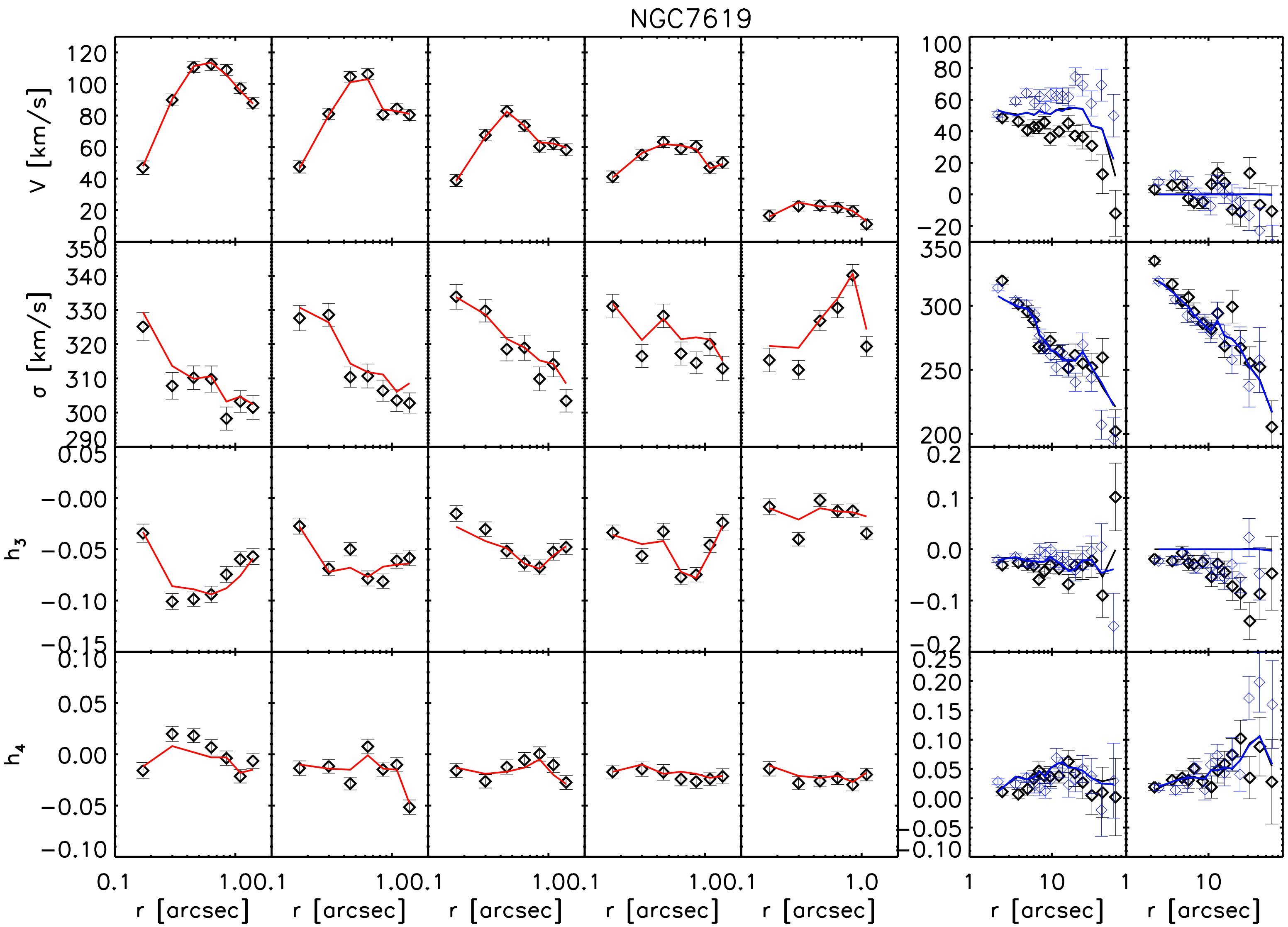

Figure C.8: Kinematic data (diamonds) and the best-fit model (lines) of NGC 7619. The first to fifth columns display SINFONI data with increasing angle from major towards minor axis. The 6th column shows both sides of the major axis data from Pu et al. (2010). The 7th column show both sides of minor axis data from the same paper. The different colors represent data from different sides.

Bibliography

Abramowitz M., Stegun I. A., 1972, Handbook of Mathematical Functions with Formulas, Graphs, and Mathematical Tables

Abuter R., Schreiber J., Eisenhauer F., Ott T., Horrobin M., Gillesen S., 2006, New Astronomy Review, 50, 398

Aller M. C., Richstone D., 2002, AJ, 124, 3035

Armitage P. J., Natarajan P., 2002, ApJ, 567, L9

Baes M., Dejonghe H., De Rijcke S., 2000, MNRAS, 318, 798

Barr J. M., Bedregal A. G., Aragón-Salamanca A., Merrifield M. R., Bamford S. P., 2007, A&A, 470, 173

Bechtold J., Siemiginowska A., Shields J., Czerny B., Janiuk A., Hamann F., Aldcroft T. L., Elvis M., Dobrzycki A., 2003, ApJ, 588, 119

Begelman M. C., Blandford R. D., Rees M. J., 1980, Nature, 287, 307

Beifiori A., Sarzi M., Corsini E. M., Dalla Bontà E., Pizzella A., Coccato L., Bertola F., 2009, ApJ, 692, 856

Bender R., 1990, A&A, 229, 441

Bender R., Moellenhoff C., 1987, A&A, 177, 71

Bender R., Saglia R. P., Gerhard O. E., 1994, MNRAS, 269, 785

Bernardi M., Sheth R. K., Nichol R. C., Miller C. J., Schlegel D., Frieman J., Schneider D. P., Subbarao M., York D. G., Brinkmann J., 2006, AJ, 131, 2018

Bernardi M., Sheth R. K., Tundo E., Hyde J. B., 2007, ApJ, 660, 267

Bertin E., Mellier Y., Radovich M., Missonnier G., Didelon P., Morin B., 2002, in D. A. Bohlender, D. Durand, & T. H. Handley ed., Astronomical Data Analysis Software and Systems XI, Vol. 281 of ASP Conf. Ser., The TERAPIX Pipeline. p. 228

Binney J., Mamon G. A., 1982, MNRAS, 200, 361

Binney J., Merrifield S., 1998, Galactic astronomy

Binney J., Tremaine S., 1987, Galactic dynamics

Bonaccini D., Hackenberg W. K., Cullum M. J., Brunetto E., Ott T., Quattri M., Allaert E., Dimmler M., Tarenghi M., Van Kersteren A., Di Chirico C., Buzzoni B., Gray P., Tamai R., Tapia M., 2002, in R. K. Tyson, D. Bonaccini, & M. C. Roggemann ed., Society of Photo-Optical Instrumentation Engineers (SPIE) Conference Series Vol. 4494 of SPIE Conf. Ser., ESO VLT laser guide star facility. pp 276–289

Bonnet H., Conzelmann R., Delabre B., Donaldson R., Fedrigo E., Hubin N. N., Kissler-Patig M., Lizon J.-L., Paufique J., Rossi S., Stroebele S., Tordo S., 2004b, in D. Bonaccini Calia, B. L. Ellerbroek, & R. Ragazzoni ed., SPIE Conf. Ser. Vol. 5490 of Society of Photo-Optical Instrumentation Engineers (SPIE) Conference Series, First light of SINFONI AO-module at VLT. pp 130–138

Bonnet H., Conzelmann R., Delabre B., Donaldson R., Fedrigo E., Hubin N. N., Kissler-Patig M., Lizon J.-L., Paufique J., Rossi S., Stroebele S., Tordo S., 2004a, The Messenger, 117, 17

Bonnet H., Ströbele S., Biancat-Marchet F., Brynnel J., Conzelmann R. D., Delabre B., Donaldson R., Farinato J., Fedrigo E., Hubin N. N., Kasper M. E., Kissler-Patig M., 2003, in P. L. Wizinowich & D. Bonaccini ed., SPIE Conf. Ser. Vol. 4839 of Society of Photo-Optical Instrumentation Engineers (SPIE) Conference Series, Implementation of MACAO for SINFONI at the VLT, in NGS and LGS modes. pp 329–343

Bower G. A., Green R. F., Danks A., Gull T., Heap S., Hutchings J., Joseph C., Kaiser M. E., et al. 1998, ApJ, 492, L111

Boylan-Kolchin M., Ma C.-P., Quataert E., 2004, ApJ, 613, L37

Boyle B. J., Shanks T., Croom S. M., Smith R. J., Miller L., Loaring N., Heymans C., 2000, MNRAS, 317, 1014

Brighenti F., Mathews W. G., 1999, ApJ, 527, L89

Burkert A., Tremaine S., 2010, ApJ, 720, 516

Buta R., Corwin Jr. H. G., de Vaucouleurs G., de Vaucouleurs A., Longo G., 1995, AJ, 109, 517

Caon N., Capaccioli M., D'Onofrio M., 1994, A&AS, 106, 199

Cappellari M., Bacon R., Bureau M., Damen M. C., Davies R. L., de Zeeuw P. T., Emsellem E., Falcón-Barroso J., Krajnović D., Kuntschner H., McDermid R. M., Peletier R. F., Sarzi M., van den Bosch R. C. E., van de Ven G., 2006, MNRAS, 366, 1126

Chandrasekhar S., 1931, ApJ, 74, 81

Chatterjee P., Hernquist L., Loeb A., 2003, ApJ, 592, 32

Chokshi A., Turner E. L., 1992, MNRAS, 259, 421

Churazov E., Forman W., Vikhlinin A., Tremaine S., Gerhard O., Jones C., 2008, MNRAS, 388, 1062

Ciotti L., Bertin G., 1999, A&A, 352, 447

Ciotti L., Pellegrini S., 2004, MNRAS, 350, 609

Conroy C., van Dokkum P., 2011, ArXiv e-prints

Cretton N., van den Bosch F. C., 1999, ApJ, 514, 704

de Souza R. E., Gadotti D. A., dos Anjos S., 2004, ApJS, 153, 411

Di Matteo T., Springel V., Hernquist L., 2005, Nature, 433, 604

Diehl S., Statler T. S., 2007, ApJ, 668, 150

Djorgovski S. B., 1985, PhD thesis, California Univ., Berkeley.

Dong X. Y., De Robertis M. M., 2006, AJ, 131, 1236

D'Onofrio M., Zaggia S. R., Longo G., Caon N., Capaccioli M., 1995, A&A, 296, 319

Dopita M., Hart J., McGregor P., Oates P., Bloxham G., Jones D., 2007, Ap&SS, 310, 255

Dopita M., Rhee J., Farage C., McGregor P., Bloxham G., Green A., Roberts B., Neilson J., Wilson G., Young P., Firth P., Busarello G., Merluzzi P., 2010, Ap&SS, 327, 245

Ebisuzaki T., Makino J., Okumura S. K., 1991, Nature, 354, 212

Eisenhauer F., et al., 2003a, in M. Iye & A. F. M. Moorwood ed., SPIE Conf. Ser. Vol. 4841 of Society of Photo-Optical Instrumentation Engineers (SPIE) Conference Series, SINFONI - Integral field spectroscopy at 50 milli-arcsecond resolution with the ESO VLT. p. 1548

Eisenhauer F., et al., 2003b, The Messenger, 113, 17

Fabricius M. H., Bender R., Drory N., Grupp F., Hill G. J., Hopp U., 2008, in M. Bureau, E. Athanassoula, & B. Barbuy ed., IAU Symposium Vol. 245 of IAU Symposium, VIRUS-W A fiber based integral field unit spectrograph for the study of galaxy bulges. pp 417–418

Fabricius M. H., Saglia R. P., Fisher D. B., Drory N., Bender R., Hopp U., 2012, submitted to ApJ

Ferrarese L., Côté P., Jordán A., Peng E. W., Blakeslee J. P., Piatek S., Mei S., Merritt D., Milosavljević M., Tonry J. L., West M. J., 2006, ApJS, 164, 334

Ferrarese L., Ford H. C., Jaffe W., 1996, ApJ, 470, 444

Ferrarese L., Merritt D., 2000, ApJ, 539, L9

Ferrarese L., van den Bosch F. C., Ford H. C., Jaffe W., O'Connell R. W., 1994, AJ, 108, 1598

Fukazawa Y., Botoya-Nonesa J. G., Pu J., Ohto A., Kawano N., 2006, ApJ, 636, 698

Gadotti D. A., 2008, MNRAS, 384, 420

Gebhardt K., Adams J., Richstone D., Lauer T. R., Faber S. M., Gültekin K., Murphy J., Tremaine S., 2011, ApJ, 729, 119

Gebhardt K., et al., 2000a, ApJ, 539, L13

Gebhardt K., et al., 2000b, AJ, 119, 1157

Gebhardt K., Richstone D., Tremaine S., Lauer T. R., Bender R., Bower G., Dressler A., Faber S. M., Filippenko A. V., Green R., Grillmair C., Ho L. C., Kormendy J., Magorrian J., Pinkney J., 2003, ApJ, 583, 92

Gebhardt K., Thomas J., 2009, ApJ, 700, 1690

Gerhard O. E., 1993, MNRAS, 265, 213

Ghez A. M., Salim S., Hornstein S. D., Tanner A., Lu J. R., Morris M., Becklin E. E., Duchêne G., 2005, ApJ, 620, 744

Gillessen S., Eisenhauer F., Fritz T. K., Bartko H., Dodds-Eden K., Pfuhl O., Ott T., Genzel R., 2009, ApJ, 707, L114

Gössl C. A., Riffeser A., 2002, A&A, 381, 1095

Graham A. W., 2004, ApJ, 613, L33

Graham A. W., Driver S. P., 2005, PASA, 22, 118

Graham A. W., Erwin P., Caon N., Trujillo I., 2001, ApJ, 563, L11

Graham A. W., Erwin P., Trujillo I., Asensio Ramos A., 2003, AJ, 125, 2951

Granato G. L., De Zotti G., Silva L., Bressan A., Danese L., 2004, ApJ, 600, 580

Grillo C., Gobat R., Lombardi M., Rosati P., 2009, A&A, 501, 461

Gualandris A., Merritt D., 2008, ApJ, 678, 780

Gültekin K., et al., 2009a, ApJ, 695, 1577

Gültekin K., et al., 2009b, ApJ, 698, 198

Häring N., Rix H., 2004, ApJ, 604, L89

Harms R. J., Ford H. C., Tsvetanov Z. I., Hartig G. F., Dressel L. L., Kriss G. A., Bohlin R., Davidsen A. F., Margon B., Kochhar A. K., 1994, ApJ, 435, L35

Holtzman J. A., Burrows C. J., Casertano S., Hester J. J., Trauger J. T., Watson A. M., Worthey G., 1995, PASP, 107, 1065

Humphrey P. J., Buote D. A., Brighenti F., Gebhardt K., Mathews W. G., 2008, ApJ, 683, 161

Humphrey P. J., Buote D. A., Brighenti F., Gebhardt K., Mathews W. G., 2009, ApJ, 703, 1257 (H09)

Johnson R., Chakrabarty D., O'Sullivan E., Raychaudhury S., 2009, ApJ, 706, 980

Kelly B. C., 2007, ApJ, 665, 1489

Kormendy J., Bender R., 2009, ApJ, 691, L142

Kormendy J., Fisher D. B., Cornell M. E., Bender R., 2009, ApJS, 182, 216

Kormendy J., Richstone D., 1995, ARAA, 33, 581

Kuijken K., Fisher D., Merrifield M. R., 1996, MNRAS, 283, 543 (K96)

Kundu A., Whitmore B. C., 2001, AJ, 122, 1251

Lauer T. R., Ajhar E. A., Byun Y.-I., Dressler A., Faber S. M., Grillmair C., Kormendy J., Richstone D., Tremaine S., 1995, AJ, 110, 2622

Lauer T. R., Faber S. M., Gebhardt K., Richstone D., Tremaine S., Ajhar E. A., Aller M. C., Bender R., Dressler A., Filippenko A. V., Green R., Grillmair C. J., Ho L. C., Kormendy J., Magorrian J., Pinkney J., Siopis C., 2005, AJ, 129, 2138

Lauer T. R., Faber S. M., Richstone D., Gebhardt K., Tremaine S., Postman M., Dressler A., Aller M. C., Filippenko A. V., Green R., Ho L. C., Kormendy J., Magorrian J., Pinkney J., 2007, ApJ, 662, 808

Lauer T. R., Gebhardt K., Faber S. M., Richstone D., Tremaine S., Kormendy J., Aller M. C., Bender R., Dressler A., Filippenko A. V., Green R., Ho L. C., 2007, ApJ, 664, 226

Longo G., Zaggia S. R., Busarello G., Richter G., 1994, A&AS, 105, 433

Lynden-Bell D., 1969, Nature, 223, 690

Magorrian J., 1999, MNRAS, 302, 530

Magorrian J., Tremaine S., Richstone D., Bender R., Bower G., Dressler A., Faber S. M., Gebhardt K., Green R., Grillmair C., Kormendy J., Lauer T., 1998, AJ, 115, 2285

Makino J., Ebisuzaki T., 1996, ApJ, 465, 527

Maoz E., 1995, ApJ, 447, L91

Maoz E., 1998, ApJ, 494, L181

Maraston C., 2005, MNRAS, 362, 799

Marconi A., Hunt L. K., 2003, ApJ, 589, L21

Mármol-Queraltó E., Cardiel N., Cenarro A. J., Vazdekis A., Gorgas J., Pedraz S., Peletier R. F., Sánchez-Blázquez P., 2008, A&A, 489, 885

Mauder H., 1973, A&A, 28, 473

McConnell N. J., et al., 2011a, ApJ, 728, 100

McConnell N. J., et al., 2011b, Nature, 480, 215

Mehlert D., Saglia R. P., Bender R., Wegner G., 2000, A&AS, 141, 449

Mei S., Blakeslee J. P., Côté P., Tonry J. L., West M. J., Ferrarese L., Jordán A., Peng E. W., Anthony A., Merritt D., 2007, ApJ, 655, 144

Mei S., Blakeslee J. P., Tonry J. L., Jordán A., Peng E. W., Côté P., Ferrarese L., West M. J., Merritt D., Milosavljević M., 2005, ApJ, 625, 121

Merloni A., Bongiorno A., Bolzonella M., et al. 2010, ApJ, 708, 137

Merritt D., 1997, AJ, 114, 228

Merritt D., 2006, ApJ, 648, 976

Merritt D., Mikkola S., Szell A., 2007, ApJ, 671, 53

Milosavljević M., Merritt D., 2001, ApJ, 563, 34

Milosavljević M., Merritt D., Rest A., van den Bosch F. C., 2002, MNRAS, 331, L51

Miyoshi M., Moran J., Herrnstein J., Greenhill L., Nakai N., Diamond P., Inoue M., 1995, Nature, 373, 127

Modigliani A., Bellester P., Peron M., 2008, SINFONI Pipeline User Manual, Issue 8.0

Modigliani A., Hummel W., Abuter R., Amico P., Ballester P., Davies R., Dumas C., Horrobin M., Neeser M., Kissler-Patig M., Peron M., Rehunanen J., Schreiber J., Szeifert T., 2007, arXiv:astro-ph/0701297

Nagino R., Matsushita K., 2009, A&A, 501, 157

Nakano T., Makino J., 1999, ApJ, 510, 155

Nandra K., George I. M., Mushotzky R. F., Turner T. J., Yaqoob T., 1997, ApJ, 477, 602

Napolitano N. R., Romanowsky A. J., Tortora C., 2010, MNRAS, 405, 2351

Navarro J. F., Frenk C. S., White S. D. M., 1996, ApJ, 462, 563

Netzer H., 2003, ApJ, 583, L5

Nowak N., 2009, PhD Thesis

Nowak N., Saglia R. P., Thomas J., Bender R., Davies R. I., Gebhardt K., 2008, MNRAS, 391, 1629

Nowak N., Saglia R. P., Thomas J., Bender R., Pannella M., Gebhardt K., Davies R. I., 2007, MNRAS, 379, 909

Nowak N., Thomas J., Erwin P., Saglia R. P., Bender R., Davies R. I., 2010, MNRAS, 403, 646

Ogando R. L. C., Maia M. A. G., Pellegrini P. S., da Costa L. N., 2008, AJ, 135, 2424

Poulain P., Nieto J.-L., 1994, A&AS, 103, 573

Prugniel P., Heraudeau P., 1998, A&AS, 128, 299

Pu S. B., Saglia R. P., Fabricius M. H., Thomas J., Bender R., Han Z., 2010, A&A, 516, A4

Rabien S., Davies R. I., Ott T., Li J., Abuter R., Kellner S., Neumann U., 2004, in D. Bonaccini Calia, B. L. Ellerbroek, & R. Ragazzoni ed., SPIE Conf. Ser. Vol. 5490 of Society of Photo-Optical Instrumentation Engineers (SPIE) Conference Series, Test performance of the PARSEC laser system. pp 981–988

Ravindranath S., Ho L. C., Filippenko A. V., 2002, ApJ, 566, 801

Reid N., Boisson C., Sansom E. A., 1994, MNRAS, 269, 713

Rhoades C. E., Ruffini R., 1974, Physical Review Letters, 32, 324

Richstone D., Ajhar E. A., Bender R., Bower G., Dressler A., Faber S. M., Filippenko A. V., Gebhardt K., Green R., Ho L. C., Kormendy J., Lauer T. R., Magorrian J., Tremaine S., 1998, Nature, 395, A14

Richstone D. O., Tremaine S., 1988, ApJ, 327, 82

Rodgers A. W., Conroy P., Bloxham G., 1988, PASP, 100, 626

Rodriguez C., Taylor G. B., Zavala R. T., Peck A. B., Pollack L. K., Romani R. W., 2006, ApJ, 646, 49

Romanowsky A. J., Strader J., Spitler L. R., Johnson R., Brodie J. P., Forbes D. A., Ponman T., 2009, AJ, 137, 4956

Rusli S. P., Thomas J., Erwin P., Saglia R. P., Nowak N., Bender R., 2011, MNRAS, 410, 1223

Saglia R. P., Bertschinger E., Baggley G., Burstein D., Colless M., Davies R. L., McMahan Jr. R. K., Wegner G., 1993, MNRAS, 264, 961

Saglia R. P., Fabricius M., Bender R., Montalto M., Lee C.-H., Riffeser A., Seitz S., Morganti L., Gerhard O., Hopp U., 2010, A&A, 509, A61

Saglia R. P., Maraston C., Thomas D., Bender R., Colless M., 2002, ApJ, 579, L13

Saha P., Williams T. B., 1994, AJ, 107, 1295

Salpeter E. E., 1964, MNRAS, 140, 796

Salviander S., Shields G. A., Gebhardt K., Bernardi M., Hyde J. B., 2008, ApJ, 687, 828

Sargent W. L. W., Young P. J., Lynds C. R., Boksenberg A., Shortridge K., Hartwick F. D. A., 1978, ApJ, 221, 731

Schmidt M., 1963, Nature, 197, 1040

Schreiber J., Thatte N., Eisenhauer F., Tecza M., Abuter R., Horrobin M., 2004, in F. Ochsenbein, M. G. Allen, & D. Egret ed., Astronomical Data Analysis Software and Systems XIII, Vol. 314 of ASP Conf. Ser., Data Reduction Software for the VLT Integral Field Spectrometer SPIFFI. p. 380

Schulze A., Gebhardt K., 2011, ApJ, 729, 21

Schwarzschild M., 1979, ApJ, 232, 236

Sérsic J. L., 1963, BAAA, 6, 41

Sérsic J. L., 1968, Atlas de Galaxias Australes (Cordoba: Observatorio Astronomico)

Seyfert C. K., 1943, ApJ, 97, 28

Shen J., Gebhardt K., 2010, ApJ, 711, 484

Shields G. A., Gebhardt K., 2004, Bull. AAS, 36, 766

Shields G. A., Menezes K. L., Massart C. A., Vanden Bout P., 2006, ApJ, 641, 683

Shields G. A., Salviander S., Bonning E. W., 2006, New Astronomy Review, 50, 809

Silge J. D., Gebhardt K., 2003, AJ, 125, 2809

Silk J., Rees M. J., 1998, A&A, 331, L1

Simien F., Prugniel P., 2000, A&AS, 145, 263

Siopis C., Gebhardt K., Lauer T. R., Kormendy J., Pinkney J., Richstone D., Faber S. M., Tremaine S., Aller M. C., Bender R., Bower G., Dressler A., Filippenko A. V., Green R., Ho L. C., Magorrian J., 2009, ApJ, 693, 946

Sirianni M., Jee M. J., Benítez N., Blakeslee J. P., Martel A. R., Meurer G., Clampin M., De Marchi G., Ford H. C., Gilliland R., Hartig G. F., Illingworth G. D., Mack J., McCann W. J., 2005, PASP, 117, 1049

Soltan A., 1982, MNRAS, 200, 115

Somerville R. S., Hopkins P. F., Cox T. J., Robertson B. E., Hernquist L., 2008, MNRAS, 391, 481

Spolaor M., et al., 2008a, MNRAS, 385, 667

Spolaor M., et al., 2008b, MNRAS, 385, 675

Thomas J., Saglia R. P., Bender R., Thomas D., Gebhardt K., Magorrian J., Corsini E. M., Wegner G., 2007, MNRAS, 382, 657

Thomas J., Saglia R. P., Bender R., Thomas D., Gebhardt K., Magorrian J., Corsini E. M., Wegner G., 2009, ApJ, 691, 770

Thomas J., Saglia R. P., Bender R., Thomas D., Gebhardt K., Magorrian J., Corsini E. M., Wegner G., Seitz S., 2011, MNRAS, 415, 545

Thomas J., Saglia R. P., Bender R., Thomas D., Gebhardt K., Magorrian J., Richstone D., 2004, MNRAS, 353, 391

Tonry J. L., Dressler A., Blakeslee J. P., Ajhar E. A., Fletcher A. B., Luppino G. A., Metzger M. R., Moore C. B., 2001, ApJ, 546, 681

Trager S. C., Worthey G., Faber S. M., Burstein D., Gonzalez J. J., 1998, ApJS, 116, 1

Tremaine S., Gebhardt K., Bender R., Bower G., Dressler A., Faber S. M., Filippenko A. V., Green R., Grillmair C., Ho L. C., Kormendy J., Lauer T. R., Magorrian J., Pinkney J., Richstone D., 2002, ApJ, 574, 740

Treu T., Auger M. W., Koopmans L. V. E., Gavazzi R., Marshall P. J., Bolton A. S., 2009, ApJ, submitted (arXiv:0911.3392)

Trujillo I., Erwin P., Asensio Ramos A., Graham A. W., 2004, AJ, 127, 1917

Tundo E., Bernardi M., Hyde J. B., Sheth R. K., Pizzella A., 2007, ApJ, 663, 53

van den Bosch R. C. E., de Zeeuw P. T., 2010, MNRAS, 401, 1770

van den Bosch R. C. E., van de Ven G., Verolme E. K., Cappellari M., de Zeeuw P. T., 2008, MNRAS, 385, 647

van der Marel R. P., Binney J., Davies R. L., 1990, MNRAS, 245, 582

van der Marel R. P., Cretton N., de Zeeuw P. T., Rix H.-W., 1998, ApJ, 493, 613

van der Marel R. P., Franx M., 1993, ApJ, 407, 525

Vestergaard M., 2004, ApJ, 601, 676

Wyithe J. S. B., 2006, MNRAS, 365, 1082

Wyithe J. S. B., Loeb A., 2003, ApJ, 595, 614

Yoo J., Miralda-Escudé J., Weinberg D. H., Zheng Z., Morgan C. W., 2007, ApJ, 667, 813

Young P. J., Westphal J. A., Kristian J., Wilson C. P., Landauer F. P., 1978, ApJ, 221, 721

Yu Q., 2002, MNRAS, 331, 935

Yu Q., Tremaine S., 2002, MNRAS, 335, 965

Zel'Dovich Y. B., Novikov I. D., 1964, Soviet Physics - Doklady, 9, 195

Acknowledgements

I would like to thank Ralf Bender for giving me the opportunity to work on this interesting project, for allocating observing time that forms the basis of this thesis and for his support during the thesis period.

I thank my supervisor Roberto Saglia for his guidance, assistance, support and understanding since I started the project.

I benefit from many discussions with Jens Thomas, Peter Erwin, Nina Nowak and Maximilian Fabricius. I acknowledge their continuous help in dealing with data and codes. I would also like to thank Chien-Hsiu Lee, Arno Riffeser and Robert Sharp for their contribution in observing and reducing the photometric and large scale kinematic data of NGC5516.

I value both the scientific and social interaction within the dynamics group led by Ortwin Gerhard.

Finally, I am most grateful to my family who has been supportive all these years, to my husband Raymond and to his family for warmly welcoming me in their home.